

# University of St Andrews



Full metadata for this thesis is available in  
St Andrews Research Repository  
at:

<http://research-repository.st-andrews.ac.uk/>

This thesis is protected by original copyright

# **OPTIMISATION OF PERFORMANCE OF TIN OXIDE BASED ANODES FOR HIGH ENERGY DENSITY LITHIUM BATTERIES**

A thesis submitted for the degree of Ph.D.

by

**Pierrot S. ATTIDEKOU**



**University  
Of  
St. Andrews**

**Supervised by Prof. John T. S. IRVINE**

Submitted March 2005



## Declarations

I, Pierrot S. ATTIDEKOU, hereby certify that this thesis, which is approximately 38000 words in length, has been written by me, that it is the record of work carried out by me and that it has not been submitted in any previous application for a higher degree.

Date 04/03/2005            signature of candidate

I was admitted as a research student in October 2001 and as a candidate for the degree of Ph.D in October 2001; the higher study for which this is a record was carried out in the University of St Andrews between 2001 and 2004.

Date 04/03/2005            signature of candidate

I hereby certify that the candidate has fulfilled the conditions of the Resolution and Regulations appropriate for the degree of Doctor of Philosophy in the University of St Andrews and that the candidate is qualified to submit this thesis in application for that degree.

Date 04/03/2005            signature of supervisor

In submitting this thesis to the University of St Andrews, I understand that I am giving permission for it to be available for use in accordance with the regulations of the University Library for the time being in force, subject to any copyright vested in the work not being affected thereby. I also understand that the title and abstract will be published, and that a copy of the work may be made and supplied by any bona fide library or research worker.

Date 04/03/2005            signature of candidate

## Table of Contents.

1.	Introduction. ....	1
1.1.	Primary batteries. ....	3
1.1.1.	Zinc-Carbon Cells. ....	3
1.1.2.	Zinc-Manganese dioxide Cells. ....	4
1.1.3.	Alkaline-Manganese Cells. ....	5
1.1.4.	Button or Coin Cells. ....	6
1.2.1.	Lead-acid batteries. ....	7
1.2.2.	Alkaline batteries. ....	8
1.2.3.	Nickel-Metal-hydride batteries. ....	10
1.3.	Lithium batteries. ....	12
1.3.1.	Electrolyte. ....	13
1.3.2.	Primary lithium batteries. ....	15
1.3.3.	Secondary lithium batteries. ....	17
1.3.4.	Secondary lithium-ion batteries. ....	20
1.3.4.1.	Electrolyte. ....	21
1.3.4.2.	Materials for positive electrodes. ....	21
1.3.4.3.	Materials for negative electrodes. ....	23
1.3.4.4.	Metal oxides anodes. ....	24
1.3.4.5.	Alloys. ....	25
1.3.4.6.	Lithium-tin alloys. ....	28
1.3.4.7.	Tin based oxide compounds. ....	30
1.3.5.	Overview of materials investigated. ....	33
1.3.5.1.	SnP <sub>2</sub> O <sub>7</sub> . ....	33

1.3.5.2.	SnO <sub>2</sub> :B <sub>2</sub> O <sub>3</sub> and doped (SnO <sub>2</sub> :B <sub>2</sub> O <sub>3</sub> ) <sub>y/2</sub> /(SnP <sub>2</sub> O <sub>7</sub> ) <sub>1-y/2</sub> with 0 ≤ y ≤ 2. ....	34
1.3.5.3.	TiP <sub>2</sub> O <sub>7</sub> and doped Ti <sub>1-y</sub> Sn <sub>y</sub> P <sub>2</sub> O <sub>7</sub> with 0 ≤ y ≤ 1. ....	35
1.4.	Aim of this work. ....	36
1.5.	References. ....	37
2.	Experimental. ....	43
2.1.	Materials. ....	43
2.1.1.	SnP <sub>2</sub> O <sub>7</sub> (cubic phase). ....	43
2.1.1.1.	Synthesis route 1. ....	43
2.1.1.2.	Synthesis route 2. ....	44
2.1.2.	Boron doped SnO <sub>2</sub> :xB <sub>2</sub> O <sub>5</sub> :(1-x)P <sub>2</sub> O <sub>5</sub> (cubic & amorphous phases). ....	44
2.1.3.	Titanium doped Sn <sub>(1-x)</sub> Ti <sub>x</sub> P <sub>2</sub> O <sub>7</sub> .(cubic). ....	45
2.2.1.	Electrode preparation. ....	45
2.2.2.	Cell preparation. ....	46
2.2.3.	Standard coin cell. ....	47
2.3.	Electrochemical process overview. ....	49
2.3.1.	Background. ....	49
2.3.2.	Capacity calculation. ....	50
2.4.	Electrochemical Testing. ....	51
2.4.1.	Galvanostatic mode. ....	51
2.4.2.	Potentiostatic mode. ....	53
2.4.3.	Advanced Electrochemical Techniques. ....	54
2.4.3.1.	SPECS. ....	55
2.5.	Characterisation Techniques. ....	59
2.5.1.	Background. ....	59

2.5.1.1.	X-ray generation.....	59
2.5.1.2.	X-Ray.....	61
2.5.1.2.a.	Bragg's law.....	61
2.5.1.3.	Powder diffraction technique.....	62
2.5.1.4.	Particles size measurement.....	64
2.5.1.5.	The STOE Transmission Diffractometer.....	64
2.5.1.6.	Preparation of sample for XRD.....	65
2.5.1.7.	In-situ XRD.....	66
2.6.	MAS-NMR.....	69
2.6.1.	Background.....	69
2.6.2.	Dipole-dipole interactions and Magic Angle Spinning (MAS) NMR..	71
2.6.3.	Zeemann interactions.....	72
2.6.4.	Chemical shift anisotropy.....	74
2.6.5.	Spin coupling interactions.....	77
2.6.6.	Quadrupolar interactions.....	77
2.6.7.	Pulse.....	78
2.6.8.	Experimental conditions.....	80
2.7.	Electron Microscopy.....	81
2.7.1.	SAED.....	81
2.7.2.	HRTEM.....	82
2.7.3.	Preparation of sample for SAED, HRTEM – EDS.....	82
2.7.4.	SEM.....	83
2.7.5.	Preparation of sample for SEM – EDS.....	84
2.8.	IR.....	85

2.9.	XPS. ....	85
2.10.	TGA, DTA. ....	86
2.11.	References. ....	88
3.	SnP <sub>2</sub> O <sub>7</sub> . ....	89
3.1.	Physical characterisation of material investigated. ....	89
3.1.1.	Powder X-ray Diffraction: (XRD). ....	89
3.1.2.	Transmission Electron Microscopy: (TEM). ....	91
3.1.2.1.	Selected Area Electron Microscopy (SAED). ....	91
3.1.2.2.	High Resolution Transmission Electron Microscopy (HRTEM). ....	94
3.1.2.3.	Scanning Electron Microscopy: (SEM-EDS). ....	97
3.1.2.4.	Thermogravimetric Analysis: (TGA/DTA). ....	99
3.1.3.	Electrochemical characterisation. ....	100
3.2.1.	Electrochemical results and discussion. ....	100
3.2.1.1.	<sup>31</sup> P NMR results and discussion. ....	104
3.2.1.2.	<sup>6</sup> Li NMR results and discussion. ....	108
3.2.1.3.	Infrared (IR). ....	111
3.2.1.4.	X-Ray Photoelectron Spectroscopy (XPS). ....	113
3.3.	SPECS. ....	116
3.3.1.	Background. ....	116
3.3.2.	Results and discussion. ....	118
3.3.3.	Region I. ....	119
3.3.3.1.	Thermodynamic aspects of SnP <sub>2</sub> O <sub>7</sub> upon discharge in region I. ....	119
3.3.4.	Region II. ....	127
3.3.4.1.	Structural characterisation of region II. ....	127

3.3.4.1.1. HRTEM.....	127
3.3.4.1.2. SAED. ....	128
3.3.4.2. Kinetic behaviour of $\text{SnP}_2\text{O}_7$ upon discharge in region II. ....	134
3.3.4.3. SPECS: Methodology of diffusion calculation. ....	135
3.3.4.4.a. Short time approximation.....	136
3.3.4.4.b. Long time approximation.....	138
3.3.4.5. $\text{SnP}_2\text{O}_7$ diffusion coefficient in region II. ....	139
3.3.4.6. Diffusion coefficient for battery at $9^\circ\text{C}$ . ....	139
3.3.4.6.a. Short time approximation for discharged battery at $9^\circ\text{C}$ . ....	140
3.3.4.6.b. Long time approximation for discharged battery at $9^\circ\text{C}$ .....	141
3.3.4.7. Diffusion coefficient for battery at room temperature ( $20^\circ\text{C}$ ). ....	143
3.3.4.7.a. Short time approximation for discharged battery at room temperature ( $20^\circ\text{C}$ ). ....	144
3.3.4.7.b. Long time approximation for discharged battery at room temperature ( $20^\circ\text{C}$ ). ....	145
3.3.5. Region III. ....	148
3.3.5.1. Electrochemistry. ....	148
3.3.5.2. Electron Microscopy of $10.4\text{Li}^+/\text{Li}_x\text{SnP}_2\text{O}_7$ .....	149
3.3.5.2.a. SAED of $10.4\text{Li}^+/\text{Li}_x\text{SnP}_2\text{O}_7$ .....	149
3.3.6. Performance. ....	153
3.3.7. Conclusion.....	155
3.3.8. References. ....	157
4. Boron doped tin pyrophosphate. ....	160
4.1. Introduction. ....	160

4.2.	Results and discussion.....	161
4.2.1.	XRD. ....	161
4.2.2.	SAED. ....	166
4.2.3.	SEM.....	168
4.2.4.	NMR.....	171
4.2.4.1.	<sup>31</sup> P NMR result.....	171
4.2.4.2.	Discussion of <sup>31</sup> P NMR.....	174
4.2.4.3.	<sup>11</sup> B NMR results.....	177
4.2.4.4.	Discussion of <sup>11</sup> B NMR. ....	180
4.3.	Electrochemistry and NMR.....	182
4.4.	Performance. ....	193
4.5.	Conclusion.....	195
4.6.	References. ....	196
5.	Titanium doped tin pyrophosphate system. ....	198
5.1.	Sn <sub>1-x</sub> Ti <sub>y</sub> P <sub>2</sub> O <sub>7</sub> .....	198
5.1.1.	Powder X-ray Diffraction: (XRD). ....	198
5.1.2.	IR.....	202
5.2.1.	Selected Area Electron Microscopy (SAED).....	205
5.2.2.	High Resolution Transmission Electron Microscopy (HRTEM).....	207
5.3.	<sup>31</sup> P NMR results and discussion.....	209
5.4.	Electrochemical characterisation. ....	211
5.4.1.	TiP <sub>2</sub> O <sub>7</sub> (y = 1).....	211
5.4.1.1.	Galvanostatic and Potentiostatic of TiP <sub>2</sub> O <sub>7</sub> .....	211
5.4.2	In-situ XRD.....	217

5.4.3.	SPECS.....	221
5.4.4.	XPS. ....	228
5.4.4.1.	Titanium Ti-2p <sub>3/2</sub> and Ti-2p <sub>1/2</sub> .....	228
5.4.4.2.	Phosphorus P-2p <sub>3/2</sub> .....	231
5.4.4.3.	Oxygen O-1s. ....	233
5.4.4.4.	Carbon C-1s. ....	235
5.5.	<sup>31</sup> P NMR results and discussion.....	237
5.6.	HRTEM & SAED of cycled material. ....	241
5.7.	IR.....	244
5.8.	Sn <sub>1-y</sub> Ti <sub>y</sub> P <sub>2</sub> O <sub>7</sub> with y = 0.5. ....	245
5.8.1.	Region I.....	245
5.8.2.	Region II.....	248
5.8.3.	Region III. ....	248
5.8.4.	Region IV.....	249
5.9.	Sn <sub>1-y</sub> Ti <sub>y</sub> P <sub>2</sub> O <sub>7</sub> with y = 0, 0.15, 0.35,0.5, 0.75 & 1. ....	249
5.10.	Conclusion.....	255
5.11.	References.....	257
6.	Conclusion.....	259

## **Acknowledgements.**

Sincerely, from the bottom of my heart, I would like to express my gratitude to all those who have helped and support me so far to achieve this work. The list is too long and I apologise in advance for those missing.

I would like to thank genuinely, my supervisor, John T. S. Irvine for giving me the opportunity of doing a PhD, for his support, advice and encouragement over the past three years. It has been a great pleasure working in his group and though, there is no other word to describe the feeling: the man is just simply GREAT.

Gratitude toward *G.S. Yuasa* for funding without which this PhD would never have been.

I would also like to thank all the members of the JTSI group, especially P. A. Connor for his help, his advice and patience and also Flaviano Garcia who has lead me toward SPECS.

My gratitude goes as well to Jesus Canales, Ross Blackley, Aurelie Debart, Loic Dupont and Wuzong Zhou (for TEM advice), to Steve Francis (for his XPS expertise) to Dave Tunstall and Philip Wormald (for their expertise in solid state NMR) and to Sylvia Williamson (for TGA/TDA and ICP) to Martin Smith and Angela Kruth (for crystallography). In the same category, many thanks for all the members of staff here at St. Andrews who have helped me (Suzanne Knowles) and often make me laugh (Bobby Carthcart, Colin Smith, Jim, etc) and to Fred Belliard for her advice.

To all my friends here in St. Andrews especially my flatmate Fabio Caiani *alias Louis* “*Dude, you see what happens when you .....!*” or “*you go with the flow*”. Many thank to Cristina Jimenez for everything, her support and she has been always there no matter what “*you could have done better, but I don't mind.....*”.

To all the friends and members of JTSI group (Fran, Kelcey, Julie, Marie, Juan Carlos, Alexandro, Steve, Cristian, Anna, John, Shin-Ichi, Belen, Pepe, Alan, Edwin, David, Anne-Laure, Ludovic, Jeff, Nadja, Jochen, Jez, Shanwen, Gil, Matt, Sneh, Gabriel “*je suis desappointe*“, Julien, Tatiana “*I've been a bitch (on the beach) all day*”, Richard “*dancing queen*”, Eileen, etc. To those, I party with and with whom I have socialised during those long nights in town (Alfonso “*Fela & Chet Baker.*”, Panos “*I like..*”, Palumi “*remember the Cellar*”, Dave & Chantal, Mehran “*the hunter*”, David Taddei “*mangeons des pates*”, Andy, Jorge, Robbie, Nancy Neitzel, Amanda, Patricia Menin, Christelle Leandri “*the meme*”, Ailsa, Jane, Bouzid Mena, Lavinia, Caroline, Stephanie, Birgit, Malcolm (for providing the *GUINNESS* in *the Cellar*) etc..

*Now lets go back to France*

Je ne pourrais pas fermer ces pages sans exprimer mes sincerés remerciements a certaines personnes qui m'ont ecoute, soutenu, aide et m'ont carrement considere comme faisant partie de leur famille durant mon parcours du combattant.

Je pense tout d'abord aux tres chers amis de *justruculation et de zingomification intense*, le duo Cedric Broustera *alias Ced* & Edouard Valton *alias Edouardo*,

*EdComPed* ou *Vieux*. Mettons leurs une note de Jazz, les gars pour que ça swingue sans oublier le Julien Pilme.

Ensuite, viennent les familles Valton de Bordeaux, je pense a Michele, Julien, Marie et Dominique. Je vous porterai toujours dans mon coeur et j'espere que vous avez compris le message que je veux vous adresser.

Puis, je me tourne vers la famille Valton et fils de Pau (St-Faust) (Michel, Mino, Lorin, Antho, Paul, Bene Tibo et Kathy. Je voudrais vous dire merci du fond du coeur. Michel, saches que tu es un exemple pour moi et le soutien de ta famille y compris celle de Bordeaux resterons toujours graver dans ma memoire.

J'aimerais exprimer ma gratitude a la famille Attane (Anne, Olivier, Isabelle, Nicole et Jean-Claude sans oublier papi et mamie, que son ame repose en paix).

Merci egalement a Herve Martinez, J. M. Sotiropoulos et au Prof Didier Astruc.

Merci a Lucia Sarasa, Sandrine Callat, Laurence Ters, Franck Grillet, Sandrine et Christelle Larrieu, J. C. et Helene Dupin, Karinne Miqueu, Marilyne Moreau, etc.

Enfin, j'aimerais remercier les membres de ma famille. Je pense aux Attidekou de Talence (Bordeaux) (Ulysse, sa maman Catherine Wuilliet et mon frere Jean Yves). A la famille Attidekou de Lome et d'Abidjan (Viviane, Blandine, Akouele) et a Roger, Benjamin, Lucienne, Rose, tantie Clementine, ses enfants, Ari Akouvi, et tout ceux que j'ai malheureusement oublie.

*Je dedie cette these a ma mere (Helene) et mon pere (Mathias)*

*Attidekou.*

## Abstract.

The goal of this work was to synthesise and investigate a tin based oxide compound,  $\text{SnP}_2\text{O}_7$  and its doped analogues, as a potential negative electrode for lithium battery.  $\text{SnP}_2\text{O}_7$  has two polymorphs: the cubic and the layered forms. It has been proven that the cubic form has a better performance on cycling compared to the layered. This work has focused on the cubic form in order to understand the mechanisms occurring upon charge and discharge in order to improve the capacity and the cycling ability. The achievement of this task requires several steps.

$\text{SnP}_2\text{O}_7$  was synthesised and fully characterised structurally and electrochemically. The structural characterisation has elucidated the complexity of the material that crystallises in a  $3 \times 3 \times 3$  superstructure with the presence of nanodomains. Electrochemical characterisation has shown that on insertion of lithium into the material, finely dispersed tin nanoparticles are formed in an amorphous lithiated pyrophosphate matrix before the tin particles alloy with lithium providing the useful capacity of the battery. This material displays an irreversible capacity of 965mAh/g and a reversible capacity of 365 mAh/g. The overall reaction of lithium toward  $\text{SnP}_2\text{O}_7$  was divided into 3 different zones and the kinetic and thermodynamic features evaluated. The thermodynamic study made on a cell with  $\text{SnP}_2\text{O}_7$  electrode has provided a very high value of entropy upon the conversion of  $\text{SnP}_2\text{O}_7$  to metallic tin plus lithiated pyrophosphate matrix. The lithiated phosphate matrix form is then reduced to another lithiated phosphate matrix, which is stable with an unusual oxidation state of phosphorus that we

believe to be  $P^{IV}$ . The lithium diffusion was estimated as  $8 \times 10^{-15} \text{ cm}^2/\text{s}$  and matches those obtained for other lithium battery materials.

The addition of borate to the tin pyrophosphate system such as  $(\text{SnO}_2:\text{B}_2\text{O}_3)_{y/2}/(\text{SnP}_2\text{O}_7)_{1-y/2}$  was studied in order to lighten the matrix and increase the specific capacity and to evaluate the role of the matrix toward capacity retention. As it has been shown that amorphous materials often cycle better than the crystalline tin composite oxides, the addition of borate should be beneficial due to the decrease in crystallinity. This study has revealed upon substitution 3 different phase domains that were characterised to be crystalline up to  $y = 0.19$ , a mix of crystalline and amorphous ( $0.25 \leq y \leq 1.75$ ) and a fully amorphous region for high borate content ( $y \geq 1.75$ ). At all levels of substitution there was a decrease in both irreversible and reversible capacity. The best capacity of borate doped samples was found in the low borate crystalline region. Therefore borate appears not to be a suitable matrix for lithium batteries.

Titanium was added to  $\text{SnP}_2\text{O}_7$  to see the effect of a smaller cation in the system. Titanium substitution has shown a co-existence of different chemistry types such as both alloying and non-alloying processes for  $\text{Sn}_{1-x}\text{Ti}_x\text{P}_2\text{O}_7$  system. Pure titanium pyrophosphate has shown complex electrochemistry and seems to form a transition metal oxide in a phosphate matrix, with additional formation of SEI that was depicted by HRTEM. The electrochemistry has shown formation of several different linephases, biphasic regions and solid solution transformations. The best

capacity found was for composition with  $y = 0.15$ , which has shown an increase of the reversible capacity of 10% over pure  $\text{SnP}_2\text{O}_7$ .

**1. Introduction.**

Energy storage has been a major area of technology since Alessandro Volta (Italy) described the first battery in 1800. The device was, in essence, the first “battery” and the first source of continuous electric current. Since then the expansion of new battery configuration has been exponential in order to improve power, capacity and decrease size.

A cell is a single electrochemical unit that has a positive side (cathode) and a negative side (anode) with different chemical potentials as shown in **Fig.: 1- 1**. They are separated by the electrolyte that solely allows ionic transportation. When batteries operate, two types of electrochemical reaction must occur in the cell. A release of electrons occurs at the anode side (oxidation) and at the cathode side these electrons are consumed (reduction). The flow of the electrons is external to the system and the electron flux gives the continuous electric current.

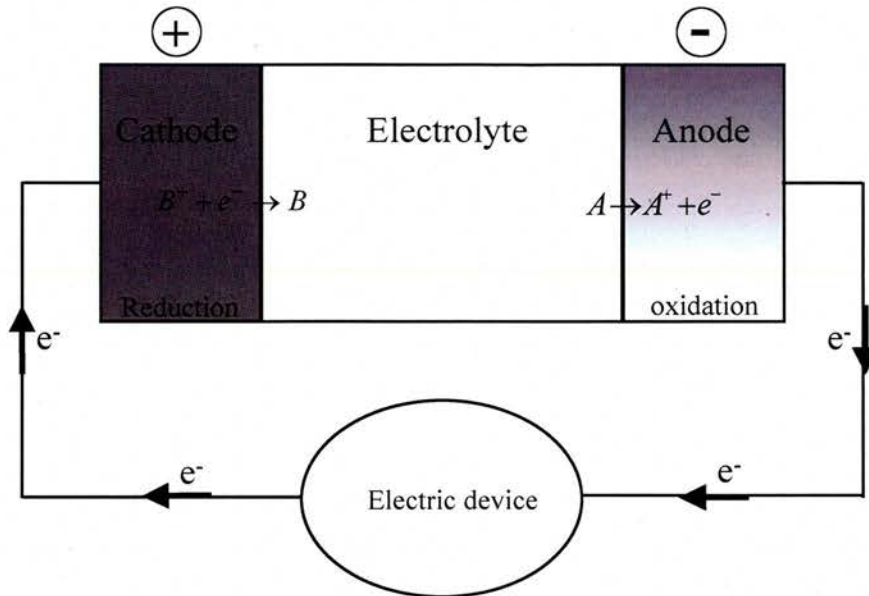


Fig.: 1- 1 Schematic diagram of battery

Batteries are classified in two useful categories: primary and secondary batteries. Primary batteries are designed to deliver a single discharge and are then discarded, therefore they are more expensive and not environment friendly but are reliable. They are typified by the Daniel cell (London, 1836) commercially used for the telegraphic system and the Leclanche cell (France, 1866).

Secondary batteries are capable of repeated charging and discharging. This concept was introduced with the discoveries of Sir William Grove (1839). Three kinds of secondary batteries are commonly used, the lead-acid battery invented by Gaston Plante (1859), alkaline and rechargeable Li-ion battery systems. The alkaline cells include both nickel-cadmium and nickel-metal hydride cells that

exhibit better capacity and energy density than lead acid cells. The Li-ion batteries display the highest capacity and energy density among the secondary batteries.

## **1.1. Primary batteries.**

Primary cells are usually designed with a cylindrical configuration or prismatic (rectangular) shape. The other common forms are the button cells to power watches and coin cells for calculator or hearing aids.

### **1.1.1. Zinc-Carbon Cells.**

The primary aqueous electrolyte batteries as typified Leclanche batteries were introduced in the middle of the 19<sup>th</sup> century. The cell provides low current at a potential of 1.5V. The first design was very primitive compared to today's. Those early cells were wet cells, which caused problems. The improvement of these led to the so called "dry cell" that is an exaggeration of terminology as the cell is not really dry. The design of the cell is based on a liquid electrolyte of ammonium chloride and zinc chloride that was immobilised in an inert powder to form a paste in zinc can.

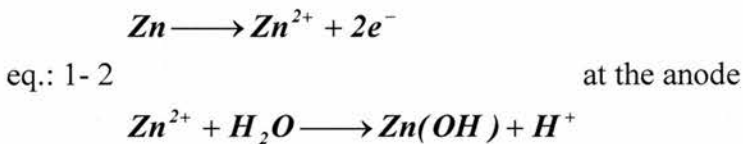
The major problems are that the zinc can take part of the reaction on discharge and becomes thinner until it perforates. This results in the cell leaks and corrosion of the housing.

An improvement to this type of cell involves the use of mercury to decrease the overpotential for hydrogen production at the zinc electrode. Despite the improvement, the capacity fades quickly with discharge rate. These cells are cheap but have been rapidly abandoned for environmental reasons.

### 1.1.2. Zinc-Manganese dioxide Cells.

Here, the anode material is zinc metal based and the electrolyte is an aqueous solution of zinc chloride saturated with ammonium chloride. The cathode is made from a mixture of refined manganese oxide and carbon that provides good electronic conductivity. Nowadays acetylene black is preferred to the graphite originally used in the Leclanche battery. The chemistry of these Leclanche cells is complicated.

The overall chemistry within the cell can be described in **eq.: 1- 1** and **eq.: 1- 2** as followed:



The reactions are pH dependent. To overcome the corrosion problem due to the pH and the release of hydrogen that raises pressure and provokes a leak in the cell,

the electrolyte was replaced by zinc chloride solution. This gave the advantage that the performance is remarkably better than the Leclanche cell in high drain duty and at low temperature. However the internal resistance is still high.

### 1.1.3. Alkaline-Manganese Cells.

The alkaline manganese battery is a variant of the Leclanche battery where the electrolyte is a concentrated aqueous solution of potassium hydroxide that provides high electric conductance. The negative electrode is a finely divided zinc powder packed around a current collector positioned at the centre of the cell. The positive electrode is a mix of electrolytic  $MnO_2$  and graphite powder packed around the anode. The separator is in electrical contact with nickel plated steel can. The overall reaction is:



( $Zn(OH)^{2-}$  ion is formed as intermediate).

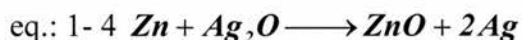
The major problem of these batteries is that the electrolyte is not very resistant to heavy discharge and often leaks. For instance the resistance rises from  $150m\Omega$  when fully charged to  $600 m\Omega$  when fully discharged. These cells are suitable for high drain duty and for use at low temperature. Alkaline cells are much superior to the Leclanche type cell. To lower the resistance, graphite powder was coated on

the positive and negative current collectors. Coating prevents the build up of corrosion products and improves electronic conduction.

#### 1.1.4. Button or Coin Cells.

Silver oxide, mercury oxide, oxygen (air) coin cells are used today in primary batteries. They are very practical cells and are so called “miniature cells”.

The overall chemistry for example of the silver oxide cell is described as follows:



The open circuit voltage is 1.6V and the discharge curve is flat and is between 1.5 and 1.55V. It offers low resistance and little polarisation. This system is used in watches and travel clocks. The other systems mentioned give basically the same advantage except that some of the components are very toxic and therefore not environmentally friendly.

## 1.2. Secondary batteries.

Secondary batteries include three main types of batteries, as mentioned above. They are (i) the lead-acid battery, (ii) alkaline battery i.e. nickel-cadmium, nickel-iron battery and nickel-metal-hydride and (iii) lithium-ion battery that will be discussed in lithium battery section.

A viable secondary battery is expected to be able to have at least 500 charge-discharge cycles<sup>1, 2, 3</sup>. This requirement is a huge challenge for the solid state chemist as the active material within the battery can be subject to too many alterations such as phase transformation, recrystallisation or other complications like loss of porosity, expansion or shedding of active material, formation of inactive material that can isolate some of the active material etc.

### 1.2.1. Lead-acid batteries.

The lead-acid system is suitable for energy storage as it can offer good reversibility and low cost. Porous lead is used as negative electrode, lead oxide as positive electrode and sulphuric acid as electrolyte. The general electrochemical process can be described as follows:



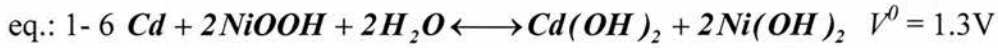
During discharge the electrolyte is consumed and on charge regenerated. The electrolyte during the process exhibits density variation. This variation is useful in tracing the stage of the battery upon cycling. One of the problems of this battery is the formation of insoluble  $PbSO_4$  that has poor electrical conductivity and furthermore is deposited on both electrodes leading to a decrease of capacity. The formation  $PbSO_4$  is also source of the increase of the internal resistance that reduces conductivity and cyclability. This phenomenon is known as sulphation and cause severe passivation. One of the main uses is for automotive starting but the system is thermodynamically unstable and can be subject to self-discharge. It displays low energy density due to the use of heavy lead electrode.

### 1.2.2. Alkaline batteries.

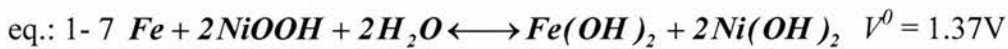
These cells are based upon nickel oxyhydroxide ( $NiOOH$ ) as a positive electrode and cadmium metal or metallic iron powder at the negative electrode.

The overall reactions are represented by:

For nickel-cadmium cell:



For nickel-iron cell:



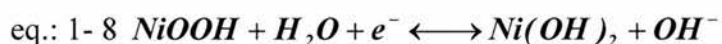
The advantages of these cells are flat discharge voltage, long cycle life up to 2000 cycles with excellent reliability but with a high cost compared to lead acid battery. In the case of nickel-cadmium cell, the toxicity of cadmium gives some concern and self discharge. The nickel-iron cell has low performance at low temperature and is subject to self discharge and corrosion problems. It has poor energy efficiency because of the low overpotential for hydrogen evolution at the iron electrode. The alkaline batteries were developed as a rechargeable battery such as nickel-cadmium and nickel-iron. Compared to the primary alkaline battery, the improvements were focused on separators that are highly stable in strong alkaline environment and also to prevent the formation of dendrites.

### 1.2.3. Nickel-Metal-hydride batteries.

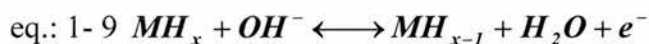
In 1970 nickel-metal-hydride batteries were introduced into the market to solve the environmental issue that was caused by the toxicity of cadmium.

In nickel-metal-hydride cell (Ni/MH) hydrogen is stored reversibly in the form of metal hydride, which forms the negative electrode. Those batteries are made with standard nickel oxide as cathode. The reactions taking place is as follows:

At the positive electrode:



At the negative electrode



The improvement of those cell required development of several complex binary metal alloys ( $AB_x$ -type alloy with  $x = 2$  or  $5$ ) where A is a mixture of rare earths and B partially substituted nickel. These alloys are claimed to have high capacity for hydrogen storage and to provide corrosion resistance e.g. in 1970  $\text{LaNi}_5$  was used. These batteries still have higher self-discharge rate and lower performance at elevated temperature.

Nickel-metal-hydride cells are sophisticated products with a quite flat discharge curve and hence more expensive. The typical operating voltage of these cells is almost the same as that of nickel cadmium (1.2 to 1.3V) with a higher self discharge and good energy density.

### 1.3. Lithium batteries.

Lithium-ion batteries<sup>4, 5</sup> have achieved immense market penetration in the area of consumer electronics such as laptops, notebook, computers and cameras etc.

The lithium battery has been mostly produced, as button and coin cells for electronic application but cylindrical and prismatic cell are also available.

The use of lithium as a negative electrode has several advantages. First of all lithium is the lightest metal in the periodical table with a molecular weight of 6.941g/mol and a specific gravity  $\rho = 0.53\text{g/cm}^3$  and hence automatically provides an excellent theoretical specific capacity of about 3860mAh/g. This value was established via this formula:

$$\text{eq.: 1-10 } Q = \int I(t).dt = \frac{m.F.\Delta x}{3600.M}$$

$\Delta x$  is the number of lithium ions inserted per formula unit,  $F$  is the Faraday constant,  $m$  is the mass of active material,  $M$  is the molecular weight of the active material and 3600 is the time conversion from seconds to hours.

Lithium has a low melting<sup>6</sup> point of 180°C and moreover its electrochemical reduction potential is very low  $E^0 = -3.045\text{V/NHE}$ . This characteristic means that

batteries made from lithium as negative electrode can offer 3V if the positive electrode is carefully chosen.

Another distinction is that electrochemical reaction involving lithium displays only one electron therefore can be used as a good reference for study and its energy density is higher than the others and lithium is able to alloy<sup>7, 8, 9, 10, 11</sup> with most of metal at room temperature except hard metals (Cu, Ti, Ni, Mo, Nb etc..).

### 1.3.1. Electrolyte.

One of the problems with respect to lithium is that it reacts violently with water. As aqueous solution can not be used as electrolyte, the options are restricted to (i) solution of lithium salt in polar organic liquid, (ii) solution of lithium salt in inorganic liquid, (iii) fused lithium salt, (iv) ionically conducting polymer or (v) ionic conducting ceramic.

The electrolyte is one of the key factors to consider in these systems, which requires good ionic conductivity and good chemical and electrochemical stability.

Thermodynamically lithium is unstable with respect to most organic liquids as with water. One of the reasons why organic liquid can be use it that it allows the formation of the passivating layer on the surface of the lithium metal. The organic liquids used are usually (i) linear esters such as methyl formate, methyl acetate, diethyl carbonate, (ii) cyclic ester such as ethylene carbonate (EC), propylene

carbonate (PC), (iii) linear ether such as dimethoxyethane or (iv) cyclic ether such as dioxolane. Mixed solvents were recently used e.g. EC-DMC<sup>12</sup> hence was found to improve performances where DMC stands for dimethyl carbonate (EC = C<sub>3</sub>H<sub>4</sub>O<sub>3</sub>, PC = C<sub>4</sub>H<sub>6</sub>O<sub>3</sub>, DMC = (CH<sub>3</sub>)<sub>2</sub>CO<sub>3</sub>).

The lithium salts commonly used<sup>13</sup> are LiClO<sub>4</sub>, LiAlCl<sub>4</sub>, LiBF<sub>4</sub>, LiPF<sub>6</sub>, LiAsF<sub>6</sub>, LiCF<sub>3</sub>SO<sub>3</sub> and LiN(CF<sub>3</sub>SO<sub>2</sub>)<sub>2</sub>. The low freezing point of some of these organic based electrolytes allows the use of lithium primary cell at lower temperature<sup>5</sup> (–30°C) compared to aqueous electrolyte cells.

One of the concerns relating to the electrolyte is their stability at higher voltage window for the charging process.

Despite the extensive studies on electrolytes, the reaction of lithium towards organic solvents remains a major problem as safety and limited cycle life is a concern. Ongoing research is focused on application of solid electrolytes or polymers in order to prevent all the undesirable reactions such as passivation phenomenon and all solid electrolyte interphase (SEI) reactions<sup>14</sup>.

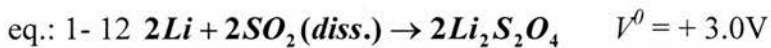
### 1.3.2. Primary lithium batteries.

Among the large choice of positive electrode material investigated to be coupled with lithium metal,  $\text{MnO}_2$  or  $(\text{CF}_x)_n$  are the mostly adopted as they can offer 3.2V output, which is twice Leclanche type batteries and the overall discharge reaction is:



The applications of these materials are for computer, memory backup and camera.

Another cell type uses  $\text{SO}_2$  (cathode) as a reagent.  $\text{SO}_2$  is dissolved in acetonitrile ( $\text{CH}_3\text{CN}$ ) and the discharge reaction is as followed:



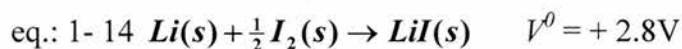
Alternatively  $\text{SO}_2$  can be used in  $\text{LiAlCl}_4$ , such as  $\text{LiAlCl}_4 \cdot x \text{SO}_2$ .

Another category of cathode uses an inorganic liquid positive electrode, thionyl chloride ( $\text{SOCl}_2$ ) or sulfuryl chloride ( $\text{SO}_2\text{Cl}_2$ ) as the active material dissolved in  $\text{LiAlCl}_4$  salt to provide conductivity. The discharge reaction is as follows:



The advantages of lithium cells are obvious, high voltage and flat discharge curves as well as high gravimetric and volumetric energy densities.

One of the important roles of the lithium battery can be found in specialised areas like medicine. Batteries are designed and implanted in the body as cardiac pacemakers, defibrillators, neurostimulators, cardiac and blood pressure monitoring devices and hearing aids. For these devices, the current drains required are very small. The lithium and iodine cell is all solid state devices in which no liquid electrolyte will be present to minimise leakage and the overall discharge reaction is:



The problem is that neither iodine nor lithium iodide has significant electrical conductivity therefore the cell should provide no current. The problem was overcome when it was found that iodine with poly-2-vinylpyridine (P2VP) gives a charge transfer complex that has electronic conductivity. The heart pacemakers devices operate with lithium iodide and poly-2-vinylpyridine (P2VP). In this type of cell, no separator is needed because in contact the lithium and the complex P2VP iodine form a thin layer of lithium iodide that acts as a separator.

### 1.3.3. Secondary lithium batteries.

The basic configuration of a secondary lithium battery relies on the use of intercalation materials that can intercalate and de-intercalate ions as a positive electrode and lithium metal as a reversible negative electrode. The charge and discharge processes are displayed in **Fig.: 1- 2** and **Fig.: 1- 3** respectively.

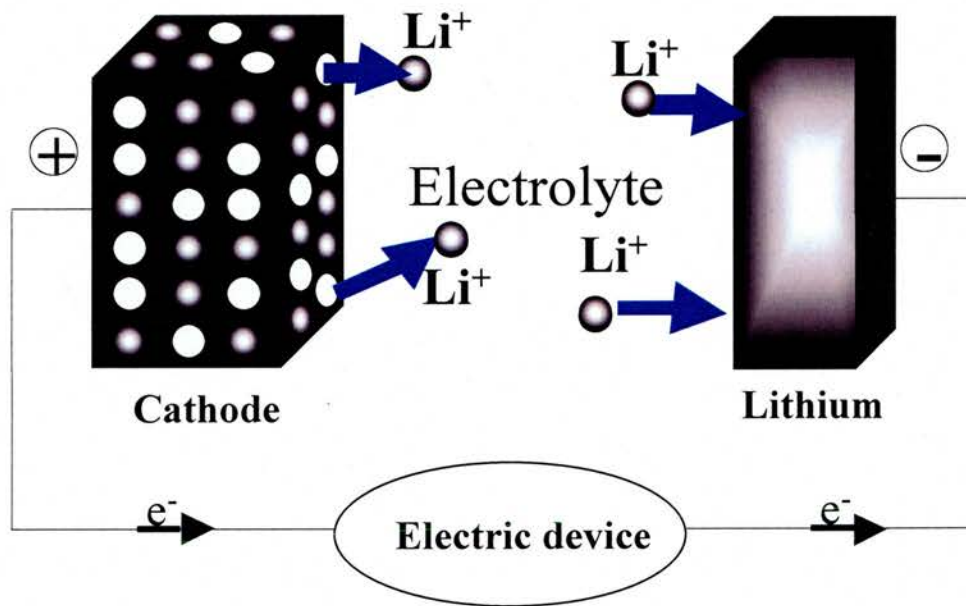


Fig.: 1- 2 Schematic representation of charge in lithium battery

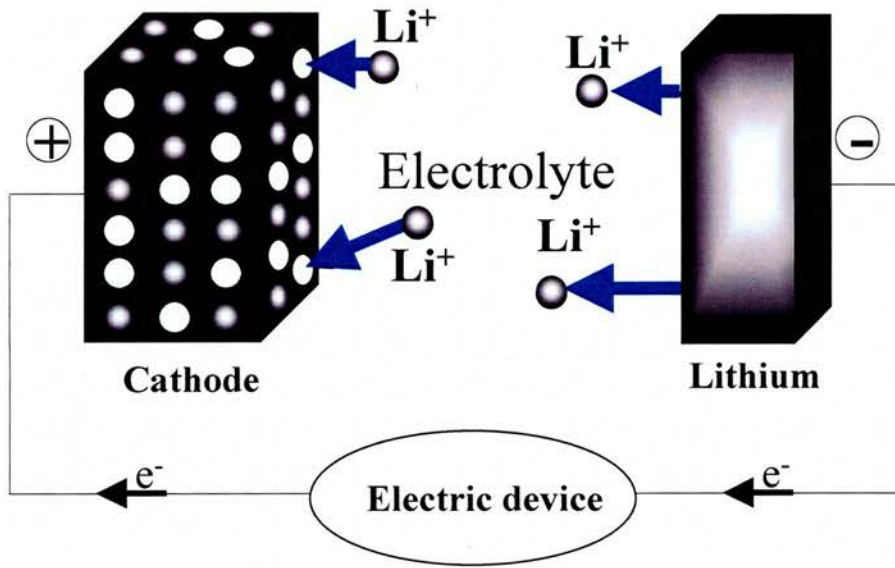
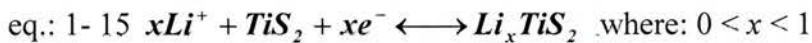


Fig.: 1- 3 Schematic representation of discharge in lithium battery.

The classic examples of intercalation species are simple metal oxides and chalcogenides such as  $\text{MoO}_2$ ,  $\text{MoS}_2$ ,  $\text{WO}_2$ ,  $\text{TiS}_2$ , or  $\text{TiO}_2$  that have been reported<sup>15, 16, 17, 18, 19</sup> as candidates for positive electrode. The reaction of  $\text{TiS}_2$  is given in **eq.: 1- 15:**



$\text{TiS}_2$  was introduced as cathode in a rechargeable battery by Exxon<sup>20,21</sup> in 1972 and was the best intercalation compound available at the time. The cycle life of these cells were demonstrated to exceed 200 cycles however, the reversible capacity is low therefore penalising the use of these materials.

The use of lithium metal at the anode side leads to dendrite formation on cycling **Fig.: 1- 4** that can short circuit cells. To overcome the problems of dendrite formation related to lithium metal, the Absorbptive Glass Micro-fibre (AGM) was introduced<sup>5</sup> using intercalation anode.

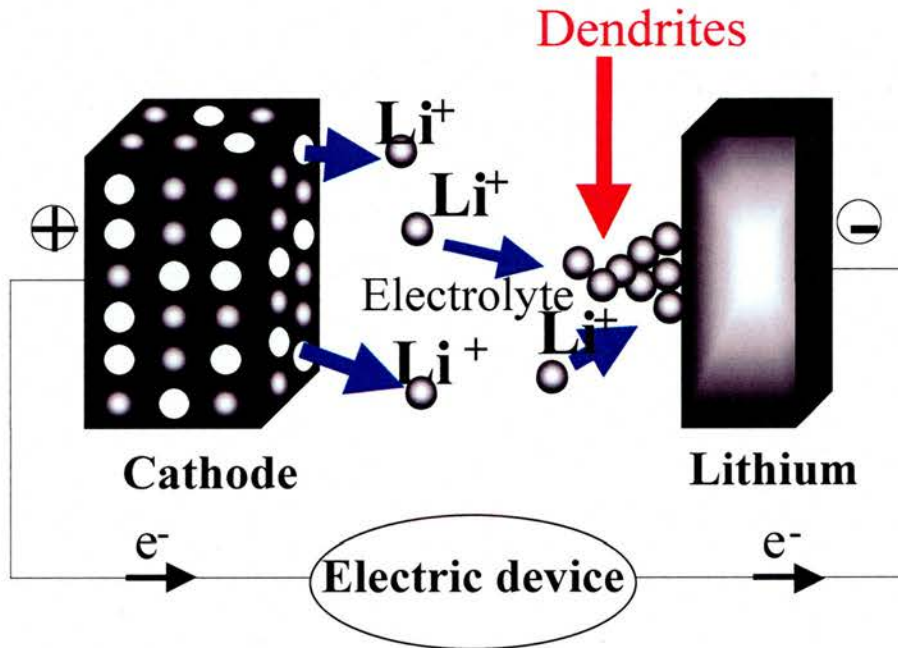


Fig.: 1- 4 Schematic representation of dendrites formation upon charge in lithium battery.

### 1.3.4. Secondary lithium-ion batteries.

The characteristic of this system is that no metallic lithium is present at any stage of the cell. The lithium ion cell can reversibly intercalate into a crystal lattice (host material) that is often the case at the cathode. At the anode, intercalation materials such as carbon, replaces the metallic lithium. Lithium ions are generated and transported via the electrolyte consisting of a lithium salt as  $\text{LiPF}_6$  or  $\text{LiClO}_4$  dissolved in organic solution or made in polymers or hydride to the host material. The overall reaction at the positive electrode is:



The lithium ions shuttle back and forth between the anode and the cathode making the process reversible. During charging, lithium ions are extracted from the cathode and inserted into the anode host whereas during discharging lithium ions are intercalated into the cathode. These cells have a peculiarity to be “Lithium-ion cell” hence the name “Rocking Chair Battery” (RCBs)<sup>22, 23, 24</sup>.

Rechargeable lithium-ion batteries were enabled by research at Oxford University in the UK in the late 1970s<sup>5</sup>.

The first commercial Li-ion cell was announced by SONY Energytech Incorporation (Japan) in 1991, and was made in  $\text{LiCoO}_2$  as a cathode<sup>25</sup> and carbon as anode. Since then, improvements have been reported in the system’s energy density and rate capacity. A large number of papers describing the properties of

$\text{Li}_x\text{MO}_2/\text{Carbon}$  ( $M = \text{metal}$ ) cells have been published<sup>26,27</sup> using different types of carbon, however none of the materials appear to have higher intrinsic capacity than graphite.

#### **1.3.4.1. Electrolyte.**

Another alternative type of technology was developed so-called PLiON<sup>TM</sup> (Plastic Lithium-ion Battery Technology<sup>TM</sup> of Telcordia) that involves employing a polymer electrolyte instead of liquid electrolyte in the lithium ion cells<sup>28</sup>. The use of solid electrolyte is to overcome problems due to SEI formation, polarisation, IR drop and chemical compatibility with electrodes in the cell. It has been considered to replace the liquid electrolyte by a dry ionic conductor polymer electrolyte having a high conductivity<sup>29, 30</sup> with a wide electrochemical stability window and a lithium transference number approaching unity. Unfortunately, the conductivity of these polymer electrolytes are still low at room temperature<sup>31</sup>.

#### **1.3.4.2. Materials for positive electrodes.**

Generally, the materials used for positive electrode must act as source of lithium ions in lithium-ion batteries.  $\text{LiCoO}_2$ <sup>25</sup> is the most widely used materials in Lithium-ion batteries and intercalates and de-intercalates around 4V versus lithium.  $\text{LiNiO}_2$  displays better specific capacity compared to  $\text{LiCoO}_2$  but is

thermodynamically unstable under delithiation due to exothermic oxidation of the electrolyte<sup>32</sup>.

Another intercalation material investigated<sup>33</sup> are lithium manganate. The spinel  $\text{LiMn}_2\text{O}_4$  has 10% less capacity than  $\text{LiCoO}_2$  and has the advantage in terms of cost and environmental safety. This material has a limited cycling performance, which was overcome by substitution leading to the new spinel phase<sup>34</sup>  $\text{LiMn}_{2-x}\text{Al}_x\text{O}_{4-y}\text{F}_y$  and by modifying their surface chemistry<sup>35</sup>.

Another approach involved the layered  $\text{LiMnO}_2$  but the material shows structural instability by reverting upon cycling from the layered phase to the spinel structure, nevertheless the cyclability is retained. However, the spinel<sup>36</sup> phase has shown rapidly capacity lost upon cycling whereas the layered phase exhibits better capacity retention behaviour.

Recently, it has been demonstrated that NaSICON<sup>37</sup> (Na super-ionic conductors) or olivine<sup>38</sup> (magnesium iron silicate) oxyanion structures made of corner sharing octahedra  $\text{MO}_6$  (where  $\text{M} = \text{Fe}, \text{Ti}, \text{V}$  or  $\text{Nb}$ ) and  $\text{XO}_4^{n-}$  tetrahedral anions (where  $\text{X} = \text{S}, \text{P}, \text{As}, \text{Mo}$  or  $\text{W}$ ) are also good candidates for positive electrode as they can be used at 90% of their theoretical capacity (165mAh/g for  $\text{LiFePO}_4$ ).

### 1.3.4.3. Materials for negative electrodes.

Carbon is currently employed as negative electrode<sup>39</sup> for all commercial Li-ion batteries. Experiments have shown that graphite or carbon is capable of hosting lithium up to a composition of  $\text{Li}_x\text{C}_6$  **Fig.: 1- 5**. The electrode reaction may be represented by:



The use of carbon seems to be ideal because it is readily available and is a cheap material of low mass. Carbon anodes exhibit limited capacity, with a practical reversible capacity of 350mAh/g for graphite<sup>40</sup>, although the theoretical capacity of carbon is 372mAh/g.

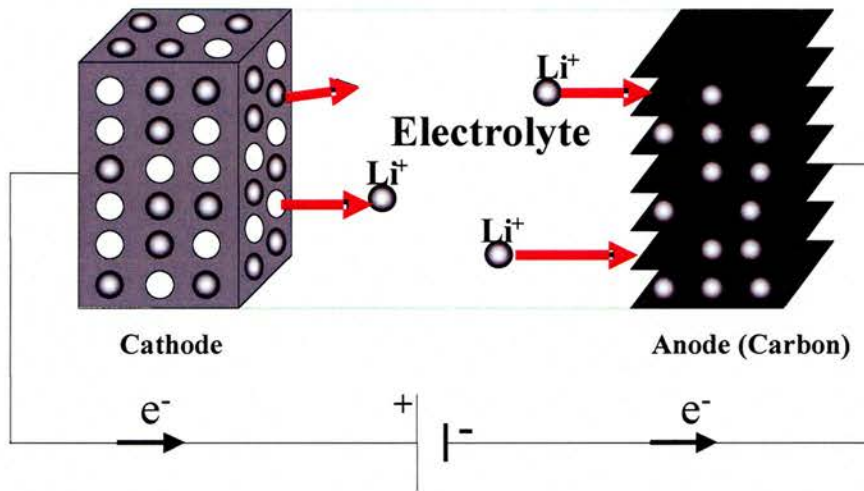


Fig.: 1- 5 Schematic representation of carbon cell.

During cycling carbon also develops a solid-electrolyte interphase (SEI).

As a result of chemical (pyrolytic process) or physical (mechanical milling) modifications of carbon, the electrochemical performance is improving and is now around 450mAh/g of reversible capacity<sup>40</sup>.

#### 1.3.4.4. Metal oxides anodes.

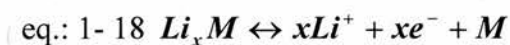
Recent studies performed on some metal oxides such as a family of vanadium oxide  $\text{Li}_x\text{MVO}_4$ <sup>41, 42</sup>, where M is a metal such as cadmium, cobalt, nickel or zinc, has indicated a good reversible capacity of 600mAh/g with good capacity retention. The problem with these materials was that the voltage on charge is too high therefore the cell voltage is reduced.

Poizot et al.<sup>43</sup> have demonstrated specific capacities as high as 700mAh/g with a good capacity retention with CoO that exhibits a peculiar reactivity towards lithium. The mechanism involves in this system is a formation of Li<sub>2</sub>O matrix that interacts electrochemically with a Co nanoparticles upon cycling. At the end of charge the metal oxide is seen to be reform with disappearance of the Li<sub>2</sub>O. Similar reactivity was also found for Co<sub>3</sub>O<sub>4</sub>.

Another alternative for anode materials are lithium titanate phases with a plateau around 1.5V due to an intercalation process. High capacity was observed from these materials typically, from 180 to 300mAh/g depending on the starting material<sup>44 79 45 46</sup> (spinel or ramsdellite). The typical charge/discharge potential range is between 1 and 2.5V.

#### 1.3.4.5. Alloys.

The electrochemical formation of Li-alloy cells containing a lithium salt dissolved in organic solvent was demonstrated by Dey<sup>47</sup> in 1971. Lithium is able to alloy at room and elevated temperature (400°C) with most metals such as (M = Mg, Ca, Al, Si, Ge, Sn, Pb, As, Sb, Bi, Zn and Pt). The mechanism involved in the alloy formation can be described as:



The alloying of the metal is a reversible process and has a high capacity. This observation makes alloys very promising negative electrode for secondary batteries. The thermodynamic potential for alloy formation is typically between 0.2 and 1V. The plateau potentials and the composition ranges of some lithium alloy phases formed at room temperature<sup>48</sup> are listed in **Table: 1- 1**. Lithium alloys have significantly less specific charge density than lithium metal however they may have very similar volumetric charge density but are much better than carbon.

Voltage vs. Li	System	Range of $x$	Temperature (°C)
0.38	$Li_xSn$	3.5 – 4.4	25°C
0.42	$Li_xSn$	2.6 – 3.5	25°C
0.485	$Li_xSn$	2.33 – 2.63	25°C
0.53	$Li_xSn$	0.7 – 2.33	25°C
0.660	$Li_xSn$	0.4 – 0.7	25°C

Table: 1- 1 Potential of some lithium tin alloy at room temperature<sup>48</sup>.

The first cell related to alloying to be commercialised was introduced<sup>4</sup> in 1980s by Matsushita and the cell performances was found to deteriorate upon cycling.

*Huggins et al.*<sup>48</sup> has also investigated kinetic and thermodynamic aspects of Li-Sn alloy and other types of alloy such as lithium-aluminium, lithium-silicon that can be formed during the charge and discharge processes, at both lower temperature and at elevated temperatures.

The main problem related to the use of lithium alloys at room temperature is the colossal volume changes<sup>49</sup> in the metal. **Fig.: 1- 6** shows the volume changes of these different types of alloys. Under cycling, this volume expansion<sup>50, 51</sup> leads to mechanical stresses that induce a loss of electrical contact between particles and drastic decrease in capacity.

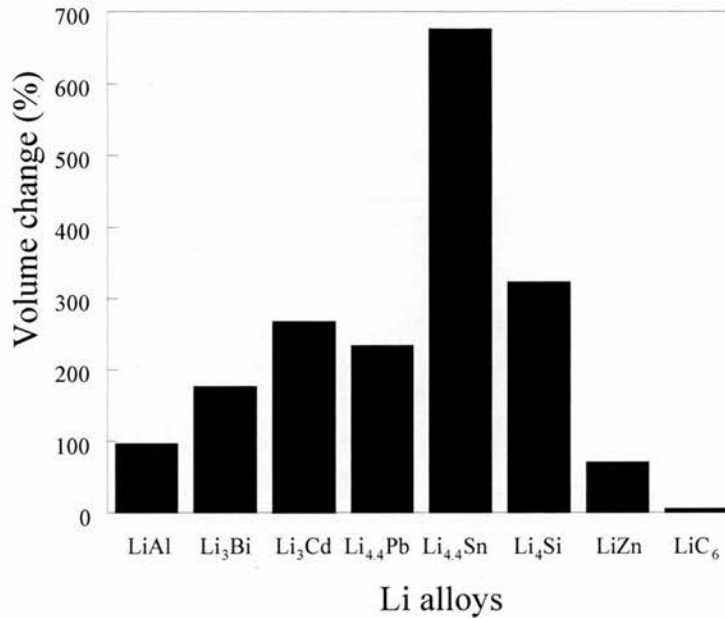


Fig.: 1- 6 Representation of volume changes of different type of alloy<sup>52</sup>.

#### 1.3.4.6. Lithium-tin alloys.

Tin has two allotropic varieties. The so called grey or alpha-tin ( $\alpha$ -tin) crystallises in the cubic structure at low temperature whereas the white or beta-tin ( $\beta$ -tin) in tetragonal structure at high temperature. Tin has low melting<sup>6</sup> point of 231.93°C.

The first study of the Li-Sn system was carried out at 527-777°C temperature range by *Foster et al.*<sup>53</sup>, more detailed investigation were later reported by Wen and Huggins<sup>54</sup>, at 360-590°C range. They have shown that lithium-tin has different phases: Li<sub>2</sub>Sn<sub>5</sub>, LiSn, Li<sub>7</sub>Sn<sub>3</sub>, Li<sub>5</sub>Sn<sub>2</sub>, Li<sub>13</sub>Sn<sub>5</sub>, Li<sub>7</sub>Sn<sub>2</sub> and Li<sub>22</sub>Sn<sub>5</sub>. Most importantly these binary phases form successively at a decreasing voltage that correlates with the experiment.

For pure tin metal, it is known that alloying causes a large volume expansion (over 300%) that causes mechanical stresses thus the electrode suffers from crumbling and cracking that lead to loss of electronic contact between particle sizes and affect the cycle life. This means that the bulk metal behaves poorly when used as an anode with lithium. None of the Li-alloys cells are used commercially despite all these advantages. Current research is focused to solve problems related to lithium alloys for use as the negative electrode and to make it viable for industries.

Several tin based phases, such as  $\text{Sn}_2\text{Fe}:\text{SnFe}_3\text{C}$  system, were investigated by *Dahn et al.*<sup>55</sup>,  $\text{Li}_x\text{Cu}_6\text{Sn}_5$  by *Thackeray et al.*<sup>56</sup> and Ni-Sn based alloy<sup>57, 58</sup>. These approaches were to prevent the volume expansion upon cycling by selecting a strong intermetallic structure (such as  $\text{Cu}_6\text{Sn}_5$ , InSb or  $\text{Cu}_2\text{Sb}$ ) that is to alloy with lithium. Therefore the ternary alloy formed upon cycling should be more favourable than the binary such as LiAl,  $\text{Li}_x\text{Sn}$  or  $\text{Li}_x\text{Si}$ .

Investigations that were reported on nano Sn and  $\text{AlSi}_{0.1}$ <sup>59</sup> suggest that a matrix buffer with low coefficient of elasticity should help to reduce the volume expansion during the reversible lithium insertion.

### 1.3.4.7. Tin based oxide compounds.

In 1995, Fuji PhotoFilm Co., Ltd., Japan filed a patent for nonaqueous Li-ion batteries in which tin oxides or other tin based composite oxide (TCO) were used as negative electrode active materials<sup>60</sup>. Following Fujifilm's publication<sup>61</sup> in 1997, much attention has been focused upon tin-based oxide compounds as Li-ion battery anode materials. The starting material may be amorphous with a stoichiometry of:  $\text{SnM}_x\text{O}_y$ , where M is the vitrifying element such as B(III), P(V), As(III) and  $x \geq 1$ . From FujiFilm's publication, the typical composition of the TCO was  $\text{SnB}_{0.56}\text{P}_{0.4}\text{Al}_{0.42}\text{O}_{0.36}$ , which was obtained by reaction of oxides at 1100°C followed by quenching. The reversible capacity of this material was found to be 600mAh/g.

Courtney and Dahn have proposed a general reaction describing the charge and discharge process. Tin-based oxides are thought to have two step reactions with lithium, e.g. for  $\text{SnO}_2$  as follows.



The first reaction has the effect of finely dispersing tin in a  $\text{Li}_2\text{O}$  matrix and the second reaction is the formation of the reversible alloy **Fig.: 1- 7**. The first discharge capacity is approximately proportional to the oxygen content plus the formation of the alloy.

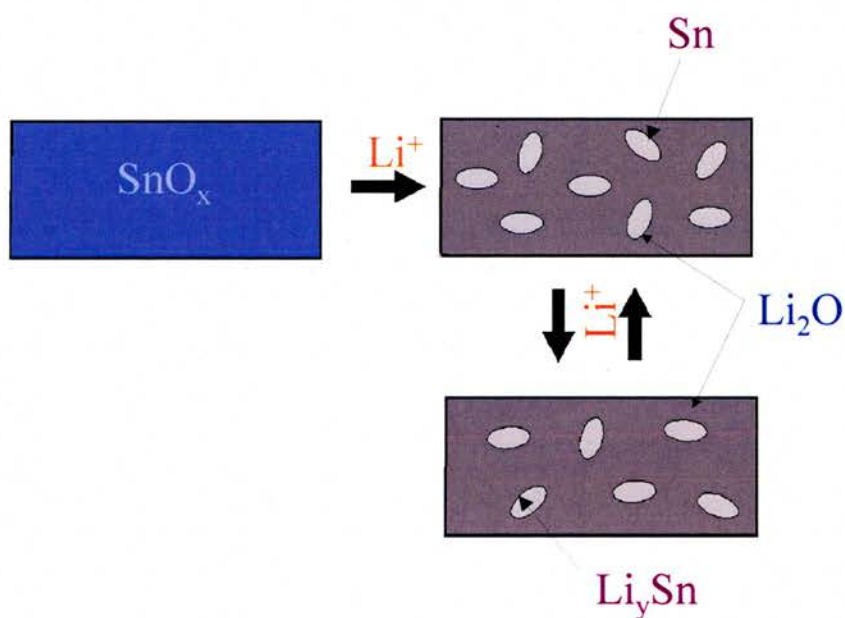


Fig.: 1- 7 Reaction mechanism schematic for the reaction of lithium with tin (II) oxide.

In comparison with carbon, tin-based oxides show a theoretical and observed capacity up to three times higher than graphite (372 and 350mAh/g).  $\text{SnO}^{62}$ ,  $^{66}$ exhibits (873 and 825mAh/g),  $\text{SnO}_2^{65}$  (781 and 650 mAh/g), and  $\text{Li}_2\text{SnO}_3^{64}$  (652 and 550mAh/g) etc... at potential of 0.2-1.2 V versus lithium.

The tin oxides and glasses show significantly better capacity retention, which has been ascribed to the small particle size of the alloyed<sup>63</sup> tin. The matrix may act to retard the aggregation of tin atoms into a large coherent volume. The role of the matrix is obviously important, and it has been shown that the amount of matrix does generally improve the cycling capacity<sup>78, 64</sup>. To make a good electrode, the matrix should be a good  $Li^+$  conductor, a poor Sn conductor and a reasonable electronic conductor. The matrix should also be light in weight in order to not lower the capacity.

It was also reported<sup>64</sup> on glassy materials that grain size; structural state and spectator atoms are some key factors controlling the reversibility. Small grain materials show better cycling behaviour than large-grain materials over the same voltage ranges. It was also shown that tin aggregates to form larger size particles on cycling. These aggregates could then be detected via XRD, and in the electrochemistry as plateaux in galvanostatic cycling, corresponding to conversion of a regular crystalline phase to another. Larger, amorphous tin grains becoming more crystalline on cycling could also explain this effect. The appearance of these more crystalline phases is tied with the loss of capacity on cycling. Obviously the best way to stop this loss of capacity is to slow the rate of aggregation.

Other metal oxides such as  $ZnO$ <sup>65</sup>,  $Sb_2O_3$  and  $PbO$  follow a similar mechanism<sup>66</sup> as tin oxide and once again the reversible capacity and the cyclability do not allow the use of these materials as a replacement of carbon negative electrode.

### 1.3.5. Overview of materials investigated.

#### 1.3.5.1. $\text{SnP}_2\text{O}_7$ .

Behm et al.<sup>67</sup> discovered that  $\text{SnP}_2\text{O}_7$  does cycle well. It also has no known adverse environmental impact. The performance of the crystalline cubic tin pyrophosphate anode was excellent for both cyclability and capacity. The reversible specific charge capacity of  $>360$  mAh/g and a capacity retention of 96% over 50 cycles when cycled between 0.2 and 1.2 V versus lithium. This performance exceeds the performance of any TCO that has been reported in the last few years and the voltage range on charge is suitable for negative electrode application for carbon replacement. This good performance must be in part due to the properties of the matrix formed upon cycling, which would be expected to have good lithium ion and reasonable electronic conducting properties, and a reasonable coefficient of elasticity that helps to prevent the expansion of tin. Behm et al.<sup>67</sup> have also proved that this good performance is related to the initial crystal structure, as the layered polymorph does not cycle.

All the members of  $M^{4+}P_2O_7$  (where  $M = Sn, Zr, Si, Ti$  etc...), show a  $3 \times 3 \times 3$  crystalline superstructure ( $P$  a  $\bar{3}$ ). Structural characterisations were performed earlier by Huang *et al.*<sup>68</sup>, and others<sup>69, 70, 71, 72</sup>, on  $M^{4+}P_2O_7$  (where  $M = Sn, Zr, Si, Ti$  etc.) by using different technique such as X-ray powder diffraction, Infrared, Raman and Mossbauer Sn spectroscopy etc.

Xiao *et al.*<sup>73</sup> have investigated the electrochemical performance of amorphous and crystalline tin pyrophosphate  $Sn_2P_2O_7$  as anodes in secondary lithium batteries. Their work focused on trying to understand of the mechanism of the lithium insertion into  $Sn_2P_2O_7$ . In their study, they claim 400mAh/g for the crystalline material and 520mAh/g for the amorphous material. It was found that the pyrophosphate group was just a spectator in the system, however they have proposed from IR experiments a cleavage of the pyrophosphate group into ( $Li_3PO_4 + LiPO_3$ ) whereas later  $^{31}P$  MAS NMR<sup>74</sup> does not reveal any peak corresponding to  $LiPO_3$ , which should be in the range of  $-22$  to  $-26$ ppm.

### 1.3.5.2. $SnO_2:B_2O_3$ and doped $(SnO_2:B_2O_3)_{y/2}/(SnP_2O_7)_{1-y/2}$ with $0 \leq y \leq$

2.

Borate species are well known to mix with phosphate<sup>75</sup> typically to form a glassy network<sup>76</sup>. So substituting borate into  $SnP_2O_7$  will change the matrix formed upon cycling and possibly favour capacity retention. As borate is lighter than phosphate this should help to increase the capacity.

Previously, Mao et al.<sup>77</sup>, have shown better cyclability with nanocomposites active/inactive TCO. Tin based material containing phosphate and borate was already investigated by Kim et al.<sup>78</sup>. They have demonstrated that the cyclability of amorphous  $\text{SnO}_2:\text{B}_2\text{O}_3:\text{P}_2\text{O}_5$  was remarkably affected by the synthetic route and hence the particle size.

### 1.3.5.3. $\text{TiP}_2\text{O}_7$ and doped $\text{Ti}_{1-y}\text{Sn}_y\text{P}_2\text{O}_7$ with $0 \leq y \leq 1$ .

The isovalent and lighter Ti should be able to progressively replace the heavy Sn cation without a significant change of the structure. Titanium compounds are well known as intercalation compounds<sup>79</sup> so this gives a chance of two mechanisms in the same material. This substitution will allow us to trace the effect on capacity retention and the chemistry of both cations towards lithium.

A complex cubic structure was reported by Sanz et al.<sup>80</sup> and Patoux et al.<sup>81</sup> for  $\text{TiP}_2\text{O}_7$  by using different techniques such as NMR and X-ray diffraction.

From this series of samples, only  $\text{SnP}_2\text{O}_7$  (above) and  $\text{TiP}_2\text{O}_7$  were electrochemically tested<sup>82</sup>. Uebou et al.<sup>82</sup> claim for the first discharge a capacity of 95mAh/g between a voltage range from 2.6 to 1V.

#### 1.4. Aim of this work.

The objectives of this thesis were to improve the capacity and the cyclability of  $\text{SnP}_2\text{O}_7$  and to understand the chemistry involved in the redox cycling.

Results from several techniques, e. g. X-ray diffraction, NMR, and electrochemical testing, will be combined to elucidate the chemical and electrochemical reactions occurring upon cycling and to achieve a better understanding of the mechanism which will enable us to improve the capacity and the cyclability.

A series of doped samples from  $\text{SnP}_2\text{O}_7$  to  $\text{TiP}_2\text{O}_7$  will be synthesised and characterised structurally and electrochemically in order to evaluate the effect of the cation on mechanism and capacity.

A series of doped samples from  $\text{SnP}_2\text{O}_7$  to  $\text{SnO}_2:\text{B}_2\text{O}_3$  will be synthesised and characterised structurally and electrochemically in order to evaluate the effect of the matrix on cyclability.

**1.5. References.**

- <sup>1</sup> K. Brandt, *Solid State Ionics* **69**, 173 (1994).
- <sup>2</sup> R. Koksang, J. Barker, H. Shi, M. Y. Saidi, *Solid State Ionics* **84**, 1 (1996).
- <sup>3</sup> G. Nagasubramanian, R. G. Jungst, *J. Powers Source* **72**, 189 (1998).
- <sup>4</sup> R. M. Dell, D. A. J. Rand, *Understanding Batteries*, R.S.C 2001.
- <sup>5</sup> C. A. Vincent, B. Scrosati, *Modern Batteries*, 2<sup>nd</sup> edition.
- <sup>6</sup> <http://www.webelements.com>
- <sup>7</sup> J. O. Besenhard, *J. Electroanal. Chem.* **94**, 77 (1978).
- <sup>8</sup> C. J. Wen, B. A. Boukamp, R. A. Huggins, W. Weppner, *J. Electrochem. Soc.* **126**, 2258 (1979).
- <sup>9</sup> J. O. Besenhard, P. Komenda, A. Pxinis, E. Wudy, *Solid State Ionics* **18-19**, 823 (1986).
- <sup>10</sup> M. S. Foster, C. E. Crouthamel, S. E. Wood, *J. Phys. Chem.* **70**, 3042 (1966).
- <sup>11</sup> C. J. Wen, R. A. Huggins, *J. Electrochem. Soc.* **128**, 1181 (1981).
- <sup>12</sup> U. Heider, R. Oesten, M. Jungnitz, *J. Powers Sources* **81-82**, 119 (1999).
- <sup>13</sup> J. R. Owen, *Chem. Soc. Rev.* **26**, 259, (1997).
- <sup>14</sup> E. Peled, *J. Electrochem. Soc.* **126**, 2047 (1979).
- <sup>15</sup> M. S. Whittingham, *J. Electrochem. Soc.* **123**, 315 (1976).
- <sup>16</sup> D. Fauteux, R. Koksang, *J. Appl. Electrochem.* **23**, 1 (1993).
- <sup>17</sup> M. Winter, J. O. Besenhard, M. E. Spahr, P. Novák, *Adv. Mat.* **10**, 725 (1998).
- <sup>18</sup> S. Morzilli, B. Scrosati, F. Sgarlata, *Electrochem Acta* **30**, 1271 (1985).

- <sup>19</sup> S. Y. Huang, L. Kavan, I. Exnar, M. Grätzel, *J. Electrochem. Soc.* **142**, L142 (1995).
- <sup>20</sup> M. S. Whittingham, *Science* **192**, 1226 (1976).
- <sup>21</sup> M. S. Whittingham, Chalcogenide battery. *US Patent* 4009052.
- <sup>22</sup> J. O. Besenhard, *Euchem Conference Proceedings*, Rosenheim, Germany, 30/04-03/05 1979.
- <sup>23</sup> D. W. Murphy, F. J. Carides, J. V. Waszczak, *Mat. Res. Bull.*, **13**, 1395-1402 (1978).
- <sup>24</sup> M. Lazzari, B. A. Scrosati, *J. Electrochem. Soc.*, **127**, 773-774 (1980).
- <sup>25</sup> T. Nagaura, K. Tozawa, *Prog. Batteries Solar Cells* **9**, 209 (1990).
- <sup>26</sup> K. Mizushima, P. C. Jones. P. J. Wiseman, J. B. Goodenough, *Mat. Res. Bull.*, **15**, 783-789 (1980).
- <sup>27</sup> M. M. Thackeray, W. I. F. David, P. G. Bruce, J. B. Goodenough, *Mat. Res. Bull.*, **18**, 461-472 (1983).
- <sup>28</sup> J.-M. Tarascon, A. S. Gozdz, C. Schmutz, S. Shokoohi, P. C. Warren, *Solid State Ionics* **86-88**, 49 (1996).
- <sup>29</sup> M. Armand, J. M. Chabagno, M. Duclot, *2<sup>nd</sup> int. meeting on Solid Electrolytes*, St. Andrews, Scotland, p. 6.5.
- <sup>30</sup> Z. Gadjourova, Y. G. Andreev, D. P. Tunstall, P. G. Bruce, *Nature* **142**, 520-523 (2001).
- <sup>31</sup> M. Armand, *Solid State Ionics* **69**, 309 (1994).

- <sup>32</sup> J. R. Dahn, U Von Sacken, M. W. Juzkow, H. Al-Janaby, *J. Electrochem. Soc.*, **138**, 2207-2211 (1991).
- <sup>33</sup> A. R. Armstrong, P. G. Bruce, *Nature*, **381**, 499-500 (1996).
- <sup>34</sup> G. G. Amatucci, N. Pereira, T. Zheng, J. -M. Tarascon, *J. Electrochem. Soc.*, **148**, A171-A182 (2001).
- <sup>35</sup> G. G. Amatucci, A. du Pasquier, A. Blyr, T. Zheng, J. -M. Tarascon, *Electrochem Acta* **45**, 255-271 (1999).
- <sup>36</sup> P.G. Bruce, A. R. Armstrong, R. L. Gitzendanner, *J. Mater.Chem.*, **9**, 193, (1999).
- <sup>37</sup> C. Delmas, A. Nadiri, J. L. Soubeyroux, *Solid State Ionics* **28-30**, 419-423 (1988).
- <sup>38</sup> A. K. Padhi, K. S. Nanjundaswamy, C. Masquelier, S. Okada, J. B. Goodenough, *J. Electrochem. Soc.*, **144**, 1604-1613 (1997).
- <sup>39</sup> M. Mohri, *J. Powers Source* **26**, 545-551 (1989).
- <sup>40</sup> J. -M. Tarascon, M. Armand, *Nature*, **414**, 359-367 (2001).
- <sup>41</sup> M. S. Whittingham, *Prog. Solid State Chem.*, **12**, 41 (1978).
- <sup>42</sup> G. L. Holleck, J. R. Driscoll, *Electrochem Acta* **22**, 644 (1977).
- <sup>43</sup> Poizot, P.; Laruelle, S.; Grugeon, S.; Dupont, L.; Tarascon, J.-M. *Nature*, **407**, 496 (2000).
- <sup>44</sup> A. D. Robertson, H. Tukamoto, J. T. S. Irvine, *J. Electrochem. Soc.*, **146**, 3958-3962 (1999).

- <sup>45</sup> J. P. Kartha, D. P. Tunstall, J. T. S. Irvine, *J. Solid State Chem.*, **152**, 397-402 (2000).
- <sup>46</sup> J. T. S. Irvine, T. Murai, H. Tukamoto, *J. Electrochem. Soc.*, **146**, 4348-4353 (1999).
- <sup>47</sup> N. Dey, *J. Electrochem. Soc.*, **118**, 1547 (1971).
- <sup>48</sup> R. A. Huggins, *Solid State Ionics* **113-115**, 57-67 (1998).
- <sup>49</sup> L. Y. Beaulieu, K. W. Eberman, R. L. Turner, L. J. Krause, J. R. Dahn, *Electrochem. Solid State*, **4**, A137 (2001).
- <sup>50</sup> J. O. Besenhard, M. Hess, P. Komenda, *Solid State Ionics* **40-41**, 525 (1990).
- <sup>51</sup> J. O. Besenhard, J. Yang, M. Winter, *J. Powers Source* **68**, 87 (1997).
- <sup>52</sup> D. Fauteux, R. Koksang, *J. Appl. Electrochem.*, **23**, 1 (1993).
- <sup>53</sup> M. S. Foster, C. E. Crouthamel, S. E. Wood, *J. Phys. Rev.*, **70**, 3042 (1966).
- <sup>54</sup> C. J. Wen, R. A. Huggins, *J. Electrochem. Soc.*, **128**, 1181 (1981).
- <sup>55</sup> O. Mao, R. A. Dunlap, J. R. Dahn, *J. Electrochem. Soc.*, **146**, 405-413 (1999).
- <sup>56</sup> K. D. Kepler, J. T. Vaughey, M. M. Thackeray, *Electrochem. Solid State lett.*, **2**, 307 (1999).
- <sup>57</sup> G. M. Ehrlich, C. Durand, X. Chen, T. A. Hugener, F. Spiess, S. L. Suib, *J. Electrochem. Soc.*, **147** (3), 886 (2000).
- <sup>58</sup> O. Crosnier, T. Brousse, D. M. Scheich, *Ionics* **5**, 311 (1999).
- <sup>59</sup> C. Wang, A. S. Appleby, F. E. Little, *J. Power Sources*, **93**, 174 (2001).
- <sup>60</sup> Y. Idota, *US Patent*. 5478671 (1995)

- <sup>61</sup> Y. Idota, T. Kubota, A. Matsufudji, Y. Maekawa, T. Miyasaka, *Science* **276**, 1395 (1997).
- <sup>62</sup> G. R. Goward, L. F. Nazar, W. P. Power, *J. Mater. Chem.*, **10**, 1241 (2000).
- <sup>63</sup> A. I. Courtney, W. R. McKinnon, J. R. Dahn, *J. Electrochem. Soc.*, **146** (1), 59-68 (1999).
- <sup>64</sup> A. I. Courtney, J. R. Dahn, *J. Electrochem. Soc.*, **144** (9), 2943-2948 (1997).
- <sup>65</sup> F. Belliard, P. A. Connor, J. T. S. Irvine, *Solid State Ionics* **135**, 163-167 (2000).
- <sup>66</sup> H. Li, X. Huang, L. Chen, *Solid State Ionics* **123**, 189-197 (1999).
- <sup>67</sup> M. Behm and J. T. S. Irvine, *Electrochim. Acta*, **47** (2002) 1727-1738
- <sup>68</sup> C. H. Huang, O. Knop, D. A. Othen, F. W. D. Woodhams and R. A. Howie, *Can. J. Chem.* **53**, 79 (1975).
- <sup>69</sup> N. Khosronavi, V. Korthuis, A. W. Sleight, *Inorg. Chem.*, **35**, 485-489 (1996).
- <sup>70</sup> J. S. O. Evans, W. I. F. David and A. W. Sleight, *Acta Cryst.*, **B55**, 333-34 (1999).
- <sup>71</sup> R. Hubin, P. Tarte, *Spectrochimica Acta*, **23A**, 1815-1829 (1967).
- <sup>72</sup> Franck Fayon, Ian J. King, Robin K. Harris, Richard K. Gover, John S. O. Evans and Dominique Massiot, *Chem. Mater.* **15** 22-34 (2003).
- <sup>73</sup> Y. W. Xiao, J. Y. Lee, A. S. Yu, and Z. L. Liu, *J. Electrochem. Soc.* **146**, (10) 3623-3629 (1999)
- <sup>74</sup> J. L. Tirado, *Materials Science and Engineering*, **R 40**, 103-136 (2003).
- <sup>75</sup> R. K. Brow, *Journal of Non-Crystalline Solids*, **194**, 267-273 (1996).

- <sup>76</sup> W. A. Buckermann, W. Muller-Warmuth, C. Mundus, *Journal of Non-Crystalline Solids*, **208**, 217-227 (1996).
- <sup>77</sup> O. Mao, R. L. Turner, I. A. Courtney, B. D. Fredericksen, M. I. Buckett, L. J. Krause, J. R. Dahn, *Electrochemical and Solid-State Letters*, **2** (1) (1999).
- <sup>78</sup> J. Y. Kim, D. E. King, P. N. Kumta, G. E. Blomgren, *J. Electrochem. Soc.*, **147** (12), (10) 4411-4420 (2000).
- <sup>79</sup> A. D. Robertson, L. Trevino, H. Tukamoto, J. T. S. Irvine, *J. of Power Sources*, **81-82**, 352-357 (1999).
- <sup>80</sup> J. Sanz, J. E. Iglesias, J. Soria, E. R. Losilla, M. A. G. Aranda, S. Bruque, *Chem. Mater.* **9** 996-1003 (1997).
- <sup>81</sup> S. Patoux, C. Masquelier, *Chem. Mater.* **14**, 5057-5068 (2002).
- <sup>82</sup> Y. Uebou, S. Okada, M. Egashira, J. I. Yamaki, *Solid State Ionics* **148**, 323-328 (2002).

## 2. Experimental.

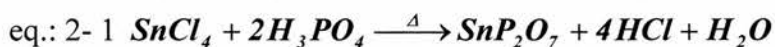
### 2.1. Materials.

#### 2.1.1. SnP<sub>2</sub>O<sub>7</sub> (cubic phase).

Two different synthesis routes were investigated to yield the desired starting material SnP<sub>2</sub>O<sub>7</sub>.

##### 2.1.1.1. Synthesis route 1.

This synthesis route<sup>1</sup> consists of mixing stoichiometric amounts of reagents, and calcining at different temperatures in the air. A high purity sample was prepared in a two step reaction, from tin tetrachloride (98+%, Acros) and concentrated ortho-phosphoric acid (85%, Prolabo) in excess following the reaction below **eq.:**  
**2- 1.**



The first step reaction occurs at 400 °C for 12 hours and the resulting fluffy white powder that looks like a meringue was reground and heated on the second step at

1000°C for 24 hours. A single-phase sample was obtained and characterised as cubic  $\text{SnP}_2\text{O}_7$ .

A layered  $\text{SnP}_2\text{O}_7$  can be synthesised and characterised via the same process by keeping the synthesis temperature at 400°C.

#### **2.1.1.2. Synthesis route 2.**

A pure cubic  $\text{SnP}_2\text{O}_7$  was also prepared by heating Tin (IV) hydrogen phosphate<sup>2</sup> ( $\text{Sn}(\text{HPO}_4)_2$ ) in air for 12 hours at 1000°C.  $\text{Sn}(\text{HPO}_4)_2 \cdot \text{H}_2\text{O}$ , can be obtained by adding a stoichiometric amount of  $\text{H}_3\text{PO}_4$  to a solution of anhydrous tin (IV) chloride, until the P:Sn ratio was 3. Although the precipitation was complete, refluxing was continued for a while. To ensure completion after refluxing, the material was washed with distilled water and then batches treated with 1 M  $\text{HNO}_3$  to ensure complete conversion to  $\text{H}_3\text{O}^+$  form. The material was washed with distilled water to a pH of 3.4-4.0, filtered and then air-dried. A white powder sample of  $\text{Sn}(\text{HPO}_4)_2 \cdot \text{H}_2\text{O}$  was obtained and characterised.

#### **2.1.2. Boron doped $\text{SnO}_2 \cdot x\text{B}_2\text{O}_5 \cdot (1-x)\text{P}_2\text{O}_5$ (cubic & amorphous phases).**

The series of boron-doped samples were synthesised via synthesis route 1 by using  $\text{H}_3\text{PO}_4$ ,  $\text{SnCl}_4$  and  $\text{H}_3\text{BO}_3$ . The only difference with these syntheses is the

change of temperature. As boron oxide is volatile, the entire series was only fired at 400°C instead of 1000°C, for 6 hours.

### 2.1.3. Titanium doped $\text{Sn}_{(1-x)}\text{Ti}_x\text{P}_2\text{O}_7$ .(cubic).

A series of isostructural titanium doped tin pyrophosphates  $\text{Sn}_{(1-x)}\text{Ti}_x\text{P}_2\text{O}_7$  were made via synthesis route 1 at 700°C and characterised to be pure. Samples with  $x = 1, 0.75, 0.5, 0.35$  and  $0.15$  were made and investigated

### 2.2.1. Electrode preparation.

The porous electrode preparation is based on the “Bellcore”-type plastic electrode method<sup>3</sup>. This is achieved by doctor blading, is scalable and allows in situ XRD to be performed in appropriate cells. A slurry was made by grinding 11.6 % by weight of the active material and 1.4 % by weight Super S carbon together, and then adding 5.5 % by weight polyvinilidene fluoride (PVDF), 9.5 % by weight propylene carbonate (PC) and 72 % by weight acetone. The slurry was stirred for 4 hours in a 50 °C water bath and then doctor bladed onto a glass plate, to form a self-supporting sheet, typically 100 – 200 µm thick after evaporation of the acetone. The electrode sheet was cut into discs, and the trapped (PC) was leached out using ether, until the individual electrodes reached constant weight. The resulting porous electrodes were dried under vacuum and transferred to an argon-filled glove box.

The various components of the slurry have different properties. The use of Super S carbon is to provide better conductivity through the electrode whereas the (PVDF) acts as a binder. The acetone allows the formation of the slurry and is dried off quickly to form the sheet. The (PC) is drained out in ether offering porosity to the electrode sheet. The pores allow homogeneous distribution of the electrolyte within the electrode. During the electrochemical insertion, the (PVDF) is assumed to be relatively inert. Although lithium can be inserted into Super S carbon, this is only to a limited extent that can be corrected depending on the carbon content. Within the electrode sheet, the percentage of the active material (A) can be estimated by **eq.: 2- 2** below, assuming a perfect homogeneous distribution of active materials contained by the electrode.

$$\text{eq.: 2- 2 } A = \frac{\text{mass of A}}{\text{mass of A} + \text{mass of PVDF} + \text{mass of carbon}} * 100$$

From this, the active mass can be calculated in each disc in order to assess the specific electrochemical response of the material.

### **2.2.2. Cell preparation.**

The coin cells were constructed using 2325 coin cell hardware (NRC Canada). The cells used a 10mm diameter lithium disc, cut from 0.38-mm thick ribbon (Aldrich), as a combined counter and reference electrode, LiClO<sub>4</sub> in EC-DMC

(Merck) was used as electrolyte, and separators from Whatman GF/F Glass Microfibre Filters.

The lithium electrode is believed to stay virtually unpolarized<sup>4</sup> due to the low current densities, thus giving a reliable reference potential. All the potentials are referenced to the Li/Li<sup>+</sup> electrode. It is worth to note that the lithium couple has a very low potential of  $E_{Li^+/Li^0}^0 = -3.045V / NHE$  and so is at a lower potential than the active material, i.e. is tested as positive electrode. The material would, however be a negative electrode in rocking chair cell application when it is used versus a well known positive electrode material such as Li<sub>x</sub>MnO<sub>2</sub> or Li<sub>x</sub>CoO<sub>2</sub>.

The choice of the separator has a great influence on performance and reproducibility, with a substantial improvement on changing from Celgard polypropylene separators<sup>5</sup> to the presently used material.

### 2.2.3. Standard coin cell.

The cell is built up in different stacking layers. A schematic diagram of the coin cell is shown on **Fig.: 2- 1**. The prepared electrode is placed in the middle of the positive stainless steel coin cell case and then a few drops of electrolyte are added. The separator is then placed on top entirely covering the electrode to avoid any short circuits. Afterwards the lithium metal anode disc is carefully placed on the separator. Then the spacer and the spring are successively positioned on top before the negative stainless steel coin cell with an insulating grommet is placed into the can.

In order to define a specific optimum pressure inside the cell, all the element thickness was carefully calculated and summarised in **Table: 2- 1** below. All these components were pressed together giving a coin cell of 2.59mm stack height.

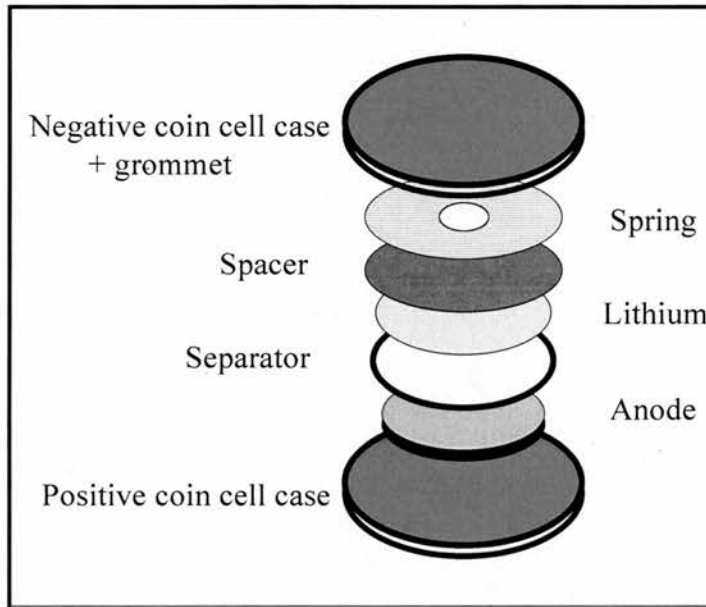


Fig.: 2- 1 Schematic diagram of the coin cell

	Thickness (mm)
Cathode: active	0.05 – 0.07
Separator: glass microfibre	0.27
Anode: lithium	0.3
Spacer: stainless steel	0.864
Spring: stainless steel	1.118
Experimental stack height	2.602 – 2.622

Table: 2- 1 Thickness optimisation of a cell.

### 2.3. Electrochemical process overview.

#### 2.3.1. Background.

The electrochemical energy storage in a material is basically storage of electrons at a certain potential level. Electrochemical insertion of lithium as a guest in a structure involves two distinct and simultaneous processes. The ions go to a vacant site or alloy with the host material. Simultaneously electrons are transferred into the electronic band of the host mostly in the case of intercalation. The most important thermodynamic aspect is based on change of concentration of the guest hence the change of free energy  $G$  with the number  $n$  of guest atoms or ions. This is the chemical potential  $\mu$ , because it is related to the insertion reaction, it corresponds to the binding energy of the guest ions in the host material thus has two contributions  $\mu_i$  and  $\mu_e$  respectively for the ion and the electron as shown in eq.: 2- 3.

$$\text{eq.: 2- 3 } \mu = \frac{\partial G}{\partial n} = \mu_i + \mu_e$$

The voltage  $E$  between electrodes is directly related to  $\mu$  in the cell. Considering that the chemical potential of a guest ion having a charge of  $-ze$  in the host material is  $\mu$  and the chemical potential of the guest itself is  $\mu_0$ , it was illustrated that for one ion inserted,  $z$  electrons will pass through the external circuit. Since the electrons move through, the potential difference  $E$  hence the work done per

ion inserted is  $-zeE$  and must be equal the change in free energy of the two electrodes that is  $(\mu - \mu_0)$ . This leads to the **eq.: 2- 4**.

$$\text{eq.: 2- 4 } \Delta G = -zeE = \mu - \mu_0$$

Therefore measuring the cell voltage at equilibrium versus charge passed between the electrode is equivalent to measuring the chemical potential as function of  $n$ . Thermodynamically, it is required that  $\mu$  increases with concentration of guest ion, as a result  $E$  decreases as the ions are added to the electrode. Charge or discharge of a cell is based on this phenomenon.

### 2.3.2. Capacity calculation.

Theoretical capacity is expressed in  $\text{mAh/g}$  and is calculated from the number of lithium ions inserted or de-inserted. This is based on the **eq.: 2- 5** below:

$$\text{eq.: 2- 5 } 1 \text{ mol of } Li^+ = 26810\text{mAh}$$

The first discharge of a cell takes into account irreversible and reversible processes whereas the reversible capacity is the useful capacity observed on cycling.

## 2.4. Electrochemical Testing.

Electrochemical tests were performed on both Macpile II and Maccor battery multi-channel testing systems under computer control. The Macpile program was set up by Y. Chabre and C. Mouget in Grenoble in 1989.

### 2.4.1. Galvanostatic mode.

Galvanostatic mode consists of applying a constant current and recording the potential versus time. From Faraday's law the capacity  $Q$  eq.: 2- 6 is proportional to time and the number of ions inserted through electron transfer.

$$\text{eq.: 2- 6 } Q = I * \Delta t = z * \frac{m * F}{M * 3600} * \Delta x$$

When  $Q$  is the capacity in  $mAh$ ,  $I$  is the current in  $A$  or  $mA$ ,  $\Delta t$  is the time in (s),  $z$  is the charge on the ion,  $m$  is the mass of the active material in (g),  $M$  is the formula weight of the active material, **3600** represents the conversion of time in seconds to hours and  $\Delta x$  the number of inserted or intercalated ions in (mols). It is worth mentioning that in this mode the system is not under equilibrium and the measured potential is affected by a polarisation voltage of a magnitude  $IR$  where  $R$  is the resistance through the cell leading to the eq.: 2- 7

$$\text{eq.: 2- 7 } E = U + IR + \eta$$

where  $U$  is the emf and  $\eta$  is the overpotential which is current dependent. Galvanostatic mode, however, can be performed under quasi thermodynamic equilibrium by using Galvanostatic Intermittent Titration Technique (GITT)<sup>6</sup>, which minimises overpotential losses.

Galvanostatic tests were performed by carefully selecting the operating voltage window, typically between 0.02 and 1.2V to limit the reactions, to only the desired ones. The current and voltage profile is shown in **Fig.: 2- 2**. On discharge a negative current is applied and the cell voltage drops until the cut off voltage is reached. The current is reversed i.e. to positive, charging the cell, and so the voltage rises until the top cut off voltage is reached. Between each discharge and charge sweep the system is relaxed for 1 hour to get close to equilibrium.

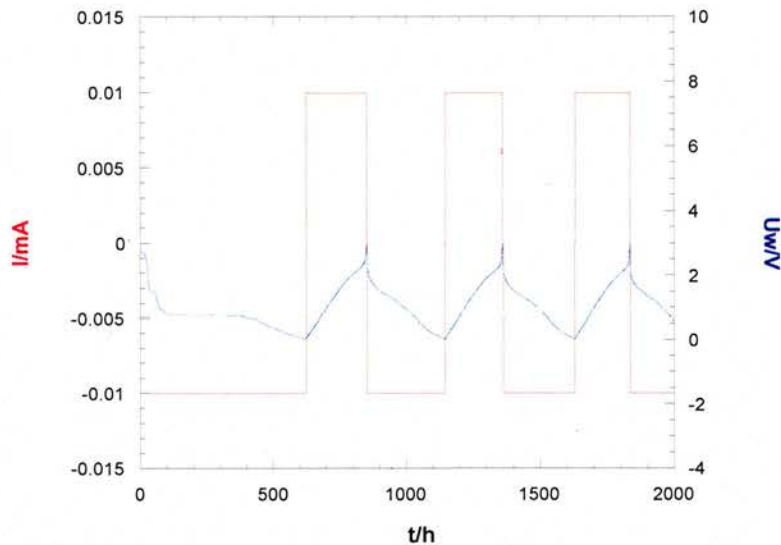


Fig.: 2- 2 Current profile versus time (in red) and voltage profile versus time (in blue) in a series of galvanostatic sweeps.

### 2.4.2. Potentiostatic mode.

In this mode the system operates by stepping the potential at a very slow rate. The charge transferred, and hence the average current, are recorded for each potential step. The next potential step is applied either when the current drops below a minimum limit or after a maximum time. These values can be set so that at the end of each step the system reaches equilibrium or close to it.

Potentiostatic tests were performed by selecting carefully the operating voltage window, typically between 0.02 and 2V, to show all reactions that might occur with a step rate of 20mV every hour. The voltage and current profile is shown in **Fig.: 2- 3**. On discharge the cell voltage is lowered step by step until the cut off voltage is reached. After relaxation, the voltage is slowly raised up step by step until the upper cut off voltage is reached. Between each discharge and charge sweep the system is allowed to relax for 1 hour to reach equilibrium. There is no relaxation between each potential step. Potentiostatic cycling is the technique of choice when studying a system for the first time as every process occurring appears as a peak, easily revealing the presence of electrochemical transformations.

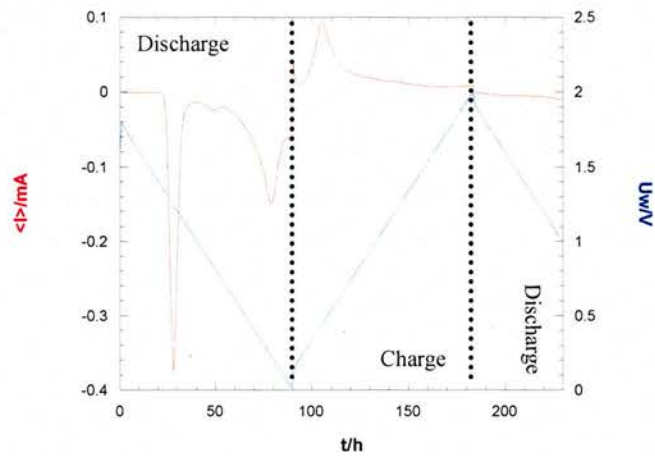


Fig.: 2- 3 Current profile versus time (in red) and voltage profile versus time (in blue) in a series of potentiostatic sweeps.

### 2.4.3. Advanced Electrochemical Techniques.

Galvanostatic Intermittent Titration Technique (GITT) and Potentiostatic Intermittent Titration Technique (PITT) methods are the standard experimental techniques used to determine lithium diffusion constants in lithium batteries. Step Potential Electro-Chemical Spectroscopy (SPECS) was introduced recently for the same goal, with more accuracy. From these three methods, on the basis of the solution to Fick's equation, lithium diffusion coefficient can be obtained.

The GITT technique was introduced by Huggins et al <sup>7 8</sup>. In GITT, a system is perturbed by imposing a constant current  $I_o$  for short time interval and the potential is recorded as a function of time during the relaxation between current pulses.

In PITT<sup>8</sup>, the system is perturbed with a potential step and the current is recorded as a function of time.

#### 2.4.3.1. SPECS.

In SPECS<sup>9</sup> as in PITT, the system is perturbed with a potential step and the current is recorded as a function of time at each step. In this work the analysis of the data will follow those described in SPECS.

This is a very powerful technique that can provide accurate information on kinetics and thermodynamics and hence leads to a phase diagram for the system. It can also be used to obtain a value for the lithium diffusion coefficient<sup>9,10</sup>.

The typical experiment started from the open circuit voltage (OCV) dropping down to 0.02V, at a step rate of  $\pm 20\text{mV}$  every 15 hours or until the current ( $I$ ) condition of  $|I| < |I_0|/50000$  was satisfied, whichever occurred first.

A significant advantage should be noticed with respect to galvanostatic methods that side reactions, as for instance electrolyte oxidation or reduction, can be treated separately.

As an aside, due to the fact that the sample is always in equilibrium, thermodynamic information can be extracted from the open circuit voltage at the

end of each step of the reaction and can lead to the determination of free energy ( $\Delta G$ ), enthalpy ( $\Delta H$ ) and entropy ( $\Delta S$ ).

The kinetics of the electrochemical insertion reaction is limited by the rate of diffusion of the guest ion and follow Fick's law **eq.: 2- 8**, which can be described by the current relaxation versus time curve.

$$\text{eq.: 2- 8 } \frac{\partial c_i(x,t)}{\partial t} = \tilde{D} \frac{\partial^2 c_i(x,t)}{\partial x^2}$$

In the data, there are two possibilities, firstly when the current relaxation does not reach *zero* and so Fick's law can not be easily solved. These are typically "two phase regions" where the compositions of the coexisting phases do not change, hence the chemical potential is constant in this two-phase region **Fig.: 2- 4**. This current decay versus time is called "anomalous behaviour" and therefore no practical kinetic information can be extracted.

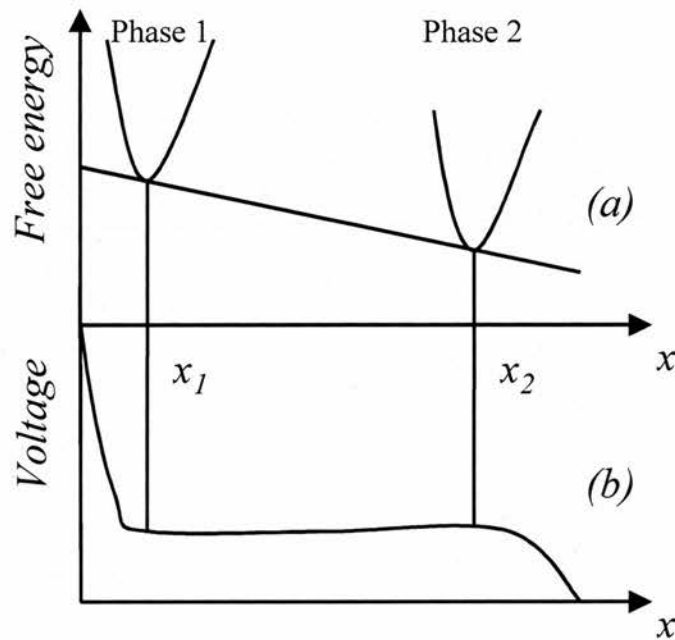


Fig.: 2- 4 Free energy & voltage profile in a phase transition region

The other alternative is when the current relaxation reaches **zero** and the current decay versus time is symmetric **Fig.: 2- 5**, the system describes a solid solution region. For this region, Fick's law can be solved and the diffusion coefficient can be calculated. The solution of the Fick's second law for time can be obtained by either of two approximations: for the short time approximation **eq.: 2- 9** and the long time approximation **eq.: 2- 10**, **Fig.: 2- 6**.

$$\text{eq.: 2- 9 } q(t) = \frac{2FS\Delta C \sqrt{D_{Li^+}}}{\sqrt{\pi}} * \sqrt{t} \quad \text{For short time approximation } (t \ll L^2/D_{Li^+})$$

$$\text{eq.: 2- 10 } q(t) = \frac{8FS\Delta C}{\pi^2} * \exp\left(-\frac{\pi^2 D_{Li^+} t}{4L^2}\right) \quad \text{For long time approximation } (t \gg L^2/D_{Li^+}).$$

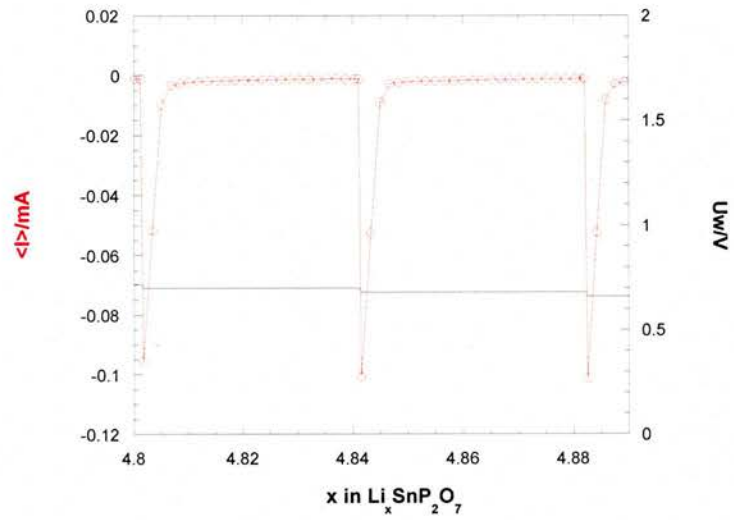


Fig.: 2- 5 Current relaxation plot in a solid solution region from a SPECS

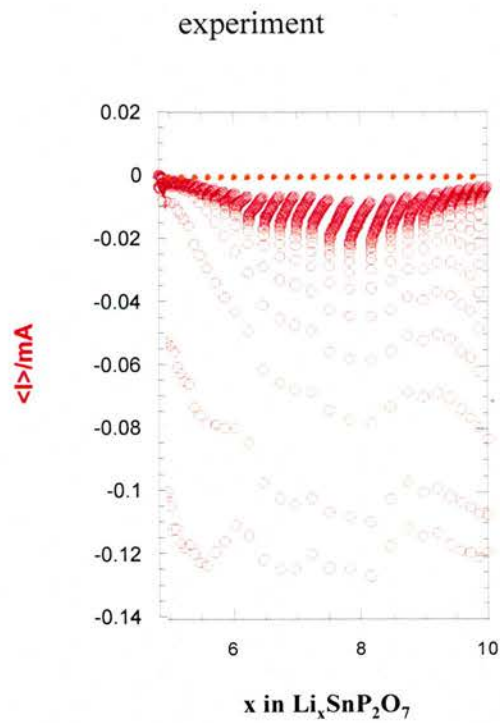


Fig.: 2- 6 Current relaxation plot in a phase transition region.

See Chapter 3 for more details of data treatment.

## 2.5. Characterisation Techniques.

### 2.5.1. Background.

#### 2.5.1.1. X-ray generation.

The most widely used source of radiation for powder diffraction is still the conventional sealed X-ray tube. Neutron sources and synchrotron radiation are used world-wide in central research facilities. A sealed X-ray tube consists of a cathode with a filament made in tungsten for instance that emits electrons that are accelerated by a high voltage (~30-60 kV) under vacuum. These electrons hit the fixed anode made of a material whose characteristic spectrum has a  $K_{\alpha}$  line of a wavelength appropriate for the diffraction experiment to be performed. Example for copper,  $K_{\alpha}$  corresponds to the  $2p \rightarrow 1s$  transition and has a wavelength of  $1.5418\text{\AA}$ .  $K_{\alpha}$  transition is a doublet because the transition has a slightly different energy for the two possible spin states of the  $2p$  electron which makes the transition relative to the spin of the vacant  $1s$  orbital. The  $3p \rightarrow 1s$  transition corresponds to  $K_{\beta}$  and has a wavelength of  $1.3922\text{\AA}$ . The target anode materials are typically a metal from Cr ( $Z = 24$ ) to Ag ( $Z = 47$ ) corresponding to  $K_{\alpha}$  radiation wavelengths between  $2.29$  and  $0.56\text{\AA}$ , of which Cu ( $Z = 29$ ) is the most commonly used with a Cu-  $K_{\alpha 1}$  wavelength of  $1.54051\text{\AA}$  and Cu-  $K_{\alpha 2}$  wavelength of  $1.54433\text{\AA}$  that is filtered out. To avoid collisions between particles and either

the incident electrons or emitted X-rays, high vacuum is necessary. The process of X-ray generation is highly inefficient (i.e. < 1%) with most of the electron energy being converted to heat and hence in order to avoid melting of the target, it must be water-cooled. This is most efficiently done by filtering and directing water in a jet onto the back of the anode. The X-rays are produced in all directions and leave the tube through four windows made of beryllium. The generated X-rays does not contain only the most intense desired  $K_{\alpha}$  lines, but also unwanted  $K_{\beta}$  and continuum radiation which are removed by a filter (e.g. nickel foil for Cu radiation, zirconium foil for Mo radiation) or a crystal monochromator (e.g. quartz). A sketch of a sealed X-ray tube is shown in **Fig.: 2- 7**.

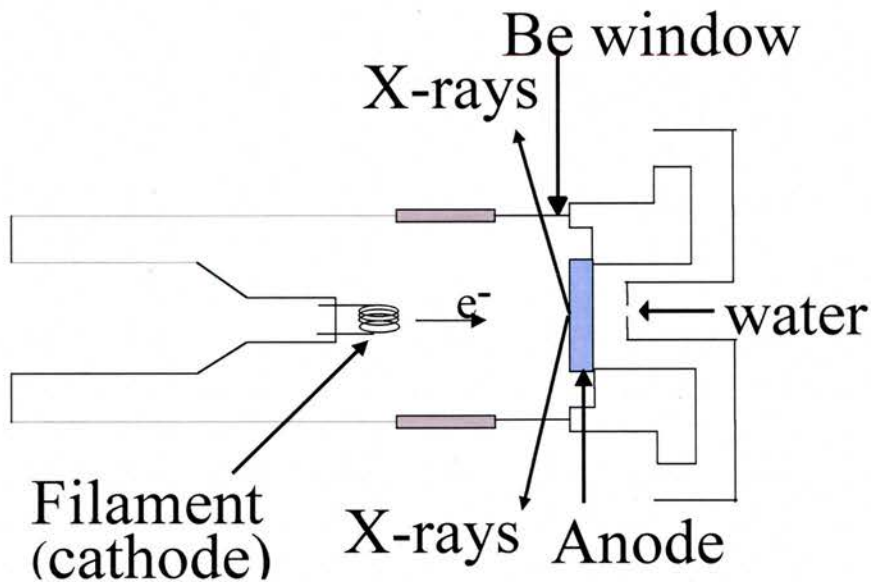


Fig.: 2- 7 Schematic of a sealed X-ray tube.

The generated X-rays are directed onto the sample specimen placed between the source and the detection system in certain geometric arrangements, which allow the diffracted X-rays photons to be collected. The incident X-ray beam can either be reflected at the surface of the sample (reflection mode) or pass through the sample bulk (transmission mode).

### 2.5.1.2. X-Ray.

#### 2.5.1.2.a. Bragg's law.

Bragg's Law is a practical way of describing X-ray diffraction. When an incident X-ray beam interacts with the lattice planes, they are diffracted at an angle of  $2\theta$ . A diffraction peak only occurs when that diffracted angle  $\theta$ , satisfies the Bragg equation linking  $\theta$  to the wavelength  $\lambda$  and the lattice d-spacing.

Considering two X-ray, beams 1 and 2 diffracted by parallel planes A and B to remain in phase. The distance  $xyz$  must be equal to an integer number of wavelengths as described by Bragg's Law **eq.: 2- 13**. The distance between the two planes d-spacings ( $d_{hkl}$ ) and the angle are related to the  $xy$  distance by:

$$\text{eq.: 2- 11 } xy = yz = d \sin \theta$$

$$\text{eq.: 2- 12 } xyz = 2 d \sin \theta = n \lambda$$

This gives Bragg's Law:

$$\text{eq.: 2- 13 } 2d \sin \theta = n\lambda$$

When this equation is satisfied, the beams are in phase and constructively interfere producing a diffraction beam as shown **Fig.: 2- 8**. At other angles the beams are not in phase and so destructively interfere.

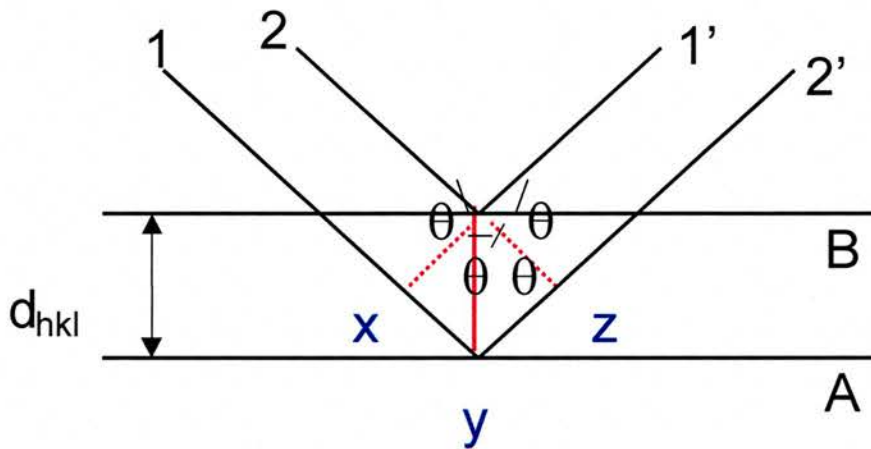


Fig.: 2- 8 Derivation of Bragg's law

Bragg's law is the simplification of the Laue equations which are the basis of X-ray diffraction. Ideally powder samples contain an infinite number of randomly oriented lattice crystallites.

### 2.5.1.3. Powder diffraction technique.

Diffraction of X-rays by polycrystalline materials, ideally considered as an ensemble of a very large number of randomly oriented crystallites, is nowadays one of the most important, powerful and widely used analytical techniques

available to the material scientist<sup>11</sup>. The basic difference between coherent scattering from planes of atoms of spacing  $d$  in a single crystal and a random powder is that diffracted beams from individual crystallites in the latter generate cones with semi-angle  $2\theta$  that satisfies Bragg's equation:

$$\text{eq.: } 2-14 \quad \lambda = 2d \sin \theta$$

where  $\lambda$  is the wavelength of the radiation used,  $d$  the lattice spacing or separation between scattering and  $\theta$  the angle of incidence or Bragg angle.

In such a powder sample the various lattice planes are also present in every possible orientation. The only requirement for diffraction is that the planes be at an angle  $\theta$  to the incident beam; with no restriction placed on the angular orientation of the planes about the axis of the incident beam. In a finely powdered sample, crystals are present at every possible angular position about the incident beam and the diffracted beams that result appear to be emitted from the sample as cones of radiation (each one is in fact a large number of closely spaced diffracted beams).

The major problem in using powder diffraction is that reflections can overlap. Therefore, improvements in both instrument resolution and data processing have facilitated the use of this technique, to characterise composition, structural arrangement (unit cell, symmetry and atomic parameters) and the particle size of crystalline materials.

#### 2.5.1.4. Particles size measurement.

Peak shape or peak broadening observed in an X-ray powder diffraction pattern are affected by the size of the crystallite. The average value of the particle can be estimated by the Scherrer formula<sup>12</sup> eq.: 2- 15:

$$\text{eq.: 2- 15 } t = \frac{0.9\lambda}{[(B_M^2 - B_S^2)^{1/2} \cos \theta]}$$

where  $t$  is the crystallite size in Å and  $\lambda$  the wavelength used by the diffractometer i.e.  $\lambda = 1.54056 \times 10^{-10}$  m for the  $\text{CuK}_{\alpha}$  radiation.  $B_M$  and  $B_S$  are the FWHM in radians of the sample and the standard respectively. Highly crystalline materials such as silicon give standard values. The calculations are performed using peaks with significant intensities.

#### 2.5.1.5. The STOE Transmission Diffractometer.

The STOE transmission diffractometer system STADI P (STOE Automated Diffractometer for powder) uses a standard high voltage generator Spellman DF4. The produced Cu radiation is contained within a guiding tube and focused towards a curved Ge(111) monochromator that selects the  $\text{Cu-K}_{\alpha 1}$  radiation. The width and height of the monochromatic beam can be defined by a slit system and two horizontal slides inserted between the monochromator and the collimator. The collimator can be changed depending on the operation mode (transmission or

capillary sample). Diffraction from the sample specimens occurs from planes, which are nearly normal to the surface and the diffracted beam obtained is then registered by a linear position sensitive detector (PSD), based on a gas proportional counter, which simultaneously collects an angular range of  $\Delta 2\theta = 6.5 - 7^\circ$ . The diffraction system is controlled using the STOE Powder Diffraction Software VISUAL X<sup>pow</sup>. For further details see the STOE manual<sup>13</sup>. Typical data acquisition suitable for structure refinement was carried out for 12 - 15 hours using a step size of  $0.05^\circ$ .

One of the main advantages of the Stoe diffractometer lies in the use of a curved monochromator capable not only of separating  $K_{\alpha 1}$  from  $K_{\alpha 2}$ , but also converting the divergent incident beam into an intense convergent diffracted beam focused onto a sharp line with consequent improvement in resolution.

#### **2.5.1.6. Preparation of sample for XRD.**

X-ray patterns were collected using the STOE diffractometer. A small amount of sample was placed two thin plastic sheets with a thin layer of vaseline which hold the powder. The sample was then rotated while collecting. A typical run on a STOE diffractometer can be done over 1 hour 30min – 2 hours or overnight (for high resolution pattern).

### 2.5.1.7. In-situ XRD.

In-situ experiments were performed on the STOE diffractometer in the same condition as the normal XRD experiment on the electrode within the battery. A schematic representation of the holder is shown in **Fig.: 2- 9** For the in-situ XRD experiment, a special sample holder of 2.3cm diameter was used to fit the battery that was fixed with two screws for the XRD data collection.

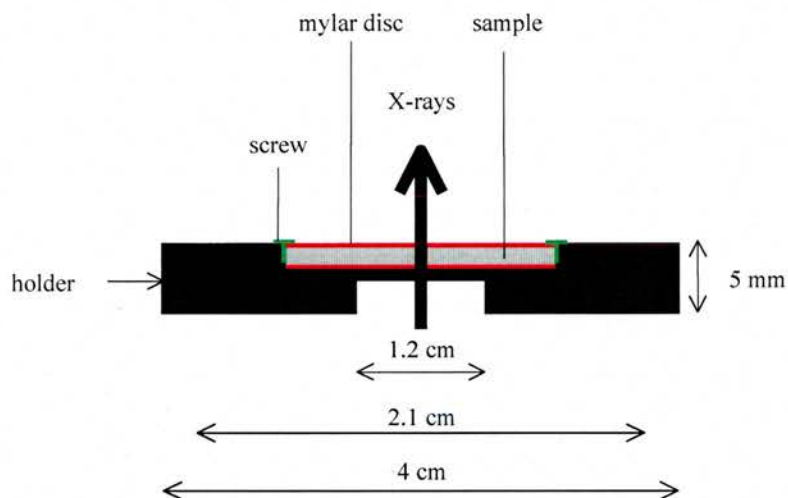


Fig.: 2- 9 Schematic representation of the sample holder for Stoe diffractometer

The battery used for these experiments was slightly modified compared to the standard coin cell described previously. A 5mm hole was punched in the middle of both negative and positive coin cell cases and in the centre of the spacer. To preserve the sealed system of the battery, plastic windows were fixed over the holes of the coin cell cases. “Roscoe bond” was used to seal the plastic windows

on the inside. At the positive case, stronger PET was used due to the higher pressure exerted at the window. At the negative end, a 0.125mm thick piece of Kapton was used as a window.

Most importantly, as the window is insulating a current collector is required for the positive side that should be in contact with the coin cell case and the electrode. For this cell, the current collector used is either copper or aluminium grid in order to maximise X-ray transmission. The aluminium grid can not be used below 0.5V to reduce aluminium-lithium alloy formation. A Nickel grid is also another candidate for these cells. It is worth to note that the Celgard separator was preferred to glass fibre separator that was used in the standard coin cell in order to prevent short circuit. A schematic representation of the in-situ battery is shown

**Fig.: 2- 10.**

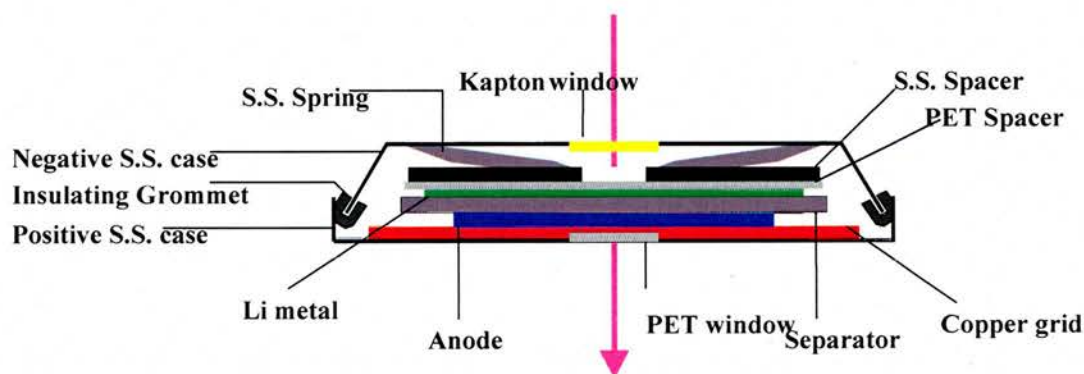


Fig.: 2- 10 A schematic representation of the in-situ battery

The aim of the holes punched in the cell case is to allow the transmission of x-rays through the sample in order to obtain a diffraction pattern of the test material without dismantling the cell. The patterns were collected overnight. This long data collection time is necessary because the PET and Kapton windows absorbed most of the x-rays during the measurement.

## 2.6. MAS-NMR.

### 2.6.1. Background.

Nuclear magnetic resonance (NMR) is a powerful technique to study structural, electromagnetic and dynamic interactions in solids. NMR occurs because many nuclei possess a property that is referred to the spin of nucleus. A single electron, proton and neutron have spin of  $\frac{1}{2}$  ( $S = \pm \frac{1}{2}$ ), with nuclear spin being the resultant of the neutron and proton spins. According to quantum mechanics the measurable component of spin of any nuclei system is quantized through the total angular momentum of particle with spin that takes values of the form  $|J| = [\sqrt{I(I+1)}] * \hbar$  where  $I$  is the spin quantum number of the nucleus which may have one of the following positive multiple values of  $\frac{1}{2}$   $I = 0, \frac{1}{2}, 1, \frac{3}{2}, 2,$

....and  $\hbar = \frac{h}{2\pi}$  where  $h$  is Planck's constant. Basically for particle with  $n$  spins,

the spin quantum number is quantized as:  $I = \sum_n S$ . Any nucleus with an even mass number and an even charge number (i.e. with even number of both proton and neutron) will have  $I = 0$ . However, angular momentum is a vector. Conventionally the direction of  $J$  is that of the spin axis. As  $I$  is defined as the spin quantum number, which is the maximum component of the momenta, nucleus must have a value of  $m_I = 2I+1$  distinct states in which the component of the angular momentum along any selected direction will have values of  $I, (I-1), \dots, (-$

$I+1$ ),  $-I$ . All nuclei with  $I \neq 0$  have a magnetic moment  $\mu$  given by :  $\mu = \gamma J$  where  $\gamma$  is the gyromagnetic ratio which has a different value for every isotope. In the absence of any fields, these states are in the same energy level. According to classical mechanics a magnetic moment interacts with a magnetic field at an appropriate frequency related to each nucleus, the so called Larmor frequency of nucleus where observation of the nuclear spin state is viable. This frequency depends upon the gyro-magnetic ratio of the nucleus and can be related to the probability of transitions occurring between nuclear levels by absorption or emission of energy quanta  $\Delta E$ .

Particles with a number of spins  $S$  have  $m_I = 2I + 1$  sublevels, which in the absence of external fields will have the same energy level but in the presence of fields these sublevels occupy different energy level if a magnetic or electric field is applied. This phenomenon rises from several interactions between particles. A Hamiltonian operator can describe the total interactions for a nucleus in a magnetic field as shown in **eq.: 2- 16** below:

$$\text{eq.: 2- 16 } \hat{H} = -\gamma \cdot \mathbf{B}_0 \cdot \hat{\mathbf{J}} = \hat{H}_D + H_z + \hat{H}_{CS} + \hat{H}_{SC} + \hat{H}_Q$$

where  $B_0$  is a static magnetic field ,  $H_D$  is the Hamiltonian that describes the dipole-dipole interactions,  $H_z$  is the Zeemann Hamiltonian,  $H_{CS}$  describes the chemical shift anisotropy,  $H_{SC}$  accounts for the spin coupling interactions and  $H_Q$  the quadrupolar interactions. Resolution of time independent Schrödinger **eq.: 2- 17** results in:

$$\text{eq.: 2- 17 } E_{m_I} = -\gamma * \hbar m_I * B_0$$

The classical resonance frequency can be deduced from that expression as:  $\omega_0 = -\gamma \cdot B_0$ .

### 2.6.2. Dipole-dipole interactions and Magic Angle Spinning (MAS) NMR.

Dipole-dipole interactions  $H_D$  describe the direct, through space dipolar interaction between the nuclear moments of two nuclei i.e. homo or heteronuclei **Fig.: 2- 11** and is solely dependent on the magnitude and the orientation of the nuclear spin involved. This interaction is averaged out in solution due to molecular tumbling. In solids however this interaction causes line broadening. Under MAS conditions, the dipole-dipole interactions are lost and sharp lines are generated close to the isotropic value with rotational side bands spaced at intervals equal of the spinning frequency. MAS is a method used to improve resolution by simulating the molecular tumbling of a solution. MAS originates from the observation that broadening Hamiltonians (e.i.  $H_D$ ,  $H_{CS}$ ,  $H_Q$ ) include a term proportional to  $(3 \cos^2 \theta - 1)$ . The dipole-dipole interaction is related to the internuclear distance and depends on  $\theta$  **eq.: 2- 18**

$$\text{eq.: 2- 18 } d \propto \frac{(3 \cos^2 \theta - 1) / 2}{r^3}$$

These terms can be reduced or eliminated by high frequency spinning of the sample at the “magic” angle of  $54^{\circ}44'$ , hence reducing broadening and improving resolution.

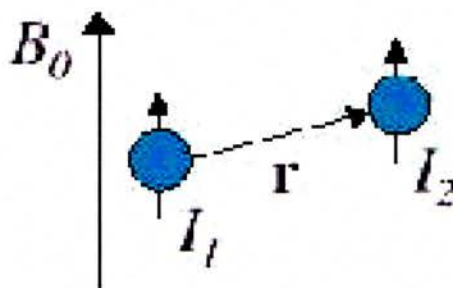


Fig.: 2- 11 Dipole-dipole interactions.

### 2.6.3. Zeemann interactions.

Transitions between atomic energy levels without applied magnetic fields do not show any splitting. In the presence of magnetic fields, the atomic energy levels are split into a large number of levels and the spectral lines are also split. The splitting up of these spectral lines of atoms within the magnetic fields is called the Zeemann effect. This phenomenon was observed for the first time by the Dutch physicist Pieter Zeemann in 1896. The splitting is related to the orbital angular momentum quantum number  $L$  of the atomic level.

The number of split levels in the magnetic field is  $2L+1$  and the following **eq.: 2-19** illustrates the Zeemann effect **Fig.: 2- 12**.  $\Delta E$  is given by the following expression:

$$\text{eq.: 2- 19 } \Delta E = \gamma \hbar B_0 = g_n \beta_n B_0$$

where  $\gamma$  and  $g_n$  are the gyromagnetic ratio,  $\hbar$  is Planck's constant,  $B_0$  the applied magnetic field and  $\beta_n$  the Lande splitting factor.

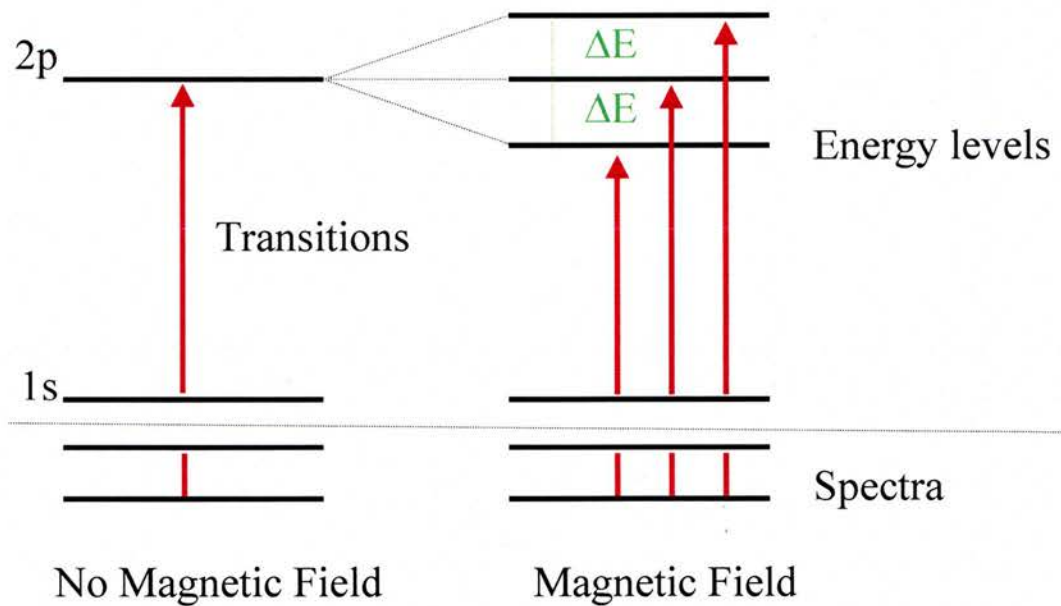


Fig.: 2- 12 Zeemann splitting effect.

#### 2.6.4. Chemical shift anisotropy.

The observed chemical shift of a nucleus is a measurement of the effective magnetic field around the nucleus, which depends on the electronic surroundings of the nucleus. The chemical shift arises because the field actually experienced by the nucleus,  $B$ , is slightly different from the external field  $B_0$  due to the effect of the electrons circulating within their atomic orbitals. This induced motion is like an electric current passing through a coil of wire generating a small magnetic field  $B'$  in the opposite direction to  $B_0$  **Fig.: 2- 13**. The nucleus is thus shielded from the external field by its surroundings electrons ( $B = B_0 - B' = B_0(1 - \sigma)$ ) where  $\sigma$  is the so called shielding constant. It is the dimensionless constant of proportionality between  $B'$  and  $B$  characteristic of the nucleus in its chemical site. As a result of nuclear shielding, the resonance frequency condition can be assigned as below **eq.: 2- 20**:

$$\text{eq.: 2- 20 } \nu = \frac{\gamma \cdot B}{2\pi} = \frac{\gamma \cdot B_0(1 - \sigma)}{2\pi}$$

Note that for a nucleus within an atom with incomplete electron shell (paramagnetic), the applied field is reinforced with a negative shielding constant and thus a higher resonance frequency, whereas in a case of a diamagnetic electron shell the shielding constant is positive and consequently lowers the resonance frequency. In order to be able to compare this effect for different

environments of a given nucleus, it is common practice to define the chemical shift in terms of difference in resonance frequencies ( $\nu$ ) between the nucleus and a reference nucleus ( $\nu_{ref.}$ ), by means a dimensionless parameter,  $\delta$  **eq.: 2- 21**:

$$\text{eq.: 2- 21 } \delta = 10^6 \frac{(\nu - \nu_{ref.})}{\nu_{ref.}}$$

The frequency difference ( $\nu - \nu_{ref.}$ ) is divided by  $\nu_{ref.}$  so that  $\delta$  is independent of the magnetic field. The factor  $10^6$  scales the value of  $\delta$  to a convenient size quoted in parts per million or ppm. The value of  $\delta$  is strictly related to  $\sigma$  via the **eq.: 2- 22** below:

$$\text{eq.: 2- 22 } \delta = 10^6 \frac{\sigma_{ref.} - \sigma}{1 - \sigma_{ref.}} \approx 10^6 (\sigma_{ref.} - \sigma)$$

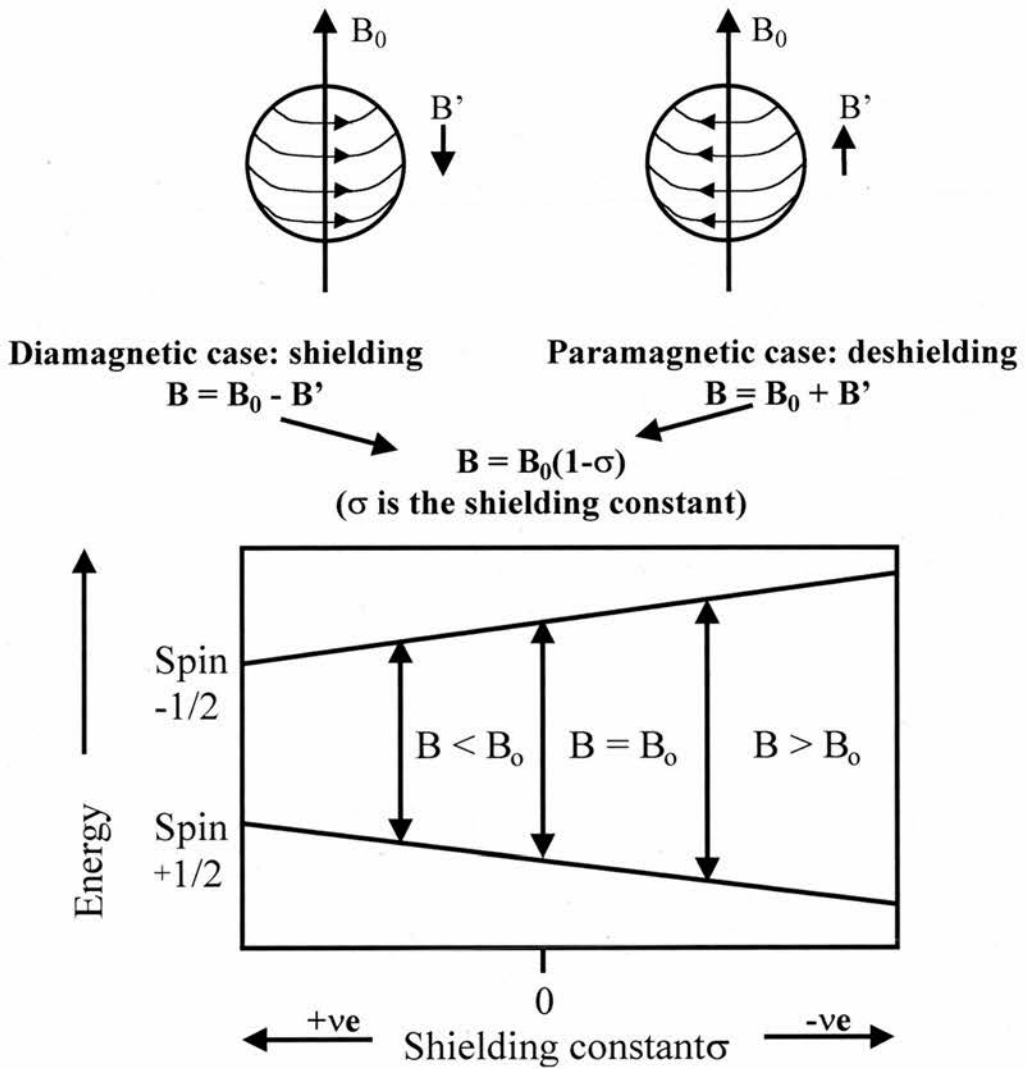


Fig.: 2- 13 Electronic shielding/deshielding of a nucleus in an applied magnetic field.

### 2.6.5. Spin coupling interactions.

Spin coupling interactions exist but are not usually seen in solid state NMR because its contribution is too small therefore it will be ignored.

### 2.6.6. Quadrupolar interactions.

The charges of the electrons and nuclei are source of large electric field gradient about position of the nucleus in most molecules or solids. The electrical quadrupole moment of non spherical nuclei **Fig.: 2- 14** ( $I > \frac{1}{2}$ ) has a number of discrete energy levels in this gradient. Spin in a magnetic field interacts with both the gradient and  $B_0$ . The electrical quadrupole interaction is smaller than the magnetic interaction. Both contributions lead to the **eq.: 2- 23** below

$$\text{eq.: 2- 23 } \Delta E = \hbar\omega = \hbar\gamma \cdot B_0 - \frac{3}{8} e^2 q Q \frac{2m_I - 1}{3I - I(I + 1)} (3 \cos^2 \theta - 1)$$

$\frac{e^2 q Q}{\hbar}$  is the quadrupolar coupling constant,  $I$  the spin quantum number of the considered nucleus,  $m_I$  the corresponding quantum number for the projectory of the spin angular momentum to  $B_0$ ,  $\theta$  is the angle between  $B_0$  and the symmetry axis of the field gradient tensor. Spinning side bands are due to in some cases small quadrupolar interactions in solids. Large quadrupolar interactions give in

addition line broadening due to second order quadrupolar interactions that can not be reduced with MAS.

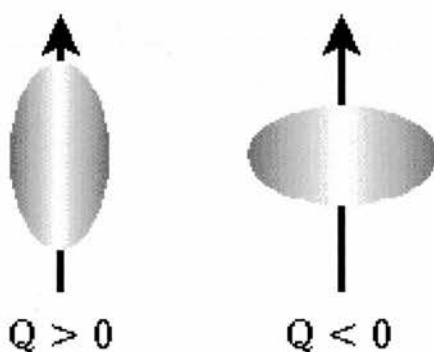


Fig.: 2- 14 Electrical quadrupole moment of non spherical nuclei

### 2.6.7. Pulse.

A pulse is defined as irradiating the sample with a RF- field with a well defined frequency, amplitude and phase for a relatively short time. The pulse length is relatively short compared to the relaxation times, therefore the influences of the relaxation can be neglected. When the RF-field has the same frequency as the resonance frequency, the phase  $\varphi$  is zero and hence the magnetisation is rotating around the x-axis in the rotating system with an angular frequency **Fig.: 2- 15**.

The NMR experiments were performed using a direct polarisation 90-FID pulse sequence **Fig.: 2- 16**. In this case, the net magnetisation ( $M_0$ ) parallel to  $B_0$ , is



**2.6.8. Experimental conditions.**

Solid state NMR experiments were carried out on a VARIAN Infinityplus spectrometer operating at a Larmor frequency of 499.78MHz for  $^1\text{H}$  and 202.466 , 73.602 and 160.469 MHz for  $^{31}\text{P}$ ,  $^6\text{Li}$  and  $^{11}\text{B}$  respectively. The samples were packed in a 4mm  $\text{ZrO}_2$  rotor with a Vespel drive tip, teflon spacers and end cap. One-dimensional (1-D) direct polarisation magic angle spinning DP-MAS-NMR spectra were recorded at a spinning speed of 10kHz using a  $90^\circ$  pulse duration and recycle delay of  $6\mu\text{s}$  and 80s for  $^{31}\text{P}$  or  $1.5\mu\text{s}$  and 0.5s for  $^6\text{Li}$  or 2s for  $^{11}\text{B}$ . All chemical shifts are expressed in ppm and referenced relative to a Lithium chloride solution for  $^6\text{Li}$ , to  $\text{H}_3\text{PO}_4$  (85 % w/w, Aldrich) solution for  $^{31}\text{P}$  and borotetrafluoroetherate solution for  $^{11}\text{B}$ .

## 2.7. Electron Microscopy.

Electron Microscopy is based upon the interaction of electron with solids. The nature of those interactions leads to various techniques, of relevance to this study on Selected Area Electron Diffraction (SAED), High Resolution Transmission Electron Microscopy (HRTEM), Scanning Electron Microscopy (SEM) and Energy Dispersive Spectroscopy (EDS).

The SAED and HRTEM micrographs were collected using a JEOL-JEM 2011 electron microscope that operates at 200kV and is equipped with a side entry  $\pm 20^\circ$  (double tilt specimen holder). The SEM images were performed on a JEOL JSM-5600 that operates in a voltage range between 3 and 20kV.

EDS microanalysis systems are coupled with both TEM and SEM instruments.

### 2.7.1. SAED.

Electron diffraction is a powerful technique in terms of determination of structural parameters i.e. cell parameters and space group. This technique is similar and hence complementary to XRD as the SAED pattern arises when Bragg conditions are satisfied. This technique gives information about local structure. The SAED pattern represents the reciprocal structure of the specimen, that can be converted into real d-spacings,  $d_{hkl}$ , via the following eq.: 2- 24.

$$\text{eq.: 2-24 } d_{hkl} = \frac{l}{d^*} = \frac{\lambda l}{\text{distance measured in SAED}}$$

where  $d^*$  represents the reciprocal distance measured on the micrograph,  $\lambda$  is the wavelength of the electron beam (0.0251 Å when operating at 200kV) and  $l$  being the camera length.

### 2.7.2. HRTEM.

High resolution images are basically generated from transmitted and elastically scattered electrons that interact with the specimen. This technique allows resolution of less than 2 Å and hence evidences the real atomic distribution such as nanodomains or atomic deficiency.

The combination of XRD, HRTEM and SAED results in a powerful tool to picture and elucidate materials.

### 2.7.3. Preparation of sample for SAED, HRTEM – EDS.

The samples were prepared by suspending a small amount of powder typically in acetone in general or in DMC for lithiated samples to prevent oxidation. A few drops of this suspension are deposited onto a perforated carbon-coated copper grid. After evaporation of acetone or the DMC, the grid is placed in the sample holder and then inserted into the microscope.

#### 2.7.4. SEM.

SEM images are generated by an electron beam. The beam is produced at the top of the microscope by heating of a metallic filament, which represents also the cathode of the instrument. The electron beam follows a vertical path through the column of the microscope and is accelerated by an anode. It makes its way through electromagnetic lenses, which focus and direct the beam down towards the sample. Once it hits the sample, other electrons (backscattered or secondary) are ejected from the sample. Detectors collect the secondary or backscattered electrons and convert them to a viewing screen similar to the one in an ordinary television, producing an image.

A schematic representation of a SEM instrument is shown in the **Fig.: 2- 17** below.

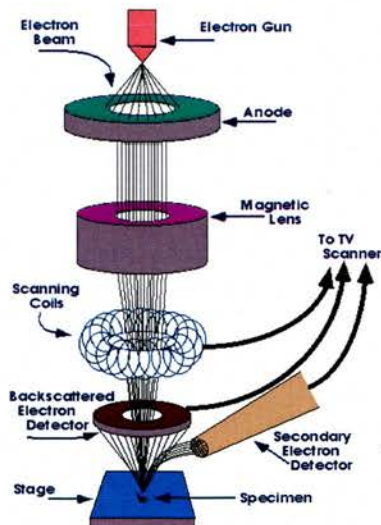


Fig.: 2- 17 Schematic representation of a SEM set up

SEM provides microstructural information such as texture, surface and particle size at a range of magnifications (20 – 100,000). Since the length of electron beam scan on the sample is smaller than the length of the TV screen, a magnification is produced equal to the following eq.: 2- 25:

$$\text{eq.: 2- 25 } \textit{Magnification} = \frac{\textit{length of TV scan}}{\textit{length of electron beam scan}}$$

By changing the size of the scan on the sample, the magnification can be changed. The smaller the area the electrons beam scans the higher the magnification. Obtaining different degrees of magnifications are important in any practical uses of the SEM.

#### **2.7.5. Preparation of sample for SEM – EDS.**

The samples were mounted onto specimen holders with electrically conducting carbon adhesive discs (Agar Scientific Ltd).

EDS is based on interaction between the electron beam and specimen. Due to the high energy of the beam, the specimen generates X-ray radiation that is characteristic to each element. The displayed pattern obtained from the EDS represents qualitatively and quantitatively the signature of the specimen composition. EDS microanalysis using an Oxford Link ISIS system is couple with the TEM machine and allows to check the homogeneity of the specimen and to determine the ratio of chemical elements.

## 2.8. IR.

Infrared spectroscopic analyses were performed on a Perkin Elmer system 2000 NIR FT- Raman spectrometer. Spectra were recorded in transmittance mode using the standard KBr pellet technique. The spectra were measured with  $2\text{cm}^{-1}$  resolution on a spectrum range of  $4000$  to  $500\text{cm}^{-1}$ .

## 2.9. XPS.

The XPS data were collected by on VG ESCALAB II spectrometer with a operating pressure of  $1 \times 10^{-9}$  mbar using an unmonochromatised  $\text{AlK}_{\alpha}$  radiation ( $1486.6\text{eV}$ ). The sampled area was 3mm diameter. Peaks were recorded with constant step energy of  $0.05\text{eV}$ , and a pass energy of  $20\text{eV}$ .

Samples were placed on a sample holder as a pellet made of a mixture of sample to be analysed and carbon as a binding energy reference in an argon filled glove box and carried quickly into the analysis chamber. The binding energy scale was calibrated with the  $\text{C}1\text{s}$  line at  $284.6\text{eV}$  from the carbon. The spectra were analysed using a peak synthesis program (CASAXPS), fitting with distribution of gaussian (80%), lorentzian (20%) and Shirley background.

## 2.10. TGA, DTA.

Thermal analysis is a technique that gives useful physical and chemical information. The two main techniques used are Thermogravimetric Analysis (TGA) and Differential Thermal Analysis (DTA).

TGA characterisation involves recording of weight loss or uptake, of a sample as function of either time or temperature showing assessment of oxidation state. This technique is normally performed under gas flow.

DTA analysis consists on recording differences in temperature between an inert reference material (alumina) and the sample as a function of temperature. Therefore, changes in the heat content can be detected, and it can also be determined whether these changes are endothermic or exothermic. These changes in heat content can correspond to thermal events such as melting, decomposition or changes in crystal structure. The combination of DTA/TGA allows tailgating evolution of reactions.

The instrumentation is based on an ultra sensitive balance within a furnace whose temperature is accurately controlled. Different atmosphere conditions depending on the chosen gas flow can be used when studying a sample. Typical TGA/DTA experiment consist of heating a sample from room temperature up to 1000°C at a fixed rate of 5-10K/min and then cooling it down after holding the temperature for 6 hours at the endpoint temperature. All our measurements were performed on

(SDT 2960 simultaneous DTA-TGA; TA instruments), which simultaneously employs both techniques.

**2.11. References.**

- <sup>1</sup> R. K. B Gover, N. D. Withers, S. Allen, R. L. Withers, J. S. O. Evans, *J. Solid State Chem.*, **166**, (2002), 42-48
- <sup>2</sup> E. Rodriguez-Castellon, A. Rodriguez-Garcia and S. Bruque, *Inorganic Chemistry*, **24**, (1985), 8
- <sup>3</sup> A. S. Gozdz, C. N. Schmutz, J. M. Tarascon, P. C. Warren, U.S. Patent 5, 552, 239 (1996)
- <sup>4</sup> C. Vincent and B. Scrosati, *Modern batteries*, 2<sup>nd</sup> edition
- <sup>5</sup> M. Behm and J. T. S. Irvine, *Electrochim. Acta*, **47** (2002) 1727-1738
- <sup>6</sup> W. Weppner, R. A. Huggins, *Ann. Rev. Mat. Sci.* **8** (1978) 269
- <sup>7</sup> W. Weppner, R. A. Huggins, *J. Electrochem. Soc.* **124**, 1569 (1977).
- <sup>8</sup> C. J. Wen, B. A. Boukamp, R. A. Huggins, *J. Electrochem. Soc.* **126**, 2258 (1979).
- <sup>9</sup> Y. Chabre, *J. Electrochem. Soc.* **138**, 329 (1991)
- <sup>10</sup> Y. Chabre, *Prog. Solid State Chem.* **23**, 1 (1995).
- <sup>11</sup> J. I. Langford and D. Louër, *Rep. Prog. Phys.*, **59**, (1996)131
- <sup>12</sup> M. T. Weller, *Inorganic Materials Chemistry*, Oxford Science Publications, Chemistry Primers, n°23 (1994)
- <sup>13</sup> The STOE powder diffractometer, Visual X<sup>pow</sup> software and user manuals.

### 3. $\text{SnP}_2\text{O}_7$ .

This chapter is divided into two parts. The first part deals mainly with the physical structural characterisation of  $\text{SnP}_2\text{O}_7$  whereas the second part is dedicated to the electrochemical characterisation of the materials supported by thermodynamics and kinetics studies.

#### 3.1. Physical characterisation of material investigated.

##### 3.1.1. Powder X-ray Diffraction: (XRD).

The X-ray powder diffraction pattern of  $\text{SnP}_2\text{O}_7$  **Fig.: 3- 1** reveals basically a simple cubic structure, which can be fitted to the space group  $P a \bar{3}$  with cell parameter  $a = 7.94\text{\AA}$ . Khosrovani *et al*<sup>1</sup>. have already reported a disordered  $3 \times 3 \times 3$  super cell unit for the analogous  $\text{ZrP}_2\text{O}_7$ . The XRD pattern of  $\text{SnP}_2\text{O}_7$ <sup>2</sup> does not exhibit any peaks at low  $2\theta$  angle, however very weak peaks that may arise from superstructure reflections are just observable around the other peaks.

Apparent crystallite size was estimated (using peak width and the Scherrer equation) to be c.130 nm for  $\text{SnP}_2\text{O}_7$  sintered at  $1000^\circ\text{C}$ . **Fig.: 3- 2** below shows the primitive  $\text{SnP}_2\text{O}_7$  structure, which can be viewed as a close packed of  $\text{SnO}_6$  octahedra linked by  $\text{P}_2\text{O}_7$  units centred at the octahedral interstices to form a

network with the general formula of  $M^{4+}(\text{P}_2\text{O}_7)$ , (with  $M = \text{Sn}, \text{Si}, \text{Ti}, \text{Pb}, \text{Zr}$ , etc...). This is a *NaCl* type three- dimensional (3D) lattice of corner sharing metal octahedra  $\text{MO}_6$  and pyrophosphate units  $\text{P}_2\text{O}_7$  with  $Z = 4$  in the primitive unit cell.

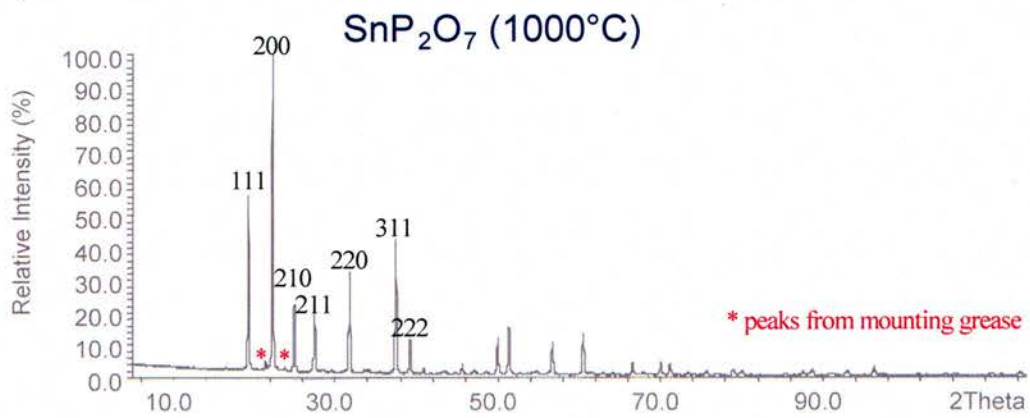


Fig.: 3- 1 X-ray powder diffraction pattern of  $\text{SnP}_2\text{O}_7$

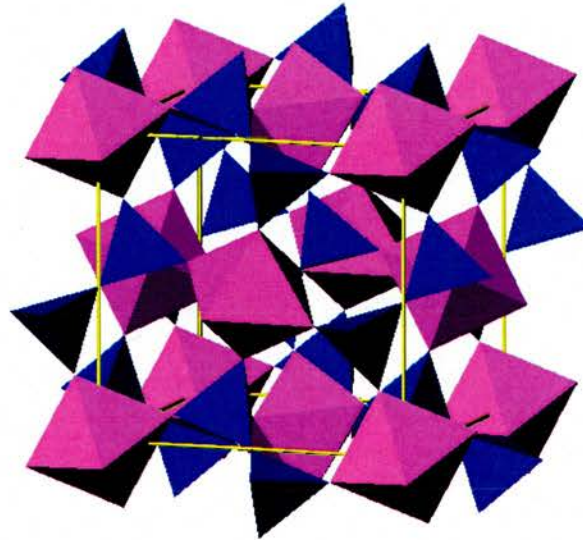


Fig.: 3- 2  $M^{4+}\text{P}_2\text{O}_7$  crystal structure.

### 3.1.2. Transmission Electron Microscopy: (TEM).

#### 3.1.2.1. Selected Area Electron Microscopy (SAED).

Like single crystal XRD, Selected Area Electron diffraction gives two kinds of information about a crystal. The positions of the diffraction spot are related to the unit cell parameters and the lattice type. The intensities of the diffraction spots are related to the arrangements of the atoms within the unit cell and their positions. The symmetry of the diffraction pattern is also related to the crystal symmetry.

Although  $\text{SnP}_2\text{O}_7$  exhibits a cubic structure by XRD, SAED performed on the materials has provided more information about the microstructural complexity of this material.

**Fig.: 3- 3** shows a number of patterns with views along different zone axes. **Fig.: 3- 3a** shows a view down the  $[1 \bar{2} 0]$  direction and displays d-spacings of 10.7 Å along the  $d_{210}$  direction and d-spacings of 23.4 Å along  $d_{001}$ .

Another specimen **Fig.: 3- 3b** observed down the  $[1 \bar{2} 1]$  shows the same sequence of spots with d-spacings of 10.7 Å along the  $d_{210}$  direction and 13.7 Å along the  $d_{111}$ .

**Fig.: 3- 3c** is a view from down the  $[1 \bar{1} 2]$  direction, where the micrograph exhibits d-spacings of 13.7 Å along the  $d_{1 \bar{1} \bar{1}}$  direction and 16.8 Å along the  $d_{110}$

direction. **Fig.: 3- 3d** is a view down the  $[\bar{1} 2 3]$  direction shows d-spacings of 10.7 Å along the  $d_{210}$  direction and 13.7 Å along the  $d_{\bar{1}\bar{1}1}$  direction.

A typical electron diffraction pattern of  $\text{SnP}_2\text{O}_7$  has emphasised the real short range structure, which is formed of a  $3 \times 3 \times 3$  superstructure hence, d-spacings represented by two sequential intense spots that are subdivided into three equidistant d- spacings are observed along several directions.

The electron diffraction micrographs observed have clearly elucidated the real superstructure of  $\text{SnP}_2\text{O}_7$  and hence leads to redefinition of the cell parameter multiplying the initial simple cubic by three along the three axes ( $a = b = c = 23.8\text{Å}$ ,  $\alpha = \beta = \gamma = 90^\circ$ ), at least for the length scales pertinent to these electron diffraction studies. On the XRD scale, this superstructure is only coherent over a limited distance and hence is manifested as a supercell.

The extra spots observed on some of the micrographs can be explained by the presence of overlapping nanodomains. An alternative explanation of these extra spots is to consider two close planes ( $P_1$  and  $P_2$ ) in reciprocal space with spots from the upper plane also being apparent in the lower reciprocal plane.

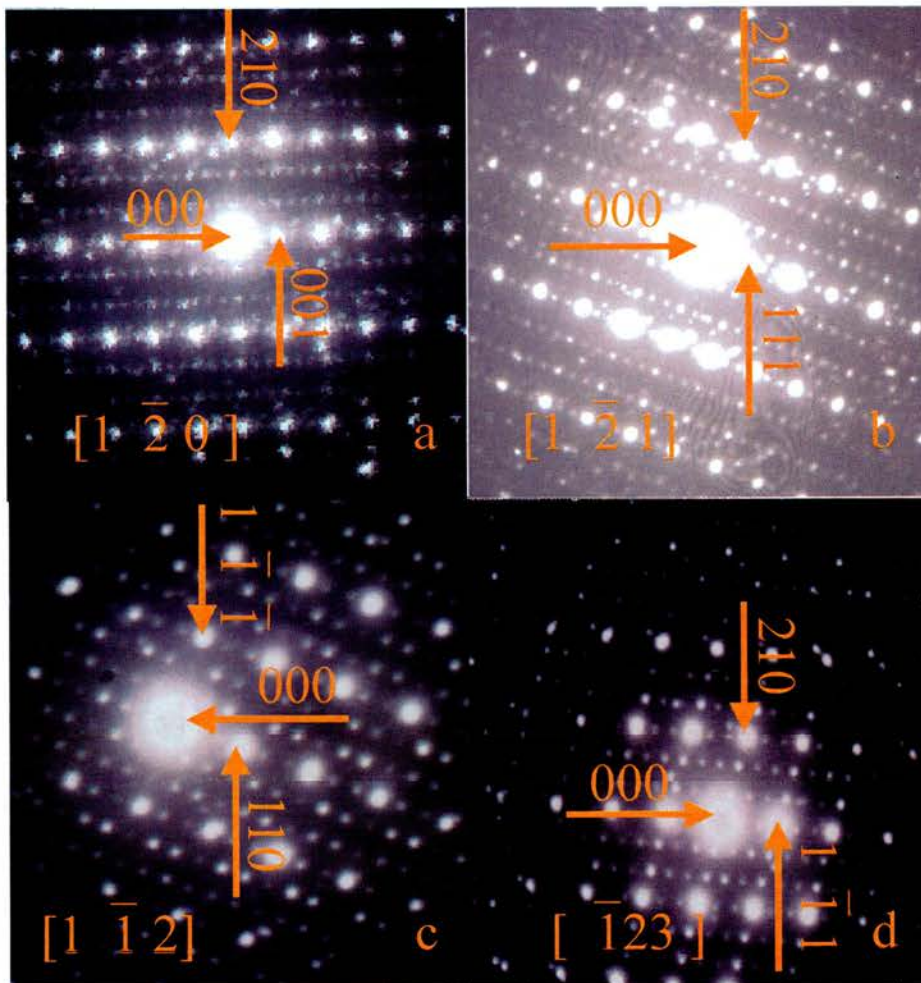


Fig.: 3- 3 SAED patterns of  $\text{SnP}_2\text{O}_7$

- (a) SAED pattern of  $\text{SnP}_2\text{O}_7$  corresponding to a view down the  $[1 \bar{2} 0]$  direction.
- (b) SAED pattern of  $\text{SnP}_2\text{O}_7$  corresponding to a view down the  $[1 \bar{2} 1]$  direction.
- (c) SAED pattern of  $\text{SnP}_2\text{O}_7$  corresponding to a view down the  $[1 \bar{1} 2]$  direction.
- (d) SAED pattern of  $\text{SnP}_2\text{O}_7$  corresponding to a view down the  $[\bar{1} 2 3]$  direction.

### 3.1.2.2. High Resolution Transmission Electron Microscopy (HRTEM).

HRTEM has also shown the complexity in the structure of this material. Nonetheless, the measured d-spacings on HRTEM images and those on SAED, has absolutely confirmed the proposed superstructure. However HRTEM has revealed an inhomogeneous distribution of reflections as nanodomains can be observed in some of the micrographs. The nanodomains seem structurally related and possibly rely on the P-O-P angle within the structure that has been shown to not be  $180^\circ$ . Using several techniques such as infra-red spectroscopy<sup>3</sup>, XRD and NMR data<sup>4</sup>, there seems to be at least 6 independent pyrophosphate groups with an angle varying between  $136$  and  $145^\circ$ .

HRTEM **Fig.: 3- 4a** exhibit patchworks of areas in which different fringes with different orientations are observable. As observed on this figure viewed down the  $[\bar{1} 2 0]$ , the d-spacing of  $13.7 \text{ \AA}$  corresponds to the  $[1 1 1]_{\text{super}}$ . (i.e. super. = supercell) direction whereas the d-spacing of  $16.8 \text{ \AA}$  is related to the  $[1 1 0]_{\text{super}}$  direction.

HRTEM image **Fig.: 3- 4b** has clearly evidenced the  $3 \times 3 \times 3$  superstructure as peculiar arrangement of reflections can be observed along the  $[1 \bar{2} 1]$  zone axis. These arrangements are periodic reflections that reveals d-spacing of  $10.7 \text{ \AA}$  that correlates with the  $[2 1 0]_{\text{super}}$  direction. The insets SAED pattern in **Fig.: 3- 4b** taken along the same zone axis matches very well these distances on the image

and reinforce the information about the superstructure. No nanodomains are observable on that figure.

The nanodomains are further confirmed in **Fig.: 3- 4c** where a nanodomain can be observed by the encircled region with d-spacing of 10.7 Å. The d-spacing of 10.7 Å, corresponds to the  $[2\ 1\ 0]_{\text{super}}$ . On the same figure are undeniably present some other regions that have different arrangement with d-spacing of 4.5 Å, which correlates with the  $[3\ 3\ 3]_{\text{primitive}}$  where primitive stand for the primitive cell and is equivalent to the  $[1\ 1\ 1]_{\text{super}}$ . This HRTEM image was viewed down the  $[\bar{1}\ 2\ 3]$  direction.

The HRTEM image **Fig.: 3- 4d** highlights different sequences of fringe arrangements with different d spacings and orientations. The d-spacings of 13.6 Å corresponds to the  $[111]_{\text{super}}$  zone axis and d-spacings of 4.5 Å is related to the  $[333]_{\text{primitive}}$  zone axis of the simple unit cell of 7.944 Å. It is also possible to distinguish the cross-region of those two different zone axes that represent a “*domain boundary*” encircled.

XRD, SAED and HRTEM have definitely shown the competing structural order between the cubic  $3\times 3\times 3$  superstructure (with  $Z = 108$ ) and the subcell of  $\text{SnP}_2\text{O}_7$ . This model is consistent with the results from previous XRD and NMR studies of  $\text{SnP}_2\text{O}_7$  and analogous  $\text{TiP}_2\text{O}_7$  compound<sup>4,5</sup>

The particle sizes were also estimated by TEM as shown in **Fig.: 3- 5** and these correlate well with those evaluated by Scherrer equation. TEM has depicted particles about  $\sim 140\text{nm}$  size in average.

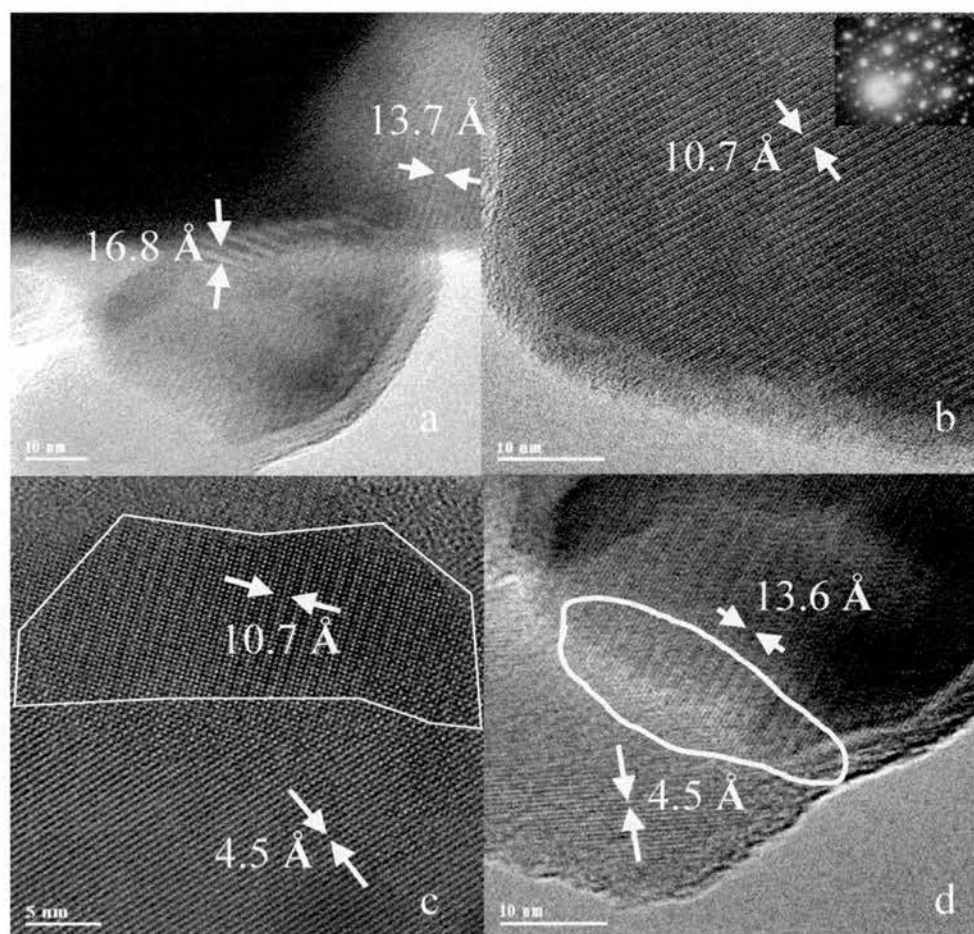


Fig.: 3- 4 HRTEM images of  $\text{SnP}_2\text{O}_7$

- a) HRTEM image of  $\text{SnP}_2\text{O}_7$  viewed along the  $[\bar{1}20]$  direction.
- b) HRTEM image of  $\text{SnP}_2\text{O}_7$  viewed along the  $[1\bar{2}1]$  direction, the inset represents the corresponding SAED pattern
- (c) HRTEM image of  $\text{SnP}_2\text{O}_7$  viewed along the  $[1\bar{1}\bar{2}]$  direction.
- (c) HRTEM image of  $\text{SnP}_2\text{O}_7$  viewed along the  $[\bar{1}23]$  direction.

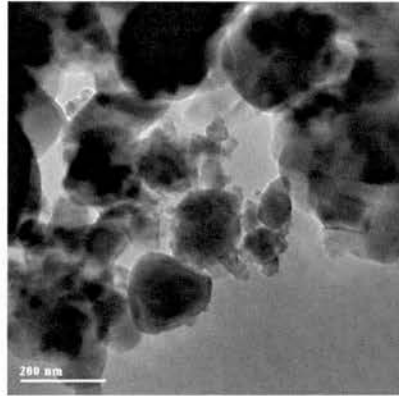


Fig.: 3- 5 Particles of  $\text{SnP}_2\text{O}_7$ .

### 3.1.2.3. Scanning Electron Microscopy: (SEM-EDS).

The main purpose of SEM was to study the morphology and hence to estimate the particles size of the investigated sample. The picture obtained from  $\text{SnP}_2\text{O}_7$  **Fig.: 3- 6** displays an excellent crystalline powder with a homogeneous sub-micron particle size of order 100nm, which correlates with the particle size estimated using Scherrer equation.

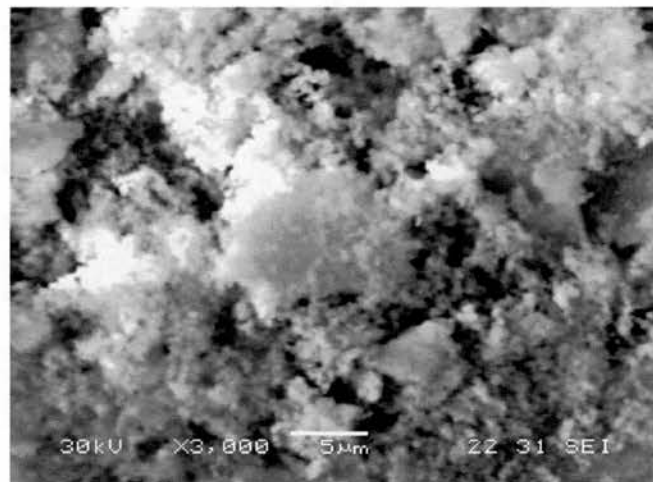


Fig.: 3- 6 SEM image of  $\text{SnP}_2\text{O}_7$

The size of the particle depends greatly on the synthesis route and the sintering temperature. The smaller they are, the shorter the required diffusion paths are for lithium insertion, the less time lithium take to diffuse, however, it should be noted that due to nanodomain formation particle size may be even smaller.

EDS microanalysis was performed using an Oxford Link ISIS system on the Transmission Electron Microscope to check the homogeneity of the sample and to determine the chemical composition of the specimens.

The average tin to phosphorus ratio was collected on 12 different areas from the same sample was measured at  $66 \pm 2 \%$  of phosphorus and  $33 \pm 2 \%$  tin. This matches the theoretical result, which should be 66.67 % for the phosphorus versus 33.33 % for the tin. The very low standard deviation of 2 % confirms the homogeneity of the sample. The same microanalysis was performed on the SEM and the obtained result matches very well the expected theoretical result. A typical spectrum collected on SEM is shown in **Fig.: 3- 7** below.

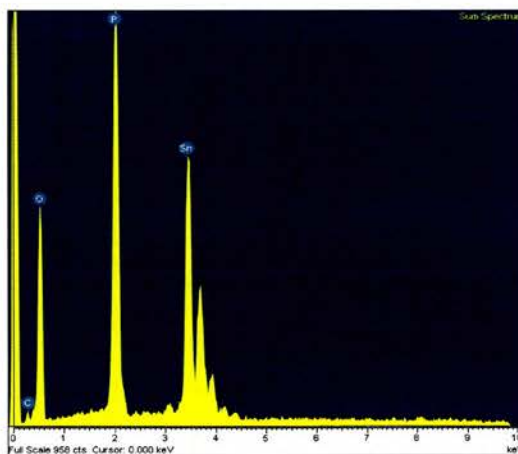


Fig.: 3- 7 EDS microanalysis spectrum of  $\text{SnP}_2\text{O}_7$ .

### 3.1.2.4. Thermogravimetric Analysis: (TGA/DTA).

A TGA experiment was performed on a small amount of  $\text{SnP}_2\text{O}_7$  sample heated in air from room temperature up to  $1000^\circ\text{C}$ . **Fig.: 3- 8** below reveals no detectable change in weight. DTA has shown no endothermic or exothermic peaks. This indicates that the compound is stable over this range of temperature.

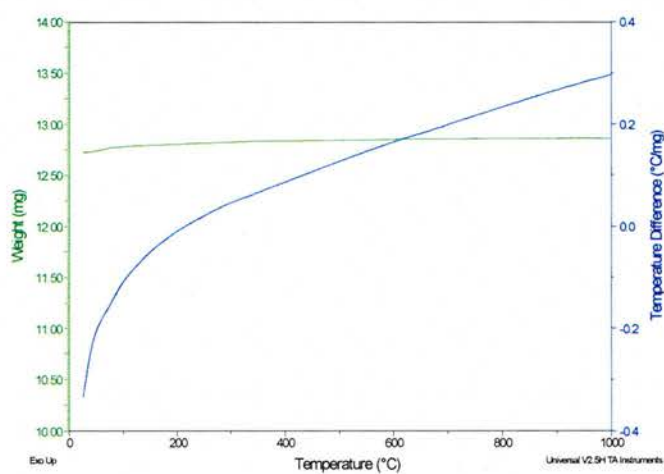


Fig.: 3- 8 TGA-DTA of  $\text{SnP}_2\text{O}_7$ .

### 3.1.3. Electrochemical characterisation.

This section is dedicated to the electrochemical study performed in order to obtain a reduction mechanism for  $\text{SnP}_2\text{O}_7$  via a combination of electrochemical testing and several characterisation techniques as described in chapter 2. Particular emphasis will be placed on the SPECS technique, which was used to distinguish the different steps of reduction and to enlighten some thermodynamic and kinetic features upon the first discharge.

#### 3.2.1. Electrochemical results and discussion.

$\text{SnP}_2\text{O}_7$  was first tested electrochemically as an anode material by *Behm et al*<sup>6</sup> and our results match very well with those reported. It can be observed in the voltammogram in **Fig.: 3- 9a**, that the first discharge from 2.0 to 0.02 V is very different from subsequent cycles. During the first discharge essentially all the irreversible processes occur.

The first discharge on the potentiostatic plot **Fig.: 3- 9a** exhibits a sharp peak about 1.2V, a small peak at 0.8V and a broad peak at 0.2V preceded by a shoulder at  $\sim 0.35\text{V}$ . The broad peak at 0.2V is related to a reversible process.

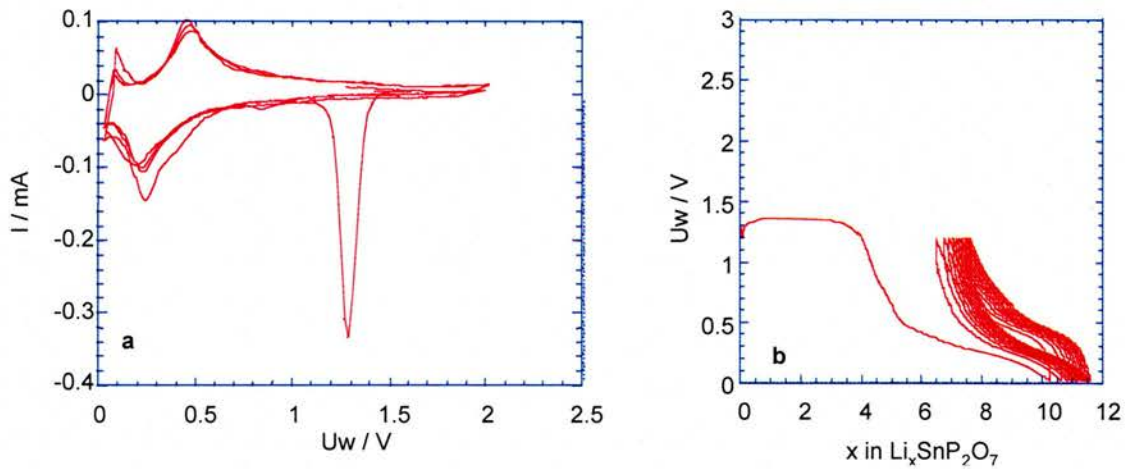
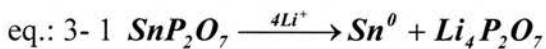


Fig.: 3- 9  $\text{SnP}_2\text{O}_7$  battery electrochemical test: (a) potentiostatic (20mV/h), (b) galvanostatic ( $0.1\text{mA}/\text{cm}^2$ ).

The peak at 1.2V is related to tin oxide reduction ( $\text{Sn}^{\text{IV}} \Rightarrow \text{Sn}^0$ ) as already reported by several authors<sup>7,8</sup>. This result suggests the possibility of the formation of  $\text{Li}_4\text{P}_2\text{O}_7$  via eq.: 3- 1.



The small peak at 0.8V was assigned to carbon reduction. This was deduced by discharging a cell that contains only carbon and binder in the electrode as positive electrode material. The result matches the peak position of carbon in the mixture as can be seen in the potentiostatic Fig.: 3- 10a and galvanostatic plots Fig.: 3- 10b. Therefore any other peak appearing on the Fig.: 3- 9a must be from the investigated active material and not from the carbon and binder.

Nonetheless the carbon galvanostatic plot shows reversible capacity, which correspond to  $\sim 45\text{mAh/g}$  of active mass in the actual electrode. This value is corrected for when evaluating the real capacity of the starting material.

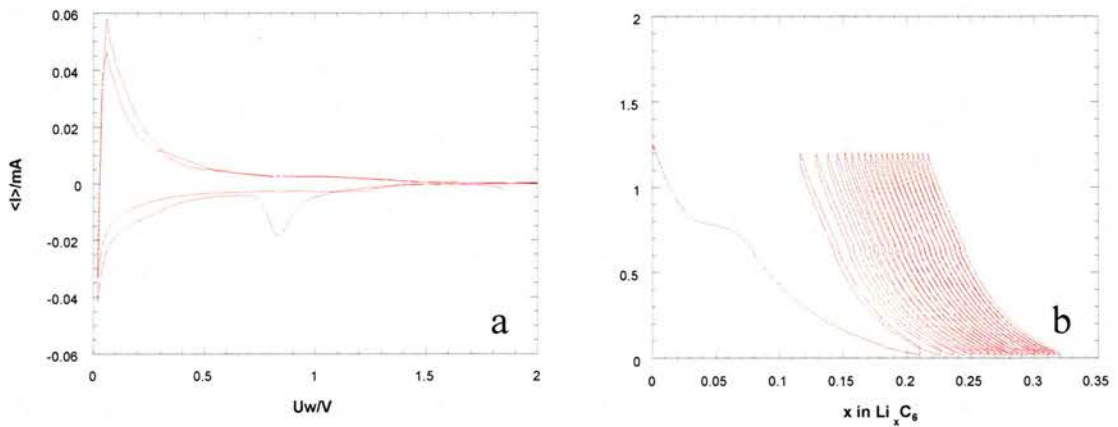


Fig.: 3- 10 (a) Potentiostatic plot of carbon, (b) Galvanostatic plot of carbon

The shoulder at 0.35V is irreversible and was attributed to pyrophosphate reduction. From **Fig. 3- 11** shows a derivative plot in the region of this peak.

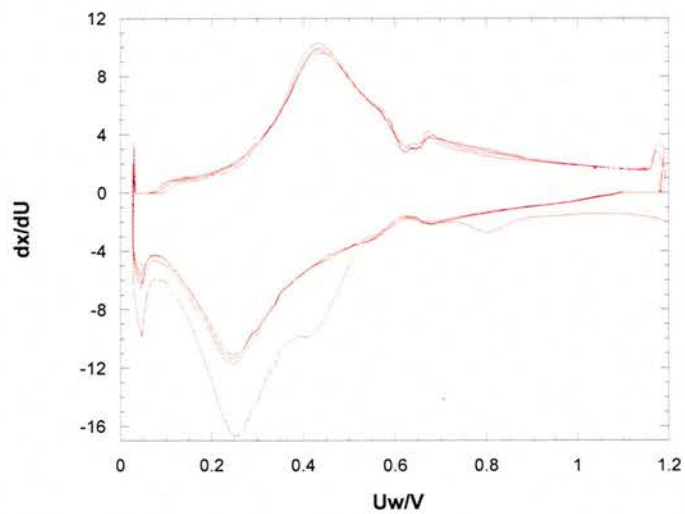


Fig.: 3- 11 Derivative  $dx/dU$  obtained from the galvanostatic test for  $\text{SnP}_2\text{O}_7$  (with a current density of  $0.1\text{mA/cm}^2$ ).

It is worth noting that the process that is related to this peak starts from about 0.6V and continues all the way down the overall reduction processes. This is shown by the extra intensity on the first sweep in this region. The fine details of the chemistry related to this peak will be discussed in more detail in the NMR section ( 3.2.1.1. ).

The formation of the reversible  $\text{Li}_x\text{Sn}$  alloys with  $0 \leq x \leq 4.4 \text{ Li}^+/\text{Li}_x\text{Sn}^0$  (eq.: 3- 2) occurs in the range about 0.4 to 0.2V. The galvanostatic plot **Fig.: 3- 9b** shows that in total  $10.9 \text{ Li}^+/\text{Li}_x\text{SnP}_2\text{O}_7$ .  $4\text{Li}^+/\text{Li}_x\text{SnP}_2\text{O}_7$  are involved in the reduction of tin and the formation of  $\text{Li}_4\text{P}_2\text{O}_7$  (eq.: 3- 1) and  $4.4\text{Li}^+/\text{Li}_x\text{Sn}$  are involved in the formation of the alloy leaving an extra  $2.5\text{Li}^+/\text{Li}_x\text{SnP}_2\text{O}_7$  to complete the experimental 10.9 lithium per  $\text{Li}_x\text{SnP}_2\text{O}_7$ .

Blank experiments have shown that lithiation of the super S carbon, which forms 1.4 % of the electrode by mass would increase the apparent capacity of  $\text{SnP}_2\text{O}_7$  by  $0.5\text{Li}^+$  per formula unit leaving  $2\text{Li}^+/\text{Li}_x\text{SnP}_2\text{O}_7$  that are presumably related to the reduction of the pyrophosphate matrix.



### 3.2.1.1. $^{31}\text{P}$ NMR results and discussion.

Investigations on phosphate compounds in the literature classify them as several  $[\text{Q}^{(n)}]$  species where  $n$  is the number of shared oxygen per  $\text{PO}_4$  unit. Considering  $[\text{Q}^{(n)}]$  species, the greater “ $n$ ” is becoming, the more phosphorus nuclei are becoming deshielded and consequently shift toward lower ppm or high field. However  $\text{P}^{\text{IV}}$  chemistry is not well characterised in the literature.

$^{31}\text{P}$  single pulse MAS NMR was used on the starting material  $\text{SnP}_2\text{O}_7$ . The spectrum shows a broad and complex peak centred at -36.7 ppm. Fayon *et al*<sup>4</sup> has reported several different phosphorus sites associated with the  $3 \times 3 \times 3$  cell and local displacements of the  $\text{PO}_4^{3-}$  tetrahedra, which is in good agreement with our result **Fig.: 3- 12**.

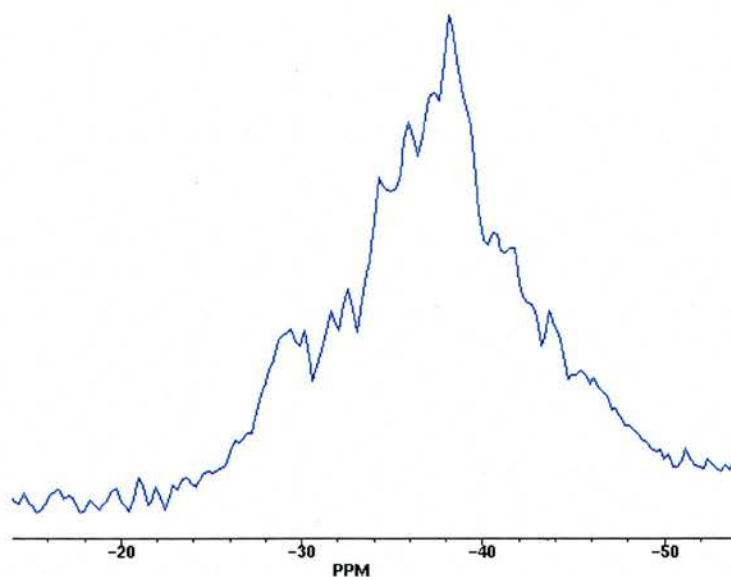
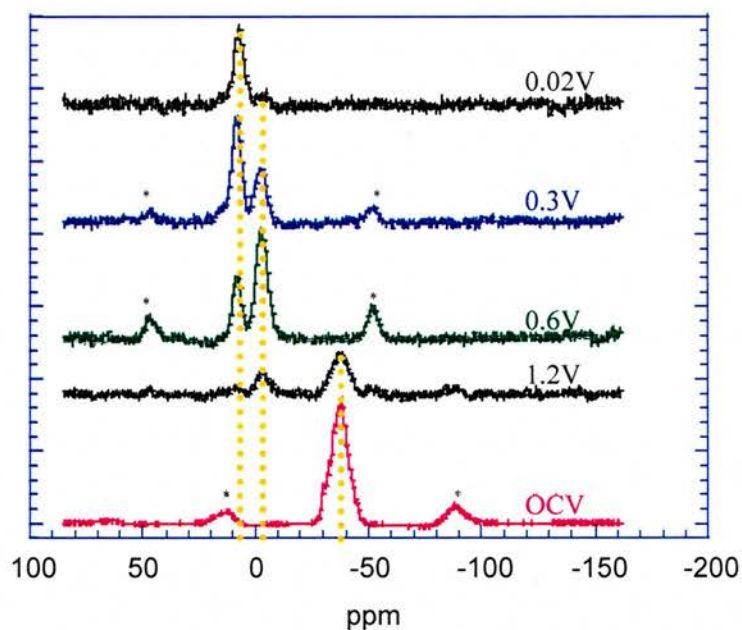


Fig.: 3- 12  $^{31}\text{P}$  MAS-NMR spectrum of  $\text{SnP}_2\text{O}_7$  at 10kHz, showing at least 11 different  $^{31}\text{P}$  sites.

This resolution of the spectrum **Fig.: 3- 12** was obtained by cutting 140 $\mu\text{s}$  off front end of the initial part of the FID before transformation. This spectrum shows at least 11 individual  $^{31}\text{P}$  sites as the number of  $\text{P}_2\text{O}_7$  groups in the asymmetric unit can be used to determine the space group.

In order to follow the evolution of the phosphate matrix, batteries were made from  $\text{SnP}_2\text{O}_7$  and discharged to different potentials. The discharged materials were then sampled by NMR to observe the peak shift, the different steps of the reduction and results are displayed in **Fig.: 3- 13** and **Table: 3- 1**.



**Fig.: 3- 13**  $^{31}\text{P}$  MAS NMR spectrum of electrode derived from  $\text{SnP}_2\text{O}_7$  and discharged to different voltage states. On further cycling the spectra are unchanged from that presented for discharged to 0.02V. (OCV = open circuit voltage and \* = spinning sidebands).

The NMR of the material discharged to 1.2V shows two lines, one intense line at -36.7 and the second less intense line at -3ppm. At the discharged state of 0.6V, one intense line at -3ppm and another less intense at 8.8ppm can be observed. For the material discharged to 0.3V, the  $^{31}\text{P}$  NMR spectrum looks similar to the spectrum of the sample at 0.6V in term of line position, however with the intensities reversed. The line at 8.8ppm has increased whilst the line at -3ppm is seen to decrease. At 0.02V, only one line with significant intensity is observed at 8.8ppm. On further cycling the phosphorus chemical shift remained unchanged.

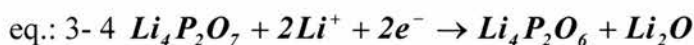
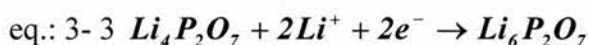
Discharged state	$\delta_1$ (ppm)	$\delta_2$ (ppm)	$\delta_3$ (ppm)
OCV	-36.7		
1.2V	-36.7	-3	
0.6V		-3	
0.3V		-3	8.8
0.02V			8.8

Table: 3- 1  $^{31}\text{P}$  MAS NMR line for battery made from  $\text{SnP}_2\text{O}_7$  discharged at different voltage state (OCV = open circuit voltage).

$^{31}\text{P}$  NMR reveals that the phosphorus environment is changing most likely due to the reduction of the  $\text{P}_2\text{O}_7^{4-}$  group. The different possibilities for  $\text{P}_2\text{O}_7^{4-}$  reduction can be a cleavage of the P-O-P bond resulting in P(V) and P(III) species or reduction of the P-O bonds to form  $(\text{P}_2^{IV}\text{O}_7)^{6-}$  or a condensation giving a  $[\text{Q}^{(2)}]$ , P(IV) species.

For comparison,  $^{31}\text{P}$  MAS NMR data were recorded from prepared standard materials or from those reported in the literature.  $\text{Li}_3\text{PO}_4$  gives a sharp line at 10ppm,  $\text{LiPO}_3$  a group of peaks between -22 and -27ppm and  $\text{Li}_4\text{P}_2\text{O}_7$  a doublet at -2.2 and -2.9ppm.

The line at -3ppm is very clearly identified with  $\text{Li}_4\text{P}_2\text{O}_7^{10}$ ,  $[\text{Q}^{(1)}]$ . This result agrees well with our electrochemical model see **eq.: 3- 1**. In order to assign the line at 8.8ppm, several assumptions can be made. Only one line was observed indicating one phosphorus environment therefore the break up of the P-O-P bond resulting in  $\text{Li}_3\text{PO}_4$   $[\text{Q}^{(0)}]$  and  $\text{LiPO}_3$   $[\text{Q}^{(2)}]$ , as was reported for  $\text{Sn}_2\text{P}_2\text{O}_7$  system<sup>11</sup>, is not plausible as there is no line near -22ppm, furthermore this does not allow for any phosphorus reduction. Even if one can consider that a line at 10ppm is close to 8.8ppm, stoichiometry considerations do not allow formation of solely  $\text{Li}_3\text{PO}_4$  from  $\text{Li}_4\text{P}_2\text{O}_7$ .  $\text{Li}_4\text{P}_2\text{O}_7$ , which is the  $[\text{Q}^{(1)}]$  species, gives rise to a line at -3ppm. Therefore any  $[\text{Q}^{(n)}]$  species with  $n \geq 2$  should give a line at lower ppm than  $[\text{Q}^{(1)}]$ , which is not observed. The possibilities are now restricted to species where the oxidation state of the phosphorus is IV. Therefore one might consider reduction of the (P-O) bonds within  $\text{Li}_4\text{P}_2\text{O}_7$  resulting in  $\text{Li}_6\text{P}_2\text{O}_7$   $[\text{Q}^{(1)}]$ , which does not contain any double resonance bonds, **eq.: 3- 3** or the same type of reduction followed by a rearrangement leading to  $\text{Li}_4\text{P}_2\text{O}_6$   $[\text{Q}^{(2)}]$  type, **eq.: 3- 4**.



In either of these cases **eq.: 3- 3** & **eq.: 3- 4**, the two phosphorus environments are equivalent and match with the result showing one line. At this stage,  $^{31}\text{P}$  NMR on its own is not powerful enough to assign this peak at 8.8ppm. Therefore lithium NMR was used to try to remove this ambiguity by the fact that if the reaction occurring is via **eq.: 3- 3** there should not be a line corresponding to  $\text{Li}_2\text{O}$  whereas if **eq.: 3- 4** is true  $\text{Li}_2\text{O}$  should be present.

### 3.2.1.2. $^6\text{Li}$ NMR results and discussion.

$^7\text{Li}$  and  $^6\text{Li}$  MAS NMR have a very narrow chemical shift range, however,  $^6\text{Li}$  has much higher resolution and can therefore provide significantly better structural information. It has already been reported for binary phosphate glasses<sup>12</sup> that the chemical shift of lithium correlates very well with the coordination numbers (CN) of the cation by oxygen.

In order to elucidate the phosphate matrix structure in the cell, batteries were discharged to 1.2, 0.6, 0.3, 0.02V and another battery was first discharged to 0.02 and then charged up to 0.6V, for the  $^6\text{Li}$  MAS NMR experiment. All the results are displayed in **Table: 3- 2** including various reference samples and traces are shown in **Fig.: 3- 14**.

All the samples show a sharp line at -0.7ppm, which is due to the residual electrolyte in the samples that contain lithium. The cells discharged to 1.2, 0.6 and 0.3V all show a broad line at about 0.2ppm. The spectrum of the cell discharged at

0.02V exhibits two broad lines centred at 0.4 and 4.2ppm. With a cell discharged to 0.02V and then charged up to 0.6V, a broad line at 0.8ppm can be observed.

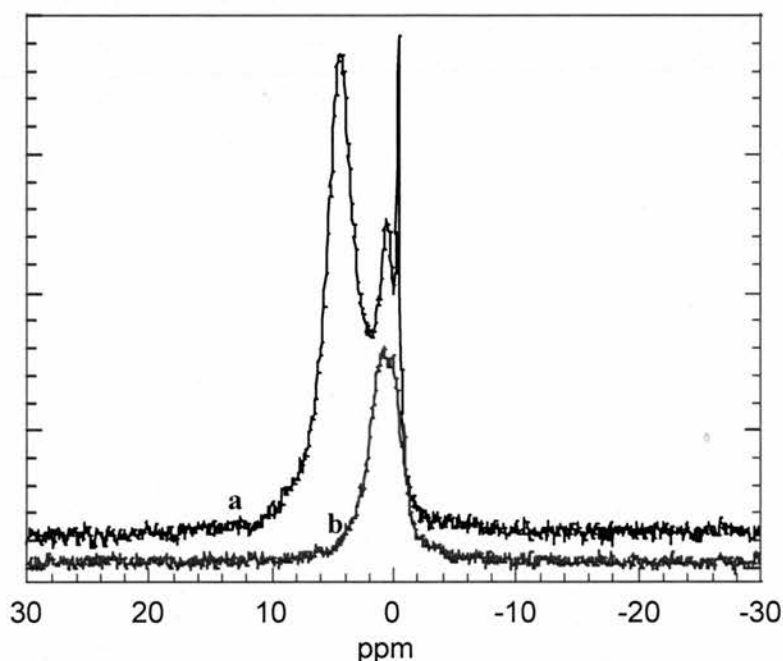


Fig.: 3- 14  $^6\text{Li}$  MAS NMR spectrum of  $\text{SnP}_2\text{O}_7$  discharged and charged to: (a) 0.02V, (b) 0.6V on charge. The sharp peak at  $-0.7\text{ppm}$  arises from residual electrolyte.

The line at  $0.2\text{ppm}$  is related to the matrix " $\text{Li}_4\text{P}_2\text{O}_7$ " as this compound gives rise to a peak at the same position. The line at  $0.4\text{ppm}$  shows a shift of  $0.2\text{ppm}$  compared to  $\text{Li}_4\text{P}_2\text{O}_7$  and might be ascribed to the " $\text{Li}_6\text{P}_2\text{O}_7$ " species suggested earlier in relation to the phosphate NMR. It seems that there is no obvious presence of  $\text{Li}_2\text{O}$ , which should give a sharp line at  $0\text{ppm}$ , as recorded for reference samples see **Table: 3- 2**. This indicates that the phosphorus oxygen matrix remains intact and that **eq.: 3- 4** is not feasible.

Compound	$\delta_1$ (ppm)	$\delta_2$ (ppm)	$\delta_3$ (ppm)
Electrolyte	-0.7 <sub>s</sub>		
Li <sub>2</sub> O	0 <sub>s</sub>		
Li <sub>4</sub> P <sub>2</sub> O <sub>7</sub>		0.2 <sub>b</sub>	
Cell discharged at 1.2V	-0.7 <sub>s</sub>	0.2 <sub>b</sub>	
Cell discharged at 0.6V	-0.7 <sub>s</sub>	0.2 <sub>b</sub>	
Cell discharged at 0.3V	-0.7 <sub>s</sub>	0.2 <sub>b</sub>	
Cell discharged at 0.02V	-0.7 <sub>s</sub>	0.4 <sub>b</sub>	4.2 <sub>b</sub>
Cell discharged and charged up to 0.6V	-0.7 <sub>s</sub>	0.8 <sub>b</sub>	

Table: 3- 2  $^6\text{Li}$  MAS NMR line for various reference samples and battery made from  $\text{SnP}_2\text{O}_7$  discharged and charged up to different voltage state. (*s* = sharp and *b* = broad).

The line observed at 4.2ppm in **Fig.: 3- 14a** can be ascribed to a lithium tin compound (probably in the form of a disordered “alloy”) and this is confirmed by the spectrum at 0.6V on charge **Fig.: 3- 14b**, which does not show a line in this position, when all the lithium has been extracted from the “alloy”. The line at 0.8ppm in the cell charged to 0.6V seems most likely to be related to “Li<sub>6</sub>P<sub>2</sub>O<sub>7</sub>”.

As the  $^{31}\text{P}$  NMR shows that the phosphorus environment is unchanged between the fully discharged, 0.02V and charged, 0.6V states. The change in the shift of the “Li<sub>6</sub>P<sub>2</sub>O<sub>7</sub>” matrix may be due to the change in the metallic part of the nanocomposite matrix as Li<sub>*x*</sub>Sn cycles to Sn increasing the lithium concentration in the matrix or, more likely, simply reflects the perturbation of the baseline due to the large 4.2ppm peak. This shift of 0.4ppm compared to the line in the cell on charge to 0.02V is still in good agreement with the results predicted by Xu *et al*<sup>13</sup> in the crystalline and glassy silicates system about the lithium chemical shift range in the tetrahedral site.

### 3.2.1.3. Infrared (IR).

IR allows the focus on “P-O” and “P-O-P” bonds, whose vibrations occur in the frequency range from  $1300\text{ cm}^{-1}$  to  $700\text{ cm}^{-1}$ . Relevant spectra are shown in **Fig.: 3- 15**.

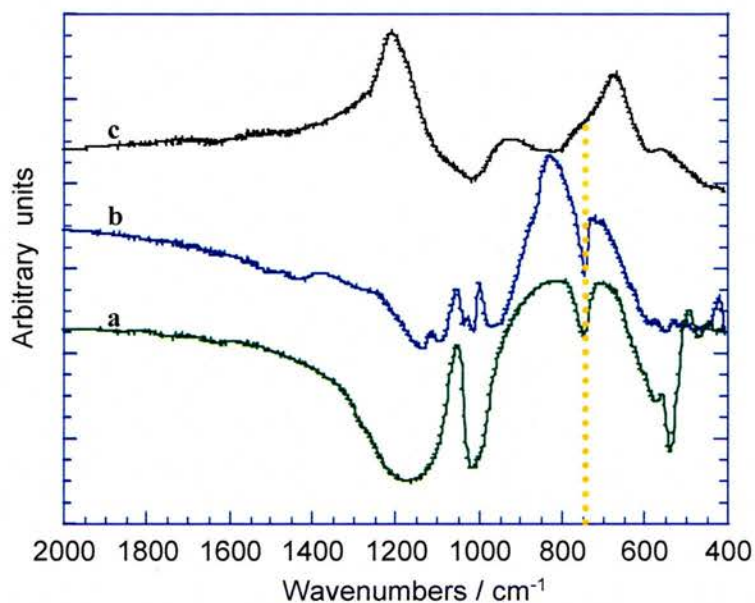


Fig.: 3- 15 IR spectrum of (a)  $\text{SnP}_2\text{O}_7$ , (b)  $\text{Li}_4\text{P}_2\text{O}_7$  and (c) lithiated or fully discharged  $\text{SnP}_2\text{O}_7$ .

In  $\text{SnP}_2\text{O}_7$ , three main bands dominate the spectrum in this range. A strong band is located in the high frequency region e.g.  $1150\text{ cm}^{-1}$ , followed by an intense and narrow band at  $1015\text{ cm}^{-1}$ . In the lower frequency part of this region is centred a weak and narrow band at  $744\text{ cm}^{-1}$ .

The  $\text{Li}_4\text{P}_2\text{O}_7$  IR spectrum has similar intense bands in the region from 1300 to  $700\text{cm}^{-1}$  however some of them are split. A strong doublet at  $1130\text{cm}^{-1}$  is followed by another doublet at  $1012\text{cm}^{-1}$  and singlet band at  $958\text{cm}^{-1}$ . A band at  $744\text{cm}^{-1}$  can also be observed.

The lithiated  $\text{SnP}_2\text{O}_7$  spectrum shows two broad bands. One at  $1015\text{cm}^{-1}$  and one is centred at  $850\text{cm}^{-1}$  but having a shoulder at  $744\text{cm}^{-1}$ .

Assuming  $C_{2v}$  symmetry of the  $\text{P}_2\text{O}_7$  group and using the characteristic frequencies of phosphorus compounds found in the literature<sup>14, 15</sup> one can assign for  $\text{SnP}_2\text{O}_7$ , bands at  $1150\text{cm}^{-1}$  to the asymmetric vibration mode  $\nu_{\text{as}}(\text{PO}_3)$ . At  $1015\text{cm}^{-1}$  can be seen the symmetric vibration mode  $\nu_{\text{s}}(\text{PO}_3)$ . The band at  $744\text{cm}^{-1}$  is related to the vibration mode  $\nu_{\text{s}}$  of the bridging (P-O-P).

The  $\text{Li}_4\text{P}_2\text{O}_7$  spectrum is similar to the  $\text{SnP}_2\text{O}_7$  spectrum but the bands have moved slightly toward lower frequency and the  $\text{PO}_3$  vibrations split into at least a doublet whereas the P-O-P vibration remains a singlet. This is due to the inequivalent environments of the  $\text{PO}_3$  groups in the crystal structure. The doublet at  $1130\text{cm}^{-1}$  is assigned to the vibration mode  $\nu_{\text{as}}(\text{PO}_3)$ . The split symmetric vibrations at  $1012$  and  $958\text{cm}^{-1}$  are ascribed to  $\nu_{\text{s}}(\text{PO}_3)$  and  $\nu_{\text{as}}(\text{PO}_3)$  respectively. However the asymmetric vibration mode  $\nu_{\text{s}}(\text{P-O-P})$  remains at  $744\text{cm}^{-1}$ .

In the lithiated  $\text{SnP}_2\text{O}_7$  both  $\text{PO}_3$  vibration modes have moved about  $200\text{cm}^{-1}$  to lower frequency implying a decrease in bond order of the terminal P-O bonds as would be anticipated for  $\text{Li}_6\text{P}_2\text{O}_7$ . The band at  $1015\text{cm}^{-1}$  is ascribed to the vibration mode  $\nu_{\text{as}}(\text{PO}_3)$  whereas the band at  $850\text{cm}^{-1}$  is ascribed to  $\nu_{\text{s}}(\text{PO}_3)$ . Consistent with this, the  $\nu_{\text{s}}(\text{P-O-P})$  vibration mode is unchanged in frequency and can be observed as the shoulder at  $744\text{cm}^{-1}$ .

#### 3.2.1.4. X-Ray Photoelectron Spectroscopy (XPS).

XPS spectra of tin and phosphorus in both  $\text{SnP}_2\text{O}_7$  and the fully discharged battery made from  $\text{SnP}_2\text{O}_7$  are depicted in **Fig.: 3- 16**. In the spectra of the fully discharged battery, the overall spectrum is dominated by O 1s and Li 1s peaks and so is considerably weakened. Due to the escape depth principle, it can be assumed that the decrease in tin and phosphorus intensities is due to an external coating around the Sn and P particles of a lithium-carbon-oxygen compound. It was suspected the absolute positions are shifted 6eV due to calibration error however, this has no effect on relative position.

Spectrum (a) in **Fig.: 3- 16** shows  $\text{Sn}3d_{5/2}$  and  $\text{Sn}3d_{3/2}$  peaks in  $\text{SnP}_2\text{O}_7$ , centred at 493.4eV and 501.8eV respectively. The fully discharged battery XPS, spectrum (b) exhibits peaks centred at 492.5 and 500.9eV corresponding to  $\text{Sn}3d_{5/2}$  and  $\text{Sn}3d_{3/2}$ . This result indicates the reduction of the oxidation state of tin from  $(\text{Sn}^{4+} \Rightarrow \text{Sn}^0)^{16, 17}$  confirming the electrochemical result, as the reduced tin is therefore available to form an alloy **eq.: 3- 2**. In spectrum (c), **Fig.: 3- 16** the

phosphorus peak  $\text{P}_{2p}$  can be observed in  $\text{SnP}_2\text{O}_7$  at 139.9eV whereas in the fully discharged battery, spectrum (d) the same peak can be seen at 139.5eV.

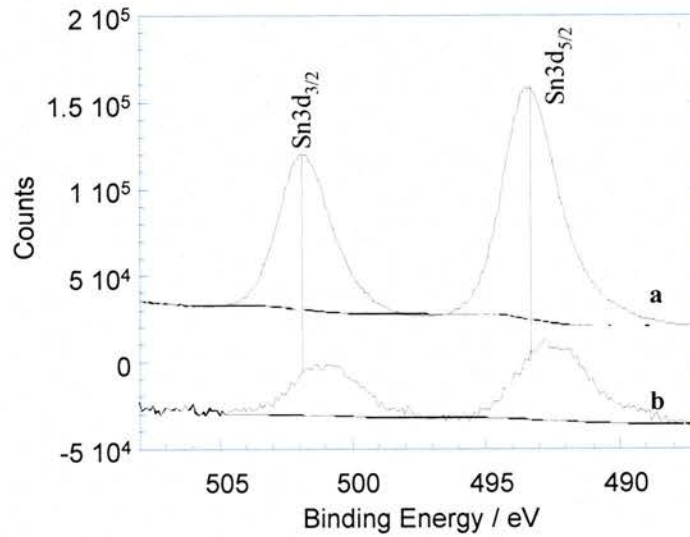


Fig.: 3- 16 XPS diagram of tin (a)  $\text{Sn}3d_{5/2}$  and  $\text{Sn}3d_{3/2}$  in  $\text{SnP}_2\text{O}_7$  (starting material), (b)  $\text{Sn}3d_{5/2}$  and  $\text{Sn}3d_{3/2}$  in fully discharged  $\text{SnP}_2\text{O}_7$  battery,

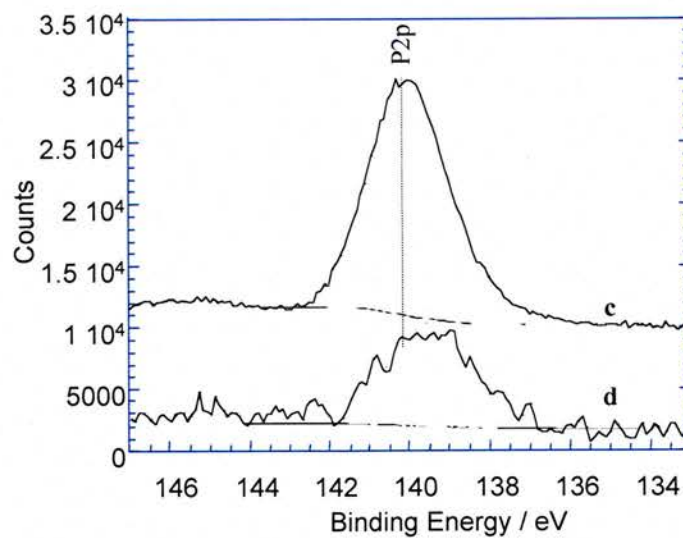


Fig.: 3- 16 XPS diagram of phosphorus (c)  $\text{P}_{2p}$  in  $\text{SnP}_2\text{O}_7$  (starting material), (d)  $\text{P}_{2p}$  in fully discharged  $\text{SnP}_2\text{O}_7$  battery.

The phosphorus has significantly shifted toward lower binding energy. This suggests a reduction in phosphorus oxidation state and hence the total charge of the phosphate group, which is consistent with the model proposed from the electrochemical studies.

### 3.3. SPECS.

#### 3.3.1. Background.

This section is focused upon thermodynamic and kinetic aspects of lithium ion insertion into  $\text{SnP}_2\text{O}_7$ . It is well known that some properties of rechargeable lithium ion battery materials such as maximum power are based on the rate of reaction, however cell design can be optimised in order to partially overcome a limitation imposed by the kinetics of the reaction. When this reaction is an insertion reaction producing a phase of variable composition, the appropriate parameter to understand the relationship of power with intrinsic electrode material characteristics is the lithium diffusion coefficient  $D_{\text{Li}^+}$ ; however, this parameter can only be calculated when the reaction taking place in the cell is controlled only by diffusion of lithium. The second Fick's law can be applied and some methods have been reported to be useful for such a purpose. Either potentiostatic or galvanostatic methods can be then used for the determination of  $D_{\text{Li}^+}$ . However, this useful parameter can not be calculated in cases where the movement of an interphase is controlling the reaction velocity for instance in two phase regions. A full knowledge of the different reaction mechanisms in the different composition ranges upon reaction with lithium must be known, since calculation of  $D_{\text{Li}^+}$  can be made only in a solid solution region.

Phase diagram determination can be achieved by the analysis of voltage versus composition curves in which, a continuous variation of the potential with composition corresponds to a solid-solution, single phase region while a constant potential plateau corresponds to a two-phase region. These extreme cases are sometimes not clearly distinguishable, as perfect plateaux are not always obtained.

Several techniques have been introduced earlier, in order to determine the reaction mechanism and composition ranges. The use of incremental capacity ( $-\partial x / \partial E$ ) has been proposed by *Thompson*<sup>18</sup> in order to trace with high resolution various processes occurring during insertion reactions. This technique easily allows to distinguish between first order ( biphasic ) and continuous ( solid solution ) transformation<sup>19,20</sup>. However, more recently, another technique called SPECS Step Potential ElectroChemical Spectroscopy<sup>21,22</sup> has been proposed that is based on the analysis of potentiostatic data. This can also provide with accuracy the same information and even allows the building up a phase diagram in an insertion system.

SPECS is based on the principle of applying a series of potentials to the system while the current relaxation versus time (  $t$  ) is recorded at each potential step. Then current gives measurable kinetic information whereas the voltage at equilibrium is directly related to the thermodynamics of the system. One advantage should be noted with respect to galvanostatic methods is that side reactions, as for instance electrolyte oxidation or reduction, can be detected. In

order to determine the lithium diffusion coefficient it is essential to have an accurate knowledge of particle size.

### 3.3.2. Results and discussion.

Cells made from  $\text{SnP}_2\text{O}_7$  were subjected to discharge under SPECS at various temperatures of -8, 5, 9, 20, 25, 30°C. The first discharge curves of  $\text{SnP}_2\text{O}_7$  versus lithium at these temperatures are all similar between 2 and 0.02V. Reaction with lithium takes place through different processes, which are related to the slope of cell voltage variation versus composition. Three distinct regions can be observed in the electrochemical titration plot **Fig.: 3- 17**, which are labelled region I, II and III and the SPECS experiment has shown three different processes that will be analysed in detail.

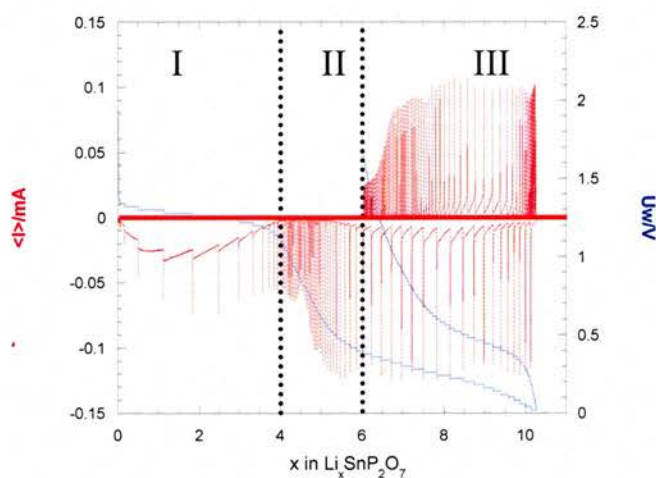


Fig.: 3- 17  $\text{SnP}_2\text{O}_7$  SPECS experiment profile (scan rate of 20mV every 15hours).

### 3.3.3. Region I.

#### 3.3.3.1. Thermodynamic aspects of $\text{SnP}_2\text{O}_7$ upon discharge in region I.

Due to the slow data collection condition applied i.e.  $\pm 20\text{mV}$  every 15 hours during these SPECS experiments, these batteries can be approximated to be at equilibrium, and so the thermodynamic rules can be applied all the way through the reduction and oxidation processes. The closeness to this state was checked by analysis of the relaxation curves.

From **Fig.: 3- 17** above, the first discharge voltage profile up to  $4\text{Li}^+/\text{Li}_x\text{SnP}_2\text{O}_7$  can be described as a plateau that is temperature dependent and hence leads to thermodynamic consideration. This plateau corresponds to the reaction described within **eq.: 3- 1**.

The chronoamperogram from **Fig.: 3- 17**, obtained strongly suggests a two phases transition, due to the anomalous behaviour of the current relaxation versus composition plot in this region I. It is clear that the current relaxation versus composition curve in this region never reaches zero, therefore kinetic studies can not be performed.

This result confirms the chemical process reported by *Behm et al*<sup>6</sup>. It has been shown earlier in the NMR section of this chapter that in region I, formation of tin metal (Sn) plus a lithiated phosphate matrix characterised as  $\text{Li}_4\text{P}_2\text{O}_7$  occurs.

These observations supported by the SPECS data have clearly demonstrated a biphasic region where it is only possible to obtain thermodynamic information that is controlled by either the formation of tin metal or lithiated phosphate matrix. However, the same behaviours were observed for cells discharged at different temperature except that the plateau voltage varied with temperature under the same condition and the plateaus are shown in **Fig.: 3- 18**.

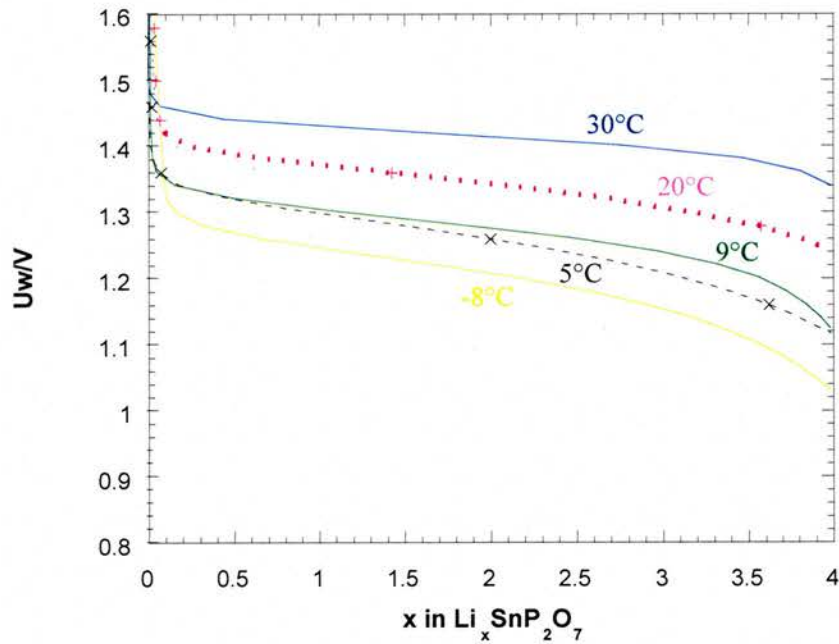


Fig.: 3- 18 Voltage profiles with temperature of  $\text{SnP}_2\text{O}_7$  plateau up to  $4\text{Li}^+$  inserted under SPECS condition (scan rate of 20mV every 15hours).

For each investigated cell at different temperature, the voltage corresponding to the plateau was collected at a fixed point of  $x = 2$ . **Fig.: 3- 19** shows the evolution of the plateau voltage versus temperature  $\Delta E = f ( T )$ . Surprisingly the extracted curve displays two different regions with different slopes. These can be fitted to two straight lines in two different temperature ranges. The crossover point of these two regions is at  $14 \pm 1^\circ\text{C}$ . Interestingly this temperature correlates with the allotropic form changes of tin from a cubic structure ( $\alpha$ -tin or grey) into a tetragonal structure ( $\beta$ -tin or white) that occurs at  $13.2^\circ\text{C}$ .

The conversion is a very slow process so called “tin plague” or “tin disease” and hence was thought to be the devils work when it was first noted as growths on organ pipes in European cathedrals<sup>23</sup>.

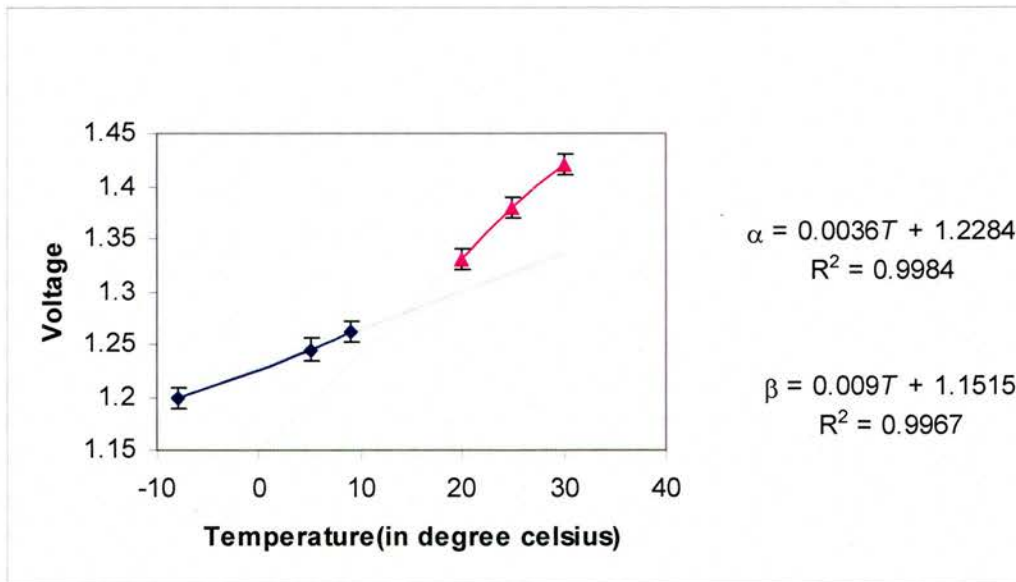


Fig.: 3- 19 Temperature control plot of voltage versus temperature.

Furthermore this result suggests that tin formation is thermodynamically the key factor that controls the potential of the plateau with temperature in this region.

Considering the *Nernst* equation and the definition of *Gibb's* equation  $\Delta G(T) = -n.F.\Delta E = \Delta H - T\Delta S$  where  $\Delta G$  is the free energy,  $n$  the number of electron,  $F$  the Faraday constant and  $\Delta E$  the cell voltage. From the temperature controlled experiments  $\Delta G$  can be generated at each temperature and allows the estimation of  $\Delta S$  and  $\Delta H$ .

In order to test the validity of this method  $\text{MnO}_2$  (EMD) was investigated at various temperature of 9, 20 and 30°C. This material is still widely investigated as a positive electrode. The electrochemical processes that occur on charge or discharge within  $\text{MnO}_2$  are essentially intercalation and deintercalation process where ordering is preserved and lithium ions go in and out of the vacant sites on discharge and charge respectively. The reaction can be summarised via **eq.: 3- 5**.



The SPECS experiment between the voltage window of 3.8 and 2.4V does not exhibit a clearly defined plateau but anomalous behaviour of the current relaxation curve can be detected **Fig.: 3- 20**.

**Fig.: 3- 21** shows voltage and current profile but the current profile has emphasised two electrochemical processes peaks at  $x \sim 0.1$  and  $0.4$ . The current profile strongly indicates phase transformations from compositions of  $\text{Li}_x\text{MnO}_2$  (with  $0.02 \leq x \leq 0.22$ ) and  $\text{Li}_x\text{MnO}_2$  (with  $0.28 \leq x \leq 0.56$ ).

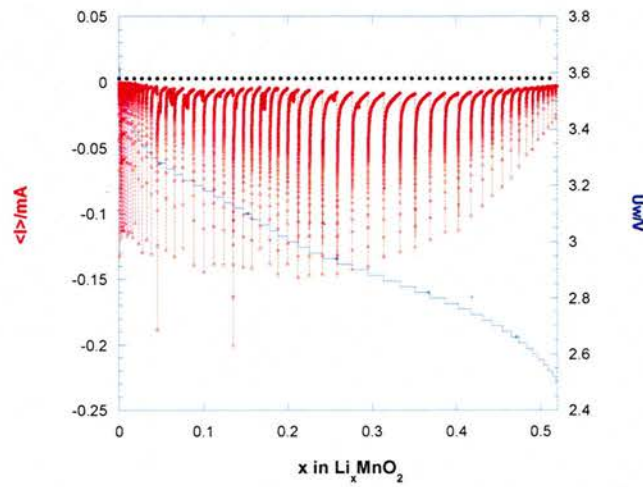


**Fig.: 3- 20** SPECS plot for  $\text{MnO}_2$ : current relaxation profile (red) & voltage profile (blue) versus composition (scan rate of 20mV every 15hours).

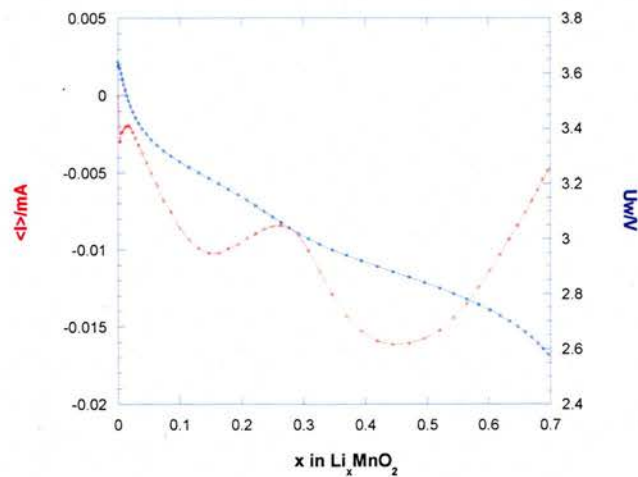


**Fig.: 3- 21** current relaxation profile (red) & voltage profile (blue) versus composition (scan rate of 20mV every 15hours).

For the thermodynamic study, the voltage was measured at a fixed point of ( $x = 0.1$ ) for the reduction process and the voltage profile versus composition is shown in **Fig.: 3- 22**.

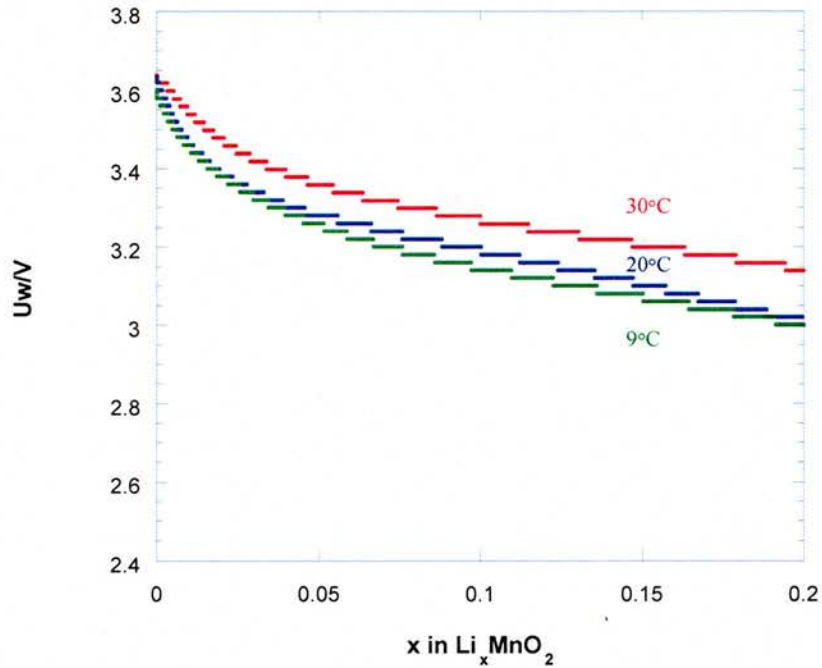


Fig.: 3- 22  $\text{MnO}_2$  voltage profile versus composition at various temperatures of 9, 20 & 30°C under SPECS conditions (scan rate of 20mV every 15hours).

**Fig.: 3- 23** displays the evolution of the free energy with temperature and the linear regression to evaluate the entropy and the enthalpy of the occurring reaction.

The straight line observed in, **Fig.: 3- 23** leads to a value for the entropy of  $\sim 55 \text{ J mol}^{-1}\text{K}^{-1}$  and the enthalpy of  $\sim -14800 \text{ J mol}^{-1}$  for  $\text{Li}_{0.1}\text{MnO}_2$ . The magnitude of the entropy obtained is in agreement with those already reported<sup>24</sup>. This result

confirms that the method<sup>25</sup> is valid and therefore can be applied to assess the entropy and enthalpy in the case of insertion of lithium in  $\text{SnP}_2\text{O}_7$ .

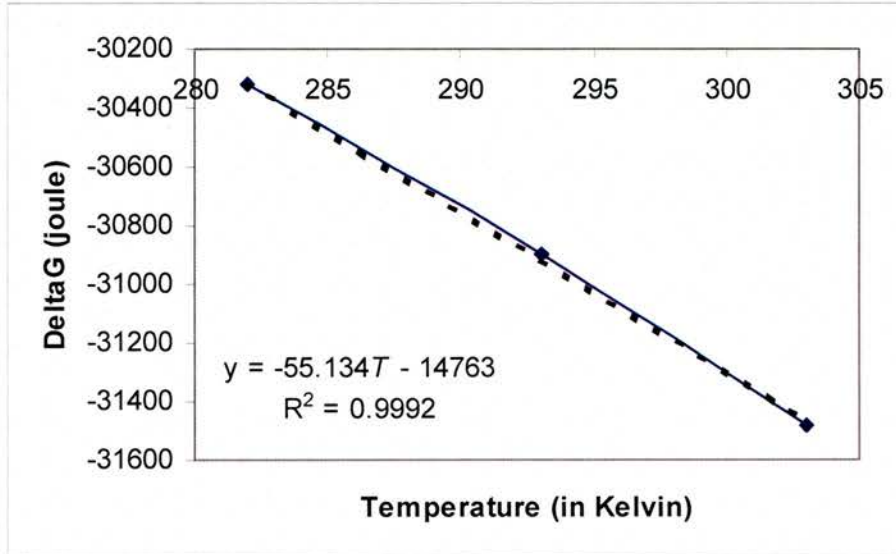


Fig.: 3- 23 Plot of  $\Delta G$  as function of temperature for  $\text{Li}_x\text{MnO}_2$  with  $x = 0.1$ .

For  $\text{SnP}_2\text{O}_7$ , the free energy plot versus temperature displays two different regions with different slopes related to  $\alpha$  and  $\beta$ -tin and is shown in **Fig.: 3- 24**. From this data, the entropy is estimated be  $\sim 1190$  and  $\sim 3473 \text{ J mol}^{-1}\text{K}^{-1}$  for the formation of  $\alpha$  and  $\beta$ -tin respectively. Whereas the enthalpy is approximately  $-148000$  and  $\sim -503900 \text{ J mol}^{-1}$  for  $\alpha$  and  $\beta$ -tin respectively.

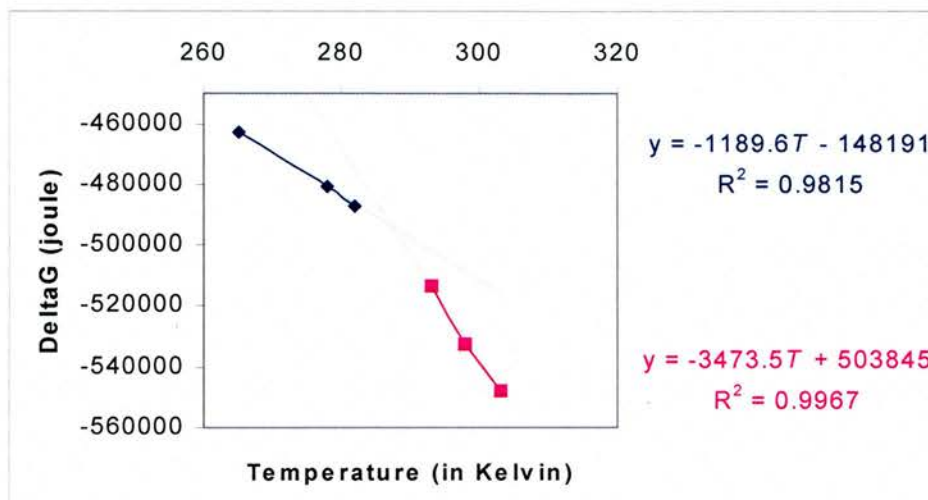


Fig.: 3- 24 Plot of  $\Delta G$  as function of temperature for  $\text{Li}_x\text{SnP}_2\text{O}_7$  in region I at  $x = 2$

The entropy values obtained from this experiment are much larger than those typically expected for a phase change such as for  $\text{Li}_{0.1}\text{MnO}_2$ . In this case  $\text{MnO}_2$  involves intercalation where  $\text{Li}^+$  enters the vacant sites of the layered material. Disordering of lithium among these occupation sites contributes as configurational entropy. However the structure remains crystalline and long range ordered. In the case of  $\text{SnP}_2\text{O}_7$  the reaction can not be described as an intercalation reaction but as a reduction reaction. After inserting  $4\text{Li}^+/\text{Li}_x\text{SnP}_2\text{O}_7$ , the system forms finely dispersed tin nanoparticles in an  $\text{Li}_4\text{P}_2\text{O}_7$  matrix that is x-ray amorphous. This is an explanation of the very large entropy value obtained as the material changes from ordered  $\text{SnP}_2\text{O}_7$  to an amorphous matrix. The crystalline structure is not kept but is destroyed increasing the disorder and hence the entropy.

### 3.3.4. Region II.

#### 3.3.4.1. Structural characterisation of region II.

##### 3.3.4.1.1. HRTEM.

In order to calculate the lithium diffusion coefficient, it is necessary to know the size of the particles. Therefore electron microscopy (HRTEM) was performed on an  $\text{SnP}_2\text{O}_7$  battery electrode discharged to  $x = 5/\text{Li}_x\text{SnP}_2\text{O}_7$ , a composition belonging to region II, as shown in **Fig.: 3- 25**. The average particle size measured (on 20 different particles) is about  $\sim 40\text{nm}$ , as it can be seen in the typical electron micrograph.

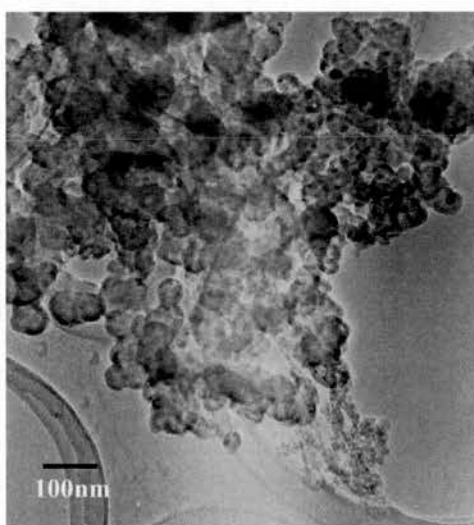
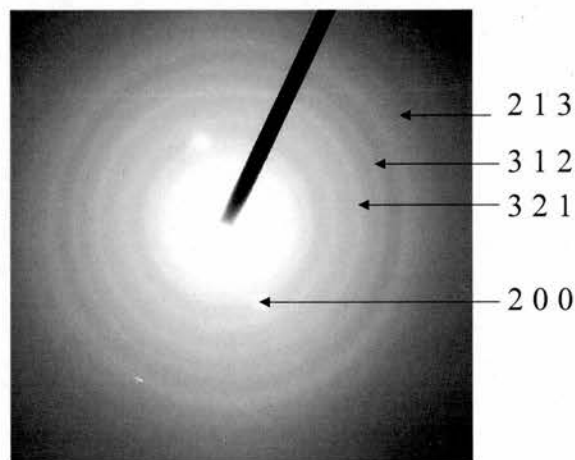


Fig.: 3- 25 HRTEM image of battery made in  $\text{SnP}_2\text{O}_7$  and discharged at  $x = 5/\text{Li}_x\text{SnP}_2\text{O}_7$ .

This particle size is much smaller than the starting material particle size as expected due to the breaking up of particles although it is worth noting that the particle size is similar to the nanodomain size due to the  $3 \times 3 \times 3$  ordering.

### 3.3.4.1.2. SAED.

In **Fig.: 3- 26** the electron diffraction (SAED) pattern of a sample with  $x = 5\text{Li}^+/\text{Li}_x\text{SnP}_2\text{O}_7$  inserted is shown. Some rings are observable, showing the morphology and the ordering state of particles have changed upon reaction from crystallites **Fig.: 3- 3** to disordered nanocrystalline particles. These particles appear to be amorphous to XRD, nevertheless, the SAED experiment in has shown that there remains a degree of crystallinity in this case. The measurement of the ring diameter leads to  $d_{hkl}$ -values which can be used to identify the pattern and hence the crystallographic parameters.



**Fig.: 3- 26** SAED pattern  $\text{SnP}_2\text{O}_7$  discharged at  $x = 5/\text{Li}_x\text{SnP}_2\text{O}_7$  (only some  $\beta$ -Sn are indexed)

The d-spacings from the data are listed in **Table: 3- 3**. These were compared with expected diffraction peaks for some possible phases for example  $\beta$ -Sn. Of these, the best evidence seems to be for  $\beta$ -Sn<sup>26, 27, 28</sup> **Table: 3- 4** and  $\text{Li}_4\text{P}_2\text{O}_7$ <sup>29, 30</sup> **Table: 3- 6** as some of the most intense reflections can be seen. It is worth mentioning that all reflections observed from the XRD pattern were not observed in the micrograph, which is not unreasonable given the low degree of crystallinity and differences between electron and X-ray scattering. Another possible phase in the system might have been  $\alpha$ -tin but as shown in **Table: 3- 5** none of the reported peaks match the SAED data.

The possible presence of  $\beta$ -Sn and  $\text{Li}_4\text{P}_2\text{O}_7$  agrees with the proposed model supported by electrochemical and NMR studies **eq.: 3- 1** but shows that these are present as nanocrystalline phases and not amorphous.

Diameter of a ring (mm)	Calculated d-spacings ( $\text{\AA}$ ) $\pm 1\%$	Theoretical d-spacings	
		( $\text{\AA}$ )	$hkl$ (Sn)
		$\beta$ -Sn S.G: I41/A MDS	
6.507	3.08		
6.901	2.90	2.915 (I = 100)	2 0 0
7.009	2.86	2.793 (I = 90)	1 0 1
8.260	2.43		
12.847	1.56		
13.983	1.43	1.442 (I = 20)	3 2 1
16.213	1.23		
17.339	1.15	1.20 (I = 5)	3 1 2
20.255	0.99	0.9824 (I = 5)	2 1 3

Table: 3- 3 Indexing of the diffraction pattern (I = peak intensity)

$d$ (Å)	Intensity	$hkl$	SAED
2.915	100	2 0 0	✓
2.793	90	1 0 1	✓
2.062	34	2 2 0	
2.017	74	2 1 1	
1.659	17	3 0 1	
1.484	23	1 1 2	
1.458	13	4 0 0	
1.442	20	3 2 1	✓
1.304	15	4 2 0	
1.292	15	4 1 1	
1.205	20	3 1 2	✓
1.095	13	4 3 1	
1.0434	3	1 0 3	
1.0401	5	3 3 2	
1.0309	2	4 4 0	
1.0252	5	5 2 1	
0.9824	5	2 1 3	✓
0.9718	2	6 0 0	

Table: 3- 4 XRD pattern indexing of  $\beta$ -Sn (taken from JCPDS-ICDD 4-673).

$d$ (Å)	Intensity	$hkl$
3.75	100	1 1 1
2.29	83	2 2 0
1.95	53	3 1 1
1.62	12	4 0 0
1.48	20	3 3 1
1.32	21	4 2 2
1.24	11	5 1 1
1.14	6	4 4 0
1.09	10	3 5 1

Table: 3- 5 XRD pattern indexing of  $\alpha$ -Sn (taken from JCPDS-ICDD 05-0390).

$d$ (Å)	Intensity	$hkl$	SAED
3.181	40	0 4 1	
3.066		1 1 2	✓
2.864	20	1 2 2	✓
2.712		1 4 1	
2.595	20	2 0 0	
2.550		2 1 0	
2.427		2 1 1	✓
1.54	10	0 2 5	✓

Table: 3- 6 XRD pattern indexing of  $\text{Li}_4\text{P}_2\text{O}_7$  based on JCPDS-ICDD 030-0222).

### 3.3.4.2. Kinetic behaviour of $\text{SnP}_2\text{O}_7$ upon discharge in region II.

Region II shows a decrease of potential from the initial plateau going from  $4$  to  $6\text{Li}^+/\text{Li}_x\text{SnP}_2\text{O}_7$ . The current relaxation curves observed in the SPECS experiment reach zero and are symmetrical **Fig.: 3- 27** suggesting a solid solution where it is possible to access lithium diffusion by solving the Fick's second law as described<sup>31</sup> in *Chapter 2*.

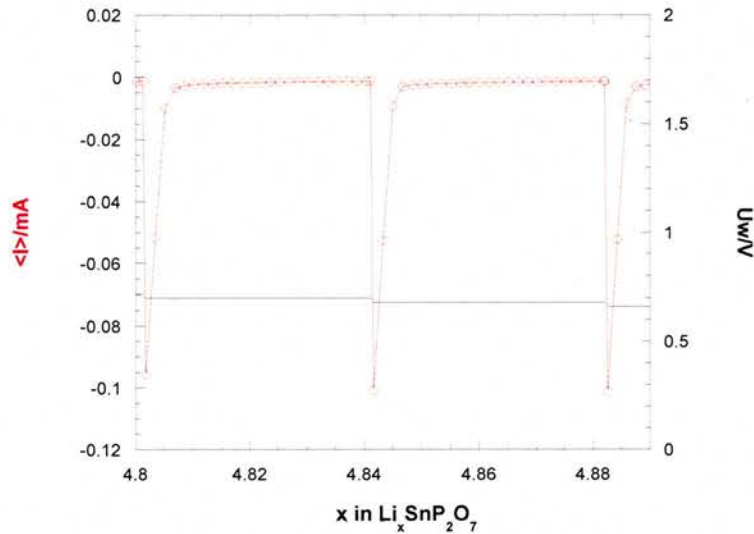


Fig.: 3- 27 Relaxation of current curve reaching symmetrically  $I = 0$  in region II for several potential steps

To get the diffusion coefficient, some other parameters, such as particle size, are needed involving other techniques such as electron microscopy for the estimation of the lithium diffusion.

**3.3.4.3. SPECS: Methodology of diffusion calculation.**

The analysis of SPECS data is concerned with the creation of a qIQx file that is recorded by the MacPile. This file contains all the parameters as  $q$ ,  $x$ ,  $t$  and  $(Q - Q_0)/\text{mAh}$ , where  $q$  is the incremental capacity,  $x$  is the number of lithium inserted,  $t$  is the time and  $(Q - Q_0)/\text{mAh}$  the capacity in mAh/g. In order to obtain the kinetic parameters each step should be analysed carefully and separately.

First of all, the time ( $t$ ) and the total charge  $[(Q - Q_0)/\text{mAh}]$  need to be offset by subtracting the zero point correction from all the data. This leads to **eq.: 3- 6** and **eq.: 3- 7**:

$$\text{eq.: 3- 6} \quad t' = t - t_0$$

$$\text{eq.: 3- 7} \quad [(Q - Q_0) / \text{mAh}] = [(Q - Q_0) / \text{mAh}] - [(Q - Q_0) / \text{mAh}]_0$$

where  $t'$  represents the corrected time,  $t$  the recorded time for each data point and  $t_0$  the first time recorded that step. In **eq.: 3- 7**  $[(Q - Q_0)/\text{mAh}]$  is the total charge passing through the system and  $[(Q - Q_0)/\text{mAh}]_0$  is the charge at the beginning of the step.

Furthermore the time is recorded in hours and needs to be converted to seconds for calculation, **eq.: 3- 8** displays this conversion called “real time” ( $t''$ ):

$$\text{eq.: 3- 8 } (t'') = 10 * \text{INT}[360 * t' + 0.5]$$

where *INT* is the integer part of the expression in bracket,  $10*360$  (= 3600) represent the conversion from seconds to hours. The Macpile only saves data every 10s hence the correction for 5 seconds.

From the corrected data a typical plot of current decay with time can be generated as seen in **Fig.: 3- 28**.

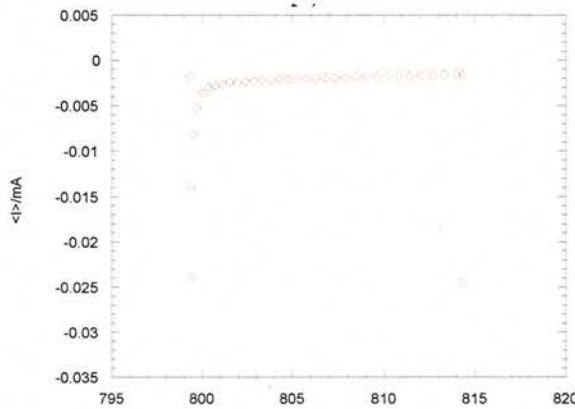


Fig.: 3- 28 Profile of current decay with time of  $\text{SnP}_2\text{O}_7$  at  $-8^\circ\text{C}$  on a step

It is worth to noticing that the accuracy of this technique depends on the evaluation of the particle size that was estimated by electron microscopy.

#### 3.3.4.4.a. Short time approximation.

For short time approximation, the solution<sup>31</sup> of Fick's second law for time gives the relation  $[(Q-Q_0)/\text{mAh}] = f\sqrt{(t'')}$  which when plotted should be a straight line

**Fig.: 3- 29.** From the linear slope the diffusion parameter,  $D_{Li^+}$ , can be calculated only when the limit condition,  $t'' \ll l^2/D_{Li^+}$ , is fulfilled, **eq.: 3- 9.**

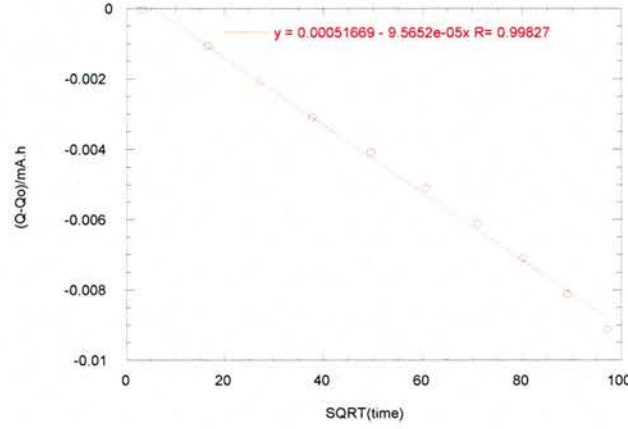


Fig.: 3- 29 Short time approximation plot of  $[(Q-Q_0)/mAh] = f[\sqrt{(t'')}]$

$$\text{eq.: 3- 9 } D_{Li^+}^{1/2} = \frac{\text{slope} * l * \pi^{1/2}}{2 * (Q - Q_0) / mAh}$$

where  $l$  stands for the thickness of the particle and is given by:

$$l = \frac{\text{Volume}}{\text{Surface}} \approx \frac{1}{3} * r \text{ and } r \text{ is the radius of the particle assuming that the particles}$$

are spherical. A roughly spherical shape of the particles was confirmed by a

HRTEM image **Fig.: 3- 25.**

### 3.3.4.4.b. Long time approximation.

For long time approximation the solution of Fick's second law for time means  $\log((Q-Q_0)/mAh) = f(t'')$  should be linear **Fig.: 3- 30**. Then, the diffusion parameter can be calculated for the condition,  $t'' \gg l^2/D_{Li^+}$ , **eq.: 3- 10**.

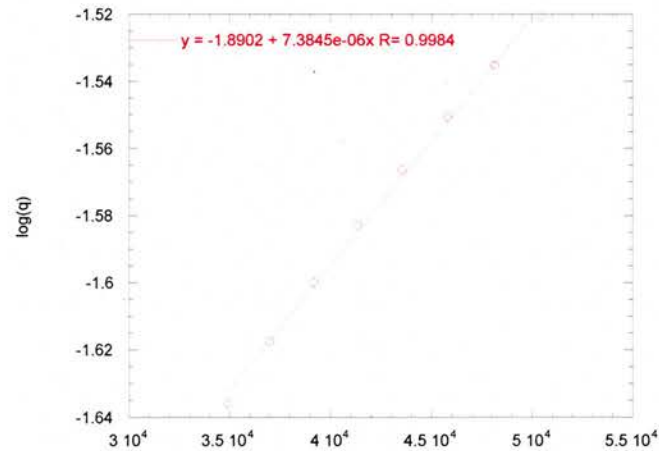


Fig.: 3- 30 Long time approximation plot of  $\log ((Q-Q_0)/mAh) = f(t'')$

$$\text{eq.: 3- 10 } D_{Li^+} = -\frac{4l^2 * \text{slope}}{\pi^2}$$

### 3.3.4.5. $\text{SnP}_2\text{O}_7$ diffusion coefficient in region II.

The SPECS technique was used to investigate batteries made with  $\text{SnP}_2\text{O}_7$  at temperatures of  $9^\circ\text{C}$  and room temperature ( $20^\circ\text{C}$ ).

### 3.3.4.6. Diffusion coefficient for battery at $9^\circ\text{C}$ .

A typical current decay curve of a step in region II of battery made from  $\text{SnP}_2\text{O}_7$  and discharged at  $9^\circ\text{C}$  is shown in **Fig.: 3- 31**. This curve corresponds to a step in region II between time value of 715.42 and 730.37 hours that is relative to  $4.9878 < x < 5.0257$  where  $x$  is the number of lithium involved.

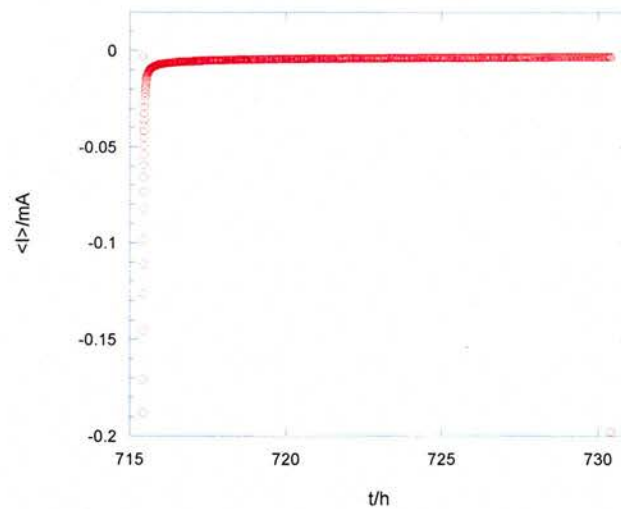


Fig.: 3- 31 Current decay curve of  $x\text{Li}^+/\text{Li}_x\text{SnP}_2\text{O}_7$  battery discharged at  $9^\circ\text{C}$

### 3.3.4.6.a. Short time approximation for discharged battery at 9°C.

The short time approximation was applied to the whole step and is shown in **Fig.: 3- 32**. This does not display homogeneous linear variation of  $q$  versus  $\sqrt{t}$ . However, linearity is clearly exhibited at the beginning of the plot for the short range approximation (except for the first data point, which needs always to be removed since it is affected by polarisation). This plot was fitted with a linear model that displays a slope of  $\sim 0.0004$  (with  $R^2 = 0.99974$ ) see **Fig.: 3- 33**.

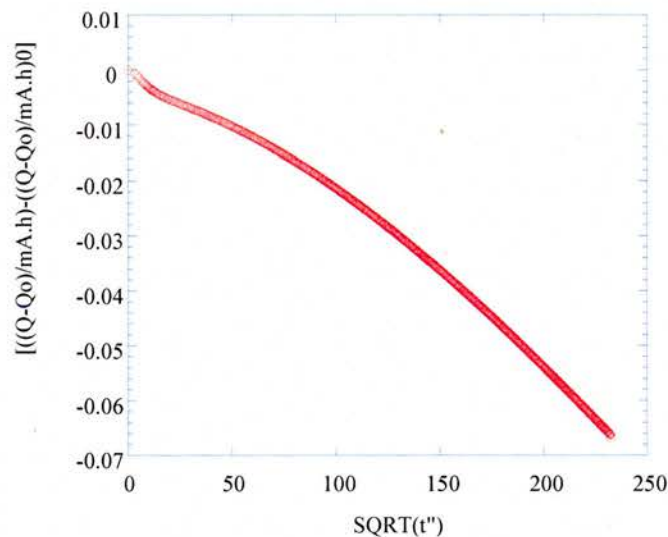


Fig.: 3- 32 Short time approximation of the whole step.

The diffusion coefficient calculated from the slope of the line is  $\sim 8 \times 10^{-15} \text{ cm}^2/\text{s}$  and satisfies the condition of short time approximation estimated ( $t \ll l^2/D \Leftrightarrow 0.03\text{s} \ll 55.55\text{s}$ ).

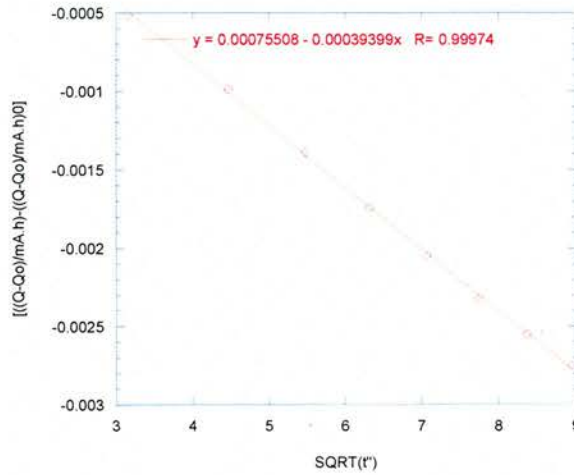


Fig.: 3- 33 Linear variation of  $q$  as function of  $\sqrt{t}$  in the short time approximation

### 3.3.4.6.b. Long time approximation for discharged battery at 9°C.

**Fig.: 3- 34** displays the variation of  $\log(q)$  as a function of *time* over the whole step and exhibits an exponential trend. The long time approximation shows a linear variation of  $\log(q) = f(t'')$  **Fig.: 3- 35** that was fitted with a linear model giving a slope of  $\sim 6.1 \times 10^{-6}$  (with  $R^2 = 0.99968$ ).

The diffusion coefficient was estimated from the slope of the line and leads to  $D_{Li^+} \sim 4 \cdot 10^{-15} \text{ cm}^2/\text{s}$ . Once again the condition of long time approximation was evaluated and satisfied to be  $(t \gg l^2/D \Leftrightarrow 54010\text{s} \gg 55.55\text{s})$ .

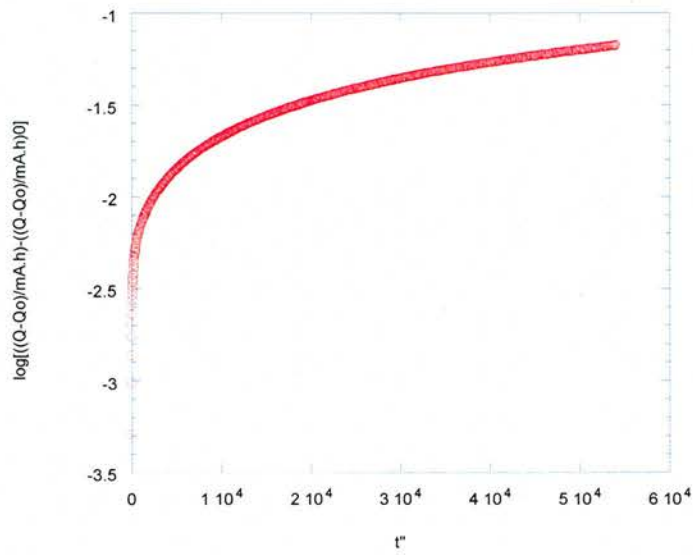


Fig.: 3- 34 Long time approximation of the whole step

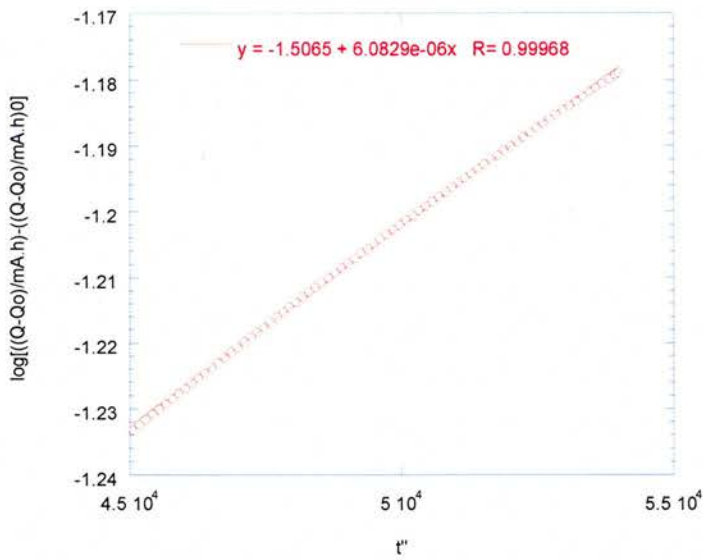


Fig.: 3- 35 Linear variation of  $\log(q)$  as function of real time  $t''$  in the long time approximation

### 3.3.4.7. Diffusion coefficient for battery at room temperature (20°C).

The same investigation as for the cell discharged at 9°C was realised for the cell at room temperature and a current decay curve is shown for one step in region II, in **Fig.: 3- 36**. The data related to the step were collected between time values of 819.64 and 834.64 hours, which corresponds to  $4.9785 < x < 5.0247$  where  $x$  is the number of lithium involved.

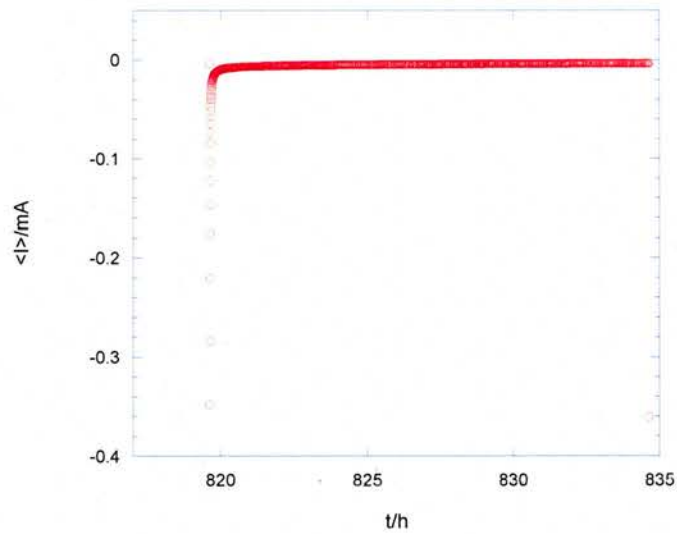


Fig.: 3- 36 Current decay curve of  $x\text{Li}^+/\text{Li}_x\text{SnP}_2\text{O}_7$  battery discharged at room temperature (20°C)

**3.3.4.7.a. Short time approximation for discharged battery at room temperature (20°C).**

The short time approximation was applied to the whole step as shown in **Fig.: 3-37**. This does not show uniform variation of  $q$  versus  $\sqrt{t}$ . However, linearity can be clearly seen at the beginning of the plot for short time approximation (except for the first data point). This plot was fitted with a linear model that displays a slope of  $\sim 0.000551$  (with  $R^2 = 0.99826$ ) **Fig.: 3-38**.

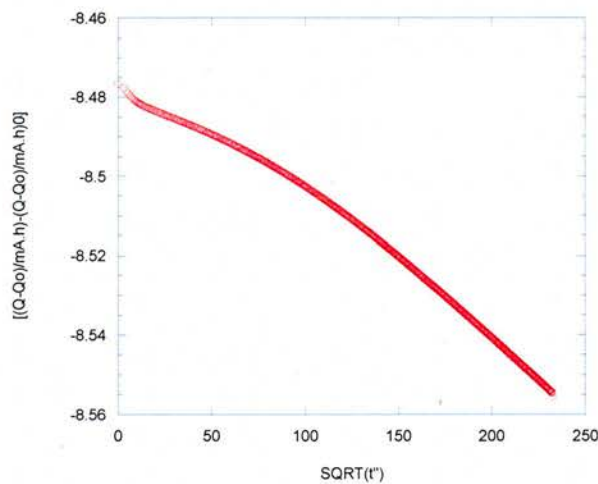


Fig.: 3-37 Short time approximation of the whole step.

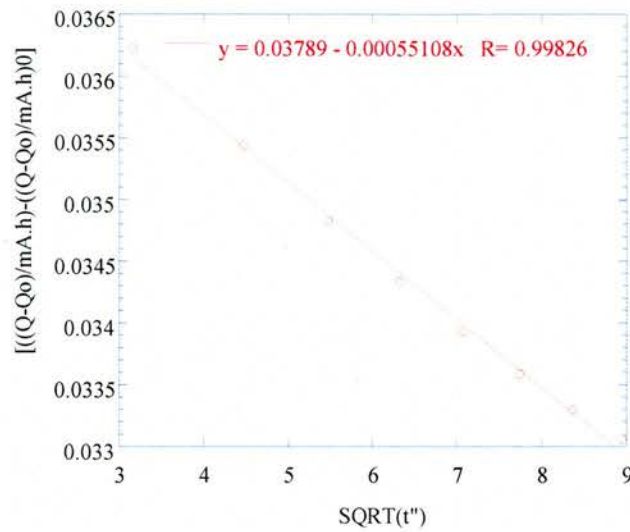


Fig.: 3- 38 Linear variation of  $q$  as function of  $\sqrt{t}$  in the short time approximation.

The diffusion coefficient was evaluated from the slope of the line to be  $D_{Li^+} \sim 8 \times 10^{-15} \text{cm}^2/\text{s}$ . The condition of short range time approximation was assessed to be  $(t \ll l^2/D \Leftrightarrow 0.03\text{s} \ll 55.55\text{s})$  and satisfied.

### 3.3.4.7.b. Long time approximation for discharged battery at room temperature (20°C).

Finally for long time approximation, the variation of  $\log(q)$  versus real time ( $t''$ ) is shown in **Fig.: 3- 39**.

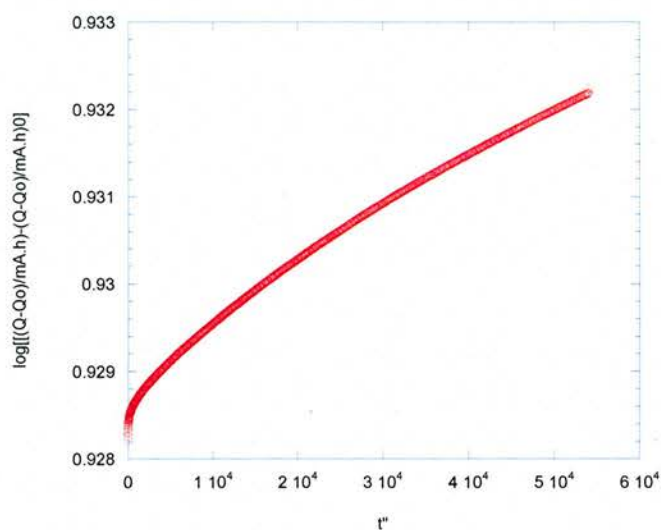


Fig.: 3- 39 Long time approximation of the whole step.

Evidence of linearity is seen in a long time approximation and is plotted in **Fig.:** 3- 40. This was fitted with a straight line, which exhibits a slope of  $\sim 1.17 \times 10^{-5}$  with  $R^2$  value of 0.99919.

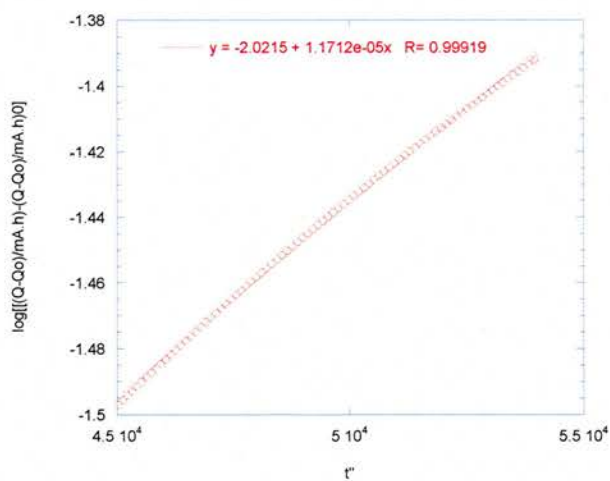


Fig.: 3- 40 Linear variation of  $\log(q)$  as function of real time  $t''$  in the long time approximation.

From the slope of the line,  $D_{\text{Li}^+}$  was estimated to be about the same magnitude of  $\sim 8 \times 10^{-15} \text{cm}^2/\text{s}$  and the condition for long time approximation were satisfied.

These diffusion coefficients obtained are listed in **Table: 3- 7** and are the same magnitude of those obtained for other lithium battery materials. Deiss<sup>32</sup> has reported for  $\text{Li}_8\text{Mn}_2\text{O}_4$  a diffusion coefficient ( $D^{\text{PITT}}$ ) of  $2.8 \times 10^{-13} \text{cm}^2/\text{s}$  using a PITT technique. The diffusion coefficients<sup>33</sup> of  $1.8 \times 10^{-14} \text{cm}^2/\text{s}$  and  $2.2 \times 10^{-16} \text{cm}^2/\text{s}$  were found for  $\text{LiFePO}_4$  and  $\text{FePO}_4$  respectively using a GITT technique.

Temperature ( in °C)	$D_{\text{Li}^+}$ ( $\times 10^{-15} \text{cm}^2/\text{s}$ )	
	Short time approximation	long time approximation
9	8	4
20	8	8

Table: 3- 7 Diffusion coefficient of lithium ion in  $\text{SnP}_2\text{O}_7$  system at 9 and 20°C.

### 3.3.5. Region III.

#### 3.3.5.1. Electrochemistry.

Region III corresponds to a plateau as it can be seen in **Fig.: 3- 17**. From electrochemical investigations and  $^{31}\text{P}$  NMR results obtained in this present work, this plateau can be ascribed to two different processes. The first process presumably starts in region II and continues in region III. It can be described via **eq.: 3- 3** and corresponds to the reduction of the pyrophosphate matrix that exhibits a distinctive peak in the potentiostatic plot at 0.35V **Fig.: 3- 11**. One possible explanation could be that in region II the process starts throughout a solid solution where the lithium diffuse and after in region III, it results in a two phase transformation that occurs at a potential close to the alloying formation. The second process results in the formation of the reversible alloy **eq.: 3- 2** that corresponds to  $4.4\text{Li}^+/\text{Li}_x\text{Sn}$  and it occurs between 0.4 and cut off voltage<sup>34</sup>. In this region, one can consider investigating thermodynamic features but it has been clearly demonstrated that more than one reaction is taking place therefore the analysis using the previous methodology is not possible. Furthermore the chronoamperogram obtained from the SPECS experiment reveals anomalous behaviour **Fig.: 3- 17** of the current relaxation which does not reach zero indicating that the alloying process occurs through a two phase transformation region. This result means that kinetic investigation is also not viable for this region, as the kinetics of the reaction, i.e. dependency of charge with time,

depends on the movements of an interphase rather than on lithium diffusion. Besides it is worth noting that the two processes happening can not be separated.

### 3.3.5.2. Electron Microscopy of $10.4\text{Li}^+/\text{Li}_x\text{SnP}_2\text{O}_7$ .

#### 3.3.5.2.a. SAED of $10.4\text{Li}^+/\text{Li}_x\text{SnP}_2\text{O}_7$ .

The SAED pattern **Fig.: 3- 41** of the materials with  $x = 10.4\text{Li}^+/\text{Li}_x\text{SnP}_2\text{O}_7$  inserted displays some rings. These rings have different d-spacings than those observed in Region II (section 3.3.4.1.2.). This illustrates that these nanocrystalline phases are electrochemically active. The measurement of the ring diameter allowed the determination of some relevant d-spacings and so to speculate on the phases present.

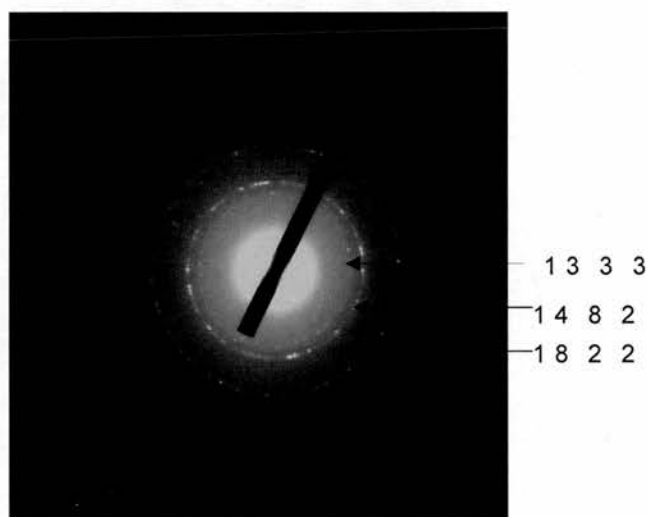


Fig.: 3- 41  $\text{SnP}_2\text{O}_7$  discharged at  $x = 10.4\text{Li}^+/\text{Li}_x\text{SnP}_2\text{O}_7$

The analysis of some of the rings on the micrograph correlate with some  $\text{Li}_{22}\text{Sn}_5$ <sup>35</sup>  
<sup>36</sup> XRD peaks reported in the ICSD Powder Diffraction Database **Table: 3- 9**.  
Once again all the reflections present in the ICSD XRD pattern can not be seen in  
the micrograph. **Table: 3- 8** exhibits the correlation between calculated and  
theoretical d-spacings for this material. This presence of the  $\text{Li}_{22}\text{Sn}_5$  phase would  
support the proposed model in **eq.: 3- 2**, however, it is not definitively shown to  
be present. Clearly some similarities indicate that a lithium tin alloy has been  
produced; however there is not really sufficient overlap to indicate that  $\text{Li}_{22}\text{Sn}_5$  has  
been formed. It is important to note that the pattern for  $\text{Li}_{22}\text{Sn}_5$  is old and does not  
have a high quality mark. Furthermore the high intensity at low d reduce  
confidence in this pattern. Looking at literature data in general, it has been  
difficult to find structural data for  $\text{Li}_{22}\text{Sn}_5$  that can be used with confidence as  
being accurate, thus these data do not disagree with  $\text{Li}_{22}\text{Sn}_5$  nanoparticles being  
formed. Furthermore it is not necessary that alloy nanocrystals will have the same  
crystal structure as the bulk alloys produce at higher temperature.

Diameter of a ring (mm)	Calculated d-spacings ( $\text{\AA}$ ) $\pm 0.5\%$	Theoretical d-spacings ( $\text{\AA}$ ) S.G: F 2 3	$h k l$ $\text{Li}_{22}\text{Sn}_5$ S.G: F 2 3
7.833	2.56	2.5635 (I=5)	3 7 1
13.650	1.47	1.445 (I=10)	13 3 3
16.00	1.21	1.21 (I=100)	14 8 2
18.590	1.10	1.162 (I=90)	18 2 2
22.620	0.88	0.8877	14 14 10

Table: 3- 8 Indexing of the pattern of  $\text{SnP}_2\text{O}_7$  discharged at  $x = 10.4\text{Li}^+/\text{Li}_x\text{SnP}_2\text{O}_7$

$d$ (Å)	Intensity	$hkl$
2.74	20	6 4 0
2.56	5	7 3 1
2.41	10	7 3 3
2.32	100	8 2 2
2.28	10	7 5 1
2.07	10	9 3 1
2.02	10	8 4 4
1.98	20	7 7 1
1.81	5	10 4 2
1.67	15	9 7 3
1.65	35	12 0 0
1.63	35	11 5 1
1.60	15	12 2 2
1.52	25	10 8 2
1.51	25	11 7 1
1.44	10	13 3 3
1.39	10	14 2 0
1.34	100	14 4 2
1.31	5	15 1 1
1.26	20	15 3 3
1.24	15	
1.22	45	15 5 3
1.21	100	14 8 2
1.21	55	11 11 5
1.20	45	16 4 0
1.16	90	

Table: 3- 9 XRD pattern indexing of  $\text{Li}_{22}\text{Sn}_5$ <sup>37</sup> (taken from ICSD 18-0753).

### 3.3.6. Performance.

$\text{SnP}_2\text{O}_7$  displays an irreversible capacity of 965mAh/g on the first discharge and 365 mAh/g of reversible capacity. As shown in **Fig.: 3- 42** the cycling plot generally shows a decrease of the reversible capacity upon cycling. However the first observation is that up to 10 cycles the reversible capacity increase slightly from 350mAh/g to reach the maximum capacity of 365mAh/g. At 20 cycles the capacity has reduced down to the initial capacity. At 50 cycles  $\text{SnP}_2\text{O}_7$  still accommodates 300mAh/g which is roughly the equivalent of the theoretical capacity of carbon actually used as an anode in a commercial cell. The cycling capacity at 100 cycles is about 270mAh/g and at 150 cycles is 250mAh/g. This is still about the practical capacity of carbon.

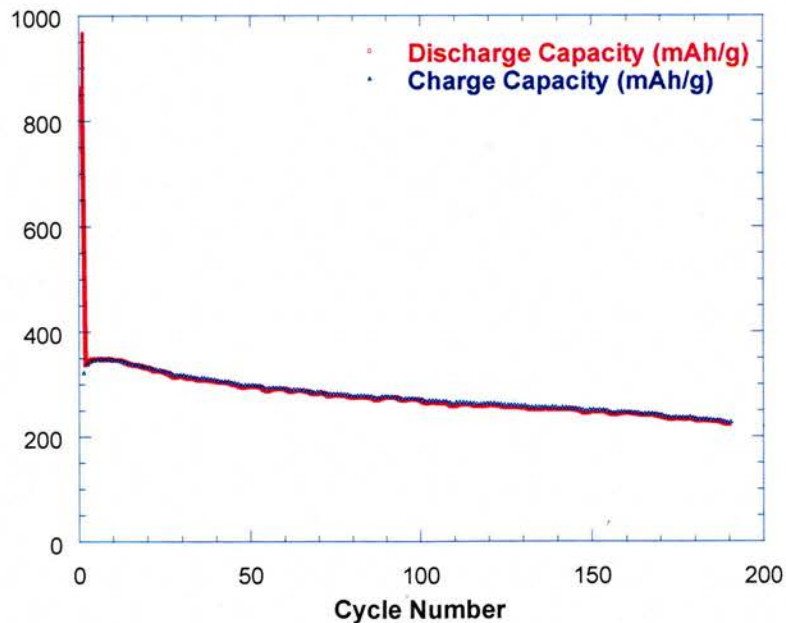


Fig.: 3- 42 Cycle life of  $\text{SnP}_2\text{O}_7$

This material show very good cycle life compared to the analogous tin based oxide, which exhibits a quick fade of the capacity over a few cycles. However the capacity of this material is penalised by the mass effect, as the molecular mass of  $\text{SnP}_2\text{O}_7$  is 292.63g/mol compared to that of carbon which is 12g/mol or even  $\text{SnO}_2$ , which has a molecular mass of 150.71g/mol.

This good cycling behaviour is related to the phosphate matrix formed upon the first discharge as previously discussed. From this study, the phosphate matrix does not show any reversible capacity and seems to be the key factor of good cycle life. The phosphate matrix seems to prevent from cracking and mechanical stresses the tin lithium alloy formed on the first discharge and therefore allows good reversibility.

This good cyclability has been achieved without any significant effort to optimise microstructure. Should the problem of large irreversible initial capacity be overcome, then this would warrant significant effort to improve the cyclability; however, for the present purposes it is sufficient to recognise that  $\text{SnP}_2\text{O}_7$  shows high cyclability compared to other tin oxide systems.

### 3.3.7. Conclusion.

$\text{SnP}_2\text{O}_7$  was synthesised and structurally characterised via several techniques. The combination of XRD and electron microscopy has revealed the complexity of this material exhibiting a disordered cubic structure resulting from a superstructure of  $3 \times 3 \times 3$ . Our result matches very well those reported by *Evans et al*<sup>2</sup> on the crystallographic characterisation and those reported by *Fayon et al*<sup>4</sup> via NMR. The investigations reported on the analogous family members of  $\text{M}^{4+}\text{P}_2\text{O}_7$  (with  $\text{M} = \text{Si}, \text{Ti}, \text{Zr}$  and  $\text{Pb}$ ) lead to the same conclusion regarding the structure.

The electrochemical properties were investigated in detail via lithium insertion with different electrochemical testing modes in order to understand the mechanism, to propose a model that fits the system and offer solutions for the better operation of the system.

The combination of electrochemistry with techniques such as NMR, IR, and XPS provide data to propose an operating model of this material under discharge. The main reactions occurring in the system can be summarised as follows.

Upon the first discharge,  $\text{SnP}_2\text{O}_7$  transforms to tin metal plus a phosphate matrix that was characterised as  $\text{Li}_4\text{P}_2\text{O}_7$  at a voltage of 1.3V. The reaction takes place through a biphasic transformation reaction.

Then the phosphate matrix formed is further reduced from  $\text{Li}_4\text{P}_2\text{O}_7$  to  $\text{Li}_6\text{P}_2\text{O}_7$  involving a two electron process around 0.35V. In the same range of potential down to zero, the tin metal alloys with lithium to form a nanocrystalline phase that was characterised to be  $\text{Li}_{22}\text{Sn}_5$  that is supported by an Isis neutron diffraction experiment reported by *Behm et al*<sup>38</sup>. The SPECS experiment has suggested once again that these reactions are based on biphasic transformations processes. The cells were thereby reversibly cycled between 0 and 1.2V.

In between the transformations described above is a solid solution region where the lithium diffuses throughout the system and reducing the voltage to the region where the reactions occur.

The galvanostatic testing of  $\text{SnP}_2\text{O}_7$  reveals that this material is a good anode candidate for carbon replacement. It exhibits a capacity of 965mAh/g but most of this capacity is irreversible and the reversibility account for 365mAh/g, which is better than carbon. Despite the good cycling behaviour of this material the huge irreversible capacity is still a problem for its commercial use. However the capacity of this material is penalised by its heavy molecular mass, therefore a chemical modification via substitution might be one of the solutions of improvement. There is clear evidence that the matrix and tin phases are nanocrystalline, forming a disordered rather amorphous composite.

**3.3.8. References.**

- <sup>1</sup> N. Khosronavi, V. Korthuis, A. W. Sleight, *Inorg. Chem.*, **35**, 485-489 (1996).
- <sup>2</sup> J. S. O. Evans, W. I. F. David and A. W. Sleight, *Acta Cryst.*, **B55**, 333-34 (1999).
- <sup>3</sup> R. Hubin, P. Tarte, *Spectrochimica Acta*, **23A**, 1815-1829 (1967).
- <sup>4</sup> Franck Fayon, Ian J. King, Robin K. Harris, Richard K. Gover, John S. O. Evans and Dominique Massiot, *Chem. Mater.* **15** 22-34 (2003).
- <sup>5</sup> J. Sanz, J. E. Iglesias, J. Soria, E. R. Losilla, M. A. G. Aranda, S. Bruque, *Chem. Mater.* **9** 996-1003 (1997).
- <sup>6</sup> M. Behm, J. T. S. Irvine, *Electrochimica Acta* **47**, 1727-1738 (2002).
- <sup>7</sup> Y. Iodata, M. Nishima, Y. Miyaki, T. Kubota and T. Miyasaki, *Eur Pat Appl.*, 651450 A1 950503, (1995).
- <sup>8</sup> I. A. Courtney, W. R. McKinnon, and J. R. Dahn , *Journal of the Electrochemical Society*, **146** (1) 59-68 (1999).
- <sup>9</sup> Robert A. Huggins, *Solid State Ionics*, **113-115**, 57-67 (1998).
- <sup>10</sup> S. Prabhakar, K. J. Rao and C. N. R. Rao *Chemical Physics letters* **139** 96 (1987).
- <sup>11</sup> Jim Yang Lee, Yaowu Xiao, Zhaolin liu, *Solid State Ionics* **133** 25-35 (2000).
- <sup>12</sup> Todd M. Alam, Sam Conzone, Richard K. Brow, Timothy J. Boyle *Journal of Non-Crystalline Solids* **258** 140-154 (1999).
- <sup>13</sup> Z. Xu, Jonathan F. Stebbins *Solid State Nuclear Magnetic Resonance* **5** 103-112 (1995).

- <sup>14</sup> R. Hubin and P. Tarte, *Spectrochimica Acta*, **23A** 1815-1829 (1967).
- <sup>15</sup> M. Gabelica-Robert and P. Tarte, *Journal of Molecular Structure* **79** 251-254 (1982).
- <sup>16</sup> Y. C. Chan, S. H. Fan, K. C. Hung, *Materials Science and Engineering* **B85** 64-69 (2001).
- <sup>17</sup> D. Dobler, S. Oswald, J. Werner, W. Arabczyk, G. Behr, K. Wetzig, *Chemical Physics* **286** 375-383 (2003).
- <sup>18</sup> A. H. Thompson, *J. Electrochem. Soc.* **126**, 608 (1979).
- <sup>19</sup> W. R. McKinnon and J. R. Dahn, *Solid State Commun.* **48**, 4 (1983)
- <sup>20</sup> W. R. McKinnon, J. R. Dahn, J. J. Murray, R. R. Haering, R. S. McMillan and A. H. Rivers-Bowerman, *J. Phys. C: Solid State Phys.*, **19**, 5135 (1986).
- <sup>21</sup> Y. Chabre, *J. Electrochem. Soc.* **138**, 329 (1991).
- <sup>22</sup> Y. Chabre, *Prog. Solid State Chem.* **23**, 1 (1995).
- <sup>23</sup> <http://www.webelements.com>
- <sup>24</sup> S. K. Mishra, G. Ceder, *Physical Review B*, **59** (9) 6120-6130 (1999).
- <sup>25</sup> Y. Reynier, R. Yazami, B. Fultz, *J. Power Sources*, **119-121**, 850-855 (2003).
- <sup>26</sup> Swanson, Tatge, *Natl. Bur. Stand. (U.S.), Circ.* **539**, 1 24 (1953).
- <sup>27</sup> J. Thewlis, A. R. Davey, *Nature* **174**, 1011-1011 (1954).
- <sup>28</sup> J. Thewlis, A. R. Davey, *Phase Transition* **38**, 127-220 (1992).
- <sup>29</sup> O. V. Yakubovich, O. K. Mel'nikov, *Kristallografiya*, **39**, 815-820 (1994).
- <sup>30</sup> A. Daidouh, M. L. Veiga, C. Pico, M. Martinez-Ripoll, *Acta Crystallographica C*, **53**, i167-i169 (1997).

- <sup>31</sup> D. Guyomard, J. M. Tarascon, *J. Electrochem. Soc.* **139**, 937-948 (1992).
- <sup>32</sup> E. Deiss, *Electrochimica Acta*, **47**, 4027-4034 (2002).
- <sup>33</sup> P. P. Prosini, M. Lisi, D. Zane, M. Pasquali, *Solid State Ionics* **148**, 45-51 (2002).
- <sup>34</sup> R. A. Huggins, *Solid State Ionics* **113-115**, 57-67 (1998).
- <sup>35</sup> G. Gladyshevskii, I. Oleksiv, P. I. Kripyakevich, *Sov. Phys. Crystallogr.*, **9**, 338 (1964)
- <sup>36</sup> J. R. Dahn, I. A. Courtney, O. Mao, *Solid State Ionics* **111**, 289-294 (1998).
- <sup>37</sup> Gladyshevskii et al., *Sov. Phys. Crystallogr. (Engl. Trans.)*, **9**, 269 (1964).
- <sup>38</sup> M. Behm, P. Connor, F. Belliard and J. T. S. Irvine, *Isis experimental report* 31/05/00.

#### 4. Boron doped tin pyrophosphate.

##### 4.1. Introduction.

Borophosphate systems with networks of inter-linked borate, phosphate and borophosphate sub-units provide an interesting area for structural and physical studies. The materials range from well defined crystalline structures to amorphous materials exhibiting only local cluster-like ordering. The mixture of boron and phosphorus in such materials also raises the potential of interesting and possibly useful physical properties. Many  $\text{MO}_x:(\text{B}_y\text{O}_z)$  compositions [where M is any metal] are known to exist in glassy forms, containing  $[\text{BO}_3]^{3-}$ ,  $\text{BO}_{3/2}$  and other borate structural sub-units.<sup>1</sup> In these materials the coordination of the boron and phosphorus is of particular interest.

Importantly FujiFilm Celltech reported<sup>2</sup> that some of these materials, based on tin, are good candidate anodes (high capacity) for lithium secondary battery applications. The first charge capacities for  $\text{SnB}_{0.56}\text{P}_{0.4}\text{Al}_{0.42}\text{O}_{3.46}$  were reported<sup>3</sup> to be more than 600  $\text{mAhg}^{-1}$  with moderate cycling stability. It was also reported<sup>4</sup> that spectator atoms help disperse tin atoms in the glassy matrix, slowing down the aggregation of Sn and thus improving the reversibility of these materials with increasing the number of spectator atoms.

As a negative lithium battery electrode, crystalline  $\text{SnO}_2$  shows good initial capacity but fades quickly<sup>5</sup>. However, cubic  $\text{SnP}_2\text{O}_7$ <sup>6</sup> was found to have good electrochemical

properties, with a reversible capacity of  $365\text{mAhg}^{-1}$  and good capacity retention. Amorphous  $\text{SnO}_2\text{:B}_2\text{O}_3$  has better theoretical capacity than  $\text{SnP}_2\text{O}_7$  and so the combination of  $\text{SnO}_2\text{:B}_2\text{O}_3$  and  $\text{SnP}_2\text{O}_7$  should be investigated in order to improve our knowledge of tin based anode materials and possibly enhance their properties.

Compositions from the series  $\text{SnP}_{2-y}\text{B}_y\text{O}_{7-y}$  ( $0 \leq y \leq 2$ ) where  $y$  represents the boron content, which is equivalent to  $(\text{SnO}_2\text{:B}_2\text{O}_3)_{y/2}/(\text{SnP}_2\text{O}_7)_{1-y/2}$  or  $\text{SnO}_2\text{:}(1-y/2)\text{P}_2\text{O}_5\text{:}(y/2)\text{B}_2\text{O}_3$  for amorphous materials, were synthesised and characterised by XRD,  $^{11}\text{B}$  and  $^{31}\text{P}$  NMR, SEM, and electron diffraction. The samples were also evaluated as anodes for lithium battery application.

## 4.2. Results and discussion.

### 4.2.1. XRD.

The XRD pattern of  $\text{SnP}_2\text{O}_7$  ( $y = 0$ ) fired at  $1000^\circ\text{C}$  **Fig.: 4- 1a** was indexed according to the cubic space group  $\text{P} \bar{3}$ , with  $a = 7.94(2)$  Å in accord with Hang *et al.*<sup>7, 8</sup> as described in Chapter 3. **Fig.: 4- 1** shows in addition to  $\text{SnP}_2\text{O}_7$  ( $y = 0$ ) fired at  $1000^\circ\text{C}$  **Fig.: 4- 1a** the analogous composition fired at  $400^\circ\text{C}$  **Fig.: 4- 1b**.

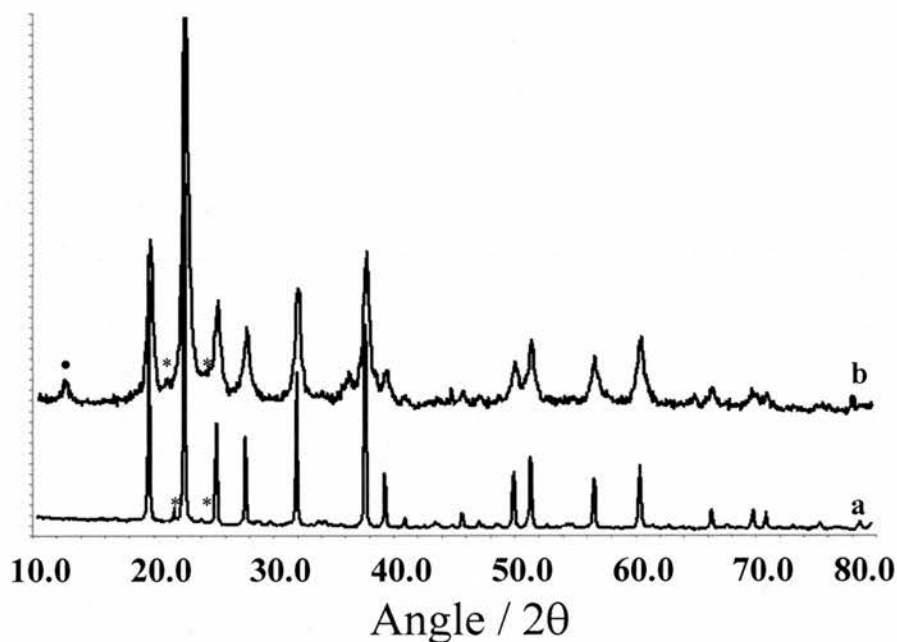


Fig.: 4- 1 XRD pattern of: (a)  $\text{SnP}_2\text{O}_7$  prepared at 1000°C and (b)  $\text{SnP}_2\text{O}_7$  prepared at 400°C. (“\*” represents peaks from mounting grease and “•” the extra peak for the layered materials)

The difference observed in peak broadening is related to the firing temperature.  $\text{SnP}_2\text{O}_7$  prepared at 400°C shows broad peaks but also a small peak at  $2\theta = 12^\circ$  two theta (marked with •) in addition to some small extra peaks. This suggests that the sample is not solely the cubic phase but also contains layered  $\text{SnP}_2\text{O}_7$  as reported by *Behm et al.*<sup>6</sup> and by *Poojary et al.*<sup>9</sup> for the analogous  $\text{SiP}_2\text{O}_7$ . Due to the fluxing ability of  $\text{B}_2\text{O}_3$ , the boron doped samples,  $y = 0.03$ ,  $0.1$  and  $0.19$ , **Fig.: 4- 2a, b & c** respectively exhibit sharper peaks than the analogous  $\text{SnP}_2\text{O}_7$  fired at the same temperature. Indeed these compositions seem to be as well crystallised and monophasic as  $y = 0$  fired at 1000°C.

The patterns from the materials containing boron show peak positions consistent with those of the cubic form of  $\text{SnP}_2\text{O}_7$  or  $\text{ZrP}_2\text{O}_7$ <sup>10</sup>. As the boron content increases, diffraction peaks become gradually broader compared to those of  $\text{SnP}_2\text{O}_7$  synthesised at 1000°C.

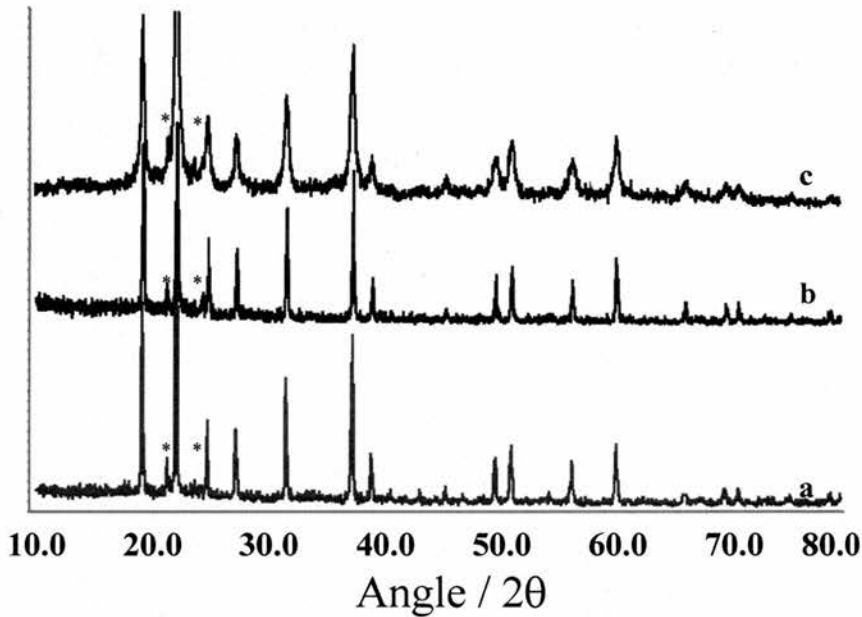


Fig.: 4- 2 XRD pattern of  $\text{SnP}_{2-y}\text{B}_y\text{O}_{7-y}$ : (a)  $y = 0.03$ , (b)  $y = 0.1$ , (c)  $y = 0.19$  all heated at 400°C. (“\*” represents peaks from mounting grease)

This peak broadening indicates a decreasing of crystallinity, however in this range there is no evidence of secondary phase formation. This is a solid solution range as the borate behaves like a dilute species in the cubic framework with no change in crystal structure, but with a change in unit cell parameter.

As boron substitution increases, unit cell parameter decreases, **Fig.: 4- 3**. The shrinkage is linearly proportional to  $y$  up to  $y = 0.19$ , closely following Vegard's law.

Apparent crystallite size was estimated (using the Scherrer equation) to be c.130 nm for  $\text{SnP}_2\text{O}_7$  prepared at  $1000^\circ\text{C}$ . The various samples in the solid solution region show decreasing crystallite sizes with increasing  $y$ . For  $y = 0.03$  the crystallite size is estimated to be  $\sim 140$  nm, 110nm for  $y = 0.1$  and 60 nm for  $y = 0.19$ .

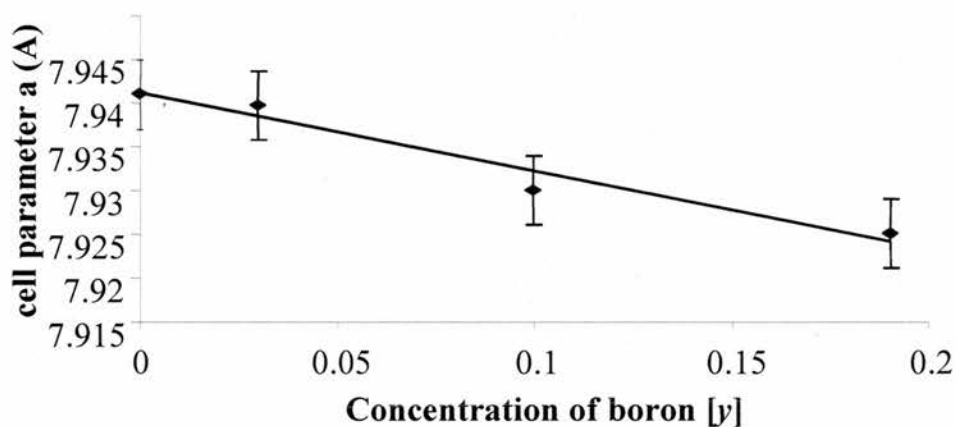


Fig.: 4- 3 Evolution of the cell parameter with boron concentration (Error bars =  $\pm 0.004$   $R^2 = 0.9866$ ).

The  $\text{SnO}_2:\text{B}_2\text{O}_3$  ( $y = 2$ ) pattern, shown in **Fig.: 4- 4a** exhibits no observable crystalline peaks as well as the other compositions of  $1.75 \leq y \leq 2$ . **Fig.: 4- 4b** shows an XRD pattern of material for  $y = 0.25$ . From this pattern, low crystallinity can be seen via broadening of peaks and there is also a clear amorphous background similar to **Fig.: 4- 4a**, which implies a mixture of crystalline and amorphous phases. The crystalline peak positions do not seem to shift once  $y$  exceeds  $0.19$ , although the peak broadening means that unit cell size can not be accurately determined.

In the range  $0.25 \leq y \leq 1.75$ , a two phase mixture, containing a glassy and a crystalline phase seems to exist. XRD technique has pictured roughly the existence of different domain with the serie of boron doped samples.

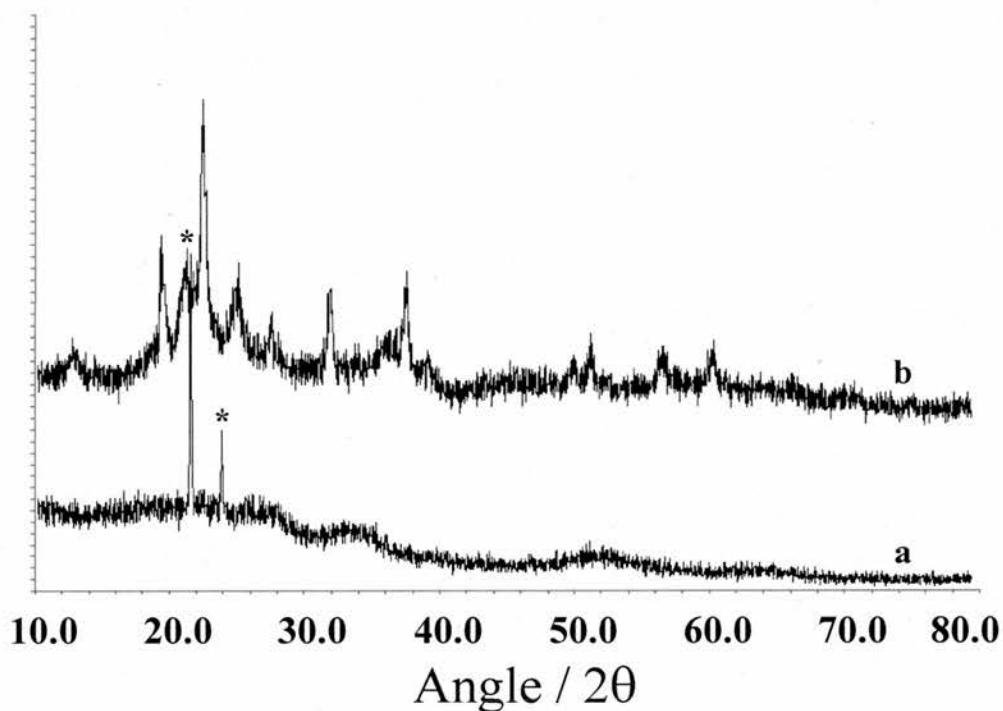


Fig.: 4- 4 XRD pattern of  $\text{SnP}_{2-y}\text{B}_y\text{O}_{7-y}$ : (a)  $y = 0.25$ , (b)  $y = 2$  all heated at  $400^\circ\text{C}$ . (“\*” represents peaks from mounting grease)

#### 4.2.2. SAED.

Selected Area Electron Diffraction (SAED) was used to study the microstructure of  $\text{SnP}_{2-y}\text{B}_y\text{O}_{7-y}$  samples in the crystalline domain. The SAED pattern of  $\text{SnP}_2\text{O}_7$  corresponding to a view down the  $[1 \bar{2} 0]$  plane is shown in **Fig.: 4- 5a**. This pattern can be described as exhibiting two consecutive intense spots subdivided into three equal subdivisions by two smaller size spots. These are superstructure reflections, which give d-spacing of 10.65 Å along the  $d_{210}$  direction and a d-spacing of 23.7 Å along the  $d_{001}$  direction, which is three times the initial simple cubic cell parameter. This is evidence of the 3x3x3 superstructure proposed by Gover *et al*<sup>11</sup>.

The same observations were seen for  $y = 0.03$  along the same zone axis implying that boron substitution does not affect the superstructure when the system is crystalline. **Fig.: 4- 5b**. **Fig.: 4- 5c** of specimen  $y = 0.19$  exhibits the same structure such as  $y = 0$  and  $y = 0.03$  along the same  $[1 \bar{2} 0]$  zone axis. **Fig.: 4- 5d** reinforces the superstructure along different zone axes such as the  $[111]$  plane that corresponds to d-spacing of 16.7 Å along the  $d_{011}$  and along the  $d_{101}$  directions.

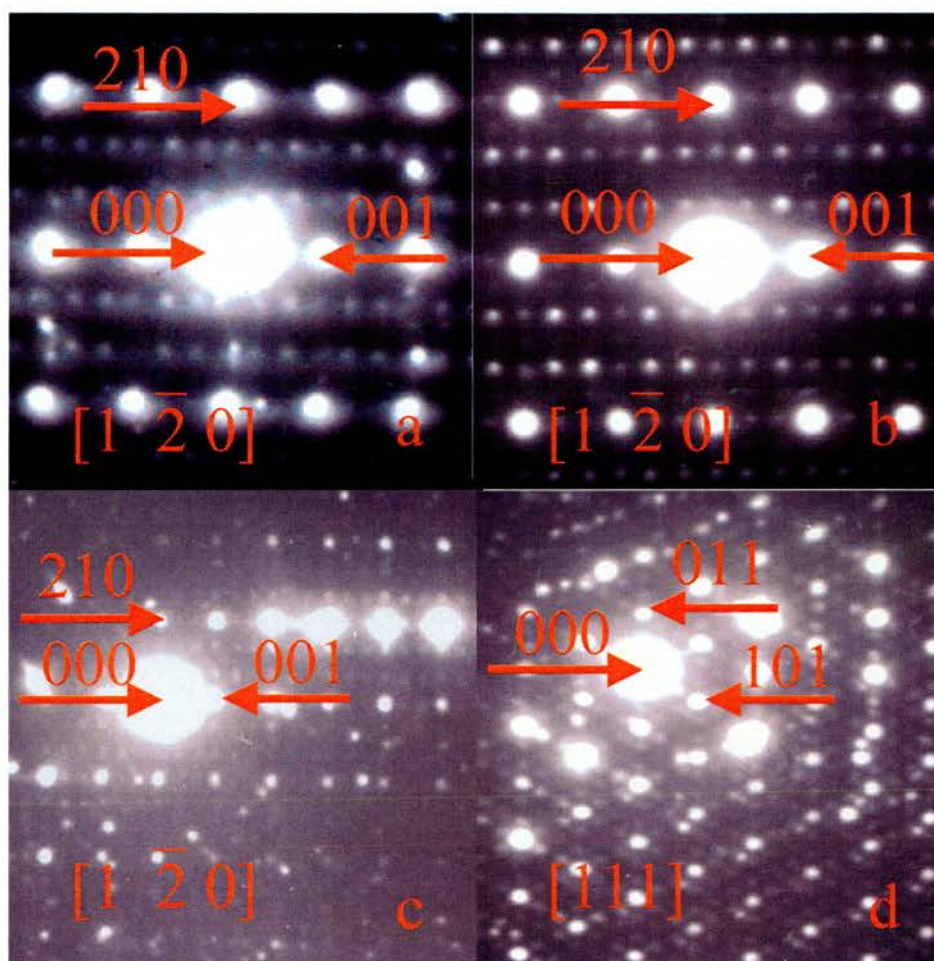


Fig.: 4- 5 a) SAED pattern viewed along the  $[1 \bar{2} 0]$  direction of  $y = 0$  ( $\text{SnP}_{2-y}\text{B}_y\text{O}_{7-y}$ ).

b) SAED pattern viewed along the  $[1 \bar{2} 0]$  direction of  $y = 0.03$  ( $\text{SnP}_{2-y}\text{B}_y\text{O}_{7-y}$ ).

c) SAED pattern viewed along the  $[1 \bar{2} 0]$  direction of  $y = 0.19$  ( $\text{SnP}_{2-y}\text{B}_y\text{O}_{7-y}$ ).

d) SAED pattern viewed along the  $[1 1 1]$  direction of  $y = 0.19$  ( $\text{SnP}_{2-y}\text{B}_y\text{O}_{7-y}$ ).

### 4.2.3. SEM.

SEM images displayed in **Fig.: 4- 6** show the change in morphology on evolution of the whole range of composition  $0 \leq y \leq 2$ . All the pictures were taken at the same magnification of (x 3000). The pictures from a to c correspond to  $y = 0, 0.03$  and  $0.19$  respectively and present a porous microstructure with agglomeration of very small particles. These particles are distinguishable but the particle size gets smaller with boron concentration. Despite the fact that  $\text{SnP}_2\text{O}_7$  was synthesised at  $1000^\circ\text{C}$ , **Fig.: 4- 6a**, the particle size is  $\sim 100\text{nm}$ , comparable to those of  $y = 0.03$  **Fig.: 4- 6b** and  $y = 0.19$  **Fig.: 4- 6c** which were only heated to  $400^\circ\text{C}$ . These observations are in agreement with the XRD peak widths.

**Fig.: 4- 6d & e** of sample with a composition  $y = 0.25$  and  $y = 0.5$  respectively show large blocks of particles made up of very small grains. **Fig.: 4- 6f, g & h** related to  $y = 1.75, 1.9,$  and  $2$  respectively do not exhibit any individual particles, but just large glassy blocks. These SEM observations indicate the phase changes that happen with borate addition. At least two phases were clearly observed. For  $0 \leq y \leq 0.19$ , a crystalline solid solution is observed whilst for composition of  $1.75 \leq y \leq 2$  boron, glassy materials were formed. In between these two ranges, SEM pictures suggest a mixture of these two aforementioned phases, which is in good agreement with the XRD results.

Across the entire range of boron content, SEM and XRD have pointed out three different domains as depicted in the phase diagram

**Fig.: 4- 7** (the non evaluated temperature region is represented by dash line).

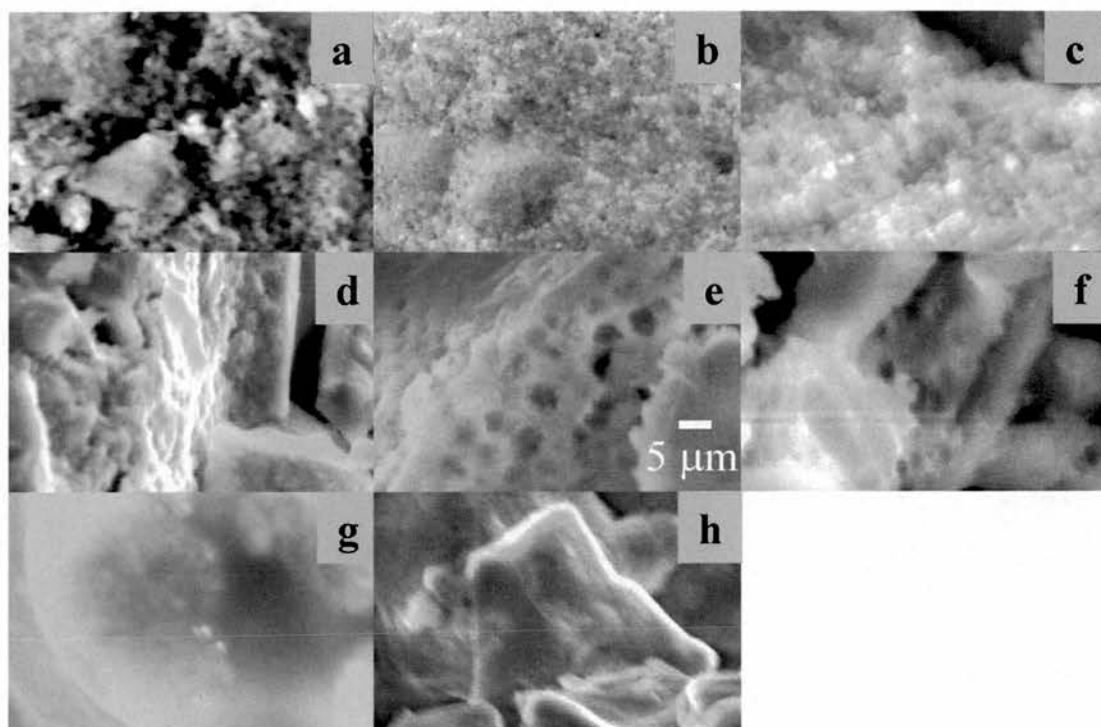


Fig.: 4- 6 SEM images of  $\text{SnP}_{2-y}\text{B}_y\text{O}_{7-y}$ : (a)  $y = 0$ , (b)  $y = 0.03$ , (c)  $y = 0.19$ , (d)  $y = 0.25$ , (e)  $y = 0.5$ , (f)  $y = 1.75$ , (g)  $y = 1.9$ , (h)  $y = 2$ , at a magnification of (x 3000).

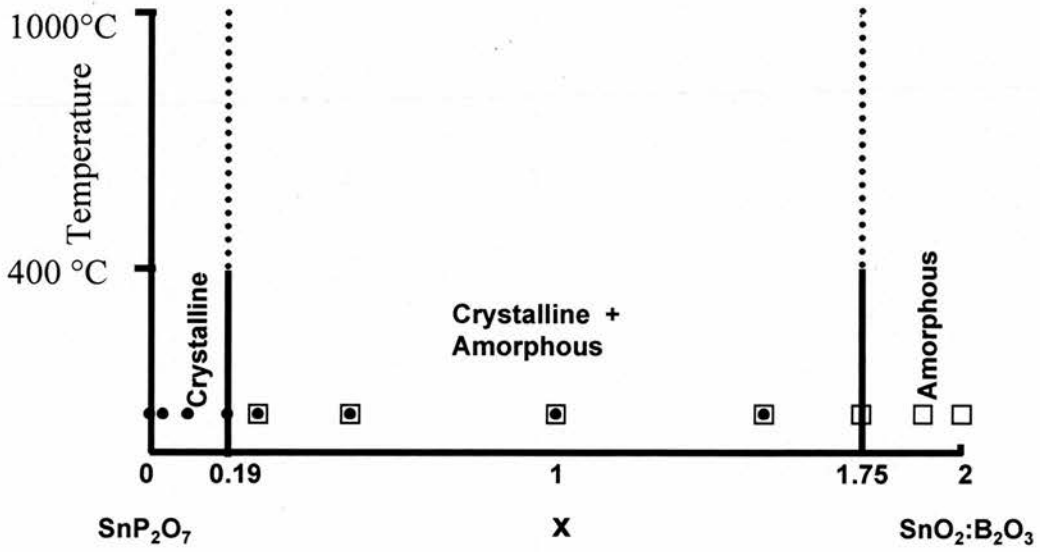


Fig.: 4- 7 Phase diagram of  $(\text{SnO}_2:\text{B}_2\text{O}_3)_{y/2}/(\text{SnP}_2\text{O}_7)_{1-y/2}$  system.

- represents crystalline phase,
- ◻ represents mixture of crystalline and amorphous phase
- represents amorphous phase.

#### 4.2.4. NMR.

##### 4.2.4.1. $^{31}\text{P}$ NMR result.

$^{31}\text{P}$  MAS NMR spectra can be clearly divided into three concentrations ranges. The pure  $\text{SnP}_2\text{O}_7$  ( $y = 0$ ) spectrum **Fig.: 4- 8a** shows a complex lineshape consisting of many isotropic sites covering a region from -26.4 to - 47.6ppm, centred around  $\sim$  - 36.7ppm as previously reported<sup>12</sup>, arising from the  $3 \times 3 \times 3$  short range superstructure.

The resolution of the individual lines making up this composition line can be improved by cutting out the initial part of the FID before transformation.

Substitution of up to  $y = 0.19$  in  $\text{SnP}_2\text{O}_7$  results in spectra **Fig.: 4- 8b, c & d** showing the same broad centre band but with an increase in a line at -30ppm.

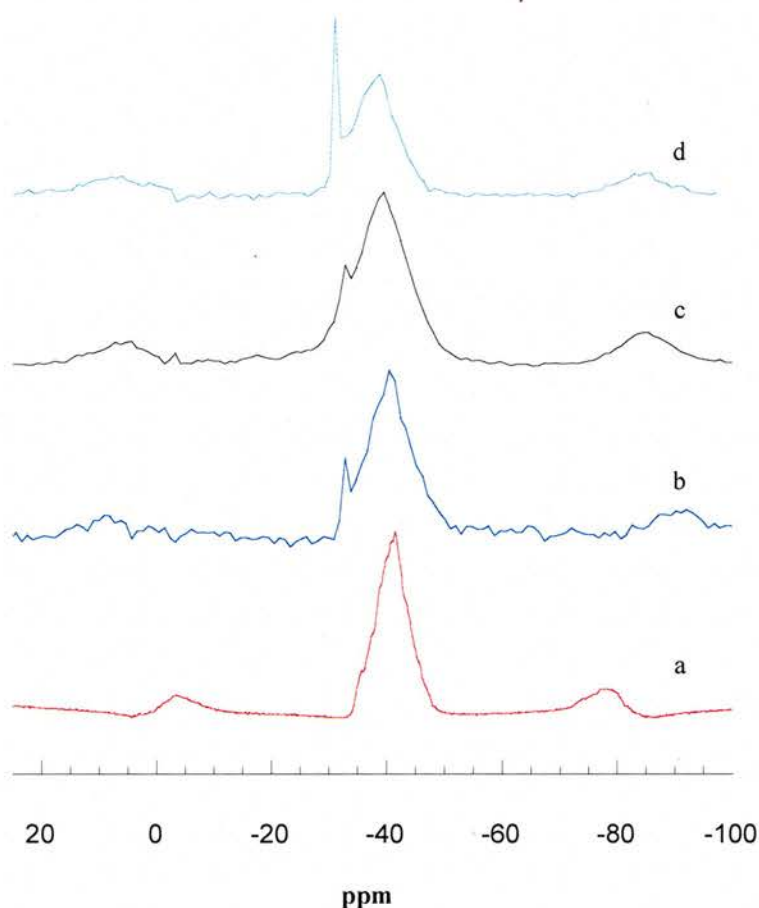


Fig.: 4- 8  $^{31}\text{P}$  DP-MAS-NMR of:  $\text{SnP}_{2-y}\text{B}_y\text{O}_{7-y}$

(a)  $y = 0$ , (b)  $y = 0.03$ , (c)  $y = 0.1$ , (d)  $y = 0.19$  (chemical shift in ppm) .

At  $y = 0.25$ , the spectrum **Fig.: 4- 9a** now shows the highest intensity at  $-16.3\text{ppm}$ , with minor intensities at  $-32.2\text{ppm}$  and  $-36.7\text{ppm}$ . Compositions in the range  $0.5 \leq y \leq 1$  gave major peaks at  $-32.2$  and  $-16.3\text{ppm}$  with a minor peak at  $-25\text{ppm}$  **Fig.: 4- 9b**. Higher boron content,  $y = 1.75$  **Fig.: 4- 9c** gave a broad peak centred at  $-18.6\text{ppm}$  with an increasing shoulder at  $-29.6\text{ppm}$ . At  $y = 1.9$ , no significant change was seen in the chemical shift of the peaks compared to  $y = 1.75$  however, the most intense peak is now at  $-29.7\text{ppm}$ , **Fig.: 4- 9d**.

The 10kHz sidebands are almost absent throughout this range of composition ( $y = 0.5$  up to 1.95) indicating that these lines are relatively narrow when the samples are static.

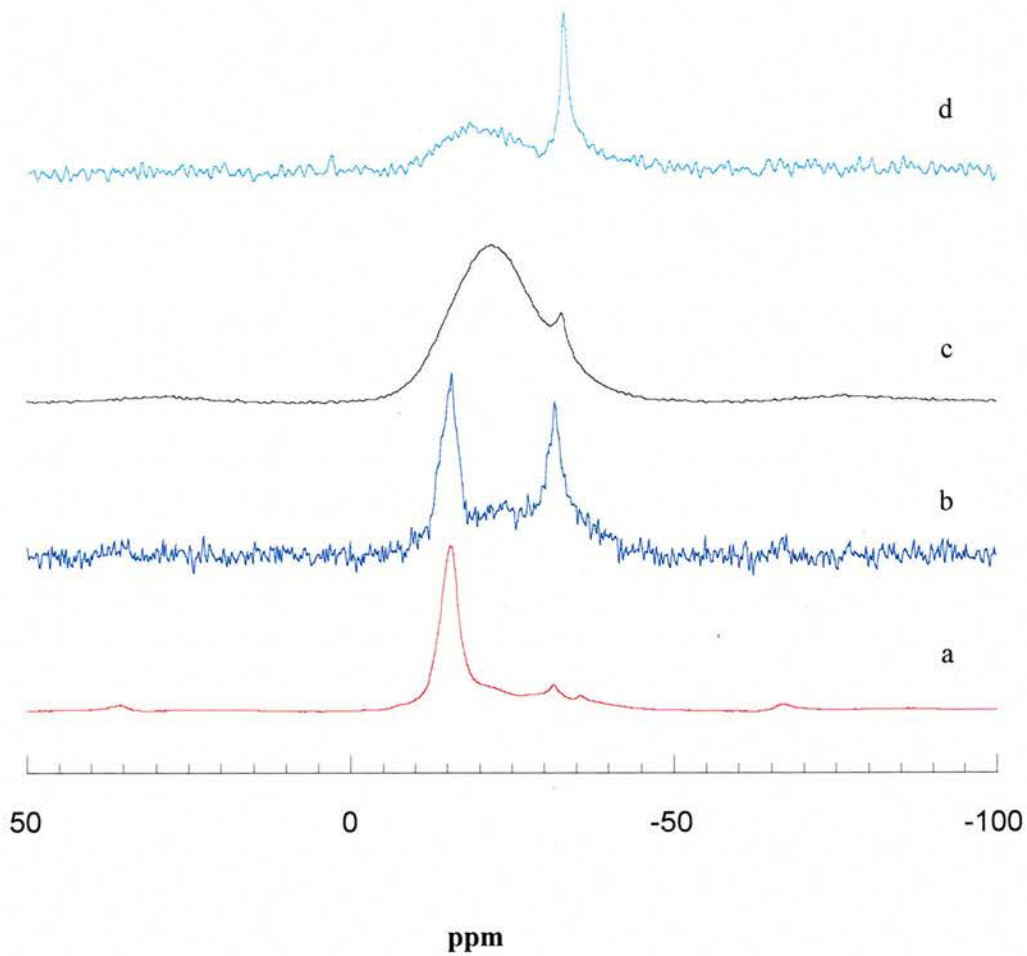


Fig.: 4-  $^{31}\text{P}$  DP-MAS-NMR of:  $(\text{SnO}_2:\text{B}_2\text{O}_3)_{y/2}/(\text{SnP}_2\text{O}_7)_{1-y/2}$  system

(a)  $y = 0.25$ , (b)  $y = 0.5$  (c)  $y = 1.75$  (d)  $y = 1.95$  (chemical shift in ppm).

Results from  $^{31}\text{P}$  NMR experiments are summarised in **Table: 4- 1**.

$y$	$\delta_1$	$\delta_2$	$\delta_3$	$\delta_4$	$\delta_5$	$\delta_6$	Structure
0	-36.7						c
0.03	-36.7		-30				c
0.1	-36.7		-30				c
0.19	-36.7		-30				c
0.25	-36.7	-32.2				-16.3	c + a
0.5		-32.2		-25		-16.3	c + a
1		-32.2		-25		-16.3	c + a
1.75			-29.6		-18.6		a
1.9			-29.7		-18.6		a

Table: 4- 1  $^{31}\text{P}$  DP-MAS-NMR lines of all the sample containing  $^{31}\text{P}$  (chemical shift in ppm).

#### 4.2.4.2. Discussion of $^{31}\text{P}$ NMR.

$^{31}\text{P}$  single pulse NMR of  $\text{SnP}_2\text{O}_7$  shows a broad peak centred at -36.7ppm, which as Fayon *et al*<sup>12</sup> showed, includes some 11 different phosphorus sites. Within the single phase region, the borate-containing materials show a  $^{31}\text{P}$  peak at -30ppm, which increases in both intensity and peak area linearly with borate content ( $0.03 \leq y \leq 0.19$ )

**Fig.: 4- 10.** This peak is obviously associated with changes in the phosphate local environment as borate replaces phosphate in the solid solution region.

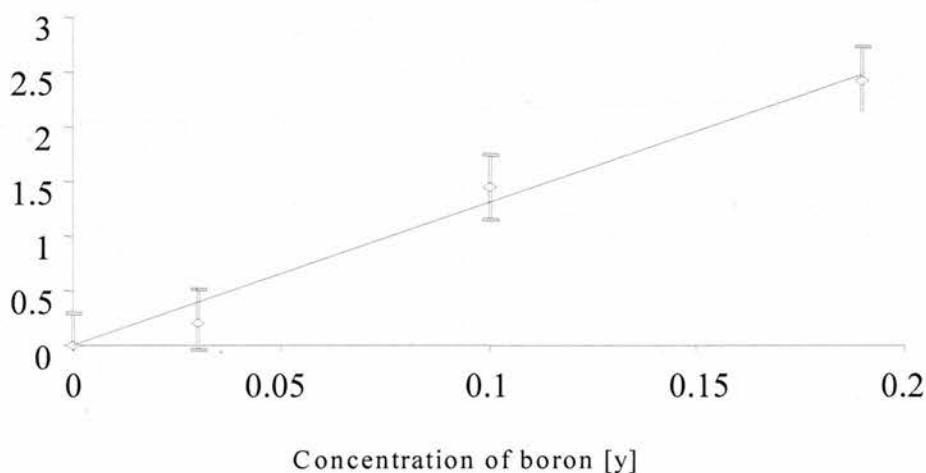


Fig.: 4- 10 Integral of  $^{31}\text{P}$  NMR peak at  $-30\text{ppm}$  versus  $y$  with  $0.03 \leq y \leq 0.19$ .

Two alternative substitution mechanisms might be considered, replacement of one phosphorus in the pyrophosphate units network by boron or the replacement of a pyrophosphate unit with two borate units. The former of these might well be expected to yield a new phosphorus environment with a different peak shift, as observed with the  $-30\text{ppm}$  peak.

The second with total replacement of a pyrophosphate group would not be expected to yield such a new phosphorus environment, probably only resulting in a small shift of the phosphorus peaks, at least on low substitution levels. Thus the pyrophosphate  $[(\text{PO}_{1/2}\text{O}_{3/1})^{2-}]_2$  units are replaced by one  $(\text{BO}_{4/2})^-$  and one  $(\text{PO}_{4/1})^{3-}$  unit on introduction of boron into the lattice. This is very similar to the situation for  $\text{BPO}_4$ <sup>13</sup> which contains  $(\text{BO}_{4/2})^-$  and  $(\text{PO}_{4/1})^{3-}$  tetrahedral units. Indeed the  $^{31}\text{P}$  NMR peak position for crystalline  $\text{BPO}_4$  exactly agrees with the position of the peak that grows

in with borate substitution, at  $-30\text{ppm}$ . The same situation has been also observed in borosilicophosphate glasses<sup>14</sup>.

The sharp contrast in the form of the  $^{31}\text{P}$  spectra between the concentrations 0.19 and 0.25 is especially noticeable, indicating strongly an abrupt change in  $^{31}\text{P}$  environments. The XRD comparison between **Fig.: 4- 2c** ( $y = 0.19$ ) and **Fig.: 4- 4a** ( $y = 0.25$ ) shows that some crystallinity survives at  $y = 0.25$ .

For compositions between  $0.25 \leq y \leq 1$ , three new peaks in the  $^{31}\text{P}$  NMR spectra can be observed as displayed in **Table: 4- 1** and **Fig.: 4- 9a & b**. The presence of new peaks in  $^{31}\text{P}$  NMR spectra, in comparison to those previously described in the solid solution region, clearly indicates new phosphorus environments. Although decreasing the extent of corner sharing of phosphate tetrahedra moves the  $^{31}\text{P}$  NMR peaks to more positive positions, the shift expected on going from pyrophosphate  $(\text{PO}_{3/1}\text{O}_{1/2})^{2-}_2$  to orthophosphate  $(\text{PO}_{4/1})^{3-}$  groups is only  $8\text{ppm}^{15,16}$ . Thus the observed peaks at  $-25$  and  $-16\text{ppm}$  must involve borate phosphate linkages in the amorphous phase. The peak at  $-32\text{ppm}$  can be attributed to  $(\text{PO}_{4/1})^{3-}$  groups in the amorphous matrix.

It appears that the phosphate does not copolymerise or condense in this system and the only species formed in the system are phosphate units  $\text{Q}^n$  with  $n = 0$  or 1 species. This has been already reported for borophosphate silicate glass<sup>14</sup>.

The spinning sideband in the mixed phase region becomes weaker, as the crystalline phase becomes more dilute. These NMR observations correlate with the phase diagram

**Fig.: 4- 7** and hence emphasise a mixed phase region with crystalline clusters in an amorphous matrix.

#### 4.2.4.3. $^{11}\text{B}$ NMR results.

The  $^{11}\text{B}$  NMR spectra **Fig.: 4- 11a, b, c, d & e** look similar for compositions in the range  $0.03 \leq y \leq 1$ , exhibiting a single line at -3.6ppm and a small broad peak (marked “\*\*”) at 12ppm **Fig.: 4- 11a, b, c & d**. This small broad peak increased with  $y$  and the line at -3.6ppm become more asymmetric with  $y$ .

At higher boron concentration ( $y \geq 1$ ) significant changes can be seen in  $^{11}\text{B}$  NMR spectra exhibiting a completely different and complex lineshape, which cover the region of  $\sim -5$  to 30ppm **Fig.: 4- 11e**. The spectrum of  $y = 2$  looks very different to that for  $y \leq 1$  with two complex broad bands centred at 0.9 and 14.1ppm, **Fig.: 4- 12**.

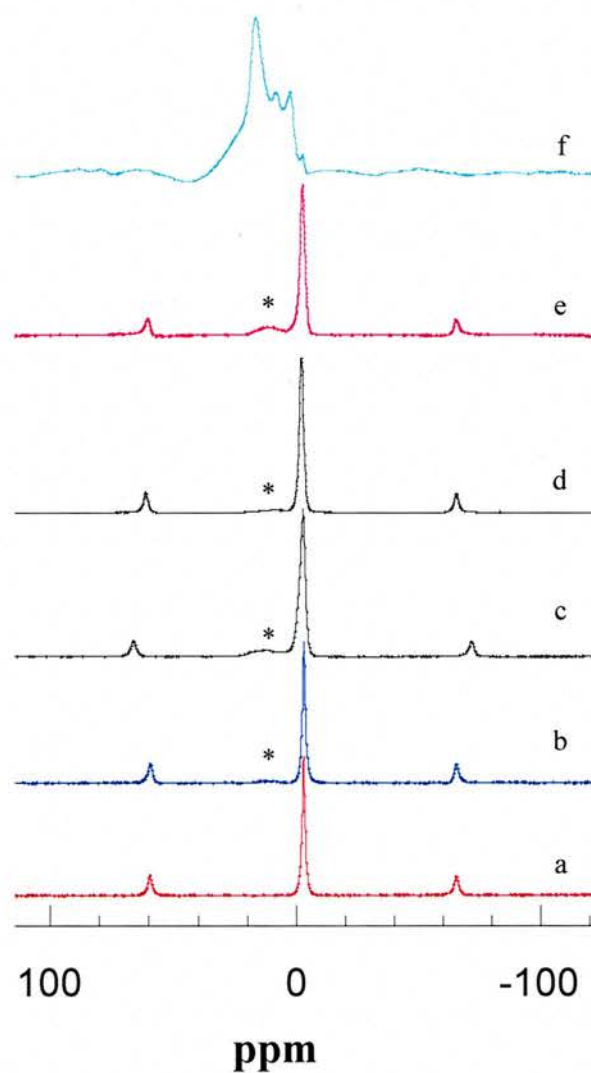


Fig.: 4-  $^{11}\text{B}$  DP-MAS-NMR of  $(\text{SnO}_2:\text{B}_2\text{O}_3)_{y/2}/(\text{SnP}_2\text{O}_7)_{1-y/2}$  system

(a)  $y = 0.03$ , (b)  $y = 0.1$ , (c)  $y = 0.25$ , (d)  $y = 0.5$ , (e)  $y = 1$ , (f)  $y = 1.75$  (chemical shift in ppm).

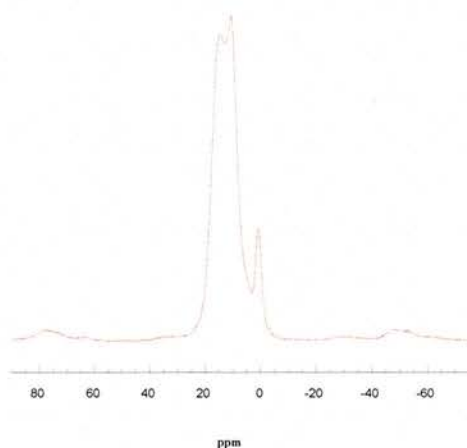


Fig.: 4- 12  $^{11}\text{B}$  DP-MAS-NMR of  $(\text{SnO}_2:\text{B}_2\text{O}_3)_{y/2}/(\text{SnP}_2\text{O}_7)_{1-y/2}$  system with  $y = 2$   
(chemical shift in ppm)

The results from  $^{11}\text{B}$  NMR experiments are summarised in **Table: 4- 2**.

$y$	$\delta_1$	$\delta_2$	$\delta_3$	$\delta_4$	$\delta_5$	$\delta_6$	$\delta_7$	Structure
0.03	-3.6							c
0.1	-3.6				12			c
0.19	-3.6				12			c
0.25	-3.6				12			c + a
0.5	-3.6				12			c + a
1	-3.6				12			c + a
1.75	-3.6	0.9	6.9			14.1		a
1.9	-3.6	0.9	6.9			14.1		a
2		0.9				14.1	19.4	a

Table: 4- 2  $^{11}\text{B}$  DP-MAS-NMR lines of all the samples containing  $^{11}\text{B}$  (chemical shift in ppm).

#### 4.2.4.4. Discussion of $^{11}\text{B}$ NMR.

The  $^{11}\text{B}$  NMR peak at  $-3.6\text{ppm}$  for  $y = 0.03$  **Fig.: 4- 11a** is most likely to be a bridging oxygen borate species such as  $(\text{BO}_{4/2})^-$  as indicated by the peak position, the evidence from the preceding discussion on the  $^{31}\text{P}$  NMR and by analogy with  $\text{BPO}_4$ <sup>17</sup>,<sup>18</sup>. A very weak broad  $^{11}\text{B}$  NMR peak at  $12\text{ppm}$  becomes just discernible for  $y=0.1$ . The position of this peak indicates that it involves non-bridging oxygen<sup>19</sup> probably three-coordinate boron  $\text{BO}_3^-$ . The peak at  $-3.6\text{ppm}$  in the  $^{11}\text{B}$  NMR (**Fig.: 4- 11a, b, c & d**) shows an increase of linewidth and becomes more asymmetric as  $y$  increased. This observation also suggests a greater contribution from other borate species and especially creation of or conversion to three coordinate boron. A decrease in proportion of non-bridging boron oxygen might be accepted as the boron concentration increases and borate neighbours become more common. All borates are bridging, some have non bridging oxygen. In the range of  $0.25 < y < 1$ , the asymmetry within the line at  $-3.6\text{ppm}$  at  $y$  values of 0.1 and above indicates an increasing disorder.

At high boron concentration ( $y \geq 1$ ) significant changes in both  $^{11}\text{B}$  and  $^{31}\text{P}$  NMR are seen, **Table: 4- 1** & **Table: 4- 2**. These shifts suggest a change in composition as a large number of phosphates are replaced by different borate species.  $^{11}\text{B}$  NMR chemical shift was assigned by analogy to those reported by *Brow et al*<sup>20</sup> for the Zn borophosphate glass system.

For compositions  $1.75 \leq y \leq 1.9$  the presence of new  $^{11}\text{B}$  NMR peaks at 6.9 and 14.1ppm is presumably related to the increase of the three or four coordinate borate

species such as  $(\text{BO}_{3/2})$ ,  $(\text{BO}_{2/2}\text{O})^-$  or  $(\text{BO}_{1/2}\text{O}_2)^{2-}$  units. In this composition range, the  $^{11}\text{B}$  NMR data show a drastic decrease of the peak at  $-3.6\text{ppm}$  associated with the crystalline bridging oxygen species  $(\text{BO}_{4/2})^-$  in the crystalline region probably linked to the appearance of non-crystalline bridging oxygen species at  $0.9\text{ppm}$ .

At  $y = 2$ , **Fig.: 4- 12**, the four-coordinate line is again more gaussian in form in a sample which, from **Fig.: 4- 4a**, the amorphous nature is confirmed. This line must be the envelope of a range of 4-coordinate boron environments.

For this composition, the 3-coordinate line dominates the spectrum, accounting for about 90% of the total spectral intensity. Furthermore, the line shape is rather a classic second-order quadrupole-broadened line of low asymmetry, implying that the boron in this sample all have the same quadrupole interaction and symmetry, and correspond to 0 or 3 bridging oxygen. The likelihood here is that all oxygen are bridging. The separation of the peaks leads to an estimate of a quadrupole interaction of about 2 MHz, which is a normal value for 3-coordinate boron<sup>21</sup>.

### 4.3. Electrochemistry and NMR.

The voltammograms of  $\text{SnP}_2\text{O}_7$ ,  $\text{SnO}_2:\text{B}_2\text{O}_3$  and some boron doped  $\text{SnP}_2\text{O}_7$  materials show both irreversible and reversible processes. The profiles vary with the starting material. In order to understand the role displayed by the phosphate and the borate in the matrix,  $^{31}\text{P}$  and  $^{11}\text{B}$  DP-MAS-NMR spectra were collected on variously cycled electrodes.

$\text{SnP}_2\text{O}_7$  **Fig.: 4- 13a** as described by *Behm and al.*<sup>6</sup>, exhibits a plateau at about 1.3V, corresponding to the insertion of around  $4\text{Li}^+/\text{Li}_x\text{SnP}_2\text{O}_7$  before the voltage curve drops down. Between 0.3V and the cut-off voltage 0.02V is located another plateau. The overall first discharge contains  $10.4\text{Li}^+/\text{Li}_x\text{SnP}_2\text{O}_7$  with the reversible cycling capacity of  $4.4\text{Li}^+/\text{Li}_x\text{SnP}_2\text{O}_7$ . The electrochemistry and the  $^{31}\text{P}$  NMR analysis were described in *Chapter 3*.

In the crystalline domain ( $0.03 \leq y \leq 0.19$ ) **Fig.: 4- 13b & c** the galvanostatic plot looks similar to  $\text{SnP}_2\text{O}_7$  with  $10\text{Li}^+/\text{Li}_x\text{SnP}_{2-y}\text{B}_y\text{O}_{7-y}$  involved in the first discharge, however the plateau at 1.3V is getting smaller (less than  $4\text{Li}^+/\text{Li}_x\text{SnP}_{2-y}\text{B}_y\text{O}_{7-y}$ ) with borate content. Between 0.3 and 0.02V, is located another plateau as in the case of  $\text{SnP}_2\text{O}_7$ . The reversible capacity varies from 2.5 to  $4\text{Li}^+/\text{Li}_x\text{SnP}_{2-y}\text{B}_y\text{O}_{7-y}$ .

In this region  $0.03 \leq y \leq 0.19$ , the shape of the discharges and hence the electrochemistry is very similar to  $\text{SnP}_2\text{O}_7$ . It is worthy to notice that in this domain, the reduction plateau does not correspond to  $4\text{Li}^+/\text{Li}_x\text{SnP}_{2-y}\text{B}_y\text{O}_{7-y}$  but becomes less,

depending on the borate content. This result indicates that phosphate and borate species are not reducible at the same potential.

This observation reveals that the plateau at 1.3V is strictly due to the lithium matrix formation and is getting less with borate content as the borate matrix is formed at lower voltage. This suggests an important thermodynamic feature, which correspond to the formation of borate and phosphate matrices.

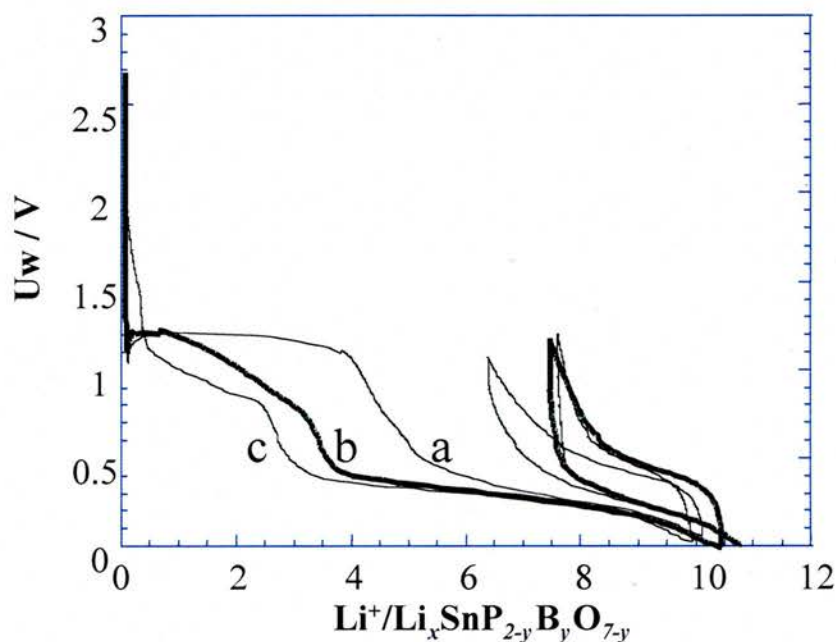


Fig.: 4- 13 Galvanostatic curve of  $SnP_{2-y}B_yO_{7-y}$  with (a)  $y = 0$ , (b)  $y = 0.1$  and (c)  $y = 0.25$  (current density of  $0.1 \text{ mA/cm}^2$ ).

The electrochemistry of  $SnO_2:B_2O_3$  **Fig.: 4- 14e** is entirely different to  $SnP_2O_7$ . There is no well defined plateau at 1.3V but a limited lithium insertion process up to  $1.5 Li^+ / Li_x : SnO_2 : B_2O_3$ , instead there is a single large plateau between 0.3V and 0.02V. The total number of lithium inserted during the first discharge is about  $7.2 Li^+ / Li_x : SnO_2 : B_2O_3$ . The reversible capacity of  $SnO_2 : B_2O_3$  is only  $\sim 2 Li^+ / Li_x : SnO_2 : B_2O_3$ .

In the amorphous domain  $1.75 \leq y \leq 2$ , the galvanostatic plots look similar to  $\text{SnO}_2:\text{B}_2\text{O}_3$ . The plateau between 0.3V and 0.02V must be related to two simultaneous processes, the reduction of  $\text{SnO}_2:\text{B}_2\text{O}_3$  into  $\text{Sn}^0$  in a lithiated borate matrix and the reversible alloy formation<sup>22</sup>.

The potentiostatic plot of  $\text{SnO}_2:\text{B}_2\text{O}_3$  also shows a very intense peak at 0.23V compared to the one observed for  $\text{SnP}_2\text{O}_7$  suggesting that multiprocesses reactions are occurring at that voltage **Fig.: 4- 15**.

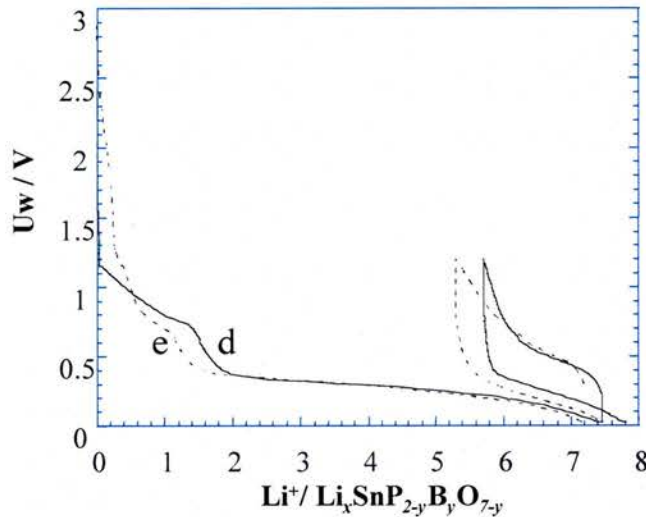


Fig.: 4- 14 Galvanostatic plot of  $\text{SnP}_{2-y}\text{B}_y\text{O}_{7-y}$  with (d)  $y = 0.5$  & (e)  $y = 2$  (current density of  $0.1\text{mA}/\text{cm}^2$ ).

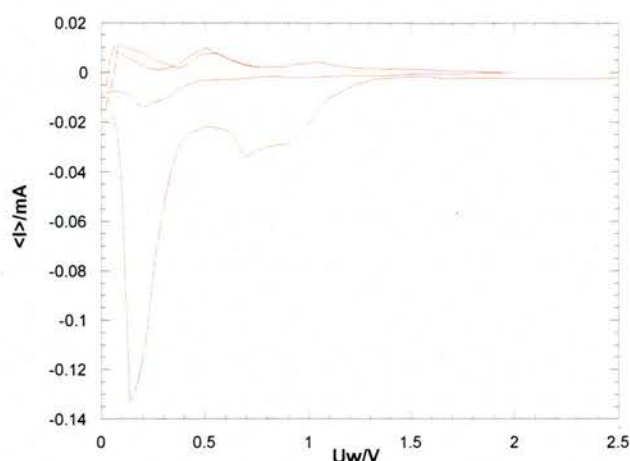
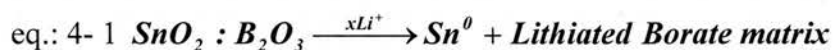


Fig.: 4- 15 Potentiostatic plot of  $\text{SnO}_2:\text{B}_2\text{O}_3$  (Scan rate of 20mV/hour).

The first discharge corresponds to a capacity of  $875\text{mAhg}^{-1}$  and  $265\text{mAhg}^{-1}$  or  $(2\text{Li}^+/\text{Sn})$  of a reversible capacity. Based on the formula weight, it would be reasonable to expect a higher capacity for  $\text{SnO}_2:\text{B}_2\text{O}_3$  than  $\text{SnP}_2\text{O}_7$  but this is not the case, indicating incomplete reduction of tin. Considering boron being more electropositive than phosphorus (Sn-O-B-), it should be more tightly bound than (Sn-O-P-) making it harder to reduce, since B-O is more polar than P-O. The low capacity implies that the borate matrix does not seem suitable for lithium battery. The electrochemistry of this system is proposed via **eq.: 4- 1** & **eq.: 4- 2**.



The electrochemical testing of these materials has reinforced the existence of two separate crystalline and amorphous domains.

The sample with  $y = 0.5$  was electrochemically tested in the mixed amorphous and crystalline domain ( $0.25 \leq y \leq 1.75$ ) and exhibited a large plateau like  $\text{SnO}_2:\text{B}_2\text{O}_3$  between 0.3V and 0.02V with a limited lithium insertion process corresponding to a non well defined plateau up to  $2\text{Li}^+/\text{Li}_x:\text{SnO}_2:\text{B}_2\text{O}_3$  **Fig.: 4- 14d**. The capacity of these cells was less than for the crystalline domain. **Table: 4- 3** displays the first discharge and reversible capacity of all the materials.

	Crystalline Domain		
$y$	1 <sup>st</sup> discharge Capacity.	Reversible Capacity.	Molecular weight
0	965	365	292.65
0.03	962	325	291.56
0.1	875	300	289.03
Amorphous domain			
0.25	934	222	283.617
0.5	731	210	274.576
2	875	265	220.332

Table: 4- 3 Illustration of electrochemical properties: first discharge capacity and the reversible capacity of some materials.

The electrochemistry in that solid solution region is similar to  $\text{SnP}_2\text{O}_7$  with  $\sim 10\text{Li}^+/\text{Sn}$  inserted on the first discharge however the reversible capacity does not fully account for  $4.4\text{Li}^+/\text{Li}_x\text{Sn}$ .

The potentiostatic plots of some specimens across the whole range of  $y$  are shown in **Fig.: 4- 16a, b, c & d**. By lack of potentiostatic data for  $y = 0.25$  composition, a derivative plot was used and display the same information. It can be observed in these plots that the intensities of the peak around 1.3V, which corresponds to the tin reduction is decreasing with boron content. Furthermore the reversible capacity is reduced as this peak decreases.

This observation strongly suggests that the borate has trapped the tin preventing full discharge therefore does not allow the formation of the reversible alloy and thus does not facilitate cyclability.

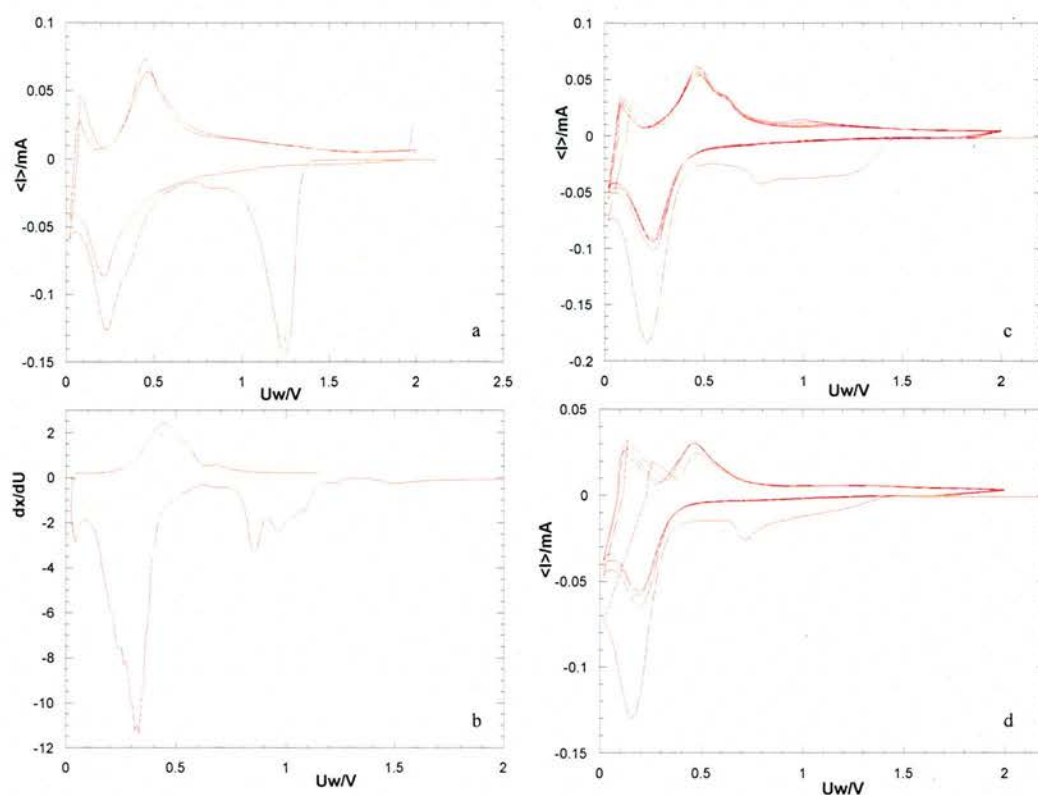


Fig.: 4- 16 a) potentiostatic plot of  $y = 0.03$ , b) derivative plot of  $y = 0.25$  (with a current density of  $0.1 \text{ mA/cm}^2$ ), c) potentiostatic plot of  $y = 0.5$ , d) potentiostatic plot of  $y = 1$  (Scan rate of  $20 \text{ mV/hour}$ ).

$^{31}\text{P}$  NMR was performed on an electrodes made from  $y = 0.1$  and 1 in order to study the phosphate chemistry under discharge to  $0.02 \text{ V}$ . The spectrum of  $y = 0.1$  exhibits a single intense peak at  $8.8 \text{ ppm}$  similar to that observed on reduction of  $\text{SnP}_2\text{O}_7$ . Thus the same dramatic shift in phosphate environment as was previously reported<sup>15</sup> occurs for the borate doped pyrophosphate solid solution. The electrode made from  $y = 1$  has clearly shown the same shift after discharge.

This is exhibited in the inset plot of **Fig.: 4- 17b**.

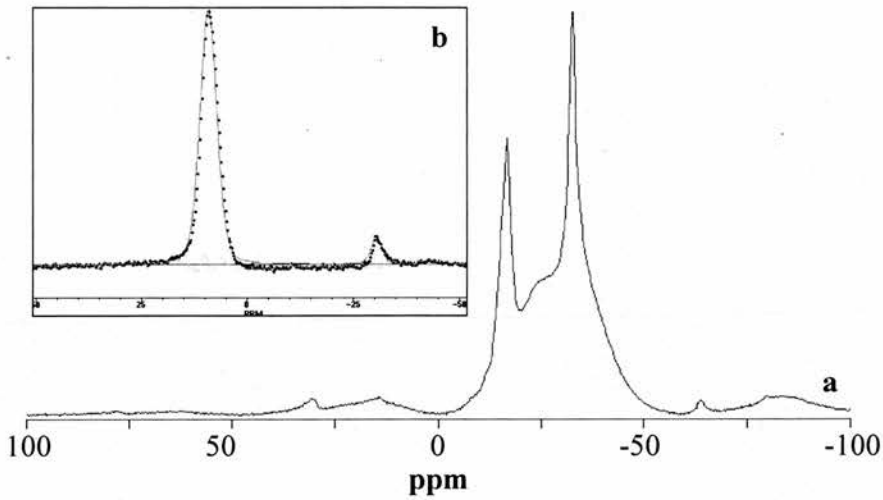


Fig.: 4- 17  $^{31}\text{P}$  DP-MAS-NMR of: (a)  $y = 1$ , (b) (inset)  $y = 1$  discharged at 0.02V  
(chemical shift in ppm).

The  $^{31}\text{P}$  NMR figure of the electrode discharged to 0.02V with  $y = 1$  has indeed indicated that some phosphate behaves as phosphate in  $\text{SnP}_2\text{O}_7$  and some residual does not.  $^{31}\text{P}$  NMR has shown two different peaks at  $\sim 8.8\text{ppm}$  and  $-30\text{ppm}$ . The peak at  $\sim 8.8\text{ppm}$  is more intense than the one at  $-30\text{ppm}$  **Fig.: 4- 17b**. Interestingly the peak at  $-30\text{ppm}$  can be associated with unreduced phosphate in a  $(\text{BO}_{4/2})^-$  environment by comparison of  $^{31}\text{P}$  chemical shift observed for the starting material **Fig.: 4- 17a**.

$^{11}\text{B}$  MAS-NMR was performed on an electrode discharged to 0.02V with  $y = 0.1$  and 2. **Fig.: 4- 18a & b** of starting material with composition of  $y = 0.1$  and electrode from  $y = 0.1$  have shown that the borate environment is also affected. The peaks giving rise to the  $-3.6\text{ppm}$  envelope become much broader with a discernible shoulder at more positive positions around  $0.9\text{ppm}$  for the discharged electrode **Fig.: 4- 18b**. The peak at  $-3.6\text{ppm}$  is assigned to four coordinate boron  $(\text{BO}_{4/2})^-$  as in the starting material  $y = 0.1$  **Fig.: 4- 18a**. The observed shoulder **Fig.: 4- 18b** is presumably related to the formation of non bridging oxygen that generally occurs in alkali borophosphate glass system. Similar behaviour was observed in lithium, potassium, sodium, rubidium and cesium borate glass<sup>23, 24, 25</sup>.

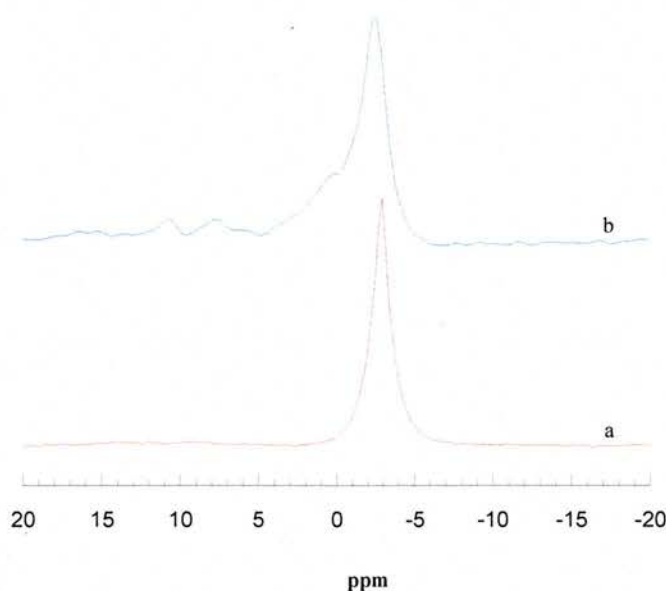


Fig.: 4- 18  $^{11}\text{B}$  NMR of (a)  $y = 0.1$  & (b) electrode from  $y = 0.1$  discharged to 0.02V  
(chemical shift in ppm).

$^{11}\text{B}$  NMR spectrum of the  $y = 2$  starting material and the discharged electrode from  $y = 2$  (to 0.02V) do not reveal new peaks or shifts that indicate boron reduction in the matrix after discharge, however, there was a major change in relative intensity.

Both spectra **Fig.: 4- 19a & b** exhibit two peaks centred at 0.9ppm and between 8 and 28ppm. The peak around the 3-coordinate position between 28 and 8ppm becomes more complex and diminishes in relative intensity, showing that the lithiation favours 4-coordinate boron **Fig.: 4- 19b**. Meanwhile the four coordinate peak at 0.9ppm has considerably increased. This result suggests a conversion of borate species into another borate species on lithium insertion.

*Buckermann et al.*<sup>26</sup>, have reported interconversion of  $\text{BO}_{3/2}$  into  $(\text{BO}_{4/2})^-$  species when inserting alkaline metal. *Stebbins et al.*<sup>17</sup> have also demonstrate by combining  $^{17}\text{O}$  and  $^{11}\text{B}$  NMR that chemical shift for non bridging oxygen bonded to boron vary considerably depending on their environment. This might explain the shift observed in position of the three and four coordinate boron that varies between samples with boron concentration.

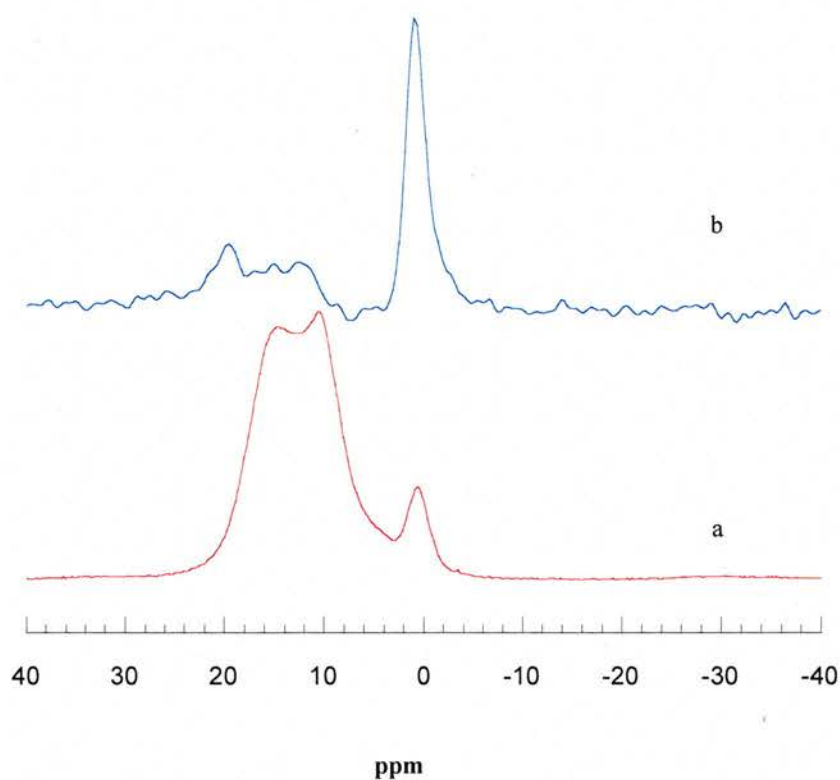


Fig.: 4-  $^{19}\text{B}$  NMR of (a)  $y = 2$  & (b) electrode made from  $y = 2$  and discharged to 0.02V (chemical shift in ppm).

$^{31}\text{P}$  &  $^{11}\text{B}$  DP-MAS-NMR has clearly shown that tin connected to borate species with peaks at 0.9 and -3.6ppm are reducible compared to the other borate, which are difficult to reduce. All the tin connected to the other borate species are trapped and therefore the number of tins available for the alloying and de-alloying process decrease.

#### 4.4. Performance.

As previously discussed,  $\text{SnO}_2:\text{B}_2\text{O}_3$  displays an irreversible capacity of 875mAh/g on the first discharge. From this reasonable value of capacity, just 265mAh/g is reversible. It can be observed up to the first 10 cycles that the capacity has increased to reach 280mAh/g. This suggests that more tin is becoming available via reduction to the alloying process upon these first cycles and consequently enhancing the capacity.

After these 10 cycles the capacity starts to fade slowly with the rate of  $\sim 0.2\%$  capacity per cycle. This means that at the 40<sup>th</sup> cycle the remaining capacity is the same as the initial reversible capacity. At 100 cycles, the loss of capacity is estimated at 40% of the initial capacity.

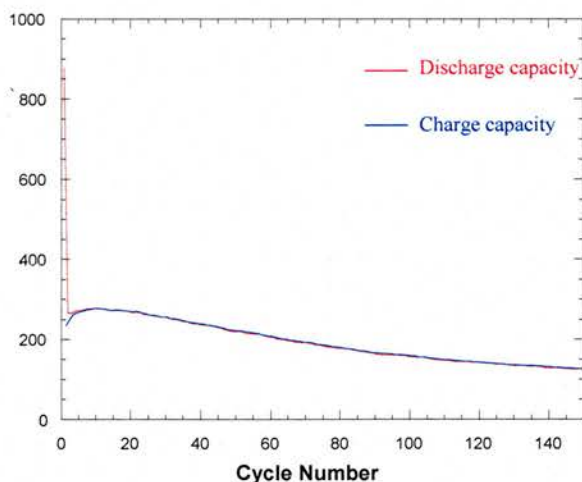


Fig.: 4- 20 Cycle life of  $\text{SnO}_2:\text{B}_2\text{O}_3$

$\text{SnO}_2:\text{B}_2\text{O}_3$  exhibits a reasonable cycling behaviour, however the reversible capacity is too low presumably due to the poor reducibility of the matrix.

**Fig.: 4- 21** shows the cycling profile of material with  $y = 0.1$  and  $0.5$ . It can be deduced from this plot that the reversible capacity decreases with boron content. This observation is not expected considering the molecular weight of the material.

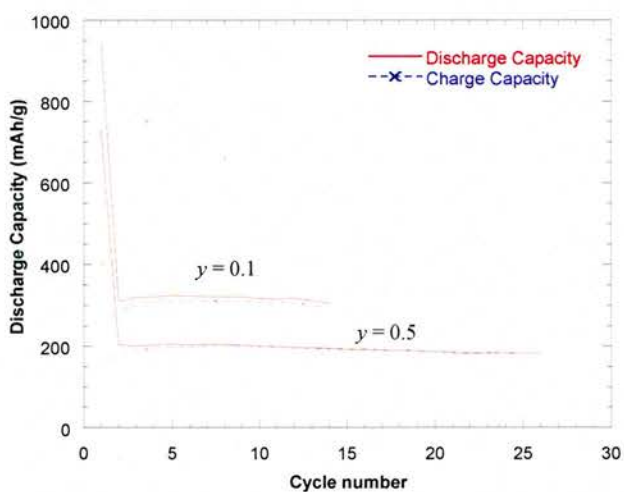


Fig.: 4- 21 Cycle life of material with  $y = 0.1$  and  $0.5$

#### 4.5. Conclusion.

Various techniques were used to investigate the  $(\text{SnO}_2:\text{B}_2\text{O}_3)_{y/2}/(\text{SnP}_2\text{O}_7)_{1-y/2}$  system. It appears clearly that this system displays three different domains going from crystalline solid solution, mixed crystalline and amorphous region to pure amorphous phase. The crystalline solid solution domain shows an isostructural XRD pattern with  $\text{SnP}_2\text{O}_7$  but with a decrease in a cell parameter following Vegard's Law. It has also been illustrated that borate substitution in the solid solution domain does not change the superstructure observed in the case of pure  $\text{SnP}_2\text{O}_7$ . Furthermore, before reaching the completely amorphous, high boron content  $y \geq 1.75$ , it appears that crystalline and amorphous clusters can co-exist in the range of  $0.19 \leq y \leq 1.75$ .

Interestingly, the electrochemistry has enlightened a thermodynamic feature of borophosphate species showing two separate reduction plateaus for phosphate and borate matrices. It also appears that bridging oxygen borate species are more easily reducible than non-bridging oxygen borate species, which leads to a loss of capacity within lithium battery.

From these observations, it is obvious that borate or borophosphate matrices are interesting and complex systems but borate is not really suitable for cyclability in lithium battery.

4.6. References.

- <sup>1</sup>A. Hayashi, M. Nakai, M. Tatsumisago, T. Minami, Y. Himei, Y. Miura, M. Katada, *Journal of Non-Crystalline Solids*, **306**, 227-237 (2002).
- <sup>2</sup>Y. Idota, T. Kubota, A. Matsufuji, Y. Maekawa, T. Miyasaka, *Science* **276**, 1395 (1997).
- <sup>3</sup>Y. Idota, M. Nishima, Y. Miyaki, T. Kubota, T. Miyasaka, *Eur. Pat. Appl.* **651**, 450 (1995).
- <sup>4</sup>I. A. Courtney, W. R. McKinnon, J. R. Dahn, *Journal of the Electrochemical Society*, **146** (1) 59-68 (1999).
- <sup>5</sup>W. Liu, X. Huang, Z. Wang, H. Li, L. Chen, *J. Electrochem. Soc.* **145**, 59 (1998).
- <sup>6</sup>M. Behm, J. T. S. Irvine, *Electrochimica Acta* **47**, 1727-1738 (2002).
- <sup>7</sup>C. H. Huang, O Knop, D. A. Othen, F. W. D. Woodhams, Howie R. A, *Canadian Journal of Chemistry* **53**, 79-91 (1975).
- <sup>8</sup>E. Tillmanns, W. Gebert, *Journal of Solid State Chemistry*, **7**, 69-84 (1973).
- <sup>9</sup>D. M. Poojary, R. B. Borade, F. L. Campbell, A. Clearfield, *Journal of Solid State Chemistry* **112**, (1) 106-112 (1994).
- <sup>10</sup> N. Khosrovani, V. Korthuis, A. W. Sleight, T. Vogt, *Inorg. Chem.* **35**, 485-489 (1996)
- <sup>11</sup>R. K. B. Gover, N. D. Withers, S. Allen, R. L. Withers, J. S. O. Evans, *Journal of Solid State Chemistry* **166**, 42-48 (2002).
- <sup>12</sup>F. Fayon, I. J. King, R. K. Harris, R. K. Gover, J. S. O Evans, D. Massiot, *Chem. Mater.* **15**, 2234 (2003).

- <sup>13</sup>A. J. Dodd, E. R. H. Van Eck, *Chemical Physics Letters* **365**, 313-319 (2002).
- <sup>14</sup>R. E. Youngman, B. G. Aitken, J. E. Dickinson, *Journal of Non-Crystalline Solids*, **263 & 264**, 111-116 (2000).
- <sup>15</sup>P. S. Attidekou, P. A. Connor, P. Wormald, D. P. Tunstall, S. M. Francis, J T. S. Irvine, *Solid State Ionics*, **175**, 185-190 (2004).
- <sup>16</sup>S. Prabhakar, K. J. Rao, C. N. R. Rao *Chem. Phys. Lett.*, **139**, 96 (1987).
- <sup>17</sup>J. F. Stebbins, P. Zhao, S. Kroeker, *Solid State Nuclear Magnetic Resonance* **16**, 9-19 (2000).
- <sup>18</sup>A. J. Dodd, E, R, H, Van Eck, *Chem. Phys. Lett.*, **365**, 313-319 (2002).
- <sup>19</sup>R. K. Brow, D. R. Tallant, *Journal of Non-Crystalline Solids*, **222**, 396-406 (1997).
- <sup>20</sup>R. K. Brow, *Journal of Non-Crystalline Solids*, **194**, 267-273 (1996).
- <sup>21</sup>J. F. Stebbins ,P. Zhao, S. Kroeker, *Solid State Nuclear Magnetic Resonance*, **16**, 9-19 (2000).
- <sup>22</sup>J. Y. Lee, Y. Xiao, Z. Liu, *Solid State Ionics*, **133**, 25-35 (2000).
- <sup>23</sup>P. J. Bray, *Journal of Non-Crystalline Solids*, **73** 19 (1985).
- <sup>24</sup>P. J. Bray, J. G. O'Keefe, *Phys. Chem. Glasses*, **4**, 37(1963).
- <sup>25</sup>A. Hayashi, M. Nakai, M. Tatsumisago, T. Minami, Y. Himei, Y. Miura, M. Katada, *Journal of Non-Crystalline Solids*, **306** 227-237 (2002).
- <sup>26</sup>W. A. Buckermann, W. Muller-Warmuth, C. Mundus, *Journal of Non-Crystalline Solids*, **208**, 217-227 (1996).

## 5. Titanium doped tin pyrophosphate system.

### 5.1. $\text{Sn}_{1-x}\text{Ti}_y\text{P}_2\text{O}_7$ .

This chapter will deal with the structural and electrochemical characterisation of the  $\text{Sn}_{1-y}\text{Ti}_y\text{P}_2\text{O}_7$  system with  $0 \leq y \leq 1$ . The main purpose is to evaluate the role the isovalent titanium cation within  $\text{SnP}_2\text{O}_7$  system already investigated (see Chapter 3) in order to try to improve the capacity of electrodes made of those materials. A series of tin/titanium pyrophosphates were synthesised, characterised and tested as a lithium battery negative electrodes.

#### 5.1.1. Powder X-ray Diffraction: (XRD).

The X-ray powder diffraction patterns of some members of the  $\text{Sn}_{1-y}\text{Ti}_y\text{P}_2\text{O}_7$  series with  $0 \leq y \leq 1$  are displayed in **Fig.: 5- 1**. All are isostructural with  $\text{SnP}_2\text{O}_7$ . Similar to  $\text{SnP}_2\text{O}_7$  the XRD pattern of  $\text{TiP}_2\text{O}_7$  **Fig.: 5- 2** contains peaks that can not be indexed in the space group  $P a \bar{3}$ , however, unlike  $\text{SnP}_2\text{O}_7$ , these are sharp. Presumably these are related to the superstructure described<sup>1, 2</sup> in the case of  $\text{SnP}_2\text{O}_7$ . The half width of the non indexed weak peaks are about the same as those of the primitive indexed peaks in the XRD patterns of  $\text{SnP}_2\text{O}_7$  and  $\text{TiP}_2\text{O}_7$ <sup>3</sup>. These observations are presumably related to the ordering as with the  $\text{TiP}_2\text{O}_7$  exhibiting long range  $3 \times 3 \times 3$  order, unlike  $\text{SnP}_2\text{O}_7$ , which only exhibits short range  $3 \times 3 \times 3$  order.

The cell parameters were refined using STOE software and the results are displayed in **Table: 5- 1** and **Fig.: 5- 3**. The primitive 1x1x1 cell is used as the  $\text{SnP}_2\text{O}_7$  only exhibits the 3x3x3 superstructure as a short range ordering.

This figure shows two regions with different slopes. The variation is linear with  $y$  in those two regions and the correlation within the two regions leads to a crossover point at  $y = 0.4$  and a cell parameter of 7.935 Å. A linear variation of the cell parameter was expected, however, a crossover was observed at  $y = 0.4$  leading to two regions with two different linear variations of the cell parameter.

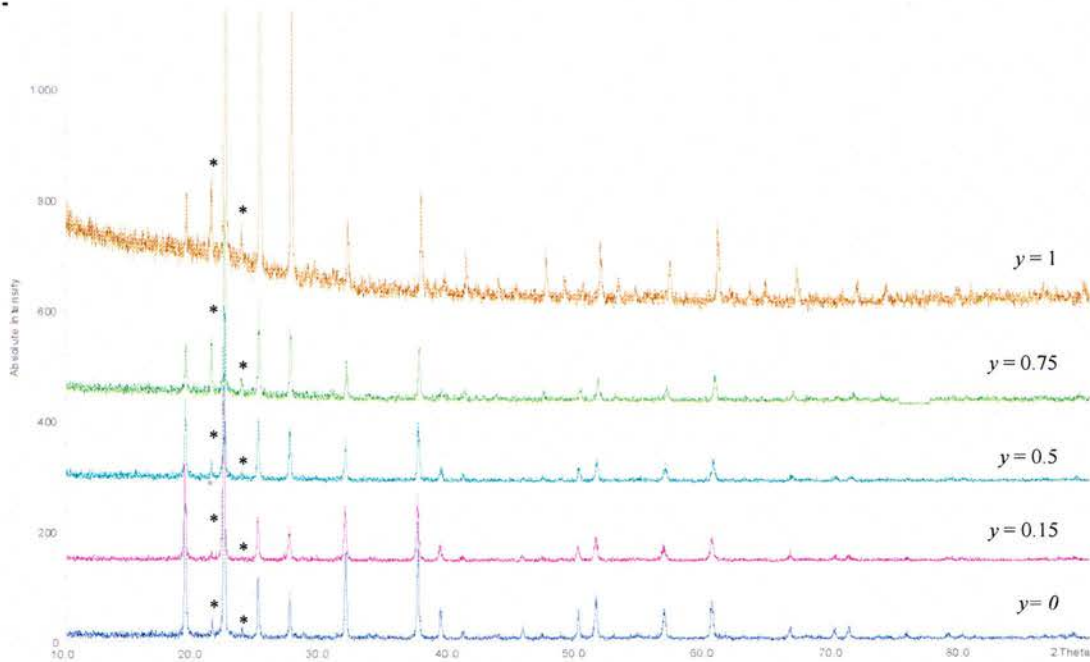


Fig.: 5- 1 XRD pattern of  $\text{Sn}_{1-y}\text{Ti}_y\text{P}_2\text{O}_7$  system with  $y = 0, 0.15, 0.5, 0.75$  and 1 (\* represents mounting grease peaks)

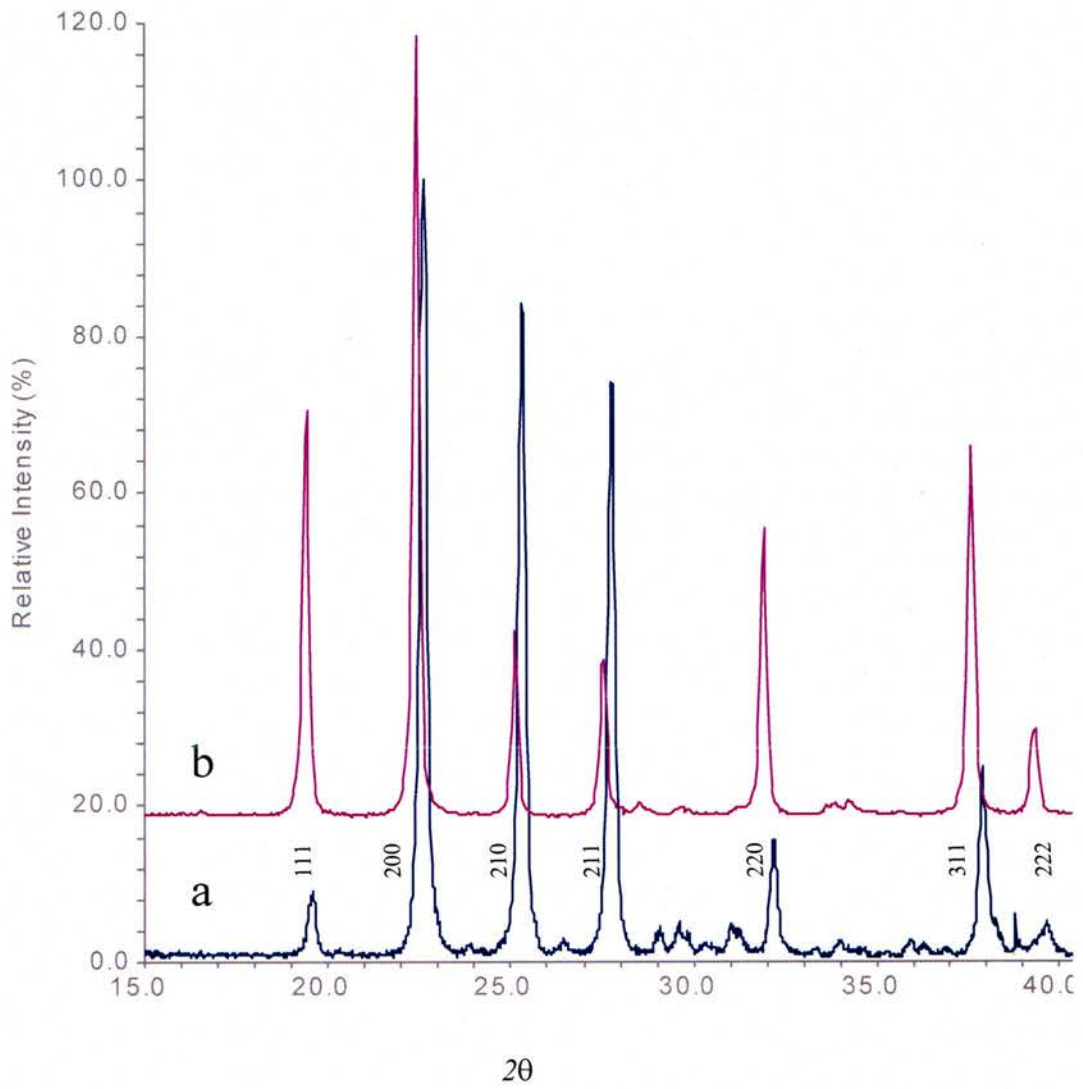
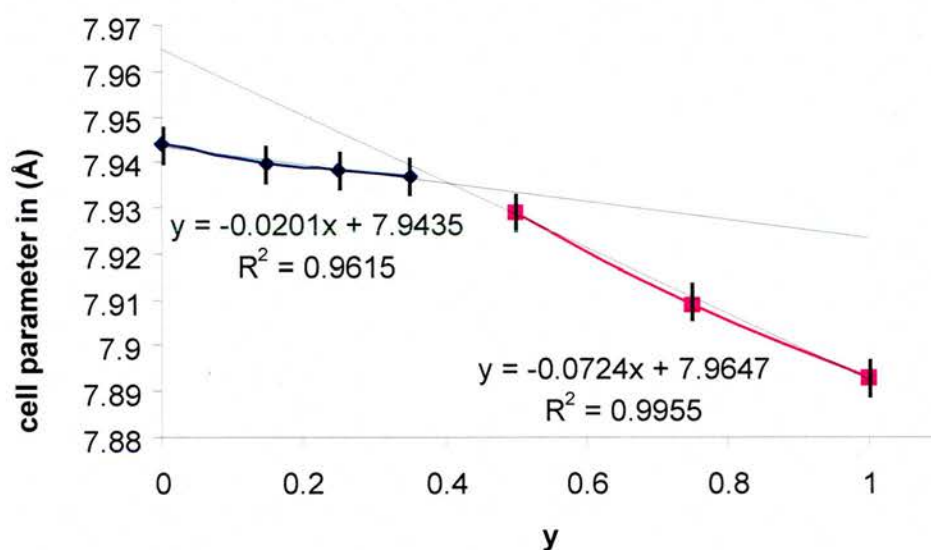


Fig.: 5- 2 XRD pattern of: a)  $\text{TiP}_2\text{O}_7$  b)  $\text{SnP}_2\text{O}_7$ .

$y$	Cell parameter (Å)
0	7.944
0.15	7.9398
0.25	7.9382
0.35	7.937
0.5	7.929
0.75	7.909
1	7.893

Table: 5- 1 Cell parameter variation with composition ( $x$ ) in  $\text{Sn}_{1-x}\text{Ti}_x\text{P}_2\text{O}_7$  systemFig.: 5- 3 Evolution of the cell parameter with titanium content,  $y$ .

This behaviour of unit cell parameter indicates competing solid solution mechanisms. When the tin atom in  $\text{SnP}_2\text{O}_7$  is replaced by titanium, this induces a decrease in observed cell parameter. This discontinuity in Vegard's slope seems to indicate some form of symmetry or phase change.

## 5.1.2. IR.

IR spectra collected on samples  $y = 0, 0.15, 0.35, 0.5, 0.75$  and  $1$  are displayed in **Fig.: 5- 4**.

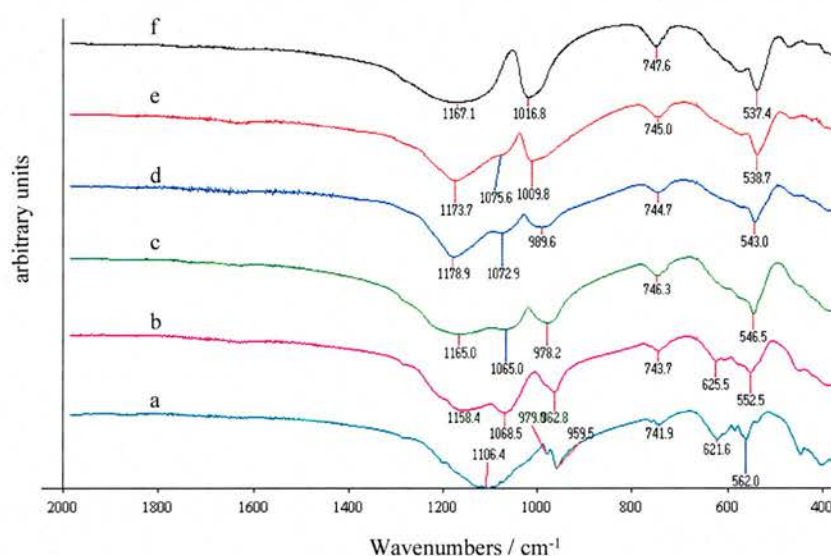


Fig.: 5- 4 IR spectra of  $\text{Sn}_{1-y}\text{Ti}_y\text{P}_2\text{O}_7$  system with (a)  $y = 1$ , (b)  $y = 0.75$ , (c)  $y = 0.5$ , (d)  $y = 0.35$ , (e)  $y = 0.15$  and (f)  $y = 0$ .

The  $\text{SnP}_2\text{O}_7$  spectrum was interpreted in Chapter 3 (IR section). Four main bands dominate the spectrum. A strong broad band located in the high frequency region i.e.  $1167\text{cm}^{-1}$  was assigned to the asymmetric vibration mode  $\nu_{\text{as}}(\text{PO}_3)$ . The following intense band at  $1016\text{cm}^{-1}$  was assigned to the symmetric vibration mode  $\nu_{\text{s}}(\text{PO}_3)$ . In the lower frequency region a weaker and narrow band at  $747\text{cm}^{-1}$  has been attributed to the vibration mode  $\nu_{\text{s}}$  of the bridging (P-O-P) and the vibration mode of M-O at  $537\text{cm}^{-1}$  (with  $M = \text{Ti, Sn}$  or mix  $\text{Ti/Sn}$ ).

The  $\text{TiP}_2\text{O}_7$  IR spectrum **Fig.: 5- 4a** exhibits a broad band at  $1106\text{cm}^{-1}$  that is assigned<sup>4</sup> by analogy to  $\text{SnP}_2\text{O}_7$  to the asymmetric vibration mode  $\nu_{\text{as}}(\text{PO}_3)$ . At  $979\text{cm}^{-1}$ , a weak band can be seen related to the symmetric vibration mode  $\nu_{\text{s}}(\text{PO}_3)$ . The band at  $959\text{cm}^{-1}$  is attributed to the  $\nu_{\text{as}}$  vibration mode of the bridging (P-O-P) and the vibration mode  $\nu_{\text{s}}$  of the bridging (P-O-P) is observed at  $747\text{cm}^{-1}$ .

On substitution, a growing shoulder is noticeable around  $1070\text{cm}^{-1}$ . This increasing peak indicates segregation of the  $\nu_{\text{as}}(\text{PO}_3)$  vibration mode. This observation can be explained by the difference in vibration energy of the  $\nu_{\text{as}}(\text{PO}_3)$  as the  $\text{PO}_3$  in the structure is located in a tetrahedra that is linked to several Ti or Sn octahedra. Therefore on substitution, the bond strength must be varying with  $y$ . The band assigned to  $\nu_{\text{s}}(\text{PO}_3)$  shows splitting for titanium pyrophosphate. This observation is probably due to the existence of different P-O-P bonds already reported<sup>4</sup>.

However a shift can be observed in the band representing the  $\nu_{\text{s}}(\text{P-O-P})$  vibration. **Fig.: 5- 5** shows the shift of the  $\nu_{\text{s}}(\text{P-O-P})$  peak versus composition. The change in (P-O-P) vibration energy with titanium content correlates with the variation observed in cell parameter **Fig.: 5- 3**. This presumably suggests that the bond strengths of the (P-O-P) in  $\text{TiP}_2\text{O}_7$  are weaker compared to  $\text{SnP}_2\text{O}_7$  and the anomalous behaviour related to the wavenumbers indicates a variation in the bond strengths.

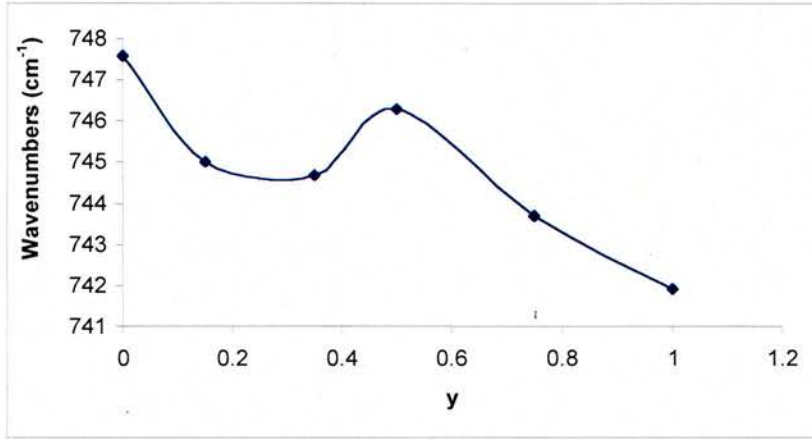


Fig.: 5- 5 Variation of the  $\nu_s$  (P-O-P) vibration energy with composition.

The metal-oxygen vibration energy is seen between 600 and 500 $\text{cm}^{-1}$  and shows a smooth parabolic variation with composition **Fig.: 5- 6**. This figure suggests that Ti-O bonds are stronger than Sn-O as the observed  $\nu_{(\text{Ti-O})}$  is greater than  $\nu_{(\text{Sn-O})}$ .

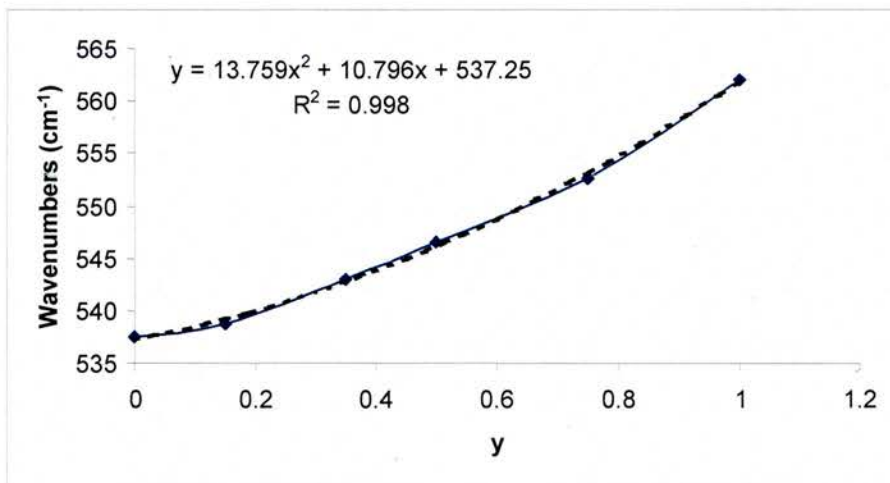


Fig.: 5- 6 Variation of the  $\nu(\text{M-O})$  vibration energy with composition.

## 5.2. Electron Microscopy Study.

### 5.2.1. Selected Area Electron Microscopy (SAED).

SAED micrographs of samples with  $y = 0.5$  and 1 **Fig.: 5- 7 & Fig.: 5- 8** show the same superstructure as  $\text{SnP}_2\text{O}_7$  ( $y = 0$ ) hence suggest the  $3 \times 3 \times 3$  superstructure across the series of samples investigated

For composition  $y = 0.5$ , the specimen was viewed down the  $[\bar{1} \bar{1} 1]$  zone axis and the measurements reveal d-spacing of  $16.9 \text{ \AA}$  for the  $d_{011}$  reflection and  $16.3 \text{ \AA}$  for the  $d_{101}$  reflection.

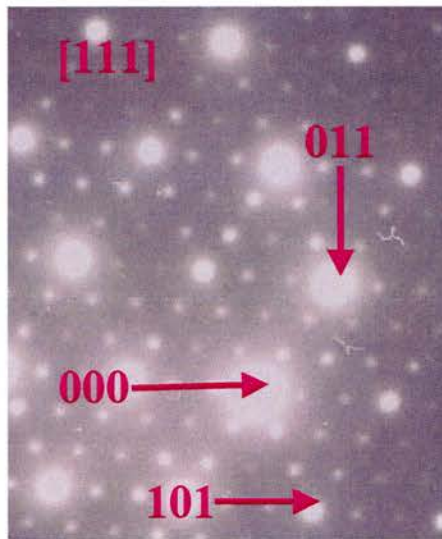


Fig.: 5- 7 SAED micrograph of specimen  $y = 0.5$  ( $\text{Sn}_{0.5}\text{Ti}_{0.5}\text{P}_2\text{O}_7$ ) corresponding to a view down the  $[\bar{1} \bar{1} 1]$  zone axis.

For composition  $y = 1$ , the specimen was viewed down the  $[0 \bar{1} 1]$  zone axis and the reflections obtained give  $22.94\text{\AA}$  for the  $d_{100}$  and  $16.38\text{\AA}$  for the  $d_{011}$ . All the d-spacing are in good agreement with our XRD results. These SAED micrograph have reinforced the presence of superstructure over the complete range of composition from  $y = 0$  to 1.

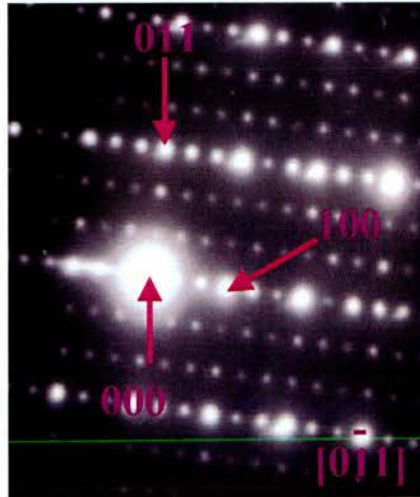


Fig.: 5- 8 SAED micrograph of specimen  $y = 1$  ( $\text{TiP}_2\text{O}_7$ ) corresponding to a view down the  $[0 \bar{1} 1]$  zone axis.

### 5.2.2. High Resolution Transmission Electron Microscopy (HRTEM).

HRTEM images have confirmed the superstructure packing across the entire range of composition of  $\text{Sn}_{1-y}\text{Ti}_y\text{P}_2\text{O}_7$  material. The measured d-spacings on the HRTEM images correlate with those of XRD indexing.

For composition  $y = 0.5$ , the specimen was viewed down the  $[\bar{1}\bar{1}1]$  direction and the inter-fringe distance gives d-spacing of  $16.25\text{\AA}$  which corresponds to  $d_{101}$  reflection **Fig.: 5- 9**. Most importantly HRTEM image has revealed homogeneous reflection distribution with no nanodomains observed in the micrograph.

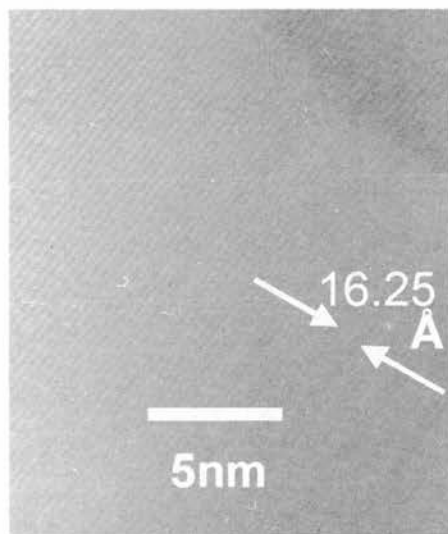
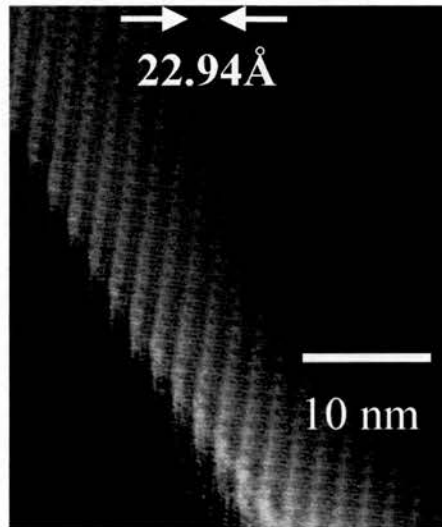


Fig.: 5- 9 HRTEM of specimen  $y = 0.5$ , viewed down the  $[1\ 1\ 1]$  direction

For composition  $y = 1$ , the specimen was viewed down the  $[0 \bar{1} 1]$  direction and the measured distance of  $22.94 \text{ \AA}$  corresponds to  $d_{100}$  reflection **Fig.: 5- 10**. Once again no evidence of nanodomains can be observed on the images.



**Fig.: 5- 10** HRTEM of specimen  $y = 1$ , viewed down the  $[0 \bar{1} 1]$  direction

The absence of nanodomains for  $y = 0.5$  and  $y = 1$  correlates with the change in Vegard's slope observed in **Fig.: 5- 3** and the variation in P-O-P wavenumber in **Fig.: 5- 5**. It therefore seems that the change occurring at  $y = 0.4$  relates no loss of full long range  $3 \times 3 \times 3$  with the formation of only short range domains of  $3 \times 3 \times 3$  order.

### 5.3. $^{31}\text{P}$ NMR results and discussion.

$^{31}\text{P}$  single pulse MAS NMR was used on the  $\text{TiP}_2\text{O}_7$ . The expanded spectrum **Fig.: 5- 11** shows several lines between  $-35$  to  $60\text{ppm}$  range with their related spinning side bands (the spinning sidebands can not be seen in this figure). These different lines can be associated with the presence of several crystallographic sites for P atoms within the unit cell.

This has been reported by Sanz et *al.*<sup>1</sup>. They have resolved the structure in a  $3\times 3\times 3$  cubic unit cell and have suggested that the lines observed in the NMR spectrum are mainly given by the P-O-P angle.

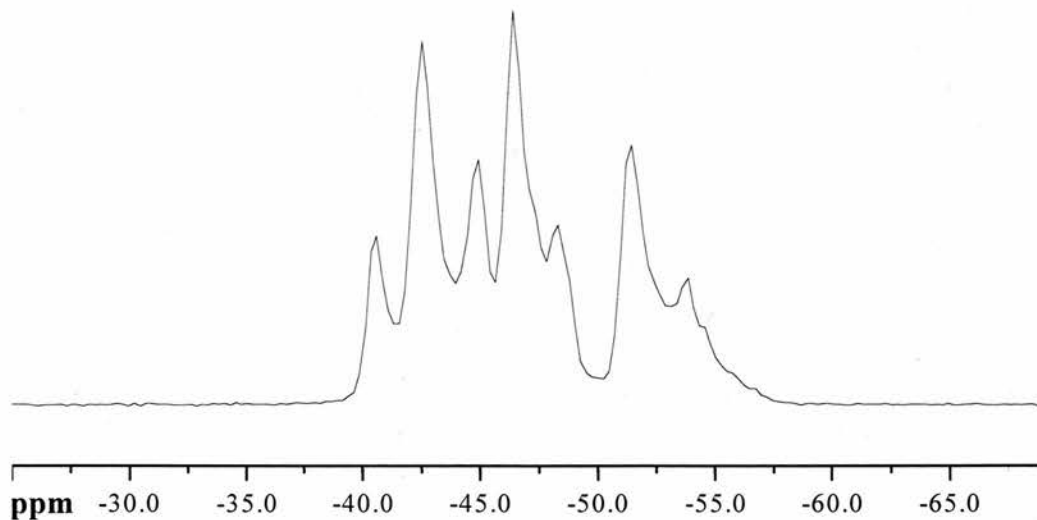


Fig.: 5- 11  $^{31}\text{P}$  NMR expanded spectrum of  $\text{TiP}_2\text{O}_7$ .

This is a local displacement of the  $\text{PO}_4^{3-}$  tetrahedra, which is in good agreement with our result.

XRD, SAED and HRTEM and NMR have confirmed that  $\text{Sn}_{1-y}\text{Ti}_y\text{P}_2\text{O}_7$  system with  $0 \leq y \leq 1$  has the same basic structure except the shrinkage in the cell parameter with composition and the presence of nanodomains rather than long range  $3 \times 3 \times 3$  structure at higher tin content. The loss of long range order might be related to the size of cation.

#### 5.4. Electrochemical characterisation.

Galvanostatic, potentiostatic and SPECS techniques will be used to investigate the electrochemical reactions that occur for these materials. However, in order to obtain the complete picture of the electrochemistry, some other characterisation techniques, as described in *Chapter 2* will be also used to support the suggested reactions.

The electrochemistry of composition  $y = 0$  was fully investigated and described in *Chapter 3*.

##### 5.4.1. $\text{TiP}_2\text{O}_7$ ( $y = 1$ ).

Cells were made from  $y = 1$  ( $\text{TiP}_2\text{O}_7$ ) composition and tested in galvanostatic and potentiostatic modes as previously described. The SPECS technique was used in order to test the battery at equilibrium and to describe with accuracy the reactions occurring in the voltage window of 0 to 3.5V.

##### 5.4.1.1. Galvanostatic and Potentiostatic of $\text{TiP}_2\text{O}_7$ .

The galvanostatic and potentiostatic plots for  $\text{TiP}_2\text{O}_7$  are shown in **Fig.: 5- 12a & b**.

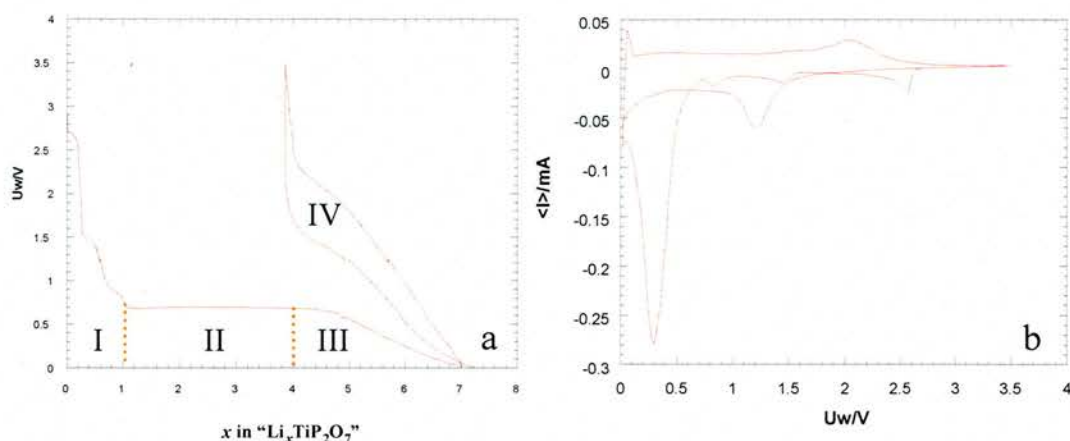


Fig.: 5- 12 (a) Galvanostatic plot of  $y = 1$  (with a current density  $0.1mA/s^2$ ) and (b) potentiostatic plot of  $y = 1$  (with a scan rate of  $20mV/h$ ).

From **Fig.: 5- 12b** it is easy to observe the reaction potential of the material. The potentiostatic plot exhibits peak positions around 2.6, 1.5, 0.8 and 0.5V on the first discharge. The galvanostatic plot **Fig.: 5- 12a**, has also shown these irreversible and the reversible process of the material in form of plateaus at different potential and drops of potential that correspond to the transformations occurring on subsequent discharge and charge. For clarity, the first discharge curve is split into 3 regions in addition to the cycling process that is called region IV. There is a plateau around 2.6V followed by a drop to around 1.5V where another plateau can be observed. The voltage drops again from 1.5V to 0.8V where is located another small plateau. These three plateaus are called region I. At 0.6V, region II, a large plateau can be seen before the potential decreases gradually to 0V in region III. These 3 plateaus indicate that at least 3 biphasic regions and

hence phases are formed on insertion. On charge, in region IV, the galvanostatic plot displays a plateau around 2V coupled to 1.5V on discharge.

In region I, the plateaus observed at 2.6 and 1.5V are expected to be related to titanium reduction<sup>10</sup>. There is a two step reduction of the titanium from  $\text{Ti}^{\text{IV}+}$  to  $\text{Ti}^{\text{III}+}$  that can be seen as a formation of polymorphs that have different reduction potential. The plateau around 0.8V must be in part due to carbon but could also be titanium reduction based.

Region II, accommodates 3 lithium before the potential drops down to 0V inserting another 3 lithium in region III. Region IV shows Li uptake/extraction capacity, which accounts for 3 lithium.

Assuming analogy to  $\text{SnP}_2\text{O}_7$  in region II, the lithium insertion would lead to the formation of irreversible lithiated pyrophosphate  $\text{Li}_4\text{P}_2\text{O}_7$  and titanium metal. The formation of titanium metal in the system would be surprising as it is not observed for  $\text{TiO}_2$ . It was reported<sup>5</sup> for transition metal compounds ( $\text{MX}_m$  with  $X = \text{O}, \text{F}, \text{S}, \text{N}$ ) such as  $\text{TiF}_3$ ,  $\text{VF}_3$ ,  $\text{FeF}_3$ ,  $\text{RuO}_2$ ,  $\text{CuO}$ , etc, that their uptake of lithium may process through multiple step reactions leading to a formation of nanocomposite metal M in addition to an amorphous matrix  $\text{LiX}_m$  but not for  $\text{TiO}_2$ . This may be plausible for  $\text{TiP}_2\text{O}_7$ , however the potential of 0.5V seems much too high for reduction to  $\text{Ti}^0$  at this stage.

An alternative in this region II is the titanium based reduction from  $\text{Ti}^{\text{III}+}$  to  $\text{Ti}^{\text{II}+}$  in addition to the reduction of the phosphate matrix from  $\text{P}^{\text{V}+}$  leading to  $\text{P}^{\text{IV}+}$

phosphate species. Those two reductions correlate with the end of region II that shows total 4 lithium inserted. With  $\text{SnP}_2\text{O}_7$  the phosphate reduction was seen around 0.35V, which should be in region III.

In order to help to understand the reaction that occurs at the 0.6V plateau, a cell from  $\text{TiP}_2\text{O}_7$  was made and cycled galvanostatically to various numbers of lithium inserted, as depicted in **Fig.: 5- 13**. The first observation is that  $\text{TiP}_2\text{O}_7$  cycles reversibly throughout the whole plateau, with increasing capacity with extent of discharge. The cycling potential is similar to those observed for lithium titanate reported<sup>6, 12</sup> with capacity between 1.5 and 2V for the  $\text{Ti}^{\text{IV}+}/\text{Ti}^{\text{III}+}$  redox couple. However  $\text{TiP}_2\text{O}_7$  discharged down to 0.6V with 4 lithium (“ $\text{Li}_4\text{TiP}_2\text{O}_7$ ”) uptake **Fig.: 5- 13b** has shown a cycling capacity with 1.7 lithium (i.e. just less than 2), which does not match the capacity of the couple  $\text{Ti}^{\text{IV}+}/\text{Ti}^{\text{III}+}$ . This supports the reduction suggested earlier from  $\text{Ti}^{\text{III}+}$  to  $\text{Ti}^{\text{II}+}$  along with the irreversible reduction of  $\text{P}^{\text{V}+}$  to  $\text{P}^{\text{IV}+}$ . This suggests that the transformation occurring may be going from “ $\text{LiTi}^{\text{III}+}\text{P}_2\text{O}_7$ ” formed in region I to “ $\text{Li}_4\text{Ti}^{\text{II}+}\text{P}_2\text{O}_7$ ” similar to  $\text{Li}_6\text{P}_2\text{O}_7$  formed in the tin system. Therefore the lithiated titanium oxide formed upon discharge cycles from  $\text{Ti}^{\text{II}+}$  to  $\text{Ti}^{\text{IV}+}$  in an amorphous reduced lithiated phosphate matrix by analogy to  $\text{SnP}_2\text{O}_7$ .

The plateau at 0.6V therefore seems to be related to the reduction of titanium from  $\text{Ti}^{\text{III}+}$  to  $\text{Ti}^{\text{II}+}$  in addition to the phosphate reduction from  $\text{P}^{\text{V}+}$  to  $\text{P}^{\text{IV}+}$  as both match the capacity in region II.

More investigation is required to elucidate the mechanism occurring at the 0.6V plateau especially, such as XRD, NMR.

Region III describes the first discharge region from this plateau at 0.6V down to 0V. This region accommodates 3 lithium that might be related to the formation of a polymeric layer “SEI”<sup>7</sup>, which is a reversible pseudo-capacitive process reported<sup>21</sup> for transition metal oxides or may also include the reduction of the phosphate matrix from  $P^{V+}$  to  $P^{IV+}$  phosphate species depending on the chemistry of region II.

The mechanism in region IV with only 3 lithium uptake/extraction should not be associated with the phosphate reduction as this is an irreversible process. The cycling capacity might have a contribution from the SEI and the titanium redox mechanism.

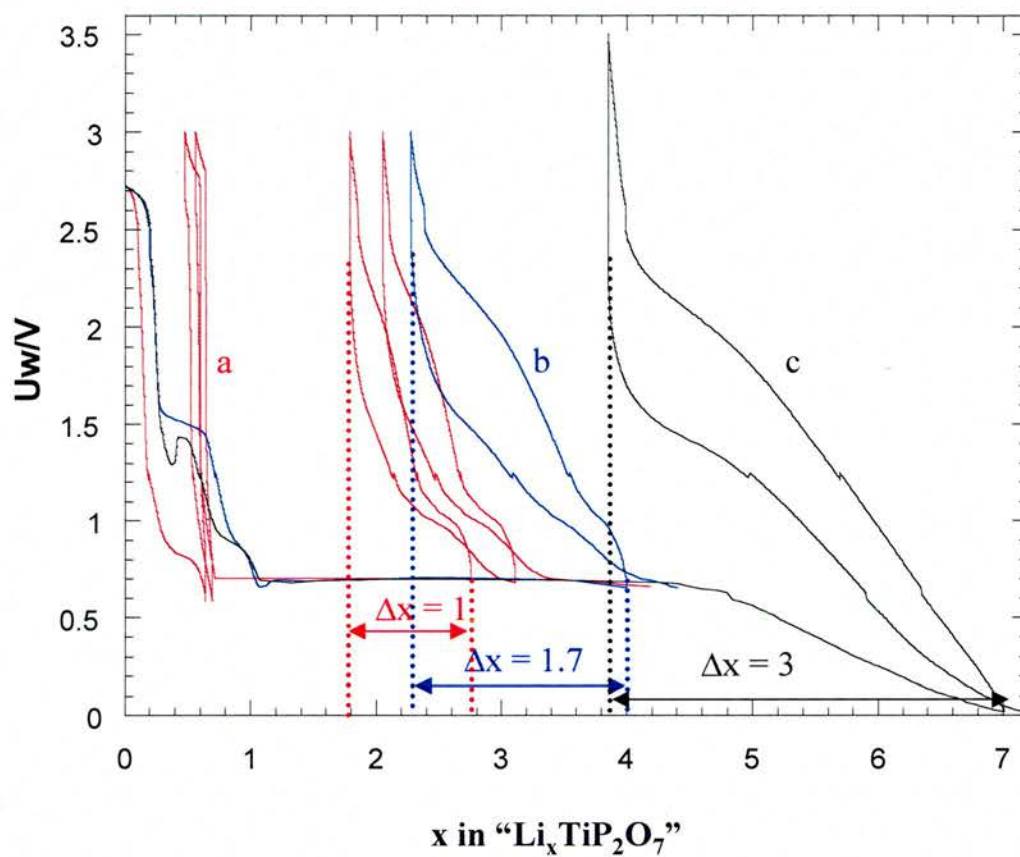


Fig.: 5- 13 Cycling behaviour of  $\text{TiP}_2\text{O}_7$  collected galvanostatically at various rates (a) current density  $0.2\text{mA/s}^2$ , (b) current density  $0.1\text{mA/s}^2$ , (c) current density  $0.05\text{mA/s}^2$ .

## 5.4.2 In-situ XRD.

In-situ XRD allows phase characterisation upon discharge and charge. The phase changes occurring during the lithium insertion were characterised using in-situ XRD after discharging and charging up the same battery made from  $\text{TiP}_2\text{O}_7$  in galvanostatic mode with a very low current density of  $0.0025\text{mA/cm}^2$  in order to remain close to equilibrium. The cell was discharged consecutively to  $x = 0.55$ , 0.87, 1.09, 2, 4, 5.5, and 7 lithium inserted. The same cell was charged up with two and then three lithium extracted respectively before being redischarged with one and two lithium inserted respectively. The XRD patterns are shown in **Fig.: 5-**

14.

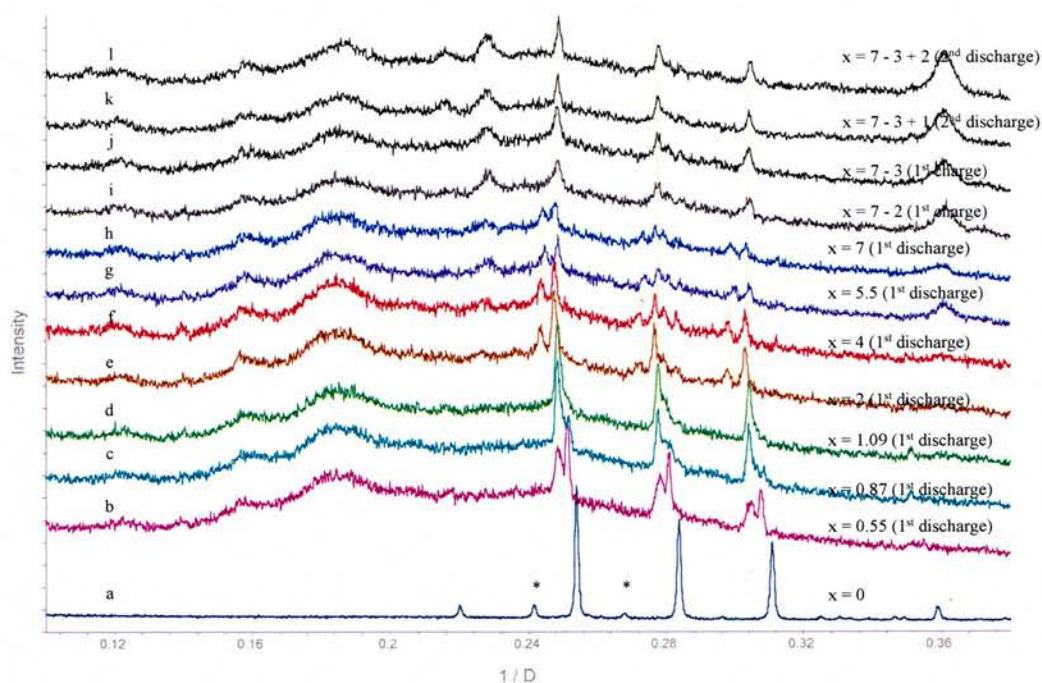


Fig.: 5- 14 XRD patterns of  $\text{TiP}_2\text{O}_7$  with different number of lithium inserted (a) ex-situ XRD pattern  $\text{TiP}_2\text{O}_7$ , From (b) to (l) are in-situ XRD pattern with  $x$  (number of lithium inserted or extracted); (\* stands for mounting grease peaks)

At  $x = 0$  lithium inserted (a), the data was collected ex-situ on a powder sample. Due to the design of the in-situ cell, there is a significant shift in position between the in-situ and ex-situ data collection methods.

At  $x = 0.55$  lithium inserted (b), the in situ XRD pattern has displayed doubling of peaks. This observation shows the interconversion of  $\text{TiP}_2\text{O}_7$  (A) to  $\text{Li}_x\text{TiP}_2\text{O}_7$  (B) that can be described as a biphasic transformation. The doubling of peaks has emphasised the coexistence of biphasic domain A-B where phase B has related structure to phase A and grows progressively on insertion.

At  $x = 0.87$  (c), it can be seen in the XRD pattern a considerable growth of phase (B) with a decrease of phase (A) that appears as a shoulder.

At  $x = 1.09$  (d), the shoulder phase (A) has disappeared and the pattern displays only phase (B).

From  $x = 2$  to  $x = 7$  (e, f, g & h) all the patterns look similar. It seems to be observed again that there is a doubling of peaks that are consistent with phase (B) and another phase (C), which can be described as a biphasic transformation. This time however, although some similarity exists in form of pattern between phase (B) and (C), they are quite different and can not be described as clear homologues. Phase (B) and (C) are seen to decrease in intensity that suggest an amorphisation

during lithium insertion. Additionally, there is a growth of fairly broad peaks at 0.224 and 0.36 1/D respectively that implies another phase D.

The spectra in **Fig.: 5- 14** (i, j, k & l) all seem to be similar and display no phase (C) peaks. There is also an increase in peak intensities for phase (B) and phase (D) but the peaks related to phase (D) are still broad. The increase in intensity of phase (B) upon subsequent charge and discharge may be related to a recrystallisation, which is not expected.

The cell parameters relative to those phases were refined in the P a -3 and summarised in

**Table: 5- 2** using the STOE software. Due to the shifting of the peak positions with the cell, a zero point correction was applied to each pattern. The refinement was performed using the same space group as  $\text{TiP}_2\text{O}_7$  and was carried out until 1 lithium inserted as this is where the  $\text{TiP}_2\text{O}_7$  based model no longer fits.

	Cell parameter a in the superstructure (Å)		Cell parameter a in the simple cubic (Å)	
$\text{TiP}_2\text{O}_7$	23.679 (S)		7.893 (S)	
$\text{Li}_{0.55}\text{TiP}_2\text{O}_7$	23.83 (S)	23.68 (S)	7.944 (S)	7.893 (S)
$\text{Li}_{0.87}\text{TiP}_2\text{O}_7$	24.14 (S)	23.83 (W)	8.048 (S)	7.944 (W)
$\text{LiTiP}_2\text{O}_7$	24.14 (S)		8.048 (S)	

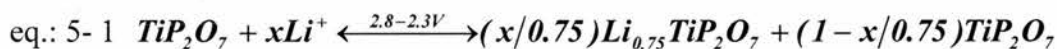
Table: 5- 2 Refined cell parameter a of different phases electrochemically lithiated of  $\text{Li}_x\text{TiP}_2\text{O}_7$  collected from in-situ XRD (S = strong & W = weak).

These results match those reported<sup>11</sup> in this region, and the cell parameter has increased as expected.

### 5.4.3. SPECS.

From the SPECS experiment **Fig.: 5- 15**, the chronoamperogram reveals anomalous behaviour in the current curve, which does not reach zero in the region of  $0 \leq x \leq 0.75$  lithium inserted. This is typical of a biphasic region<sup>8, 9</sup> behaviour. This was also emphasised in the in-situ XRD experiment for  $x = 0.55$  that exhibits a doubling of peaks. Under the equilibrium condition as experienced using the SPECS technique,  $\text{TiP}_2\text{O}_7$  is reduced to  $\text{Li}_{0.75}\text{TiP}_2\text{O}_7$  in the same biphasic manner as presented below in **eq.: 5- 1** by *Yasushi et al*<sup>10</sup>.

The overall reaction that occurs in the SPECS experiment **Fig.: 5- 15** is depicted in **eq.: 5- 1** and is seen as partial reduction of the titanium.



$$0 < x < 0.75$$

For the same plateau, the galvanostatic experiment has shown a small number of lithium inserted **Fig.: 5- 13a, b & c** and this is presumably depending on the current rate. This observation suggests a kinetic dependency of the reaction that occurs in the system.

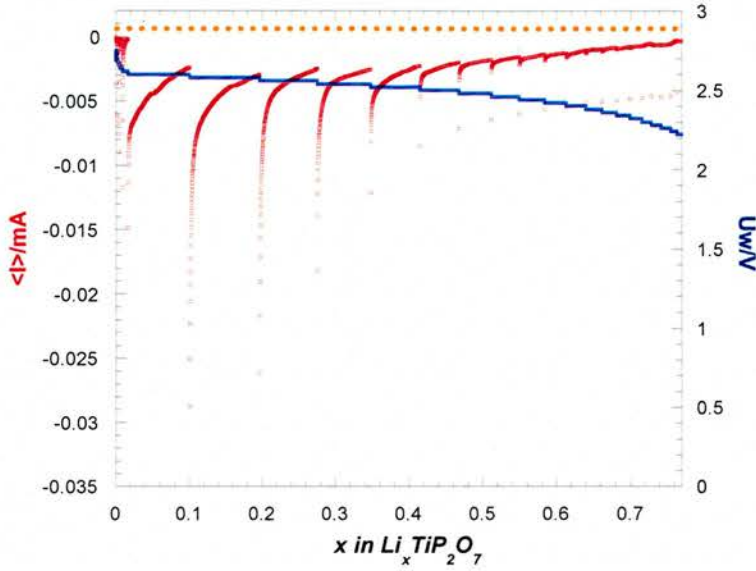
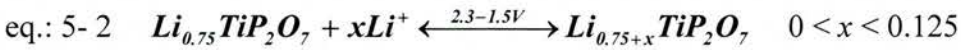


Fig.: 5- 15 Anomalous behaviour of the current (in red) from SPECS experiment between 2.3 and 2.8V for  $\text{TiP}_2\text{O}_7$  upon discharge ( $\pm 20\text{mV}$  every 15 hours).

**Fig.: 5- 16** shows the SPECS data for the region down to 1.5V where the number of lithium inserted is between  $0.75 < x < 0.875$ . In this voltage region, which is not a plateau, the chronoamperogram reaches zero, which suggests a typical solid solution region<sup>11</sup> as a symmetrical behaviour of the current relaxation can be seen. This indicates a single phase region where lithium diffusion is controlling the kinetics of the reaction throughout the system. The equation describing the reaction is stoichiometrically depicted in **eq.: 5- 2**.



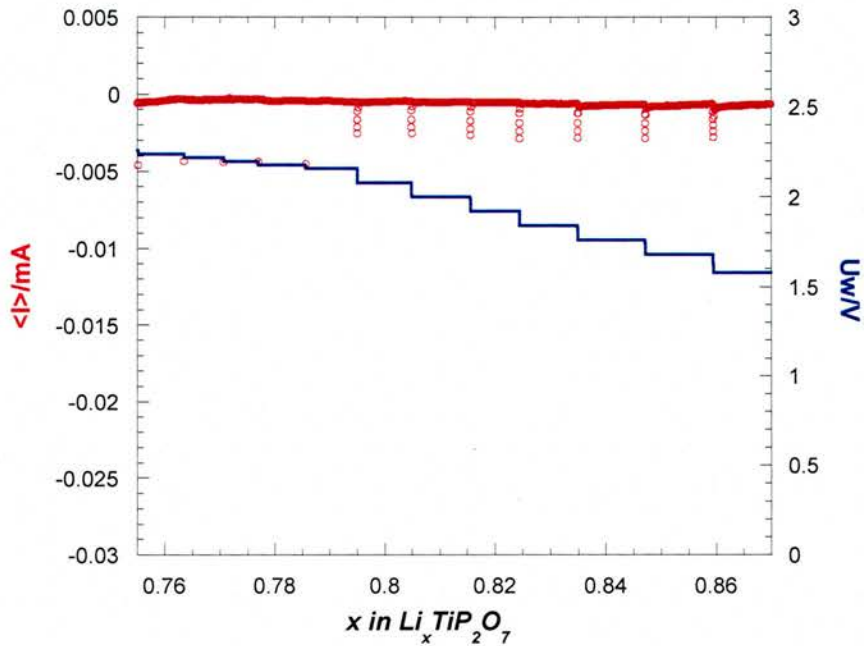


Fig.: 5- 16 Symmetrical behaviour of the current relaxation from the SPECS experiment indicating a solid solution between 2.3 and 1.5V for  $\text{TiP}_2\text{O}_7$  upon discharge ( $\pm 20\text{mV}$  every 15 hours).

At the plateau around 1.5V, the chronoamperogram shows anomalous behaviour with  $0.875 < x < 1.02$  lithium inserted into  $\text{Li}_x\text{TiP}_2\text{O}_7$ . This can be described as titanium based reduction from  $\text{Ti}^{\text{IV}+}$  to  $\text{Ti}^{\text{III}+}$  plateau that has been reported<sup>12</sup> about 1.4V for rutile  $\text{TiO}_2$ , anatase<sup>13</sup> and the NASICON type titanium phosphate<sup>14</sup>.

The overall lithium inserted from the open circuit voltage to the end of this plateau around 1.5V accounts for 1.02 lithium. The extra 0.02 lithium is of similar order to the experiment error in the capacity.

The chronoamperogram for  $0.87 < x < 1.1$  **Fig.: 5- 17** once again has shown anomalous behaviour that indicates a biphasic region. The change in the current relaxation curve in the encircled region in **Fig.: 5- 17** indicates a change in the electrochemistry. This is presumably due to the onset of lithium insertion into the carbon around 1V, which contributes to 0.007 lithium by this voltage, in addition to the active material inserted. The electroactivity of the carbon at this potential might be preventing the system from reaching equilibrium and induces the anomalous behaviour of the current relaxation therefore.

Additionally, the biphasic mechanism observed from the SPECS experiment is supported by the in-situ XRD experiment between 0.87 and 1.09 lithium inserted that shows an increase in peaks intensity of phase (B) and a progressive decrease of phase (A), which disappears at  $x = 1.09$ .

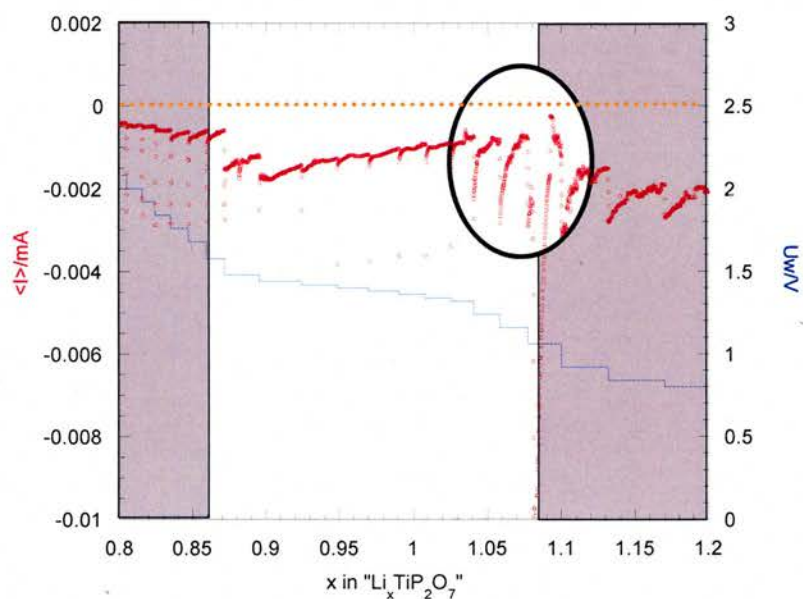
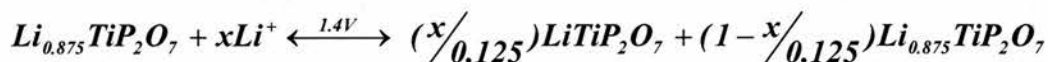


Fig.: 5- 17 Anomalous behaviour of the current between 1.5 and 1.1V for  $\text{TiP}_2\text{O}_7$  upon discharge ( $\pm 20\text{mV}$  every 15 hours).

The electrochemistry in this biphasic region is described through eq.: 5- 3.

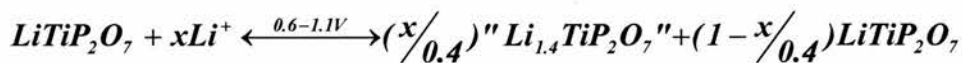
eq.: 5- 3



$$0 < x < 0.125$$

Between  $1.02 < x < 2$  lithium inserted (1.1-0.6V), the chronoamperogram **Fig.: 5-18** shows once again anomalous behaviour characteristic of a biphasic region. Considering that the Super S carbon reduction happens around 0.8V and accounts for 0.09 lithium reacting across a voltage range of 2.6-0.5V therefore, the actual lithium reacting with the active material after the correction is  $x = 1.41$ . The reaction describing this biphasic region may be written as follow **eq.: 5- 4**:

eq.: 5- 4



$$(0 < x < 0.4)$$

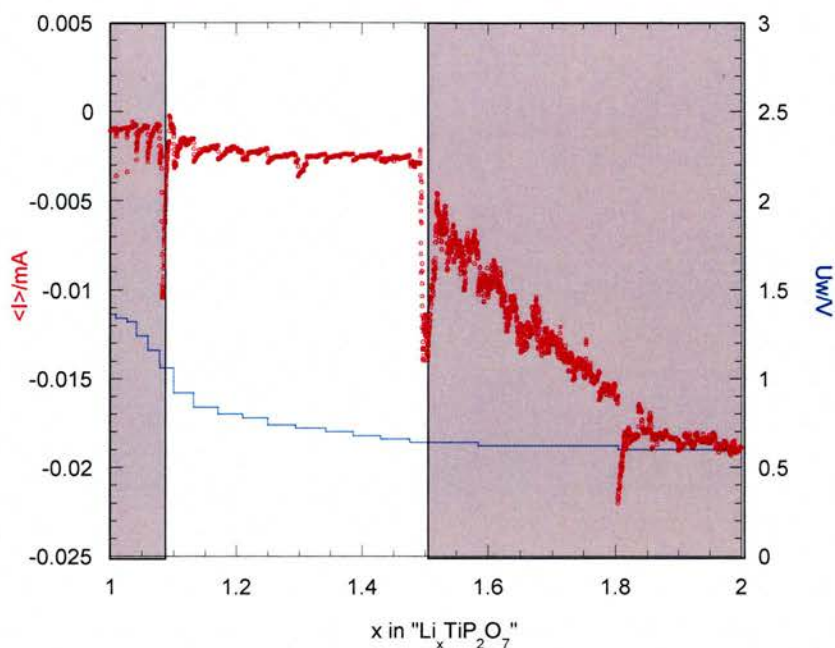


Fig.: 5- 18 Anomalous behaviour of the current between 1.2 and 0.6V for  $\text{TiP}_2\text{O}_7$  upon discharge ( $\pm 20\text{mV}$  every 15 hours).

The in-situ XRD patterns collected for 1.09 and 2 lithium inserted are quite different with, a new phase (C) in addition to (B) for  $x = 2$ .

A large plateau around 0.6V as displayed in **Fig.: 5- 19** describes the next voltage range. The chronoamperogram of this region ( $1.5 < x < 7$ ) shows anomalous behaviour of the current relaxation that is a typical response of biphasic mechanism. These mechanisms suggest formation of several phases throughout this region that is supported by the in-situ XRD spectra from  $x = 2$  to  $x = 7$  lithium inserted. It can be observed clearly in those patterns (**Fig.: 5- 14**) the presence of 3 phases (B), (C) and (D).

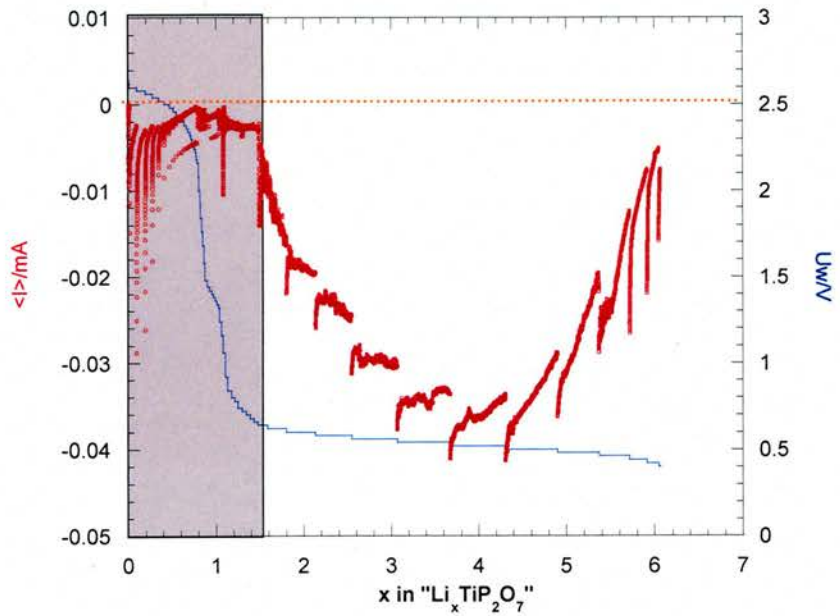


Fig.: 5- 19 Anomalous behaviour of the current at the plateau around 0.6V for  $\text{TiP}_2\text{O}_7$  upon discharge ( $\pm 20$  mV every 15 hours).

#### 5.4.4. XPS.

XPS technique was used to evaluate qualitatively the oxidation state of the ( $\text{TiP}_2\text{O}_7$ ) on discharge to different potentials of 1.4, 0.5, 0.02V and in addition discharged to 0.02V and charged up to 2.5V. In the 1.4 and 0.5V spectra, there are similar low energy shoulders across all the data. It is assumed that this is an instrumental artefact or sample handling, therefore these peaks will be ignored in the following discussion.

##### 5.4.4.1. Titanium $\text{Ti-2p}_{3/2}$ and $\text{Ti-2p}_{1/2}$ .

All the titanium spectra are shown in **Fig.: 5- 20**. From this figure, it can be observed the binding energy of  $\text{Ti-2p}_{3/2}$  and  $\text{Ti-2p}_{1/2}$  electrons<sup>15</sup> can be observed at 459.4 and 465eV respectively and correlates with  $\text{Ti}^{\text{IV}+}$  in the starting material labelled OCV.

Upon discharge to 1.4V, the centre of the peak envelope binding energy of  $\text{Ti-2p}_{3/2}$  and  $\text{Ti-2p}_{1/2}$  electrons has shifted toward lower energy to 458.5 and 464.0eV respectively. These binding energy  $\text{Ti-2p}_{3/2}$  peaks have two components fitted at 459.4 and 458.5eV, which suggests oxidation states of the titanium  $\text{Ti}^{\text{IV}+}$  and  $\text{Ti}^{\text{III}+}$ . It was reported<sup>16</sup> binding energy of 458.5eV for  $\text{Ti-O}_{(2-x)}$  and  $\text{TiO}_2\text{-As}_2\text{O}_5$ . This result correlates well with our electrochemistry result, which at this potential with 0.9 lithium inserted has suggested a biphasic system. In addition, the in-situ

XRD experiment has shown doubling of peaks in this region indicating a formation of different species. The XPS has illustrated that in this potential range, the reduction is titanium based.

For the material discharged to 0.5V, once again the centre of the peak envelope has shifted toward lower binding energy to 458.5 and 463.4eV for the Ti-2p<sub>3/2</sub> and Ti-2p<sub>1/2</sub> electrons respectively. The two fitted components of the observed binding energy exhibit a shift of 0.5eV compared to those observed at 1.4V. This might be related to a change in the oxidation states possibly Ti<sup>III+</sup> and Ti<sup>II+</sup>. It was reported<sup>16</sup> the electron of the Ti-2p<sub>3/2</sub> binding energy having peaks at 458.6 for TiO and a 457.9eV for Ti-OH. This is supported by the SPECS experiment that shows biphasic mechanism and the in-situ XRD experiment that reveals formation of several phases.

For the cell discharged at 0.02V, the Ti-2p<sub>3/2</sub> and Ti-2p<sub>1/2</sub> electrons binding energies are at 458.5 and 463.8eV respectively. Basically no change in peak envelop position can be observed but the peak is weaker and broader, therefore the possibility of having Ti<sup>III+</sup> and Ti<sup>II+</sup> should be taken in consideration as suggested for the cell discharged to 0.5V. It is worth noting that when the cell was discharge to a voltage of 0.02V, the signal noise increased making the fitting more difficult. This perhaps due to the SEI built up at the surface of the sample.

For the material discharged to 0.02V and charged up to 2.5V, Ti-2p<sub>3/2</sub> and Ti-2p<sub>1/2</sub> electrons binding energies have returned to the high energy side of 458.4 and

463.5eV respectively, which might be related to  $Ti^{IV+}$  and  $Ti^{III+}$ . From this experiment, it can be considered that a redox process is taking place in titanium.

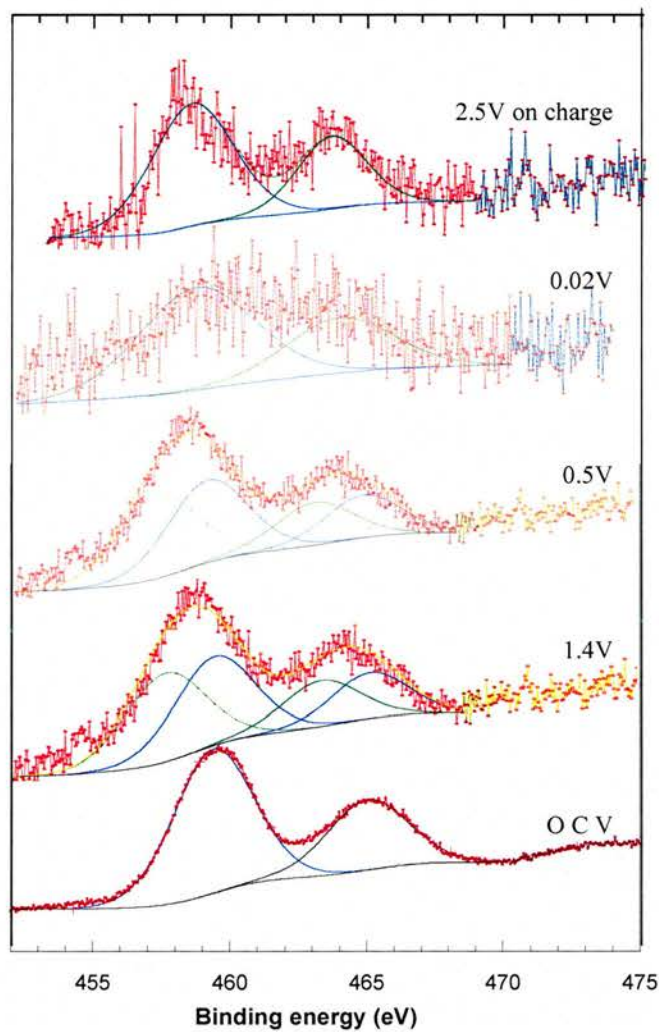


Fig.: 5- 20 Titanium XPS spectrum of pure and discharged  $TiP_2O_7$ .

#### 5.4.4.2. Phosphorus P-2p<sub>3/2</sub>

**Fig.: 5- 21** shows the XPS spectra of phosphorus. The binding energy of the P-2p<sub>3/2</sub> electrons is observed around 133.4eV for the starting material, labelled OCV.

For the material discharged to 1.4V (with 0.9 lithium inserted), the peak representing the binding energy of the P-2p<sub>3/2</sub> electrons in the spectrum has a main peak centred at 133.4eV. This is consistent with the position observed at the OCV with no observed shift. This suggests that at 1.4V no reaction is happening in the phosphorus sites and is titanium centred.

At 0.5V, only a symmetrical peak can be observed with a binding energy of the P-2p<sub>3/2</sub> electrons around 132.8eV. This result indicates that all the phosphorus are equivalent but present a shift of 0.6eV compared to that observed at 1.4V that suggests a change in the phosphorus environment in the plateau. This shift of 0.6eV was observed for SnP<sub>2</sub>O<sub>7</sub> discharged to 0.02V. This observation suggests that the phosphorus is electrochemically active at this voltage.

The spectrum at 0.02V shows an asymmetric peak. The binding energy of the P-2p<sub>3/2</sub> electrons is observed at 132.8eV and does not show any change in the phosphorus environment compared to 0.5V. This was also observed in the case of SnP<sub>2</sub>O<sub>7</sub>. However, the signal to noise has increased for this spectrum and this may be related to SEI built up at the surface of the sample.

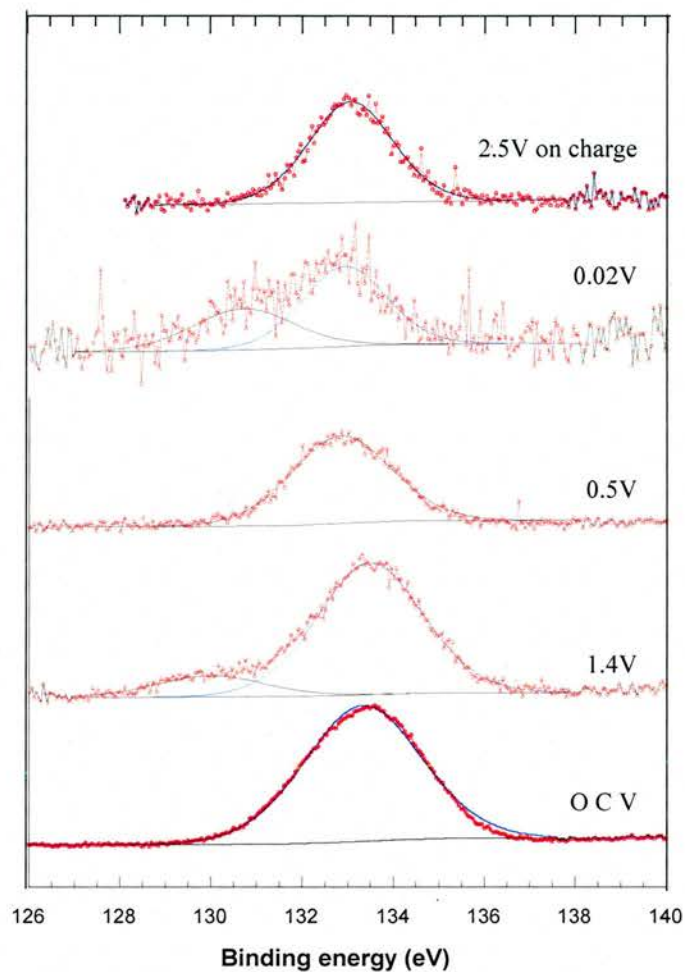


Fig.: 5- 21 Phosphorus XPS spectrum of pure and discharged TiP<sub>2</sub>O<sub>7</sub>

The spectrum of the material discharged at 0.02V and charged up to 2.5V exhibits no alteration in the binding energy of the P-2p<sub>3/2</sub> electrons at 132.9eV. This indicates that the phosphorus reduction is irreversible around 0.5V.

#### 5.4.4.3. Oxygen O-1s.

Oxygen spectra are displayed in **Fig.: 5- 22**. The O-1s electrons binding energy in titanium pyrophosphate labelled OCV shows a symmetrical peak around 530.6eV. This peak should be considered as averaging the contribution of bridging oxygen BO and non- bridging oxygen NBO.

At 1.4V, an asymmetrical peak can be observed in the spectrum depicting at least two component of oxygen binding energy. These two peaks are centred at 531.7 and 532.3eV respectively. This might be probably related to the change in oxygen environment compared to the OCV as the electrochemistry analysis SPECS has suggested a two phases region at this potential, consistent with XRD and SPECS data, both oxygen peaks are shifted indicating titanium reduction (**eq.: 5- 2**).

The next spectrum discharge to 0.5V exhibits a symmetrical peak centred at 531.4eV suggesting equivalent oxygen environments. This observed peak has displayed a shift of 0.8eV compared to the one from the OCV. This suggests that the oxygens have different environments at this voltage either through redox or structural changes, or more likely both.

At 0.02V; the spectrum exhibits a symmetrical peak that indicates equivalent environment of oxygen. This peak is centred at 531.4eV and shows no alteration from 0.5V oxygen peak.

When the material was discharged to 0.02V and charged up to 2.5V, the O-1s electrons binding energy shows a symmetrical peak at 531.6eV. By comparison, the oxygen main peak has shifted toward higher binding energy of 0.2eV. This suggests that the oxygen are involved in the redox mechanism presumably as an oxide.

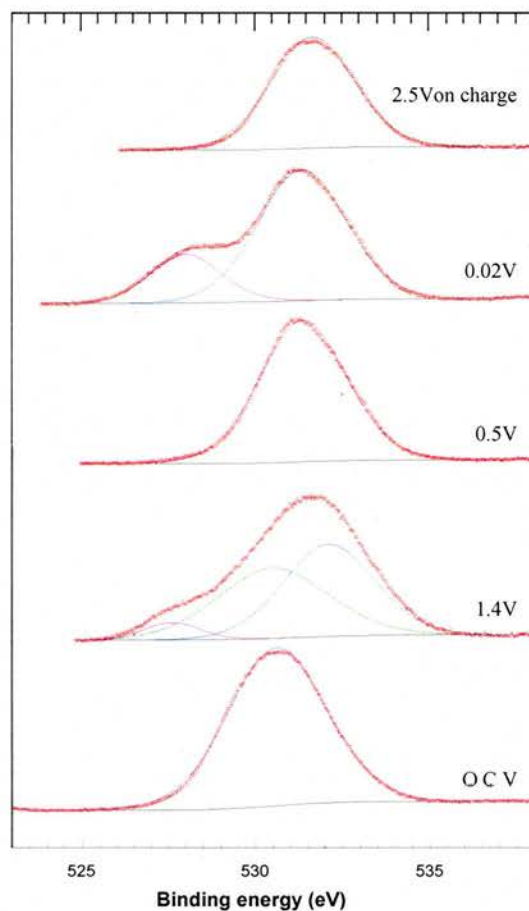


Fig.: 5- 22 Oxygen XPS spectrum of pure and discharged  $TiP_2O_7$

#### 5.4.4.4. Carbon C-1s.

**Fig.: 5- 23** displays the carbon spectra. Super S carbon was added to the starting material to act as an internal reference as it is present in the real electrodes.

In the initial  $\text{TiP}_2\text{O}_7$ , the peaks corresponding to the C-1s electrons binding energy shows at least two environments of carbon. This is usually the case as there is always contamination carbon peak arising from the atmosphere and the sample holder made in carbon stick. The binding energy at 283.7eV is related<sup>17</sup> either to the contamination carbon layer or the carbon from the sample holder whereas the small shoulder centred at 286.3eV must be attributed to the super S carbon.

For the material discharged to 1.4V, an asymmetrical envelope can be fitted by contributions of peaks centred at 283.7, 286.3 and 289.1eV. The binding energy of the C-1s electron from the contamination layer or the sample holder is still present at 283.7eV therefore the other two binding energy observed as the one at 286.3eV might be attributed to the super S carbon and the one at 289.1eV might be arising from the residual carbon in the electrolyte<sup>18</sup> ( $\text{LiClO}_4$ : EC: DMC).

At 0.5V, the spectrum can be fitted with at least three peaks at 283.8, 285.9 and 288.9eV. The assignation of those peaks leads to ascribe to peak at 283.8 to the contamination layer, the peak at 285.9eV presents a shift of 0.4eV that suggests a change in the Super S carbon environment, therefore this peak is assigned to carbon in  $\text{LiC}_6$ . Wertheim et al<sup>19</sup> have reported earlier a binding energy of

285.2eV for  $\text{LiC}_6$  and 284.6eV for carbon. The peak at 288.9eV is related to residual electrolyte.

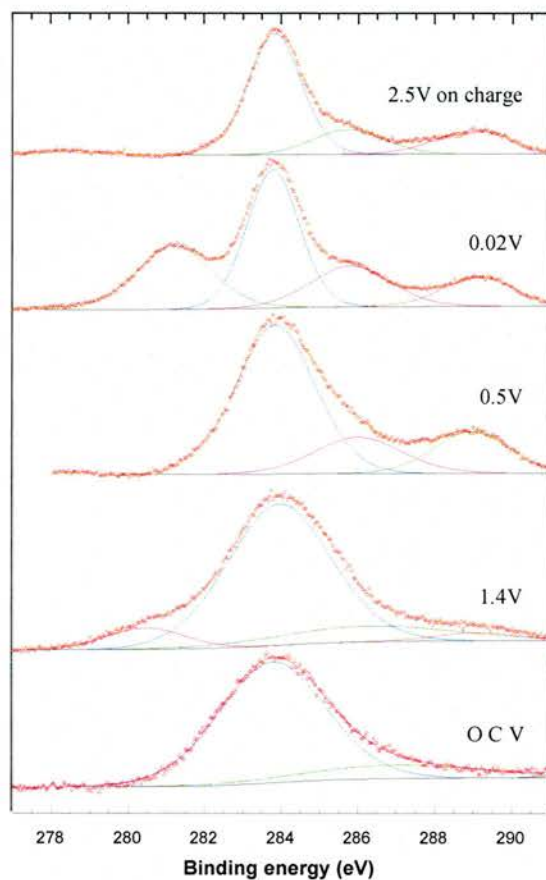


Fig.: 5- 23 Carbon XPS spectrum of pure and discharged  $\text{TiP}_2\text{O}_7$ .

Most importantly, the discharged material to 0.02V, shows peaks at 283.8, 285.9 and 288.9eV. Once again, the peak at 283.8eV is related to the contamination layer, the peak at 285.9eV is ascribed to  $\text{Li}_x\text{C}_6$  whereas the residuals peak still present at 288.9eV.

When the material was discharged to 0.02V and charged up to 2.5V, the spectrum shows 3 peaks. The peak at 283.8eV is assigned to the contamination layer, the

peak at 286.1eV is assigned to the Super S carbon as this peak shows a shift of 0.2eV toward high binding energy. The peak at 288.9eV is still related to the residual electrolyte.

### 5.5. <sup>31</sup>P NMR results and discussion.

In order to follow the evolution of the phosphate matrix, cells were made from  $\text{TiP}_2\text{O}_7$  and discharged to different potentials of 1.4, 0.5, 0.02 and discharge and charged up to 2V. The discharged electrodes were then sampled by NMR to observe the peak shift and possibly assign the different steps of the reduction. The spectrum are shown in **Fig.: 5- 24** and **Table: 5- 3**.

The <sup>31</sup>P MAS NMR of the electrode discharged to 1.4V ( $x = 1$ ) shows the same chemical shift as the starting material centred at  $-47\text{ppm}$  but the relative intensity of the lines are modified. At 0.5V with  $x = 2$  (the number of lithium inserted), the spectrum displays the same lines as the starting material and another broad line centred at  $-2.4\text{ppm}$ . At 0.5V discharge with 4 lithium inserted, the lines centred at  $-47\text{ppm}$  disappears and the spectrum shows two lines at  $-2.4$  and  $6.5\text{ppm}$ . At the discharged state of 0.02V, only one intense line can be observed at  $6.5\text{ppm}$  and is increased in intensity compared to the one at 0.5V. From the electrode discharged and charged up to 2V, only one broad line centred at  $3.7\text{ppm}$  was observed with a Full Weight Half Height (FWHH) of  $3.2\text{kHz}$ . Spinning sidebands were observed in this spectrum implying presence of crystalline phase.

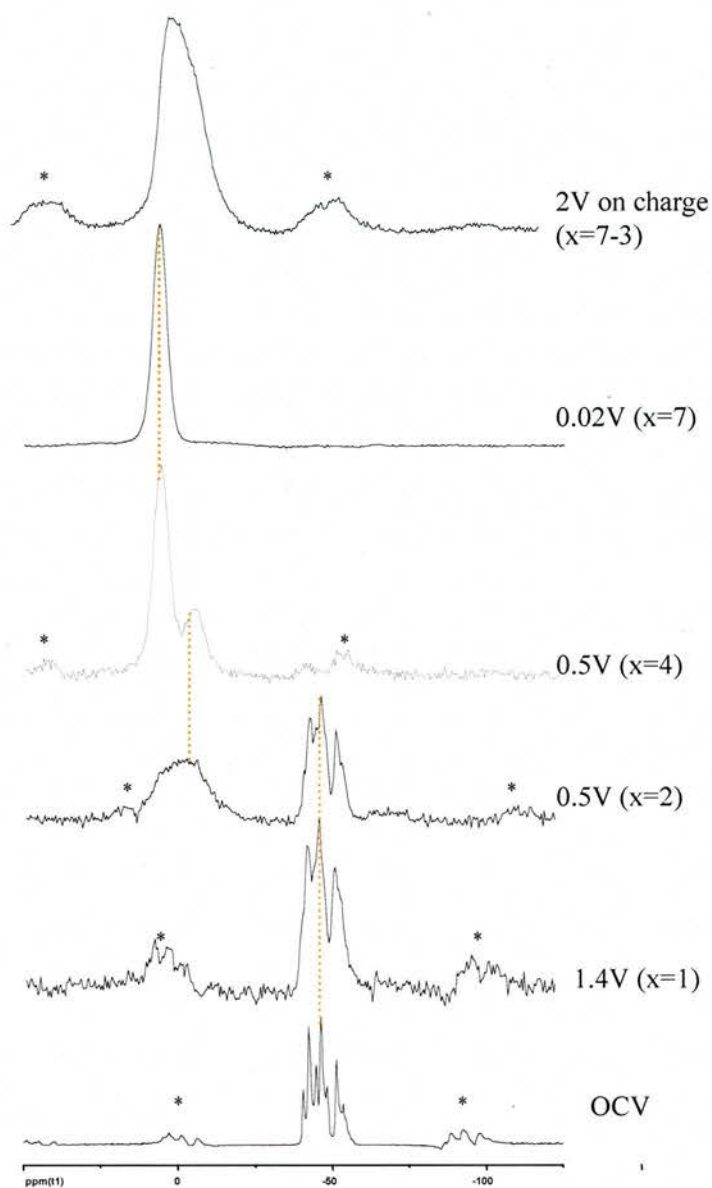


Fig.: 5- 24  $^{31}\text{P}$  MAS NMR spectrum of electrode derived from  $\text{TiP}_2\text{O}_7$  and discharged to different voltage states from the OCV to 0.02V and charge up to 2V. (OCV = open circuit voltage and \* = spinning sidebands).

From the  $^{31}\text{P}$  MAS NMR the alteration of the intensity without change in chemical shift between the OCV and 1.4V suggests this is titanium based reduction from IV+ to III+ to give a lithiated  $\text{Ti}^{\text{III+}}\text{P}_2\text{O}_7$  that was described in **eq. 5- 3**. The change in intensity is presumably due to the electronic and structural changes during the reduction of the titanium. This observation is in perfect agreement with titanium XPS result at this voltage and the result obtained from the SPECS experiment and the in-situ XRD described earlier.

At 0.5V with 2 lithium inserted, the spectrum displays two phosphorus environments. The lines centred at  $-47\text{ppm}$  are similar to those observed at 1.4V and suggest a lithiated titanium pyrophosphate with the titanium being III+, II+ or mix III+/II+. The other broad line observed at  $-2.4\text{ppm}$  seems more likely to be pyrophosphate group bound to lithium ( $\text{Li}_4\text{P}_2\text{O}_7$ ) as observed for  $\text{SnP}_2\text{O}_7$ . This suggests formation of a lithiated phosphate matrix and hence a phase segregation that correlates with the in-situ XRD result as several phases (B), (C) and (D) were observed in this voltage range.

At 0.5V with 4 lithium inserted the spectrum looks very different from the previous one at the same voltage. There are no lines centred at  $-47\text{ppm}$ , with new peaks at  $-2.4$  and  $6.5\text{ppm}$ . This shift implies formation of a much more ionic species, such as  $\text{Li}_4\text{P}_2\text{O}_7$  as was observed starting from  $\text{SnP}_2\text{O}_7$ . This could imply disproportionation with expulsion of  $\text{Ti}(\text{O})$  from the matrix; however as cycling experiments indicate the Ti is still redox active. It therefore seems that Ti is still bonded to the phosphate matrix but not in the same covalent manner as  $\text{TiP}_2\text{O}_7$  or  $\text{LiTiP}_2\text{O}_7$ . This may be consistent with phase such as  $\text{Li}_4\text{Ti}^{\text{II+}}\text{P}_2\text{O}_7$  or a perhaps

some form of nanocomposite. The spectrum shows similarity to those starting from  $\text{SnP}_2\text{O}_7$  with lithiated pyrophosphate matrix with  $\text{P}^{\text{V}}$  and a reduced lithiated pyrophosphate matrix with  $\text{P}^{\text{IV}}$  respectively. In addition a shift of 0.6eV was observed in the phosphorus XPS spectrum similar to the case for  $\text{SnP}_2\text{O}_7$  and the SPECS has revealed biphasic mechanism.

The spectrum of the electrode discharged to 0.02V shows only one peak at 6.5ppm that confirms complete reduction of the phosphate matrix from  $\text{P}^{\text{V}}$  to  $\text{P}^{\text{IV}}$  and correlates with the XPS data.

The lack of spinning side bands in the structure suggests that the phosphate matrix is amorphous and this is supported by the in-situ XRD, which shows a decrease in peaks intensity.

The spectrum of the electrode discharged to 0.02V and charged up to 2V shows a broad line, which might be a contribution of overlapping lines but the presence of spin sidebands reveals a crystalline behaviour. This would be consistent with reoxidation of some titanium that is intimately bound to the phosphate matrix.

$x$ (number of lithium inserted)	Voltage	$\delta$ of the main peaks(in ppm)	
0	OCV	-47	
1	1.4V (D)	-47	
2	0.5V (D)	-2.4	-47
4	0.5V (D)	-2.4	6.5
7	0.02V (D)	6.5	
4	2V (C)	3.7	

Table: 5- 3  $^{31}\text{P}$  NMR peaks position of the discharged and charged electrode made from  $\text{TiP}_2\text{O}_7$ . (D = discharge, C = charge, OCV = open circuit voltage,  $\delta$  chemical shift in ppm).

#### 5.6. HRTEM & SAED of cycled material.

The HRTEM pictures **Fig.: 5- 25a** & **b** taken at  $x = 4$  definitely shows a change in the structure of the material on lithium insertion. Both crystalline and amorphous structure can be observed in the picture. **Fig.: 5- 25a** shows very well in the central region, the remaining unreduced material that was observed from the in-situ XRD experiment. The inset SAED picture shows the directions of those reflections, which are  $d_{024}$  and the  $d_{1200}$  based on the  $3 \times 3 \times 3$  unit cell. **Fig.: 5- 25b** focuses on the edge region that exhibits a completely different microstructure and morphology as the fringes have disappeared<sup>20</sup>.

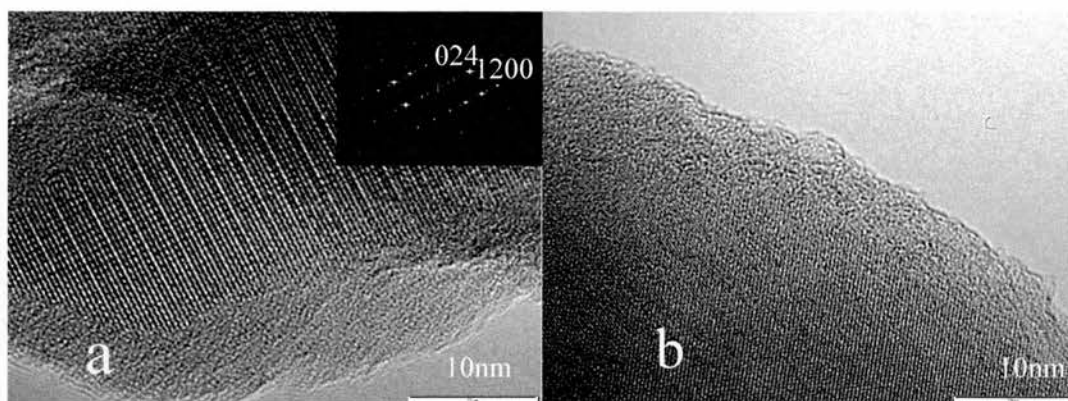


Fig.: 5- 25a & b HRTEM images of  $\text{Li}_x\text{TiP}_2\text{O}_7$  (with  $x = 4$  lithium and a current density of  $0.1\text{mA}/\text{cm}^2$ ).

*(These pictures were recorded by Dr. Loic DUPONT at the University of Picardie Jules Verne Amiens in France).*

This result leads to conclude that upon discharge at 0.5V plateau, the Lithiated  $\text{TiP}_2\text{O}_7$  is transformed to an amorphous phase. This supports the in situ XRD experiments, which reveals amorphisation of the material under discharge in this region. The amorphous matrix is supported by the NMR result. However, in situ XRD and NMR have shown recrystallisation on charge.

EDS was performed in the amorphous region and the result is shown in **Fig.: 5-26**. This has confirmed the titanium to phosphate ration to be  $\text{Ti}/\text{P} = 1/2$ , which is unchanged from the initial composition.

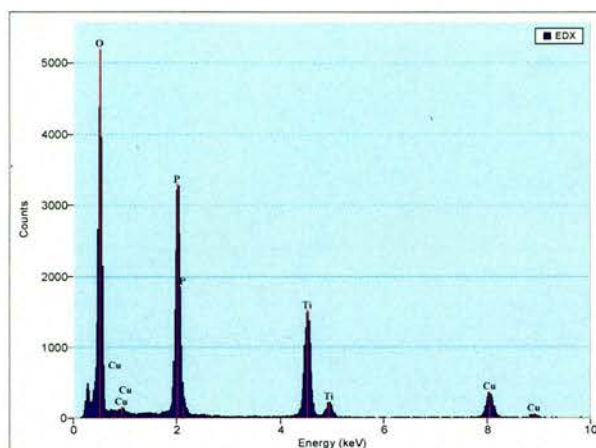


Fig.: 5- 26 EDS spectrum of  $\text{TiP}_2\text{O}_7$  under discharge with 4 lithium inserted.

**Fig.: 5- 27** also shows the formation of a polymeric layer as reported by *Poizot et al*<sup>21</sup>. The polymeric layer is reported to be pseudo capacitive and so would contribute to increase the number of lithium inserted upon discharge and cycling.

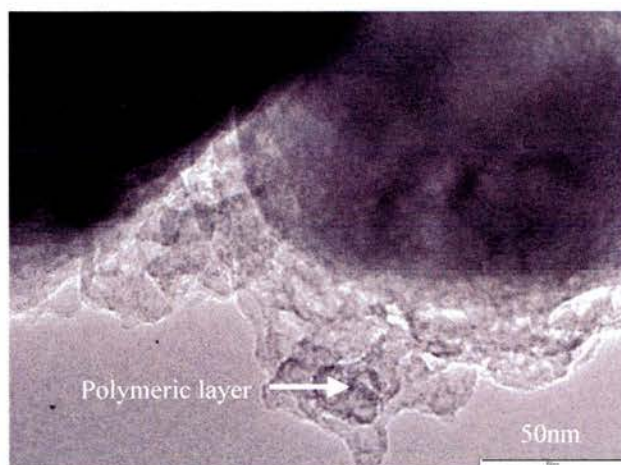


Fig.: 5- 27 HRTEM image of  $\text{Li}_x\text{TiP}_2\text{O}_7$  (with  $x = 4$  lithium and a current density of  $0.1\text{mA}/\text{cm}^2$ ) exhibiting a polymeric layer.

(This picture was recorded by Dr. Loic DUPONT at the University of Picardie Jules Verne Amiens in France)

## 5.7. IR.

IR was used to probe whether the P-O-P bond is conserved upon discharge. A sample of  $\text{TiP}_2\text{O}_7$  was fully discharged and an infrared experiment was recorded. The IR pattern is shown with that of the starting material  $\text{TiP}_2\text{O}_7$  in **Fig.: 5- 28a & b**.

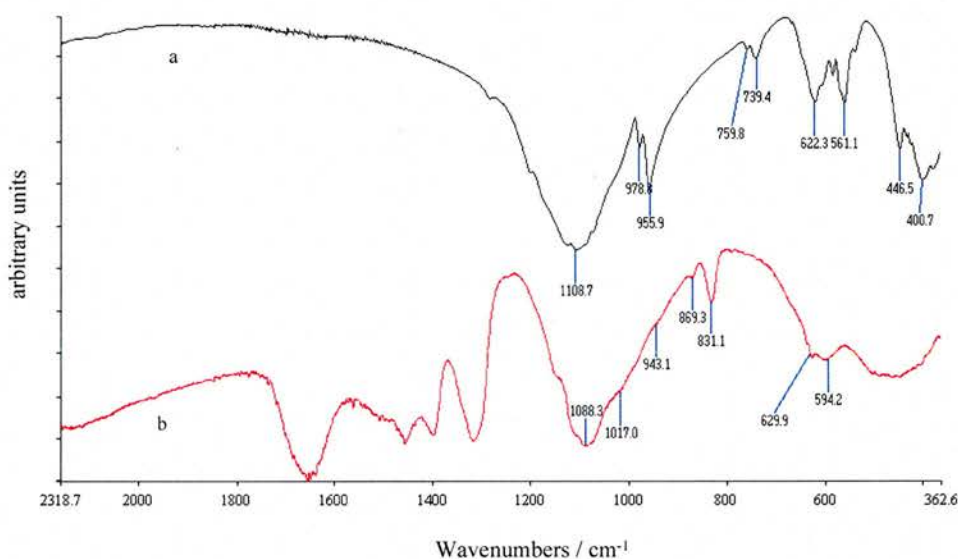


Fig.: 5- 28 IR spectrum of (a)  $\text{TiP}_2\text{O}_7$  & (b)  $\text{TiP}_2\text{O}_7$  after the first discharge

**Fig.: 5- 28a** is the IR spectrum of  $\text{TiP}_2\text{O}_7$  and **Fig.: 5- 28b** the IR spectrum of the fully reduced sample. The IR spectra of reference samples such as the electrolyte and lithiated super S carbon were collected in order to assign the peaks seen in the spectra. Peaks beyond  $1200 \text{ cm}^{-1}$  are due to the lithiated super S carbon. The main changes on reduction are loss of  $978$  and  $956 \text{ cm}^{-1}$  ( $\text{PO}_3$ ) vibration modes **Fig.: 5- 28a** and the  $759$  and  $739$  (P-O-P) vibration modes **Fig.: 5- 28a**, which are replaced by peaks at  $869$  and  $831 \text{ cm}^{-1}$  **Fig.: 5- 28b**. These peaks are assigned to the (P-O-

P) shifted to higher wavenumber. The  $\nu_{as}(\text{PO}_3)$  shows a small shift as expected for reduced phosphorus<sup>22</sup>.

### 5.8. $\text{Sn}_{1-y}\text{Ti}_y\text{P}_2\text{O}_7$ with $y = 0.5$ .

The electrochemical properties of  $y = 0.5$  were studied in detail using a SPECS experiment. As displayed in **Fig.: 5- 29**, the discharge curve can be divided into 4 different regions based on the processes that occur under discharge (inset I, II, III IV).

#### 5.8.1. Region I.

Region I (**Fig.: 5- 29** inset I) shows the same behaviour as  $\text{TiP}_2\text{O}_7$  with at least three different processes observable in the chronoamperogram. The inset, region I shows three distinguishable anomalous regions suggesting three different biphasic transformation regions. All these transformations that occur are described stoichiometrically in the following **eq.: 5- 5**, and **eq.: 5- 7**.

eq.: 5- 5



$$0 < x < 0.14$$

eq.: 5- 6



$$0.14 < x < 0.35$$

eq.: 5- 7



$$0.35 < x < 0.5$$

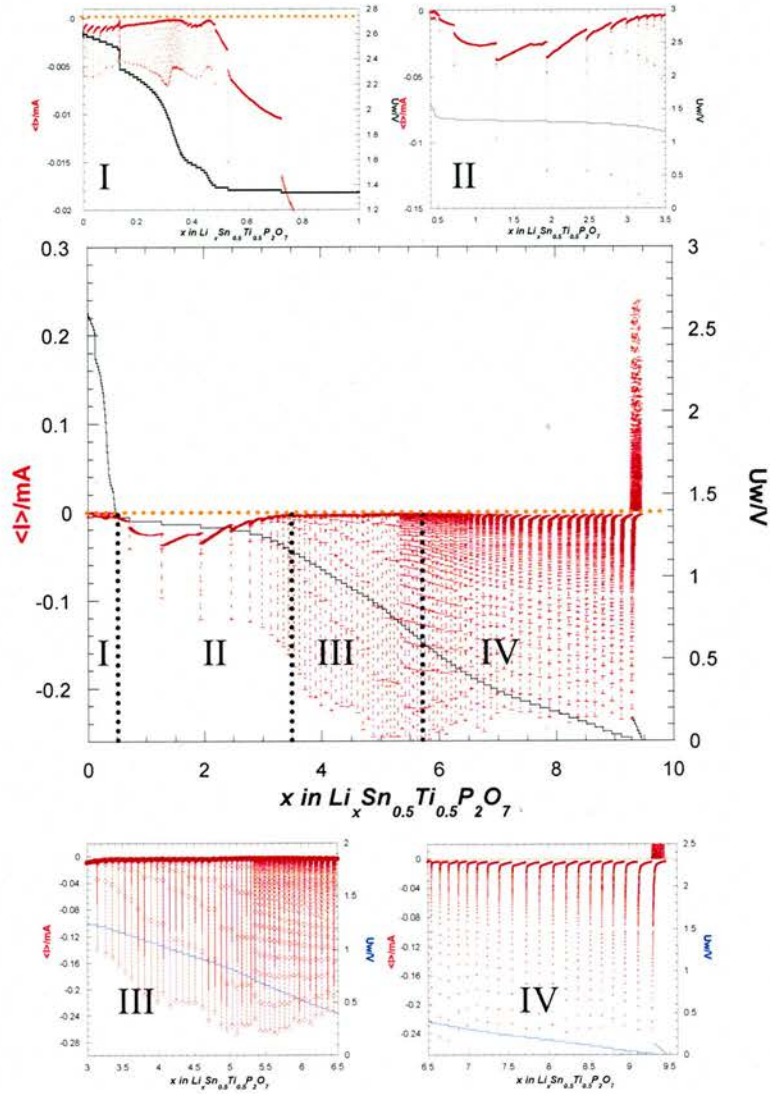


Fig.: 5- 29 SPECS experiment of  $y = 0.5$ .

The lithium insertion in this region accommodates 0.5 lithium ions and accounts for the reduction from  $\text{Ti}^{\text{IV}+}$  to  $\text{Ti}^{\text{III}+}$  of all the titanium (IV) available in the system. In this region more transformations were detected compared to  $\text{TiP}_2\text{O}_7$ . This may be due to the presence of tin. These phases were not characterised other than using the SPECS technique to determine their compositions.

### 5.8.2. Region II.

Region II (**Fig.: 5- 29** inset II) exhibits basically the same behaviour as  $\text{SnP}_2\text{O}_7$  at the 1.3V plateau, which was described in *Chapter 3-NMR section equation 3-1*. This region accommodates 3 lithium ions and corresponds to the reduction of all tin (IV) to metallic tin in addition to titanium reduction observed for  $\text{TiP}_2\text{O}_7$  in this voltage range. Once again the chronoamperogram shows anomalous behaviour that indicates biphasic transformation domain as for  $\text{SnP}_2\text{O}_7$ .

### 5.8.3. Region III.

This region (**Fig.: 5- 29** inset III) describes a solid solution region as the current reaches zero. This suggests lithium diffusion through the system before the next reaction potential is reached. The number of lithium ions involved in this region is approximately 3 to 3.5 and can be related to the phosphate reduction and possibly the formation of polymeric layer as observed for  $\text{TiP}_2\text{O}_7$ .

#### 5.8.4. Region IV.

In region IV (**Fig.: 5- 29** inset IV), the chronoamperogram exhibits anomalous behaviour that suggests a biphasic transformation domain. Based on  $\text{SnP}_2\text{O}_7$  and  $\text{TiP}_2\text{O}_7$ , several reactions occur in this region. Definitely for  $\text{SnP}_2\text{O}_7$ , the tin metal formed around the 1.3V plateau in region II, alloys reversibly with lithium as described in *equation 3-2* in this region. Furthermore the reduction of phosphate as shown in *Section 3-NMR, eq.: 3-3* occurs in the same voltage region.

On cycling, it would be expected for  $(0.5*\text{Li}_{4.4}\text{Sn})$  to cycle and hence exhibit  $2.2x$  on cycling plus possibly  $1x$  for titanium. Surprisingly the reversibility accommodates with  $4x$ . This may suggest possibly, further reduction of titanium on the first discharge as seen for  $x = 1$  or the contribution of the polymeric layer that is pseudo-capacitive.

#### 5.9. $\text{Sn}_{1-y}\text{Ti}_y\text{P}_2\text{O}_7$ with $y = 0, 0.15, 0.35, 0.5, 0.75$ & $1$ .

In order to compare the role of the cation within the system, batteries were made from materials with compositions  $y = 0, 0.15, 0.35, 0.5, 0.75$  and  $1$  in  $\text{Sn}_{1-y}\text{Ti}_y\text{P}_2\text{O}_7$ .

The potentiostatic plot of the materials  $y = 0, 0.15$  and  $0.35$  are shown in **Fig.: 5- 30**. These plots typically show several peaks: a major peak at 1.3, and a broad shoulders around 1.1, 0.8, 0.4 and 0.2V on the first discharge. There is no obvious peak at 2.6V unlike the case of  $\text{TiP}_2\text{O}_7$ .

The peak at 1.3V can be ascribed to tin reduction (*see eq.: 3-1*). The shoulder at 1.1V must be related to titanium reduction as this peak grows with titanium content.

The peak at 0.8V is present a small peak and is related to carbon reduction. The shoulder at 0.4V is related to the phosphate reduction as previously explained for  $y = 0$  (*see eq.: 3-3*).

The peak at 0.2V is related to the formation of tin alloy (*see eq.: 3-2*) and probably to the amorphisation of the system.

In comparison, galvanostatic plots **Fig.: 5- 31a & b** ( $y = 0.15$  &  $0.35$ ) show a decrease in number of lithium ions inserted upon the first discharge with  $y$ . This is related to the number of tin atoms available in the system to give capacity from reversible lithium-tin alloy. However, the titanium reduction is not well understood and seems to be  $\text{Ti}^{\text{IV}+} \rightarrow$  mixed  $\text{Ti}^{\text{III}+/\text{II}+}$ ,  $\text{Ti}^{\text{II}+}$  or  $\text{Ti}^0$  as observed for  $\text{TiP}_2\text{O}_7$ . There are no reduction plateaus around 2.5 and 1.5V as observed in the SPECS experiments for  $\text{TiP}_2\text{O}_7$  and  $\text{Sn}_{0.5}\text{Ti}_{0.5}\text{P}_2\text{O}_7$ . This strongly indicates that the relevant processes are kinetically limiting.

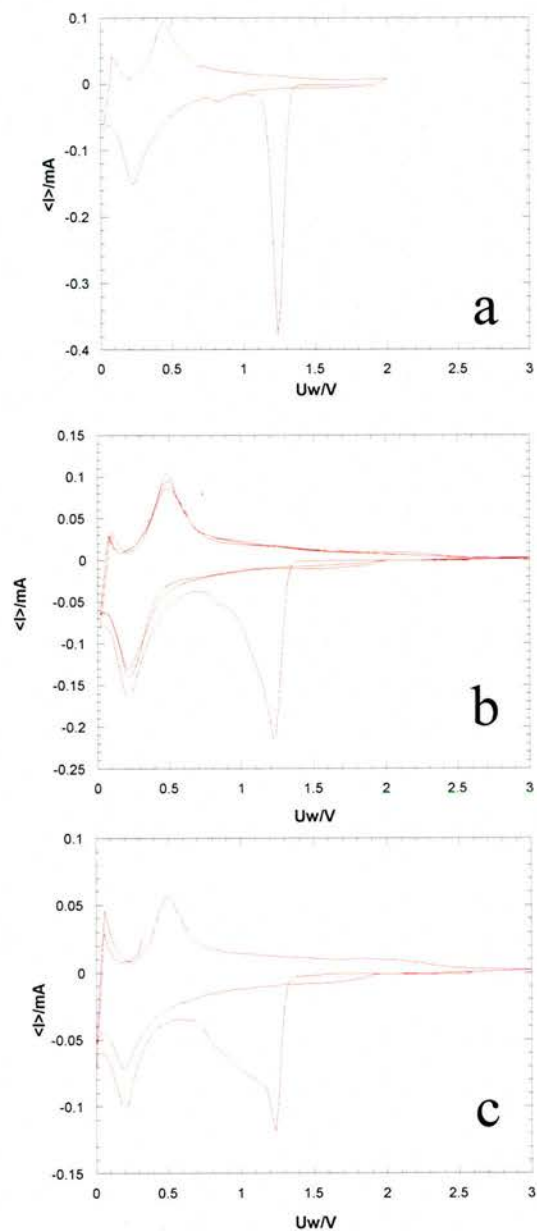


Fig.: 5- 30 Potentiostatic plot of  $y = 0, 0.15, 0.35$ .

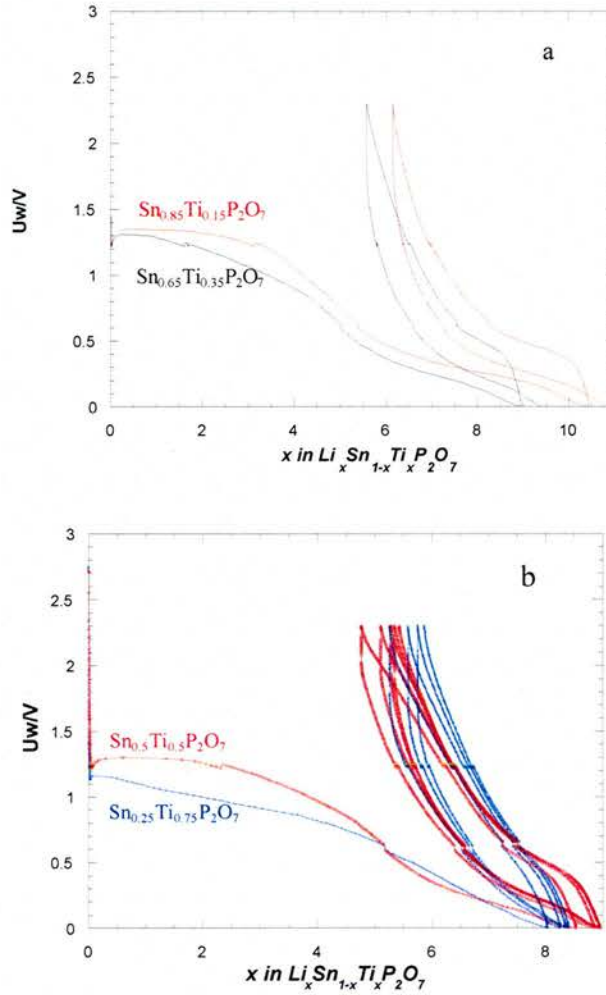


Fig.: 5- 31a & b (a) Galvanostatic plot of  $y = 0.15$  &  $0.35$ , (b) galvanostatic plot of  $y = 0.5$  &  $0.75$  (with a current density of  $0.1 \text{ mA/cm}^2$ ).

Even for  $y = 0.5$  this galvanostatic plot shows the first plateau reached is the reduction of  $\text{Sn}^{4+}$  to  $\text{Sn}^0$ . This is due to the kinetic limitation since galvanostatic discharge is often very fast compared to either potentiostatic or SPECS experiment seen for the same composition  $y = 0.5$ .

The shape of the plateau at 1.3V changes with tin content.

The first discharge capacity, the reversible capacity and capacity after 10 cycles were summarised in **Table: 5- 4**.

$Sn_{1-y}Ti_yP_2O_7$			
$y$	<i>First discharge capacity (mAh/g)</i>	<i>First charge capacity (mAh/g)</i>	<i>Capacity retention after 10 cycles</i>
1	853.23	377.32	93%
0.75	910.33	314.74	98%
0.5	923.40	381.50	86%
0.35	908.53	334.15	69%
0.15	1003.67	409.92	100%
0	965	365	100%

Table: 5- 4 Capacity on the first discharge, charge and capacity retention after 10 cycles of compositions  $y = 0, 0.15, 0.35, 0.50, 0.75$  & 1.

The first discharge and charge capacities do not show a linear trend, which would be expected according to the change in molecular mass. However, the best capacity was observed at low titanium substitution of  $y = 0.15$ . This might be possibly related to the different chemistry of these two cations on reduction and oxidation within the battery or to the structure effect seen in the XRD characterisation of starting material.

It is worth noting that in the plot of capacity versus  $y$  the titanium substitution shows a decrease in capacity but does not show linearity as can be seen in **Fig.: 5-32**.

The anomalies seen in the capacity behaviour might correlate with the anomalous behaviour observed in the plot of the cell parameter versus  $y$ . This might be related as well to an error on the mass of the active material or to possible unreacted material.

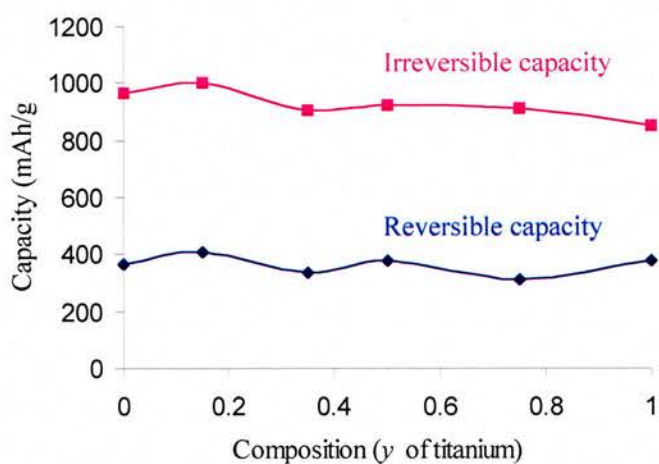


Fig.: 5- 32 Irreversible and reversible capacities plot versus composition of  $\text{Sn}_{1-y}\text{Ti}_y\text{P}_2\text{O}_7$  cycled galvanostatically (with a current density of  $0.1\text{mA}/\text{cm}^2$ ).

### 5.10. Conclusion.

The crystallographic structure and the electrochemistry of the  $\text{Sn}_{1-y}\text{Ti}_y\text{P}_2\text{O}_7$  system with  $0 < y < 1$  were investigated in this chapter. Structurally, there was no alteration of the  $3 \times 3 \times 3$  short range superstructure over all the range. It is noteworthy that for  $y = 0$  the structure has nanodomains, but not long range order. By about  $y = 4$  the average structure also shows long range order.

On substitution, a discontinuity around  $y = 0.4$  in a Vegard's slope seems to indicate some form of symmetry or phase change. This is due to the short range ordering that generates nanodomains depending on the size of the cation.

IR experiments show a change in position depending on the ratio of titanium or tin for the vibration mode related to the  $\nu_s(\text{P-O-P})$ . However a smooth parabolic variation was observed for the metal oxygen vibration mode  $\nu(\text{M-O})$ .

The electrochemistry of  $y = 0$  is very different from that of  $y = 1$  despite the similarity in the crystallographic structure. A SPECS experiment has emphasised the multi-step reduction through different mechanisms leading to biphasic regions and solid solution regions. These phase changes are supported by in-situ XRD experiment and NMR.

$\text{TiP}_2\text{O}_7$  upon discharge shows multi-step reductions that are titanium based from  $\text{Ti}^{\text{IV}+}$  to  $\text{Ti}^{\text{III}+}$  ( $\text{LiTiP}_2\text{O}_7$ ) from the OCV down to 1.4V, followed by bi or

multiphase mechanisms to 0.6V plateau. These multiphase mechanisms are more likely consistent with the reduction of  $Ti^{III+}$  to  $Ti^{II+}$  coupled with the phosphate reduction from  $P^{V+}$  to  $P^{IV+}$ . This suggests nanocomposite ionic phase such as  $Li_4Ti^{II+}P_2O_7$  where only the titanium is redox active. After the 0.6V plateau, the lithium uptake in this region down to 0.02V is possibly related to the polymeric layer SEI or an “interfacial mechanism”.

For the mixed system  $y = 0.5$ , SPECS experiment has shown both chemistry related to  $SnP_2O_7$  as well as  $TiP_2O_7$ . The titanium is subject to a multi-step reduction from  $Ti^{IV+}$  to  $Ti^{III+}$  down to 1.6V. After at 1.3V, the plateau of tin reduction from  $Sn^{4+}$  to  $Sn^0$  can be observed. The reversible capacity is higher than for Sn-Li alloys and so thought that titanium in the system might be reduced further than  $Ti^{III+}$  leading to  $Ti^{II+}$ .

For comparison, the galvanostatic experiment of  $y = 0, 0.15, 0.35, 0.5, 0.75$  and 1 show the best irreversible and reversible capacity for  $y = 0.15$  with a 100% capacity retention after 10 cycles and an increase of 10% of the capacity over  $SnP_2O_7$ .

From this study it was found that slight substitution of titanium in  $SnP_2O_7$  does improve both irreversible and reversible capacity but more investigation is needed to fully understand the variation of the capacity with composition, which probably is in relation with crystallographic structure.

5.11. References.

- <sup>1</sup> J. Sanz, J. E. Iglesias, J. Soria, E.R. Losilla, M. A. G. Aranda, S. Bruque, *Chem. Mater.* **9**, 996-1003 (1997).
- <sup>2</sup> E. Tillmanns, W. Gebert, *J. of Solid State Chemistry* **7**, 69-84 (1973).
- <sup>3</sup> N. Khosrovani, V. Khorthuis, A. W. Sleight, T. Vogt, *Inorg. Chem.* , **35**, 485-489 (1996).
- <sup>4</sup> R. Hubin, P. Tarte, *Spectrochimica Acta*, **23A**, 1815-1829 (1967).
- <sup>5</sup> H. Li, P. Balaya, J. Mayer, *J. Electrochem. Soc.*, **151** (11), A1878-A1885, (2004)
- <sup>6</sup> A. D. Robertson, H. Tukamoto, J. T. S. Irvine, *J. Electrochem. Soc.*, **146** (11), 3958-3962 (1999).
- <sup>7</sup> V. Eshkenazi, E. Peled, L. Burstein, D. Golodnitsky, *Solid State Ionics* **170**, 83-91 (2004).
- <sup>8</sup> M. E. Arroyo y de Dompablo, A. Varez, F. Garcia-Alvarado, *J. Solid State Chem.* **153**, 132-139 (2000).
- <sup>9</sup> S. Scharner, W. Wepper, P. Schmid-Beurmann, *J. Electrochem. Soc.*, **146**(3) 857-861 (1999).
- <sup>10</sup> Y. Uebou, S. Okada, M. Egashira, J. I. Yamaki, *Solid State Ionics* **148**, 323-328 (2002).
- <sup>11</sup> S. Patoux, C. Masquelier, *Chem. Mater.* **14**, 5057-5068 (2002).
- <sup>12</sup> A. Khun, R. Amandi, F. Garcia-Alvarado, *J. Power Source* **92**, 221-227 (2001).

- <sup>13</sup> S. Y. Huang, L. Kavan, I. Exnar, M. Grätzel, *J. Electrochem. Soc.*, **142**, 143-143 (1995).
- <sup>14</sup> C. Delmas, A. Nadiri, J. L. Soubeyroux, *Solid State Ionics* **28-30**, 419-423 (1988).
- <sup>15</sup> B. V. R. Chowdari, G. V. Subba Rao, G. Y. H. Lee, *Solid State Ionics*, **136-137**, 1067-1075 (2000).
- <sup>16</sup> [www.lasurface.com](http://www.lasurface.com)
- <sup>17</sup> J. C. Dupin, D. Gonbeau, I. Martin-Litas, P. Vinatier, A. Levasseur, *J. Electron Spectroscopy and Related Phenomena* **120**, 55-65 (2001).
- <sup>18</sup> K. Edström, T. Gustafsson, J. O. Thomas, *Electrochimica Acta*, **50**, 397-403 (2004).
- <sup>19</sup> G. K. Wertheim, P. M. Van Attekum, S. Basu, *Solid State Commun.*, **33**, 1127 (1980).
- <sup>20</sup> L. Kavan, J. Procházka, T. M. Spitler, M. Kalbáč, M. Zúkalová, T. Drezen, M. Grätzel, *J. Electrochem. Soc.*, **150(7)**, A1000-A1007 (2003).
- <sup>21</sup> P. Poizot, S. Laruelle, S. Grugeon, L. Dupont, J-M. Tarascon, *Nature* **407**, 496-499 (2000).
- <sup>22</sup> A. Shaim, M. Et-tabirou, *Materials Chemistry and Physics*, **80**, 63-37 (2003).

## 6. Conclusion.

This work has investigated the lithium insertion behaviour of a range of polyanionic materials;  $M^{4+}-XO_n^{n-}$ , where  $M = \text{Sn, Ti}$  and  $X = \text{P, B}$ . Materials or systems such as  $\text{SnP}_2\text{O}_7$ ,  $\text{SnO}_2:\text{B}_2\text{O}_3$ ,  $(\text{SnO}_2:\text{B}_2\text{O}_3)_{y/2}/(\text{SnP}_2\text{O}_7)_{1-y/2}$  (with  $0 < y < 2$ ),  $\text{Sn}_{1-y}\text{Ti}_y\text{P}_2\text{O}_7$  (with  $0 < y < 1$ ) and  $\text{TiP}_2\text{O}_7$ , were synthesised and studied using several characterisation techniques.

When substituting borate for pyrophosphate species in the  $\text{SnP}_2\text{O}_7$  parent phase, observations from  $^{31}\text{P}$  and  $^{11}\text{B}$  MAS NMR, XRD and SEM experiments have allowed us to construct a phase diagram for the series of materials. In this series, our studies found three distinct structural regions, crystalline, amorphous and a mixed phase region.

The boron doped  $\text{SnP}_2\text{O}_7$  system has shown less capacity than  $\text{SnP}_2\text{O}_7$ , which shows the importance of the matrix in the electrochemical performance of the material. It also shows that the phosphate matrix is more suitable for lithium battery applications than its borate analogue.

It was found by means of XRD and electron microscopy that  $\text{SnP}_2\text{O}_7$ ,  $\text{TiP}_2\text{O}_7$  and  $\text{Sn}_{1-y}\text{Ti}_y\text{P}_2\text{O}_7$  doped system (with  $0 < y < 1$ ) are isostructural, exhibiting a  $3 \times 3 \times 3$  superstructure. However, two distinctive linear variations of the unit cell are observed with substitution. Nanodomains were found for the  $y = 0$  material ( $\text{SnP}_2\text{O}_7$ ) but no evidence of nanodomains for the  $y = 1$  material ( $\text{TiP}_2\text{O}_7$ ). This is

assumed to be related to the short range ordering that generates nanodomains depending on the size of the cation. When the octahedra are large, as in the case of  $\text{SnO}_6$ , octahedral tilting or distortion may lead to the observed nanodomains and the resulting distorted cubic superstructure.

The lithium insertion mechanism of the entire series of samples were investigated and elucidated. Electrochemical measurements have shown that titanium doping of  $\text{SnP}_2\text{O}_7$  is seen to increase the reversible capacity, the best capacity was observed for the  $y = 0.15$  sample with 10% increase over  $\text{SnP}_2\text{O}_7$ . The electrochemistry has shown two different chemistries, lithium alloying into tin for  $\text{SnP}_2\text{O}_7$  and a non alloying mechanism into titanium. It was also shown that these different chemistries coexist in the mixed system.

These materials have shown very interesting chemistry that is worthwhile to be studied in a reduced phosphate matrix. This matrix facilitates very high cyclability in the case of tin. Although less than the tin, the titanium still shows a remarkable degree of reversible reaction. It will be interesting in the future to probe other cations in this matrix.